A BAYESIAN APPROACH TO UNDERSTANDING MULTIPLE MINERAL PHASE AGE SPECTRA AND REASSESSMENT OF THE ^{40}K DECAY MODES

Jack Carter

Submitted in Fulfilment of the Requirements for the Degree of Doctor of Philosophy

University of Glasgow

Scottish Universities

Environmental Research Centre

April 2021

Abstract

The application of $^{40}Ar/^{39}Ar$ geochronology is extensive. Geological ages have been determine for events spanning from the Early Solar system to recent historical volcanic eruptions. The ubiquity of the parent isotope ^{40}K means this method is also applicable across all of the terrestrial planets and their satellites. However, the technique has limitations. The aim of this thesis is to address two limitations; (1) Is it possible to obtain meaningful ages from multiple grain assemblages that contain multiple ages and phases? and (2) Does the ^{40}K decay constant need revisiting?

To address this first question I develop a Bayesian modelling framework to fit both the age spectrum and cumulative release of ^{39}Ar, the parameters that best describe the data (e.g., the age, diffusion kinetics, and mixture weights) are inferred. Chapter 2 sets out this modelling framework and shows that for simple mixtures with highly informative priors it is possible to infer geologically meaningful information. Despite this I make a number of limiting assumptions that are address in Chapter 3. Chapter 3 shows an extension of this method to a non-parametric framework where the number of distinct age components is also treated as an unknown. By modelling a range of mixtures I show that is it possible to get ages of geological meaning with the limited prior information available in nature. The final part of this research question invloves establishing the sources of the glacial flood sediments from Moses Coulee and Ephrata fan. These sediments are linked to the catatrophic flooding of fresh water across the Columbia Basin, down the Columbia River and outwashing to the Pacific Ocean during the last ice-age. During the period from ∼22000 to ∼13000 years ago, there were potentially hundreds of such flooding events in the region. I use the non-parametric Bayesian model to estimate components age of both sediments to link back to known source lithologies. The determination of Mesoprotezeroic age components in both samples requires that glacial Lake Missoula is a source of both of these samples. These data and model output may also suggest that the Moses Coulee formed before the Grand Coulee or that the glacial megafloods in the Pacific Northwest were larger than previous estimations.

The second concern address the ^{40}K decay constant. In this section I create a theoretical argument based on energy conservation to illicit the inclusion of an electron capture (EC) to ground state decay mode. This decay mode has been ignored in previous studies due to a lack of experimental verification. I used the theory of β decay to estimate the strength of this decay mode and show that by the inclusion of the decay K-Ar ages ($\leq$1 Ga) may shift by 2% to be younger than previously estimated.

Dedication

To my Mum and Dad.

Acknowledgements

Completing this PhD would only have been possible with the help and guidance that I have received throughout a long, and a some points difficult, journey. In particular I would like to thank both Prof. Darren Mark and Prof. Marissa Tremblay for being great advisors and pushing me to do better work. I would further like to thank them for teaching me the basics of geology, for which I started out knowing nothing. Thank you so much for putting up with me for 4 years.

A special thanks also to Ross Dymock, the Argon lab technician. I am geniunely not sure where I would have been without your help and I'm happy to call you a friend as well as a colleague.

Further thanks to Anne, Vinnie, and Kathy technicians in SUERC. To the many tea breaks, laughs and the ability you all have to keep spirits up. I'm so happy to have worked with you and thank you for laughing at my awful jokes.

To the researchers at SUERC, in particular Katie Preece, Sevi Modestu, Annemarie Pickersgill, and Ben Cohen. Thank you for all your help throughout and answering my most basic questions.

A special thanks also to Dr. Ryan Ickert for introducing interesting concepts, showing off the cool lab instruments, highlighting big picture problems and seeding the idea for a re-evaluation of the potassium decay scheme.

To Rasika, we started of Phd's at the same time, we've been to three different continents together, we've been on fieldwork, (I never thought I'd ever have done field work, especially not on Mull where I have never seen rain) and you have been my office mate throughout. I can't even begin to thank you for all help you've given me and I can only hope that I've manage to give you even a morsel in return. Thank you for putting up with me for 4 years. I know how annoying I can be.

Thanks to Joel Gombiner for Missoula flood sample which brought the mathematical modelling together with geology.

Finally, thank you Mum, Dad, and my sister Charlotte. I know you switch off whenever I talk about science but you've help without knowing for which I will always be grateful.

Declaration

I declare that, except where explicit reference is made to the contribution of others, that this dissertation is the result of my own work and has not been submitted for any other degree at the University of Glasgow or any other institution.

John Carter

Contents

1 Introduction **18**

1.1 Introduction 18

1.2 $^{40}Ar/^{39}Ar$ geochronology 19

1.2.1 Experimental limitations 20

1.2.2 Geological complexities 20

1.2.3 Overcoming limitations and complexities 23

1.3 ^{40}K decay 26

1.4 Aims and Objectives 28

1.5 Thesis Outline 29

2 A Bayesian approach to the deconvolution of $^{40}Ar/^{39}Ar$ data from mineral mixtures **31**

2.1 Introduction 31

2.2 Methods 36

2.2.1 Phenomenology represented in the model 36

2.2.2 Bayesian framework 38

2.3 Results 41

2.3.1 Case study 1: VanLaningham & Mark (2011) 41

2.4 Case study 2: Kula et al. (2010) 50

2.5 Case study 3: a hypothetical *in-situ* Martian experiment 55

2.6 Discussion 59

2.6.1 Model fits and parameter estimation 60

2.6.2 Comparison to other approaches 66

2.6.3 Future work 67

2.6.4 Applications 70

2.7 Conclusions 72

3 Stepwise heating of $^{40}Ar/^{39}Ar$ blind mixtures with applications to bulk sediment provenance studies **75**

3.1 Introduction . . . 75

3.2 Expectation of Arrhenius and age spectra datasets from the stepheating of mineral assemblages . . . 77

3.3 Model . . . 80

3.3.1 Bayesian inference . . . 81

3.3.2 Stick-breaking process . . . 82

3.3.3 Occam's Razor . . . 83

3.3.4 $^{40}Ar/^{39}Ar$ non-parametric Bayesian model . . . 85

3.3.5 Sampling . . . 90

3.4 Blind Mixtures . . . 90

3.5 Results . . . 95

3.5.1 Madagascar orthoclase . . . 97

3.5.2 Pennsylvania labradorite . . . 99

3.5.3 Oregon labradorite . . . 101

3.5.4 Benson Mine orthoclase . . . 103

3.5.5 JC anorthite . . . 105

3.6 Model testing . . . 107

3.6.1 Alder Creek sanidine . . . 108

3.6.2 Heidelberg biotite and Alder Creek sanidine . . . 110

3.7 Blind Mixture Results . . . 112

3.7.1 Blind Mixture 1 . . . 113

3.7.2 Blind Mixture 2 . . . 114

3.7.3 Blind Mixture 3 . . . 115

3.7.4 Blind Mixture 4 . . . 116

3.7.5 Blind Mixture 5 . . . 117

3.8 Discussion . . . 117

3.9 Conclusion . . . 121

4 Reconstructing the source of Pleistocene glacial megafloods in North America **122**

4.1 Introduction . . . 122

4.2 Glacial Lake Missoula megafloods . . . 123

4.3 Study areas . . . 127

4.3.1 Moses Coulee . . . 128
4.3.2 Ephrata Fan . . . 129
4.4 $^{40}Ar/^{39}Ar$ as a provenance tool . . . 130
4.5 Methods . . . 132
4.6 Results . . . 133
4.6.1 Ephrata Fan results . . . 133
4.6.2 Moses Coulee results . . . 136
4.6.3 Data Summary . . . 139
4.7 Model . . . 142
4.8 Modelling results . . . 143
4.8.1 Ephrata Fan . . . 144
4.8.2 Moses Coulee . . . 147
4.9 Discussion . . . 153
4.9.1 Provenance of the Moses Coulee and Ephrata Fan sediments . . . 153
4.9.2 Glacial megafloods of the Pacific NorthWest . . . 155
4.9.3 Broader implications for bulk sediment provenance studies . . . 157
4.10 Conclusion . . . 158

5 Production of ^{40}Ar by an overlooked decay mode of ^{40}K with implications for K-Ar geochronology 159

5.1 Introduction . . . 159
5.2 ^{40}K decay . . . 159
5.3 Historical Overview . . . 161
5.4 Why there must be an EC_{ground} decay mode . . . 162
5.5 Theory and calculation of EC_{ground}/β^+ . . . 163
5.6 Comparison with other evaluations . . . 167
5.7 ^{22}Na . . . 169
5.7.1 Comparison with ^{22}Na . . . 169
5.8 Experimental verification of EC_{ground} decay mode . . . 171
5.8.1 X-ray counting experiments . . . 172
5.8.2 Conclusions and recommendations from SUERC counting experiment . . . 173
5.9 Relevance for geochronology . . . 174
5.10 Conclusion . . . 177

6 Final insights and further uses of Bayesian methods in $^{40}Ar/^{39}Ar$ geochronology **178**

6.1 Introduction 178

6.2 Final thoughts and insights 178

6.3 Model and experimental improvements 180

6.4 Further uses of Bayesian inference in $^{40}Ar/^{39}Ar$ geochronology 181

6.4.1 Age spectrum, Arrhenius array, and K/Ca spectrum 181

6.4.2 Turning the Bayesian crank on provenance studies 183

A Appendix **185**

Bibliography **211**

List of Tables

2.1 Deconvolution model results for the VanLaningham & Mark (2011) mixtures, compared to known ages for mixture 47

2.2 Modeled ages, using both nonrestrictive and restrictive priors for muscovite components in mixtures created by Kula et al. (2010), with comparison to known ages. 55

2.3 Modeled ages, using both nonrestrictive and restrictive priors for biotite components in mixtures created by Kula et al. (2010), with comparison to known ages. 55

2.4 Estimated parameter values for a hypothesised Martian mixture. 58

3.1 Individual component age used in the blind mixture study.a Renne et al. (1998). 92

3.2 Model ages inference from the nonparametric model output compared to the individual component ages measured by VanLaningham & Mark (2011). 111

3.3 Results of blind mixture study. Number of inferred components, ages of the components and then guess of the components are shown compared to the known mixture components. 119

4.1 Summary of the model inferences for the Ephrata Fan sediments 147

4.2 Summary of the model inferences for the Moses Coulee sediments . . . 152

5.1 Evaluations of decay mode branches and total decay constant used in age determination. $\lambda_{^{40}Ar}$ is the partial decay constant for the ^{40}Ar branch, including both the EC* and EC_{ground} components. Uncertainties from the β^+/β^- and $\mathrm{EC}_{ground}/\beta^+$ do not substantially change the uncertainties in $\lambda_{^{40}Ar}$ or λ_TT. 175

A.1 Ages assumed for the synthetic two-component muscovite mixture, and estimated ages of each component from our Bayesian inversion 195
A.2 Blind mixture 1 data 196
A.3 Blind mixture 2 data 197
A.4 Blind mixture 4 data 198
A.5 Blind mixture 5 data 199
A.6 Blind mixture 6 data 200
A.7 18-IAF-09S-EPH step heating data 201
A.8 18-IAF-10S-EPH step heating data 202
A.9 18-IAF-09S-EPH (silt) step heating data 203
A.10 18-IAF-05-MOS step heating data 204
A.11 18-IAF-05-MOS (silt) step heating data 205
A.12 18-IAF-06-MOS step heating data 206
A.13 18-IAF-06-MOS (silt) step heating data 207
A.14 18-IAF-05-MOS (64 - 125μm step heating data 208
A.15 18-IAF-06-MOS (64 - 125μm step heating data 209

List of Figures

1.1 Alder Creek sanidine age spectra 19
1.2 Example age spectra adapted from Rex et al. (1993) 21
1.3 Example age spectra adapted from Kula & Baldwin (2011) 22
1.4 Example Arrhenius displaying the results of heating of simple and complex datasets. 24
1.5 Potassium decay scheme adapted from McDougall & Harrison (1999) . 28

2.1 Age spectra created by VanLaningham & Mark (2011) and Bayesian posterior model results. 42
2.2 Arrhenius plot for mixture 2 (75% ACs and 25% HD-B1 by mass) . . . 44
2.3 Prior information used in our Bayesian deconvolution of mixture 2 . . . 45
2.4 Comparison of cumulative argon release observed and model predicted . 47
2.5 Log likelihood of each model age spectra (L1) and cumulative release spectra (L2), as well as the summed log likelihood (L1 + L2), for mixture 2 of VanLaningham & Mark (2011) 48
2.6 Pair plot showing the posterior sampling of each component's age (Ma), activation energy (E_a, kJ/mol) and frequency factor (cm^2s^{-1}) for mixture 2 49
2.7 Age spectra (**A**, **B**, **C**) and cumulative release curves (**D**, **E**, **F**) of muscovite mixtures created by Kula et al. (2010) 53
2.8 Age spectra (**A**, **B**, **C**) and cumulative release curves (**D**, **E**, **F**) of biotite mixtures created by Kula et al. (2010) 54
2.9 (**A**) Mineral abundances in weight % of the Murray mudstone formation measured by CheMin at Telegraph Peak, after Rampe et al. (2016) . . 57
2.10 Individual cumulative release curves for the three K-bearing components in our synthetic Martian regolith dataset: jarosite, plagioclase, and sanidine 58

3.1 Age spectra and Arrhenius array of blind mixture 1 80
3.2 Age spectra and Arrhenius array of Alder Creek sanidine (VanLaningham & Mark (2011)) 84
3.3 Absolute test log probabilities of the age spectrum and Arrhenius dataset of the HD-B1 and ACs mixture 87
3.4 Prior for the number of components in the model 88
3.5 Priors used for parameters in blind mixture models 89
3.6 Age spectra of the individual components used to make the blind mixtures in this study 92
3.7 Age spectra of all step-heated blind mixtures analysed in this study . . 94
3.8 Visualisation of all blind mixture incremental heating dataset using probability density plots 95
3.9 Arrhenius data of the blind mixtures 96
3.10 Individual component Arrhenius arrays of components used in the blind mixture study 97
3.11 Model results for Madagascar orthoclase 98
3.12 Number of domains and volumes for Madagascar orthoclase model . . . 98
3.13 Activation energy and Frequency far of Madagascar orthoclase 99
3.14 Model results for Pennslyvania labradorite 100
3.15 Number of domains and volumes for Pennslyvania labradorite 100
3.16 Activation energy and frequency factor for Pennslyvania labradorite . . 101
3.17 Data and model fit for Oregon labradorite 102
3.18 Number of domains and volumes for Oregon labradorite 102
3.19 Activation energy and frequency factor for Oregon labradorite 103
3.20 Data and posterior model for Benson Mine orthoclase 104
3.21 Number of domains and volumes for Benson Mine orthoclase 104
3.22 Activation energy and frequency factor for Benson Mine orthoclase . . 105
3.23 Data and posterior model for JC anorthite 106
3.24 Number of domains and volumes for JC anorthite 106
3.25 Activation energy and frequency factor for JC anorthite 107
3.26 Data and posterior nonparametric model for Alder Creek sanidine . . . 108
3.27 Number of components and component age for the nonparametric model of Alder Creek sanidine 109

3.28 Activation energy and Frequency factor for non-parametric Alder Creek sanidine model . . . 109
3.29 Data and posterior model for Heidelberg biotite and Alder Creek sanidine mixture . . . 110
3.30 Number of components, weights and ages for Heidelberg biotite and Alder Creek sanidine . . . 111
3.31 Model results for blind mixture 1 . . . 113
3.32 Model results for blind mixture 2 . . . 114
3.33 Model results for blind mixture 3 . . . 115
3.34 Model results for blind mixture 4 . . . 116
3.35 Model results for blind mixture 5 . . . 117
3.36 Figure showing the model output of the blind mixture datasets . . . 118

4.1 Maximum extent of the Laurentide and Cordilleran Ice Sheets across northwestern North America . . . 124
4.2 Overview map of U.S Pacific Northwest megaflood landscape, adapted from O'Connor et al. (2020) . . . 126
4.3 Geologic map of U.S Pacific Northwest megaflood landscape . . . 127
4.4 Digital elevtaion model of the study are labeled with the major physiographic features and locations of sampled sediment . . . 128
4.5 Photograph of the Moses Coulee samples from the Great Bar . . . 129
4.6 Photographs of the Ephrata Fan samples . . . 130
4.7 A Age spectrum and B Arrhenius array of the 18-IAF-09S-EPH sediment 134
4.8 Age spectrum and Arrhenius array of 18-IAF-10S-EPH . . . 135
4.9 Temperature for each step against the cumulative time for the experiment on 18-IAF-09S-EPH . . . 135
4.10 Age spectra and Arrehnius array for samples 18-IAF-05S-EPH . . . 137
4.11 Age spectrum and Arrhenius array of the 18-IAF-06S-EPH sediment . . . 138
4.12 Temperature for each step against the cumulative time for the experiment on 18-IAF-05S-MOS . . . 138
4.13 KDE of the stepheating datasets of the Ephrata Fan and Moses Coulee sediments . . . 139
4.14 Minimum and maximum ages for the Ephrata Fan datasets . . . 140
4.15 Minimum and maximum ages for the Moses Coulee datasets . . . 141
4.16 Age prior for both the Ephrata Fan and Moses Coulee sediments . . . 142

4.17 Model results for 18-IAF-09S-EPH 144
4.18 Model results for 18-IAF-10S-EPH 145
4.19 Model results for 18-IAF-10S-EPH (silt) 146
4.20 Model results for 18-IAF-05-MOS 148
4.21 Model results for 18-IAF-05-MOS (silt) 149
4.22 Model results for 18-IAF-06-MOS 150
4.23 Model results for 18-IAF-05-MOS (silt) 151
4.24 Figure showing the model output of all Ephrata Fan and Moses Coulee Samples 154
4.25 Potential flood pathways fulfilling the requirement that glacial Lake Missoula is a source of both Ephrata Fan and Moses Coulee flood sediments 156

5.1 Decay scheme of ^{40}K after McDougall & Harrison (1999) and Leutz et al. (1965) 162
5.2 Comparison of theoretically calculated (EC_{ground}/β^+) ratios of ^{40}K . . . 168
5.3 Decay scheme of ^{20}Na after Bé et al. (2006) and Leutz et al. (1965) . . 169
5.4 Comparison of experimentally measured (EC/β^+)* ratios of ^{22}Na (grey circles) adapted from Kunze et al. (1990) with our theoretically determined value (black solid line) 170
5.5 Spectra measured for the laboratory background (**A**), KCl spectra (**B**), and KCl with background subtracted (**C**) 172
5.6 Change in age, Δage, is the age of a given sample with the decay mode to ground state included, subtracted from the age with the decay mode to ground state omitted. 176

6.1 Age spectrum, the Arrhenius array, and the K/Ca spectrum of the Heidelberg biotite and Alder creek sanidine mixture created by VanLaningham & Mark (2011) 182
6.2 Model results of VanLaningham & Mark (2011) including K/Ca spectrum 182
6.3 Age, activation energy, and K/Ca values of each inferred component . . 183

A.1 Arrhenius plots for case study 1, wherein we re-analyze the mixtures of neutron fluence monitors reported by VanLaningham & Mark (2011)) . 186
A.2 Cumulative release spectra and models of all mixtures created by VanLaningham & Mark (2011) 186

A.3 Pair plot showing the posterior sampling of model parameters for mixture 1 . . . 187
A.4 Pair plot showing the posterior sampling of model parameters for mixture 3 . . . 187
A.5 Pair plot showing the posterior sampling of model parameters for mixture 4 . . . 188
A.6 Posterior age spectra and cumulative release spectra for case study 2 using the Kula et al. (2010) muscovite mixtures . . . 188
A.7 Posterior age spectra and cumulative release spectra for case study 2 using the Kula et al. (2010) biotite mixtures . . . 189
A.8 Pair plot showing the posterior sampling of model parameters for the 3:1 IV18:NY25 muscovite mixture . . . 189
A.9 Pair plot showing the posterior sampling of model parameters for the 1:1 IV18:NY25 muscovite mixture . . . 190
A.10 Pair plot showing the posterior sampling of model parameters for the 1:3 IV18:NY25 muscovite mixture . . . 190
A.11 Pair plot showing the posterior sampling of model parameters for the 3:1 IV8:PM1 . . . 191
A.12 Pair plot showing the posterior sampling of model parameters for the 1:1 IV8:PM1 . . . 191
A.13 Pair plot showing the posterior sampling of model parameters for the 1:3 IV8:PM1 . . . 192
A.14 Individual incremental and cumulative release spectra for a synthetic mixture of K-bearing minerals detected at Telegraph peak on Mars . . . 192
A.15 Pair plot showing the posterior sampling of model parameters for the synthetic Martian mixture . . . 193
A.16 Age spectrum for Mixture 2, case study 1, compared to posterior age spectra from two models, one assuming spherical geometry and the other an infinite sheet . . . 193
A.17 Comparison of modeled component ages of HD-B1 and ACs in Mixture 2, case study 1, using either a spherical geometry (horizontal axis) or an infinite sheet geometry (vertical axis) for HD-B1 . . . 194
A.18 Arrhenius plots from step degassing measurements Kula et al. (2010) . . . 194

A.19 Age spectrum for the synthetic two-component muscovite mixture (grey) and the mean posterior model from our Bayesian inversion of these synthetic data (red). 195

Chapter 1

Introduction

1.1 Introduction

Geochronology is the determining of the age and history of Earth's, and other terrestrial bodies, rocks and minerals. Such time determinations allow for the delineation of complex past geological events associated with early solar system events (e.g., Renne (2000)), mass extinctions (e.g., Renne et al. (2013)), historical observations (e.g., Renne et al. (1997)) and other processes. The K-Ar geochronometer is of particular usefulness due to the ubiquity of K and ∼1.25 Ga half life it can date material spanning from the early Solar System (∼4.5 Ga) to historical events (∼1 ka). Despite the decades of work in K-Ar geochronology there exist a number of limitations to its application. A particular limitation, and focus of this PhD study, is the geochronology of complex assemblages of minerals and ages. Such mineral assemblages are frequently observed in some of the most important geological locations on Earth (e.g., Indus and Bengal Fans, Channeled Scablands of the Northwestern USA, Himalayas, etc...). Currently, such samples are first prepared in order to separate into distinct phases before dating. However, there are a number of scenarios where this preparation is not possible, hence dealing with multiple mineral mixture is a necessity. In order to gain geologically meaningful information from such complex samples new techniques are required.

The focus of this PhD is to develop a method for unmixing complex mineral mixtures using Bayesian methods (**Hypothesis 1**). A second part of this thesis is the re-examination of the ^{40}K decay scheme (**Hypothesis 2**). I begin with an introduction to ^{40}Ar/^{39}Ar geochronology and current frameworks for dealing with complexities that arise from the mixing of multiple materials. Following this, I focus on the K-decay scheme and introduce the reason for re-examination.

1.2 $^{40}Ar/^{39}Ar$ geochronology

$^{40}Ar/^{39}Ar$ geochronology requires that Ar is released from a mineral under vacuum by heating or ablation, either using a laser or a furnace. Incremental step heating, which generally sees the temperature of a sample gradually increased during the course of an experiment, allows for multiple measurements of the $^{40}Ar^*/^{39}Ar_K$ ratio which is proportional to the apparent age of a mineral/rock. Such data are typically presented on an age spectrum (Figure 2), where the $^{40}Ar^*/^{39}Ar_K$ ratio observed during each heating step, is plotted as a function of cumulative ^{39}Ar release (Merrihue & Turner (1966)). If a reproducible $^{40}Ar^*/\ ^{39}Ar_K$ ratio (statistically indistinguishable at 2σ), as shown in Figure 1.1, is distributed across ca. 60% (Fleck et al. (1977)) of ^{39}Ar release, one can infer that the sample cooled geologically instantaneously, resulting in a plateau that is reported as a weighted mean by inverse variance of the steps comprising the plateau (McDougall & Harrison (1999)). This $^{40}Ar/^{39}Ar$ age is typically interpreted to be geologically meaningful (e.g., an eruption age for volcanic rock).

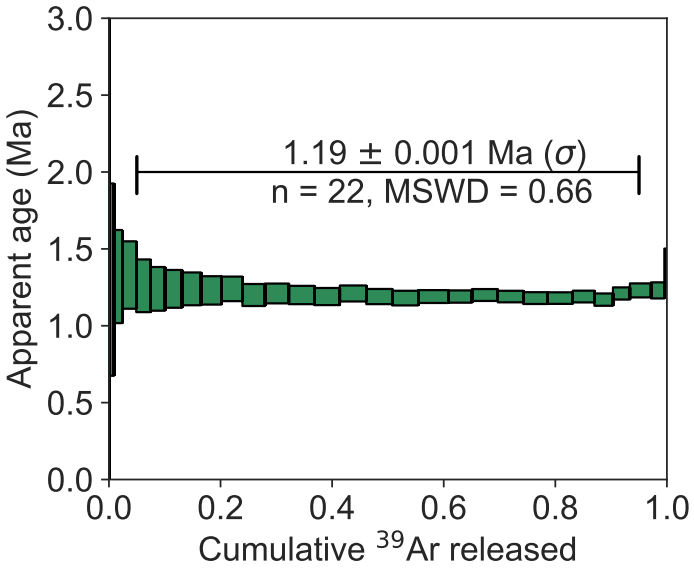

Figure 1.1: Age spectra of Alder Creek sanidine modified from VanLaningham & Mark (2011). Green boxes are the reported ages of each time temperature step. Data in the figure is at 1σ.

However, there exists a number of geological complexities and analytical limitations that prevent utilisation of the $^{40}Ar/^{39}Ar$ technique to all K-bearing minerals, rocks, sediments, and soils. It is the application of the $^{40}Ar/^{39}Ar$ technique to such complex

materials that has driven my interest and is the basis of my PhD research.

1.2.1 Experimental limitations

As the $^{40}Ar/^{39}Ar$ technique requires the transmutation of ^{39}K to ^{39}Ar via neutron activation $^{39}K(n,p)$ ^{39}Ar in the core of ^{235}U fission reactor the kinetic energy released from this reaction can displace the daughter product (^{39}Ar) from its original lattice site which can cause recoil-loss and recoil-redistribution (Jourdan et al. (2007)). It has been shown that the average ^{39}Ar recoil distance is ca. 0.08 μm (Onstott et al. (1995)) and therefore recoil can be problematic for $^{40}Ar/^{39}Ar$ dating of fine-grained materials (Paine et al. (2006)). Experimental artefacts due to recoil loss or redistribution of ^{39}Ar and ^{37}Ar (e.g., Onstott et al. (1995)) can yield age spectra release patterns with no apparent age significance (Turner et al. (1977)).

1.2.2 Geological complexities

Harrison (1983) reviewed some of the geological complexities and their effect on age spectra patterns (e.g., episodic gas loss or multiple episodic losses, phase changes, weathering, mixed phases). Age spectra may also be affected by sampling limitations, lack of mineral separation, large grain size distributions or the presence of multiple diffusion domains. In such situations, the conventional plateau method of interpretation is inappropriate. This has been demonstrated by a number of studies using artificial mixtures to explore the impact of multiple mineral components on age spectra. Rex et al. (1993) showed that mixing a hornblende with a younger biotite that was less retentive of Ar produced monotonically increasing age spectra (Figure 1.2), similar to the shape conventionally interpreted to reflect Ar diffusive loss during slow cooling (Turner (1968)).

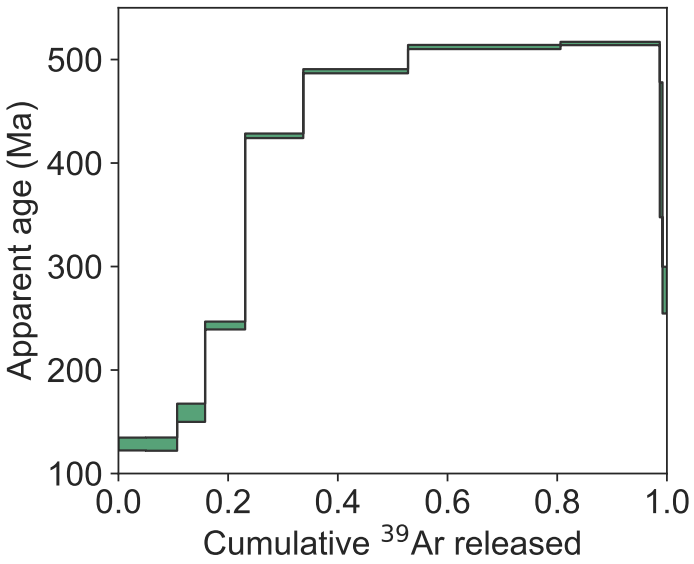

Figure 1.2: Age spectra adapted from Rex et al. (1993). Note the similarity in patterns between this synthetic mixture of a less retentive, younger biotite with an older hornblende and diffusive loss described by Turner (1968). This figure highlights the lack of validity in using the plateau method for datasets such as this.

Kula et al. (2010) mixed two muscovite samples and two biotite samples, each of different ages (Figure 1.3). Individually, muscovite and biotite samples yielded flat age spectra consistent with an interpretation of rapid cooling. However, when mixed and step heated, the muscovite samples yielded relatively flat intermediate-age plateaus with plateau age varying as a function of the mixing proportion, while the biotite mixtures yielded highly complex and discordant age spectra. In exploring the range of effects that degassing multiple mineral components simultaneously has on $^{40}Ar/^{39}Ar$ release spectra, these studies and others demonstrate that the conventional method of interpreting an age 'plateau' from $^{40}Ar/^{39}Ar$ release spectra is erroneous.

Although multi-component $^{40}Ar/^{39}Ar$ age spectra (Figures 3 and 4) cannot be interpreted via conventional methods, a number of different approaches have been attempted to maximise information recovery from the complicated age spectra resulting from mixtures. Among these, several are semi-quantitative or descriptive in nature. For example, Gillespie et al. (1982) model how, in a mixture of two minerals that have substantially different activation energies, the Ar from the two minerals is effectively separated by detailed step heating analyses. Gillespie et al. (1982) illustrate their model with both a theoretical age spectrum and an age spectrum of mixed fel-

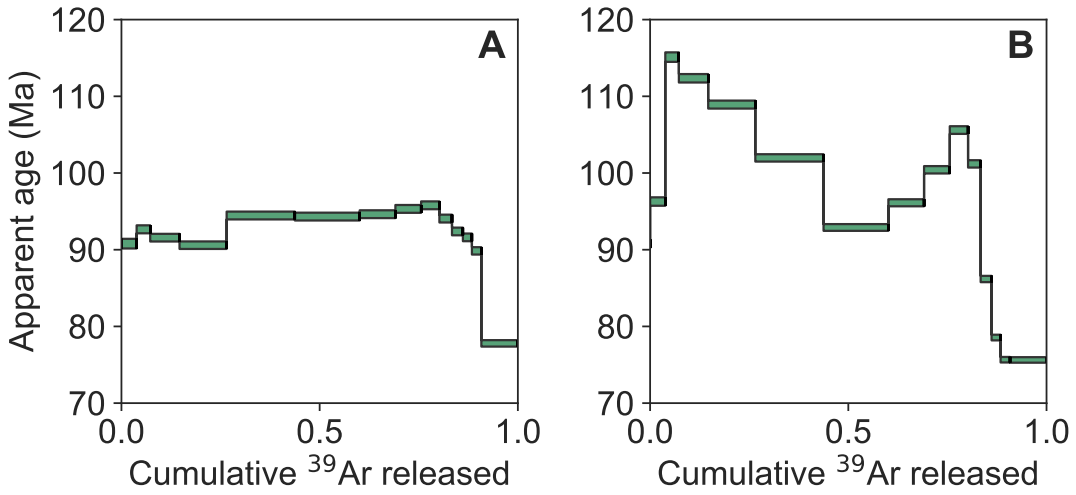

Figure 1.3: Example age spectra adapted from Kula & Baldwin (2011). A mixture of two muscovite samples are distinct ages $\sim$ 72 Ma and $\sim$ 148 Ma in 3:1 ratio of young to old. B mixture of two biotite samples of distinct ages $\sim$ 75 Ma and $\sim$ 145 Ma in 3:1 ratio of young to old.

sic minerals from a partially degassed granitoid xenolith in basalt. The application of the model in Gillespie et al. (1982) is limited to qualitative analysis of the two component age spectra with no direct fit of the data and no recovery of age information. Forster & Lister (2004) proposed a method to interpret complex age spectra from two-component mixtures of micas that involves statistically analysing age spectra for frequently measured ages (FMA) and using these FMAs to define asymptotes in the spectra. In their interpretation, an upward-converging age asymptote represents the minimum age of one component, while a downward-converging asymptote represents a maximum age of the other. While this method could be used to infer the presence of multiple mineral components, it only provides an upper or lower bound on the age of any mineral component; in cases where mineral components of the same phase are mixed, resulting in intermediate plateau ages, the recovered information may have no geological meaning (e.g., Kula et al. (2010)). VanLaningham & Mark (2011) created synthetic mixtures of well-constrained ^{40}Ar/^{39}Ar mineral standards, including Taylor Creek Rhyolite sanidine (TCRs), Alder Creek sanidine (ACs), Heidelberg biotite (HD-B1). The authors showed that the shape of the age spectra resulting from stepwise degassing of these samples could be predicted, but they do so with a great deal of prior knowledge about the different components (K concentration, ^{40}Ar/^{39}Ar age of the monitor minerals, Gaussian distributed release of Ar, and the mean and variance of the Gaussian release from the individual phases). VanLaningham & Mark (2011)

suggest that it may be possible to invert their age spectra to solve for the ages of the individual mineral components, should enough degassing steps be conducted during sample analysis.

1.2.3 Overcoming limitations and complexities

Several of the issues detailed above can be avoided by careful selection of samples, detailed petrographical characterisation, or robust and precise preparation of individual mineral components or development of novel experimental approaches. For example, ^{39}Ar and ^{37}Ar recoil from fine-grained materials led to the development of the vacuum encapsulation method (e.g., Dong et al. (1995)). Whereby $^{39}Ar_K$ and ^{37}Ar loss during neutron irradiation is trapped within a quartz vial which is later broken under vacuum to quantify the amounts of each isotope lost, and added to a samples ^{39}Ar and ^{37}Ar budget to calculate a total fusion ^{40}Ar/^{39}Ar age (Huneke & Villa (1981)).

Although the inability to separate mineral components in some geological materials can be tackled by performing high resolution step-heating experiments, this approach can only be used if the Ar diffusion kinetics of the different mineral phases are sufficiently contrasting (Jessberger et al. (1974), Dong et al. (2000)). Furthermore, by quantitatively measuring the temperature at each step by use of a furnace or laser co-axially aligned with an optical pyrometer another source of distinct information is available alongside the age spectra; the Arrhenius array (Figure 1.4). The Arrhenius array is derived by plotting the natural log of the diffusion coefficient against the inverse of the laboratory heating temperature obtaining estimates of the activation energy (E_a; proportional to the gradient) and frequency factor (D_0; proportional to the intercept). The diffusion coefficient is calculated from the inverse of the ^{39}Ar release function assuming a single diffusion length scale (Fechtig & Kalbitzer (1966)). In the degassing of a bulk sample, individual mineral diffusivities will be highlighted in Arrhenius space, for example the presence of multiple activation energies will be signified by a mixture of multiple slopes, the same is true for frequency factor derived from the intercept (D_0). It has further been acknowledged that the presence of multiple diffusivities can be highlighted through the use of more detailed heating patterns; both repeated and cyclic heating steps (e.g., Harrison et al. (1991)). In this thesis I use detailed heating schedules, greater than 50 steps in some cases, to extract the maximum amount of information from a sample mixture, this is combined by utilising both cyclic heating and isothermal heating steps following the summary of Harrison et al. (1991).

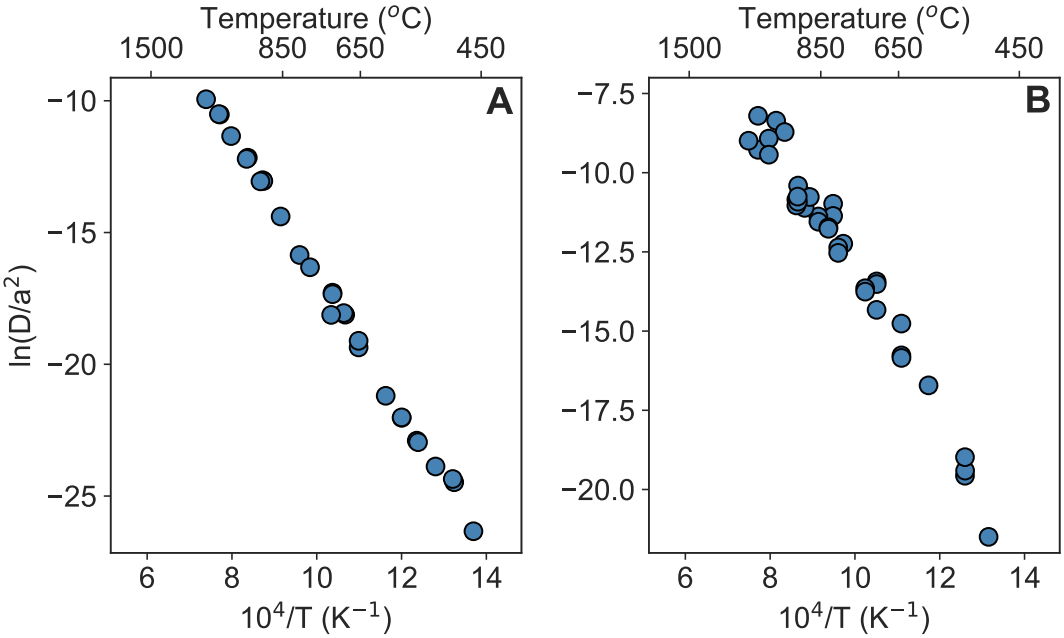

Figure 1.4: Example Arrhenius displaying the results of heating of simple and complex datasets. Panel A shows a modified Arrhenius array from Cassata & Renne (2013) of a single sandine sample. Panel B displays the Arrhenius array of a blind mixture sample analysed in Chapter 3 of this study. Note the differences in structure between each dataset. Panel A shows a simple linear array interpreted as Ar loss by simple volume diffusion. Panel B is far more complex with potentially multiple slopes and intercepts interpreted as the presence of multiple phases and curvilinear patterns which can results from multiple phases of differing diffusion kinetics or the presence of multiple domains (e.g., Lovera et al. (2002)). Uncertainties are smaller than the markersize in both datasets.

A number of studies have conducted incremental step heating on assemblages of minerals to varying degrees of success (e.g., Dong et al. (2000), Hemming et al. (2002), VanLaningham et al. (2006, 2008), Kula et al. (2010), VanLaningham & Mark (2011), Villaseñor et al. (2016)). Dong et al. (2000) developed a method of thermal separation by which high resolution step heating experiments on clay-like material can allow for separation of diagenetic and detrital components if release kinetics are suitably contrasted. VanLaningham et al. (2006) described a new method that characterised the bulk sediment of 14 Pacific Northwest rivers by the $^{40}Ar/^{39}Ar$ incremental heating method. The authors determined that the age spectra shape, determined by the specific mineral components of the bulk sediment, has the potential to be used as a means

of fingerprinting the contributions of each individual river into the continental margin. However, a direct estimate of age was not achieved. Both Kula et al. (2010) and VanLaningham & Mark (2011) presented studies of the analysis of synthetic mixtures to: (1) question the validity of mica age spectra by showing how mixing mica from different sources can dramatically affect the age spectra shape (Kula et al. (2010)), and (2) conduct a feasibility test of mixing neutron fluence monitors to attempt an un-mix apriori, the authors found that with a suite of prior information the age spectra could be reproduced by forward modelling (VanLaningham & Mark (2011)). Despite a wealth of studies, which have shown that useful temporal information is available from the stepwise heating of mineral assemblages, there lacks a modelling framework to fit the age spectra and extract "true" ages of each mineral component within multi-mineral mixtures.

A way forward with regards to dating multi-component mineral mixtures is to use a quantitative numerical approach. Such approaches have been used to interpret age spectra from multi-component mixtures. Each of these approaches is rooted in the Multiple Diffusion Domain model (MDD) originally formulated by Lovera et al. (1989). The MDD model was introduced to interpret complex $^{40}Ar/^{39}Ar$ age spectra from alkali feldspars that in many ways resemble age spectra from multi-component mineral mixtures. The MDD model assumes that individual K-feldspar crystals contain multiple diffusion domains that are non-interacting and are characterised by different diffusion length scales (Lovera et al. (1989, 2002)). In the case of multi-component mineral mixtures, different components essentially act as separate, non-interacting domains (which themselves might exhibit MDD behaviour). For example, Cassata et al. (2010) used the MDD model framework to interpret $^{40}Ar/^{39}Ar$ age spectra from polymineralic samples of Martian meteorites ALH84001 and Nakhla. These authors report multi-mineral phase MDD-type models that reproduce the ^{39}Ar and ^{37}Ar diffusivities calculated from step heating results. Cassata et al. (2010) then use these models to explore time-temperature histories consistent with the observed $^{40}Ar/^{39}Ar$ age spectra. Analogous multi-mineral phase MDD-type models have been implemented since (e.g., Shuster & Cassata (2015)). Although Cassata et al. (2010) and subsequent studies are able to find time-temperature histories that agree with their observed age spectra, their forward modelling approach is limited by subjective choices with regards to the diffusion kinetics, model fits and the range of time-temperature histories they explore.

Boehnke et al. (2016) also applied multi-mineral phase MDD type modelling to

interpret $^{40}Ar/^{39}Ar$ age spectra obtained from whole rock chips of the Jilin chondrite and the Apollo 16 lunar breccia 67514. In contrast to the forward modelling approach of Cassata et al. (2010), Boehnke et al. (2016) use a global optimisation algorithm to invert both the Arrhenius plot for multi-mineral phase MDD diffusion kinetics and the age spectra for time-temperature history. Their inversion method is able to resolve the observed age spectra and place constraints on the timing and duration of shock-related heating events. Of the existing numerical approaches to interpreting multi-mineral component mixtures, the Boehnke et al. (2016) approach is the least restrictive in terms of number of required assumptions. Nonetheless, their approach requires highly computational processes that prevent the direct estimation of uncertainty on parameters such as age and diffusion kinetics (Boehnke et al. (2016)). Based on the experiments of VanLaningham & Mark (2011) and the modelling approach of Boehnke et al. (2016), my work will test the hypothesis that through utilisation of temperature-controlled step heating and recovery of diffusion kinetics as well as $^{40}Ar^*/^{39}Ar$ age, a Bayesian model will be able to deconvolve complex multi-mineral component mixtures (e.g., sediments) (**Hypothesis 1**).

1.3 ^{40}K decay

The latter part of this thesis (Chapter 5) is a focus on the ^{40}K decay scheme. ^{40}K has a dual decay to ^{40}Ca and ^{40}Ar with the latter being the basis of the K-Ar dating technique. Due to the abundance of potassium bearing minerals and their importance in rock formation (McDougall & Harrison (1999)), the K-Ar chronometer is one of the most widely applied geologic tools. The K-Ar decay system is most often used by the variant $^{40}Ar/\ ^{39}Ar$ method, wherein some of the ^{39}K in the sample, the dominant stable isotope of K, is transmuted to ^{39}Ar by irradiation with fast neutrons, thereby allowing both the parent and the daughter nuclides to be measured as isotopes of Ar (Merrihue & Turner (1966)). Furthermore, the ∼1250 million year half-life (Aldrich & Nier (1948), Wasserburg & Hayden (1955)) and the ability to measure the isotope ratio of small amounts of Ar allows this method to be applied across the largest span of geological time; from volcanic eruptions recorded in historical literature (observed volcanic eruptions e.g., Preece et al. (2018), Renne et al. (1997)), to the earliest events in the solar system (e.g., Renne (2000)).

Despite decades of work and longstanding interest in ^{40}K decay, there remains

uncertainty over the nature of the decay scheme (Figure 1.5). There is a consensus that most ^{40}K decays by β^{-1} emission to ^{40}Ca or by electron capture to ^{40}Ar via an excited state, and that a small amount ($\sim$0.001 %) of ^{40}K decays to ^{40}Ar via positron emission. The early but influential review of ^{40}K decay by Beckinsale & Gale (1969) included these decay modes, and also included a prediction of a second electron capture decay directly to the ground state of ^{40}Ar that would add an additional $\sim$2% to the rate of decay from ^{40}K to ^{40}Ar, although this decay has never been observed experimentally.

Many subsequent workers both in nuclear physics and geochronology, have ignored this prediction. The influential review by Min et al. (2000) described this decay mode as "unverified" and having a "questionable" existence. As such, it is common for this decay mode to be ignored (e.g., Renne et al. (2010, 2011)) without sound scientific basis.

As part of my research I examine the ^{40}K decay modes and test the hypothesis that a second electron capture decay mode directly to the ground state of ^{40}Ar is a real and critical component of ^{40}K decay (**Hypothesis 2**) that is today overlooked. If this decay mode is real, it is vital that an assessment of the impact of this decay mode is made on modern ^{40}Ar/ ^{39}Ar ages collected using high-precision noble gas mass spectrometers. Age uncertainty (precision) has now reached a level whereby such changes in the decay constant of ^{40}K may be significant for multi-chronometer inter-comparisons (e.g., Mark et al. (2017)).

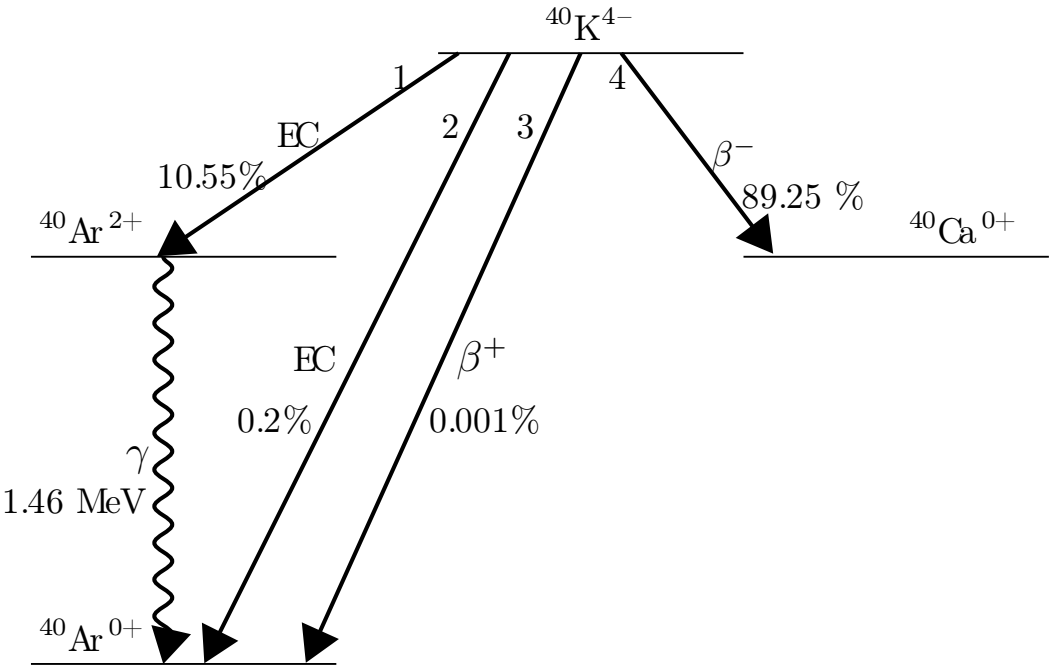

Figure 1.5: Potassium decay scheme adapted from McDougall & Harrison (1999). (1) Shows the electron capture to excited state decay of ^{40}Ar ($^{40}Ar^{2+}$) then followed immediately by γ emission de-excitation to the ground state of ^{40}Ar. (2) Direct decay to ^{40}Ar ground state via electron capture. (3) Direct decay by positron emission to ground state of ^{40}Ar. (4) Direct decay by beta emission to the ground state of ^{40}Ca, the basis of the K-Ca chronometer.

1.4 Aims and Objectives

In terms of organisation and structure, my thesis is divided into two sections: (1) a Bayesian approach to understanding multi-mineral phase age spectra; and (2) reassessment of the ^{40}K decay modes.

(1) A Bayesian approach to understanding multi-mineral phase age spectra.

Aim: To test Hypothesis 1 (above) through development of a robust Bayesian framework that can use prior information, $^{40}Ar/^{39}Ar$ age spectra and sample-specific diffusion kinetics to determine the ages of individual mineral components within a multi-mineral component mixture. Specific research objectives are:

- a) To use the data of VanLaningham & Mark (2011) to develop the Bayesian model and test the limitations of the approach across a range of scenarios.

- b) To test the accuracy of the model by conducting double-blind experiments and determining the ages of the individual mineral components within complex mineral mixtures.

- c) To apply the model to a real-world geological problem.

All code for these models can be found at https://github.com/jackcarter9/Thesis-Codes.

(2) Reassessment of the ^{40}K modes

Aim: To mathematically describe the theoretical basis of the predicted decay modes of ^{40}K to ^{40}Ar and test Hypothesis 2 (above), which states the ground state decay to ^{40}Ar age is a real and critical component of ^{40}K decay.

- a) Demonstrate the robust nature of ^{40}K decay mode predictions using analogous calculations for other radioisotopes.

- b) Design an experiment that could be utilised to test the mathematical basis for a ground state decay to ^{40}Ar.

- c) Quantify the impact of any changes in the ^{40}K decay constant to high precision ^{40}Ar/^{39}Ar geochronology.

1.5 Thesis Outline

This thesis consists of six chapters, with the current information being part of Chapter 1. Chapter 2 firstly provides a brief introduction to ^{40}Ar/^{39}Ar dating. The second section presents the Bayesian methods and I outline the multiple mineral component ^{40}Ar/^{39}Ar Bayesian model. The Bayesian model is then applied to three published

data sets: (1) mixtures of neutron fluence monitors (VanLaningham & Mark (2011)); (2) mixtures of both a pair of biotites and pair of muscovites created by Kula et al. (2010); and (3) synthetical step heating data for a Martian regolith sample with mineralogy defined by Rampe et al. (2016). I conclude this chapter with an evaluation of the Bayesian model, a comparison with other model approaches, a look to future development of the framework, and potential applications of this method.
Chapter 3 presents an extension of the model to a nonparametric framework. The premise of nonparametric modelling is explained and then formulated with respect to $^{40}Ar/^{39}Ar$ dating. The model is applied to step wise heated *'blind mixture'* datasets analysed in this study. The model output is then compared to what is *true* and a discussion of the nonparametric approach follows. Finally, I discuss potential applications of this model to non-conventional geological settings. Chapter 4 applies the general model principles of Chapter 3 to a geologically interesting case study: a glacial megaflood provenance investigation. Details of the experimental methodology are discussed. The most important conclusion from this study is that my analyses and interpretive framework show that bulk sediment provides an integrated provenance signal, which can be interpreted by using the formulated nonparametric Bayesian model.

Chapter 5 then introduces a section on the re-evaluation of the decay constant of ^{40}K. The nature of the decay is introduced, with an historical overview of the current usage in the field of geochronology. I then focus on the currently unobserved decay mode; electron capture directly to the ground state. A theoretical argument is put forward as to why this decay mode should exist and the influence of the inclusion of this mode is discussed for both the K-Ar and $^{40}Ar/^{39}Ar$ chronometers.

The final chapter, Chapter 6 concludes the thesis, summarising the key outcomes and detailing recommendations when utilising the approach I have defined to interpreting complex $^{40}Ar/^{39}Ar$ age spectra from mineral components. I finally discuss the possibility to extract even more meaningful information from the approach by using the Bayesian crank method and including more mineral specific datasets (i.e., the K/Ca spectrum).

Chapter 2

A Bayesian approach to the deconvolution of $^{40}Ar/^{39}Ar$ data from mineral mixtures

2.1 Introduction

In this Chapter I present a Bayesian model to interpret complex $^{40}Ar/^{39}Ar$ age spectra that are the result of mixing. I begin this Chapter with an introduction to $^{40}Ar/^{39}Ar$ analysis and conventional interpretative frameworks. I then formulate the Bayesian un-mixing model, and implement for the three case studies. The initial tests of this model are conducted on data from incremental heated mixtures of neutron fluence monitors created by VanLaningham & Mark (2011). Secondly, mixtures produced by Kula et al. (2010), which contain the same mineral phases with different ages, are tested as a potential limiting scenario. Finally, I interrogate a forward modelled age spectrum for a reconstructed Martian regolith sample as a geologically interesting case study.

The $^{40}Ar/^{39}Ar$ method is widely used to date geological events that span the entire 4.6 Ga of Solar System history (e.g., Renne et al. (1997), Renne (2000), Preece et al. (2018)). In most applications of the $^{40}Ar/^{39}Ar$ method, single mineral phases or phenocryst-free groundmass from igneous or metamorphic rocks are selected for analysis following standard sample preparation techniques that include acid leaching, magnetic separation and hand-picking under optical microscope (e.g., McDougall & Harrison (1999)). Isolating mineral phases for $^{40}Ar/^{39}Ar$ dating often, though not always, allows for straightforward interpretation of the resulting datasets.

$^{40}Ar/^{39}Ar$ data from step degassing measurements are typically presented and interpreted on an age spectrum plot, where the $^{40}Ar^*/^{39}Ar$ ratio ($^{40}Ar^*$ denoting radiogenic ^{40}Ar derived from the decay of ^{40}K) observed during each heating step, which is proportional to the apparent step age, is plotted as a function of cumulative ^{39}Ar release (Merrihue & Turner (1966)). If a reproducible $^{40}Ar^*/^{39}Ar$ ratio (heating steps that are statistically indistinguishable at 2 σ) and therefore age is reproduced in over 60% (Fleck et al. (1977)) of the ^{39}Ar continuous release, we typically infer that the sample cooled geologically instantaneously, resulting in a spatially uniform distribution of $^{40}Ar^*$. In such cases, we identify concordance from the age spectrum as a plateau. Once a plateau has been identified, we report the $^{40}Ar/^{39}Ar$ age of that sample as a weighted mean by inverse variance of the steps comprising the plateau (McDougall & Harrison (1999)), and this $^{40}Ar/^{39}Ar$ age is typically interpreted to be geologically meaningful (e.g., an eruption age for a volcanic rock).

We can also make geologic inferences about processes affecting the distribution of ^{40}Ar and therefore the $^{40}Ar^*/^{39}Ar$ release spectra in single mineral-component samples. For example, diffusive loss of $^{40}Ar^*$ for samples with single diffusion domains manifests as monotonically increasing steps in an $^{40}Ar/^{39}Ar$ spectra (Turner (1968)). Depending on the setup of the step degassing experiment, it is possible to calculate the kinetics of Ar diffusion in a sample from the release of reactor-induced ^{39}Ar or ^{37}Ar, which allows us to model the geologic time-temperature history that would result in the observed $^{40}Ar/^{39}Ar$ release pattern (e.g., Foland (1994), Cassata et al. (2010)). Recoil loss and excess ^{40}Ar also affect age spectra in predictable ways. Recoil loss of reactor-induced ^{39}Ar normally manifests as initial steps with high $^{40}Ar^*/^{39}Ar$ and old ages, due to ^{39}Ar loss from the edges of mineral grains, and lower $^{40}Ar^*/^{39}Ar$ and thus younger ages for high-temperature steps (Onstott et al. (1995)). Excess ^{40}Ar ($^{40}Ar_{ex}$), which is thought to be either inherited argon from older grain contamination or non-radiogenic ^{40}Ar contamination (Kelley (2002)), typically manifests as saddle shape release spectra with relatively high $^{40}Ar/^{39}Ar$ ratios at the beginning and end of step heating spectra (Lanphere & Dalrymple (1976)).

There are a number of potential applications of $^{40}Ar/^{39}Ar$ geochronology, however, for which mineral separation is not feasible. For example, $^{40}Ar/^{39}Ar$ dating is frequently utilized for provenance analysis of sediments and sedimentary rocks in tectonic and paleoclimate studies (Copeland & Harrison (1990), Hemming et al. (1998), Singer et al. (2004)), but at present is largely restricted to coarse-grained sediments for which

individual mineral grains can be obtained. Isolation of individual grains is difficult for fine-grained materials and even if such a separate could be produced, the amount of material would still preclude single grain analyses. Bulk sediment provenance analysis of fine-grained sediments via $^{40}Ar/^{39}Ar$ geochronology has been used to understand source changes through time in marine or lacustrine depositional environments (e.g., VanLaningham et al. (2006)), but owing to a lack of interpretive frameworks, interpretations are restricted to simply identifying changes in source region through time and not determining the ages of different mineral component ages. Extraterrestrial meteorite samples are another example where $^{40}Ar/^{39}Ar$ geochronology of multiple mineral phases is often required due to very small sample sizes. Similarly, potential *in-situ* rover-based $^{40}Ar/^{39}Ar$ geochronology on future missions to Mars, the Moon or other rocky bodies (e.g., Morgan et al. (2017)) would require analyses of multiple mineral phases, as sample preparation on such missions has been limited to simple sieving (Farley et al. (2014)).

For situations where single mineral components cannot be isolated, conventional interpretations of $^{40}Ar/^{39}Ar$ spectra are inappropriate. This has been demonstrated by a number of studies using artificial mixtures to explore the impact of multiple mineral components on age spectra. Rex et al. (1993) showed that mixing a hornblende with a younger biotite that was less retentive of Ar produced a monotonically increasing age spectra, similar to the shape conventionally interpreted to reflect Ar diffusive loss during slow cooling (Turner (1968)). Kula et al. (2010) mixed two muscovite samples and two biotite samples, each of different ages. Individually, muscovite and biotite samples yielded flat age spectra consistent with an interpretation of rapid cooling. However, when mixed and step heated, the muscovite samples yielded relatively flat intermediate-age plateaus with plateau age varying as a function of the mixing proportion, while the biotite mixtures yielded highly complex and discordant age spectra. In exploring the range of effects that degassing multiple mineral components simultaneously has on $^{40}Ar/^{39}Ar$ release spectra, these studies and others (discussed below) demonstrate that the conventional method of interpreting an age 'plateau' from an $^{40}Ar/^{39}Ar$ release spectra is erroneous. To extend $^{40}Ar/^{39}Ar$ to the realm of multi-component mineral mixtures it is clear that new analytical techniques are needed, I present a method based on Bayesian parameter inference to obtain the age(s) of each component in a multi-component mineral $^{40}Ar/^{39}Ar$ dataset. Firstly, I discuss prior modelling techniques to extract age information from muti-component mineral $^{40}Ar/^{39}Ar$ datasets and present

my model in the methods section.

Although multi-component $^{40}Ar/^{39}Ar$ age spectra cannot be interpreted via conventional methods, a number of different approaches have been attempted to maximise information recovery from the complicated age spectra resulting from the mixing of multiple reservoirs. Among these, several are semi-quantitative or descriptive in nature. For example, Gillespie et al. (1982) model how, in a mixture of two minerals that have substantially different activation energies, the Ar from the two minerals is effectively separated by detailed step heating analyses. Gillespie et al. (1982) illustrate their model with both a theoretical age spectra and an age spectra of mixed felsic minerals from a partially degassed granitoid xenolith in basalt. The application of the model in Gillespie et al. (1982) is limited to qualitative analysis of the two component age spectra with no direct fit of the data and no recovery of age information. Forster & Lister (2004) proposed a method to interpret complex age spectra from two-component mixtures of micas that involves statistically analysing age spectra for frequently measured ages (FMA) and using these FMAs to define asymptotes in the spectra. In their interpretation, an upward-converging age asymptote represents the minimum age of one component, while a downward-converging asymptote represents a maximum age of the other. While this method could be used to infer the presence of multiple components, it only provides an upper or lower bound on the age of any component; in cases where components of the same phase are mixed, resulting in intermediate plateau ages, the recovered information may have no geological meaning (e.g., Kula et al. (2010), VanLaningham & Mark (2011)) created synthetic mixtures of well-constrained $^{40}Ar/^{39}Ar$ mineral standards, including Taylor Creek Rhyolite sanidine (TCRs), Alder Creek sanidine (ACs), Heidelberg biotite (HD-B1). The authors showed that the shape of the age spectra resulting from stepwise degassing of these samples could be predicted, but they do so with a great deal of prior knowledge about the different components (K concentration, $^{40}Ar/^{39}Ar$ age of the monitor minerals, Gaussian distributed release of Ar, and the mean and variance of the Gaussian release from the individual phases). VanLaningham & Mark (2011) suggest that it may be possible to invert their age spectra to solve for the ages of the individual mineral components, should enough degassing steps be conducted during sample analysis.

Quantitative numerical approaches have also been used to interpret age spectra from multi-component mixtures. Each of these approaches is rooted in the Multiple Diffusion Domain model (MDD) originally formulated by Lovera et al. (1989). The MDD

model was introduced to interpret complex $^{40}Ar/^{39}Ar$ age spectra from alkali feldspars that in many ways resemble age spectra from multi-component mixtures (e.g., complex irratic patterns from multiple gas reservoirs). The MDD model assumes that individual K-feldspar crystals contain multiple diffusion domains that are non-interacting and are characterized by different diffusion length scales (Lovera et al. (1989, 2002)). In the case of multi-component mixtures, different components essentially act as separate, non-interacting domains (which themselves might exhibit MDD behavior). For example, Cassata et al. (2010) used the MDD model framework to interpret $^{40}Ar/^{39}Ar$ age spectra from polymineralic samples of Martian meteorites ALH84001 and Nakhla. These authors report multi-phase MDD-type models that reproduce the ^{39}Ar and ^{37}Ar diffusivities calculated from step heating results. Cassata et al. (2010) then use these models to explore time-temperature histories consistent with the observed $^{40}Ar/^{39}Ar$ age spectra. Analogous multi-phase MDD-type models have been implemented since (e.g., Shuster & Cassata (2015)). Although Cassata et al. (2010) and subsequent studies are able to find time-temperature histories that agree with their observed age spectra, their forward modelling approach is limited by subjective choices with regards to the diffusion kinetics model fits and the range of time-temperature histories they explore. Boehnke et al. (2016) also apply a multi-phase MDD type modelling approach to interpret $^{40}Ar/^{39}Ar$ spectra obtained from whole rock chips of the Jilin chondrite and the Apollo 16 lunar breccia 67514. In contrast to the forward modelling approach of Cassata et al. (2010), Boehnke et al. (2016) use a global optimization algorithm to invert both the Arrhenius plot for multi-phase MDD diffusion kinetics and the age spectra for time-temperature history. Their inversion method is able to resolve the observed age spectra and place constraints on the timing and duration of shock-related heating events. Of the existing numerical approaches to interpreting multi-component mixtures, the Boehnke et al. (2016) approach is the least restrictive in terms of number of required assumptions. Nonetheless, their approach requires computational intensive processes that prevented the direct estimation of uncertainty on parameters such as age and diffusion kinetics (Boehnke et al. (2016)).

In this Chapter I describe an approach for the deconvolution of multi-component $^{40}Ar/^{39}Ar$ age spectra using a Bayesian model. The overarching goals of the modelling are threefold: (1) to reproduce the age spectra generated during laboratory degassing, (2) to deconvolve the Ar released from each component, and (3) to determine the age of each component. To demonstrate the strengths and challenges of this approach,

I present three case studies. In each case study I use our Bayesian inversion model to quantitatively fit observed or simulated $^{40}Ar/^{39}Ar$ age and cumulative ^{39}Ar release spectra and recover the ages of the individual components in the mixture. In the first case study, I reevaluate $^{40}Ar/^{39}Ar$ step-heating data from mixtures of neutron flux monitor standards reported by VanLaningham & Mark (2011) as described above, using only prior knowledge about the number and composition of components in each mixture. The second case study utilises the mixtures of muscovite and biotite samples of different ages reported by Kula et al. (2010). I use this case study to demonstrate a limiting case for our approach, as I cannot effectively 'un-mix' the ages of components with the same composition without prior knowledge of both the mixing fraction and number of components. In the third case study, I use plausible compositions and ages for components in the Martian regolith to generate synthetic $^{40}Ar/^{39}Ar$ age spectra. I then use our Bayesian inversion method with reasonable priors to model these synthetic data. This case study demonstrates the utility of our method for interpreting complex $^{40}Ar/^{39}Ar$ data to obtain geologically meaningful ages from whole rock meteorite or mission-returned samples, or *in-situ* on potential future planetary exploration missions.

2.2 Methods

2.2.1 Phenomenology represented in the model

In order to develop a Bayesian approach to interpreting $^{40}Ar/^{39}Ar$ spectra from multi-component mixtures, we must first define models that represent the physical processes affecting the argon systematics in these mixtures. First, consider a single component in a mixture. For this individual component, I assume that the length scale of argon diffusion is defined by the grain size, and that the diffusion geometry can be approximated as a sphere with radius a. Although the assumption of a spherical geometry is a mathematical idealisation, it is a reasonable approximation for most mineral grains (Lovera et al. (1989), Harrison et al. (1991), Lovera et al. (2002), Gautheron & Tassan-Got (2010)). In addition to a spherical geometry, I also assume that diffusion is isotropic and that Fick's second law describes the distribution of argon in the system:

$$\frac{\partial C}{\partial t} = \frac{D(T)}{a^2}\Delta^2 C \tag{2.1}$$

Where C is the concentration of argon, t is time, D is the diffusivity, and T is temper-

ature. A Fickian diffusion model implies that argon will move from regions of higher concentrations to regions of lower concentrations. I assume the boundary condition that the concentration C at a distance a, the grain boundary, is zero. With this condition equation 2.1 can be solved for the fractional loss (f) of a diffusant as derived by Crank (1979) and then discretized by Fechtig & Kalbitzer (1966).

Following on from the assumption of Fickian diffusion, I also assume that the diffusion of Ar is thermally driven and that the temperature dependence of diffusivity D can be described with an Arrhenius relationship:

$$\frac{D(T)}{a^2} = \frac{D_0}{a^2}\exp\left(\frac{-E_a}{RT}\right) \tag{2.2}$$

Where D_0 is the frequency factor, E_a is the activation energy, R is the gas constant, and T and a are as defined above. The parameters E_a and D_0 are a function of a particular noble gas and mineral pair and control the temperature sensitivity of the system in question. In the case studies I present here, I also assume that each component of the mixture has cooled through its closure temperature over a geologically-instantaneous time interval and remained a closed system since, resulting in a spatially uniform distribution $^{40}Ar^*$. I also assume spatially uniform production of radiogenic ^{40}Ar and reactor-induced ^{39}Ar in individual components (i.e., no zonation of parent K). More complex process-based models can be incorporated into the Bayesian framework that I outline below. For example, I can use the same overall Bayesian framework to examine cases of a non-uniform distribution of $^{40}Ar^*$ in individual components (e.g., due to thermally-driven loss). I present simple, yet geologically reasonable cases, in order to gain a basic understanding of the Bayesian model behavior, which could be obscured by introducing more complex processes and boundary conditions.

With these assumptions, we can predict the age and cumulative release spectra for a single component with a laboratory heating schedule from equations 2.1 and 2.2, as we expect the fractional release of $^{40}Ar^*$ and ^{39}Ar to be essentially equivalent in each heating step (e.g., Foland & Xu (1990)). This mathematical framework for predicting the age spectra of individual components now allows us to consider the age spectra for multiple components. The multi-component age spectra problem can be treated as a mixture model, where the measured data is a linear combination of the end member distributions. Similar to detrital zircon and grain size distribution models, our data are non-negative with a mixing fraction, ϕ, that must sum to one (e.g., Sambridge & Compston (1995), Yu et al. (2016), Sharman & Johnstone (2017)).

Given these constraints, the generalized equation for a multi-component age (Eq. 2.6) and cumulative release (Eq. 2.5) spectra can be represented as:

$$\phi = \sum_{i=1}^{k} \phi_i = 1 \tag{2.3}$$

$$\mu = \sum_{i=1}^{k} \mu_i = \frac{\sum_{i=1}^{k} \phi_i F_i}{(\sum_{i=1}^{k} \phi_i F_i)} \tag{2.4}$$

$$F_m = \sum_{i=1}^{k} \phi_i F_i \tag{2.5}$$

$$\mathrm{Age}_m = \sum_{i=1}^{k} \mu_i \mathrm{Age}_i \tag{2.6}$$

where Age_m and F are the measured $^{40}Ar^*/^{39}Ar$ age and cumulative ^{39}Ar release of a particular heating step, μ_i, ϕ_i, Age_i, $\delta \mathrm{F}_i$, F_i are the mixing fraction, volume fraction, age, incremental and cumulative release curves of each component i in the mixture for i = (1, 2, ..., k components) respectively. Using these assumptions and physical representations for the argon systematics in multi-component mixtures, I developed a Bayesian framework to estimate the mixture fraction, diffusion kinetics, age spectra, and cumulative release spectra of each component from observed multicomponent age spectra and cumulative release spectra defined by equations 2.5 and 2.6.

2.2.2 Bayesian framework

Bayesian inference is a statistical technique that involves fitting a probability model to data in order to estimate parameters in the model (Gelman et al. (2013)). Central to Bayesian inference is Bayes theorem (Eq. 4) which states that the posterior probability $\mathrm{P}(\theta|y)$ or the probability of a model parameter θ given the data y, equals $\mathrm{P}(y|\theta)$ the likelihood of the data given the model parameters, multiplied by the prior probability of the model parameter, $\mathrm{P}(\theta)$ and divided by the probability of the data, P(y).

$$P(\theta|y) = \frac{P(y|\theta)P(\theta)}{P(y)} \tag{2.7}$$

The calculation of *P(y)* is often intractable for problems with many variables, although it can be solved for with nested sampling (Skilling et al. (2006)). However, because *P(y)* is a normalising constant that simply scales the posterior probability, Eq. 2.7 can

be recast as a proportionality relationship given as:

$$P(\theta|y) \propto P(y|\theta)P(\theta) \tag{2.8}$$

The advantage of the Bayesian approach is that our initial knowledge about model parameters are incorporated in probability density functions called priors P(θ). In cases where we know very little about the true value of a model parameter θ we can give that parameter a highly uninformed prior probability distribution; in cases where we have physical constraints on θ we can incorporate this information into P(θ). We obtain an estimate of the model parameters (the posterior), by updating our initial knowledge (the prior (P(θ)) conditional on our observations (the likelihood P(y | θ) and by drawing samples from the posterior (P($\theta|y$)).

For the multi-component $^{40}Ar/^{39}Ar$ problem, our observed data, y, are the age spectra and cumulative release spectra obtained from laboratory degassing experiments. Our model parameters θ include the activation energy E_a, frequency factor D_0, and grain size a, for Ar diffusion in each component, the age of each component Age, and the volume fraction, ϕ. The Bayesian proportionality relationship for the multi-component $^{40}Ar/^{39}Ar$ problem is as follows:

$$\begin{aligned} P(E_{a(i)}, D_{0(i)}, Age_{(i)}, a_{(i)}, \phi_{(i)}|y) \propto P(y|E_{a(i)}, D_{0(i)}, Age_{(i)}, a_{(i)}, \phi_{(i)}) \\ P(E_{a(i)}, D_{0(i)}, Age_{(i)}, a_{(i)}, \phi_{(i)}) \end{aligned} \tag{2.9}$$

where i represents each component in the mixture. We follow Gallagher (2012) by adopting a sum of squares for our log likelihood function for both of our age spectra (Eq. 2.10) and cumulative release spectra (Eq. 2.11) observations. These are expressed as follows:

$$L1 = -\frac{1}{2}\sum_{i=1}^{N}\left(\frac{\text{obs}_1 i - \text{model}_1 i}{\sigma_1 i}\right)^2 \tag{2.10}$$

$$L2 = -\frac{N}{2}ln(2\pi) - \frac{N}{2}ln(\sigma_s^2 i) - \frac{1}{2\sigma_{2i}^2}\sum_{i=1}^{N}(\text{obs}_{2i} - \text{model}_{2i})^2 \tag{2.11}$$

For the likelihood of the age spectra observation L1 (given in Eq. 2.10), obs_{1i} is the observed age, model_{1i} is the model predicted age, and σ_{1i} is the error in the observed age for each experiment time-temperature step i. In the case of the cumulative release spectra, we define our log likelihood to take the form of a normal distribution given by Eq. 2.11 (L2), wherein obs_{2i} is the observed cumulative ^{39}Ar release, model_{2i} is

the model-predicted cumulative ^{39}Ar release, and σ_{2i} the observation error for the cumulative ^{39}Ar release. Unlike the age spectra model, we have an observed uncertainty for each step, we include uncertainty in each step of the cumulative release model as a nuisance parameter, σ_{2i}, this is incorporated as a vector that is the same length of the data, N, that we then estimate with the Bayesian model. The total likelihood of the model is calculated by summing L_1 and L_2. Given the way in which we define both likelihoods, the age spectra likelihood carries the dominant weight in the likelihood summation ($L_1 + L_2$). This is illustrated in Figure 2.5.

To predict the observed age spectra and cumulative release spectra, and to recover the desired model parameter posterior distributions in Eq. 2.7, we couple a forward model for multiphase age and cumulative release spectra as outlined in Section 2.1 with stochastic sampling via a Markov Chain Monte Carlo (MCMC) method. MCMC's are used to map out and sample probability distribution functions by stochastically exploring parameter space in such a way that a histogram of the samples produces the target prior distribution. For model parameters with priors that do not have a gradient (e.g., parameter(s) described by a uniform distribution), I couple a Metropolis and No U-Turn sampler (NUTS; Hoffman & Gelman (2014)), which I describe in more detail below. I use the NUTS sampler for all other parameters in the model. The NUTS sampler was developed by Hoffman & Gelman (2014) as an extended form of the Hamiltonian Monte Carlo (HMC) formulated by Duane et al. (1987). Like all MCMC methods, HMC samplers are rooted in the Metropolis-Hastings algorithm, which follows the following procedure: (1) start with an initial, random model, (2) propose a new model, (3) compute the acceptance probability α the proposed model, (4) assess if the model should be accepted by random comparison, and (5) repeat for a duration depending on the complexity of the model, typically at least $\sim 10^5$ iterations (Metropolis et al. (1953)). The acceptance criteria in our Metropolis Hastings algorithm is expressed as follows (after Gallagher et al. (2009)):

$$\alpha = \min\left(\frac{p(k')p(y|k')q(k|k')}{p(k)p(y|k)q(k'|k)}\right) \tag{2.12}$$

where k is the current model and k' is the proposed model. The first two terms in the numerator and denominator of Eq. 2.12 are the prior and likelihood of the proposed and current models, respectively. The last term in both the numerator and denominator (q(k|k')) is the proposal function, used to propose a new model vector k', given the current model state k. Unlike the random walk nature of the Metropolis-

Hastings sampler with the acceptance criteria for each proposal as defined in equation 2.12, NUTS takes advantage of first-order gradient information of the likelihood. In the model I use compound steps, meaning I use a combination of the NUTS and Metropolis samplers for our model depending on the distribution I have chosen for our parameters. I implemented our compound samplers in the probabilistic python library pymc3 (Salvatier et al. (2016)). Code used to generate the models discussed here are available in a Github repository (https://github.com/jackcarter9/Bayesian-multi-component-40Ar-^{39}Ar-dating).

2.3 Results

2.3.1 Case study 1: VanLaningham & Mark (2011)

As a first test for our Bayesian modeling framework, I reassess the $^{40}Ar/^{39}Ar$ age spectra generated by VanLaningham & Mark (2011). I chose these mixtures because they consist of neutron fluence monitors of known age that individually exhibit simple $^{40}Ar/^{39}Ar$ age spectra (i.e., define an age plateau). Additionally, VanLaningham & Mark (2011) conducted their experiments using a temperature-controlled furnace, which enables us to investigate diffusion kinetic parameters from their results. I only assume to know the number and composition of components in the mixture in our prior information.

Figure 2.1 shows the step heating results for the four mixtures originally presented in VanLaningham & Mark (2011). As an example, I focus on Mixture 2 (Figure 2.1B), comprised of 75% ACs and 25% HD-B1 by mass. From Figure 2.1B, we observe that Ar release from the older HD-B1 is greater during the early low-temperature heating steps, which is due to a combination of the argon diffusion kinetics in these two phases and the larger grain size of ACs relative to HD-B1 in this mixture. As the Ar from HD-B1 is exhausted, Ar release from the younger ACs becomes dominant in the high temperature steps. The exhaustion of Ar from HD-B1 results in monotonically-decreasing step ages from a 'pseudo plateau' at $\sim$ 12 Ma corresponding to 0–25% of the cumulative ^{39}Ar released to another 'pseudo plateau' at 2.2 Ma corresponding to 50 - 90% of the cumulative ^{39}Ar release. It is important to note that neither of these 'pseudo plateaus' corresponds to the known age of either ACs (1.19 $\pm$ 0.014 Ma (2σ analytical uncertainty), VanLaningham & Mark (2011); solid horizontal line, Figure 2.1B) or HD-B1 (24.59 $\pm$ 0.24 Ma, VanLaningham & Mark (2011); dotted horizontal line, Figure

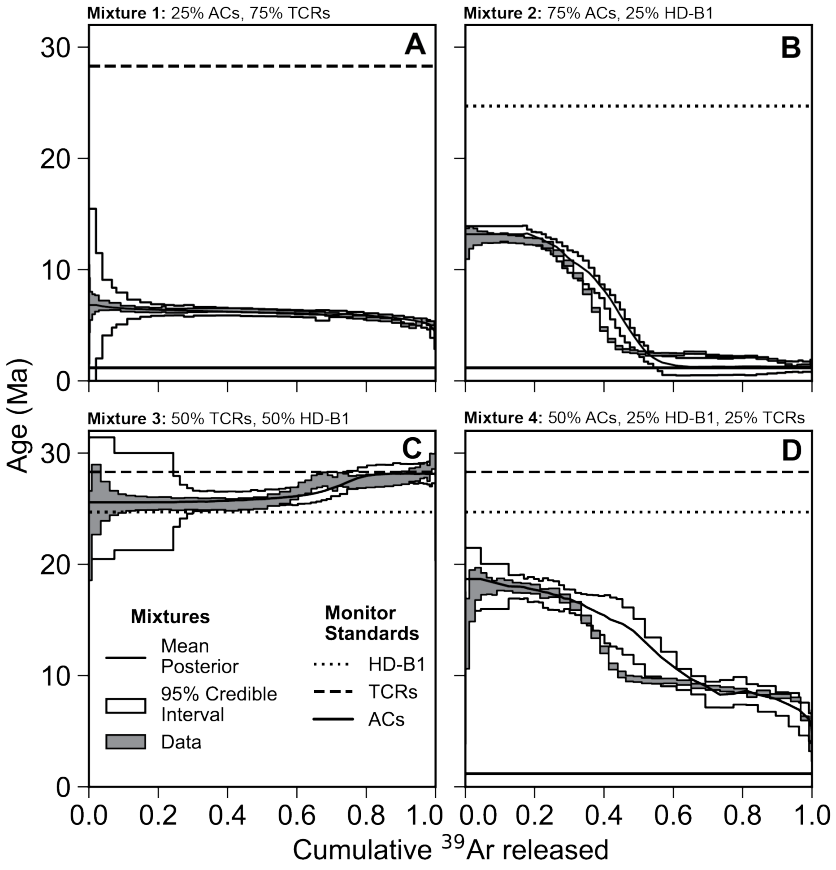

Figure 2.1: Age spectra of the mixtures created by VanLaningham and Mark (2011) (gray boxes), the mean posterior predictive model of our Bayesian inversion (black solid line), and the 95% credible interval of the posterior model (white boxes). The neutron flux monitor standards used in these mixtures include Alder Creek sanidine (ACs, dotted-dashed line), Heidelberg biotite (HD-B1, dotted line), and Taylor Creek Rhyolite sanidine (TCRs, dashed line). The accepted ages of the monitor standards in each mixture are indicated by horizontal lines. Known proportions of the monitor standards by mass in each mixture are indicated above each panel.

2.1B). Note for comparison I used the ages for the fluence monitors as reported by VanLaningham & Mark (2011) from their analyses of the individual age components. The ages of the individual components were calculated using the decay constants of Steiger & Jäger (1977) and the age (28.02 Ma) of Fish Canyon Tuff sanidine (Morgan et al. (2014)) as reported by Renne et al. (1998). For the purpose of our comparison of modelled and predicted component ages, the absolute age of the mineral standards is irrelevant (e.g., Mark et al. (2017)).

While Figure 2.1 demonstrates that the shape of the age spectra for these mixtures depends on the ages of the components in the mixture, what is not immediately apparent in Figure 2.1 is the role of Ar diffusion kinetics in these components. In Figure 2.2, I show an Arrhenius plot calculated for mixture 2, with the log of effective diffusivity, $\ln(\frac{D_{eff}}{a^2})$, shown as a function of inverse temperature. Figure A.1 also shows Arrhenius plots for mixtures 1, 3, and 4. I calculated the effective Ar diffusion coefficients normalized for grain size ($\frac{D_{eff}}{a^2}$) using the fraction of ^{39}Ar released from each step in the degassing experiment after the equations in Fechtig & Kalbitzer (1966). I refer to an effective diffusion coefficient because each component of the mixture has a different diffusivity at each temperature in the degassing experiment. Therefore I expect the calculated diffusivity for a particular temperature step to be a linear combination of the diffusivity in each phase i, weighted by their relative contributions f_i (e.g., Smith & Kay (1999)):

$$\frac{D_{eff}}{a^2} = \sum_{i=1}^{n} f_i \left(\frac{D}{a^2}\right) \tag{2.13}$$

The Arrhenius behaviour I observe for mixture 2 (Figure 2.2) is curvilinear and plots between argon diffusion parameters reported in the literature for sanidine (Cassata & Renne (2013)) and biotite (Harrison et al. (1985)), the two phases present in this mixture. This is consistent with our expectation that the effective diffusivity is a linear combination of the end-member diffusivities of each phase in the mixture (Eq. 2.13). At low temperatures and gas release fractions, we expect Ar diffusion from biotite to dominate and for diffusivities calculated for mixture 2 to have a slope similar to the slope for biotite reported by Harrison et al. (1985). However, we note that temperatures of the furnace used to conduct the experiments by VanLaningham & Mark (2011) are not calibrated below ∼800 °C. Therefore we suspect that temperatures 800 °C in Figure 2.2 are poorly constrained, and that this results in a much steeper slope than expected

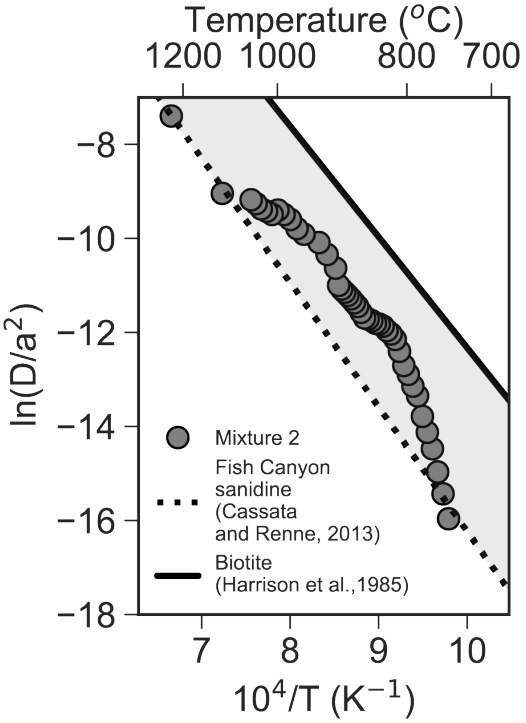

Figure 2.2: Arrhenius plot for mixture 2 (75% ACs and 25% HD-B1 by mass), calculated after Fechtig & Kalbitzer (1966). I compare the Arrhenius behavior of this mixture to kinetic parameters determined from step degassing experiments on Fish Canyon sanidine (experiment FCs-1, Cassata & Renne (2013)) and biotite (Harrison et al. (1985)). As mixture 2 was sieved to a 20-63 μm size fraction, I normalised to the sanidine diffusivities (dashed line) by a diffusion length scale of a = 32 μm and the biotite diffusivities (solid line) to a = 10 μm, assuming a spherical geometry for both. This provides endmember constraints for comparison with the mixture's Arrhenius behavior, as a larger diffusion length scale for biotite would shift diffusivities down and vice versa for a smaller sanidine diffusion length scale. The effective Ar diffusivities calculated for mixture 2 plot between the two end member diffusivities for sanidine and biotite.

from the kinetics reported by Harrison et al. (1985). I hypothesize that the temperature calibration also affects some of our model predictions (see Discussion section). At high temperatures and high gas release fractions, Ar from biotite becomes exhausted, and the diffusivities I calculate approach those expected for sanidine (Cassata & Renne (2013)).

Having demonstrated that the endmember diffusion kinetics are consistent with the mixture results, I use the endmember kinetics to inform the priors in our Bayesian inversion. Figure 2.3 shows the prior distributions for the variables that are utilized in our inversion for mixture 2. I assume there are two components in the mixture a priori and that the mixture is compositional in nature. Therefore the mixing coefficients of both components follow a Dirichlet distribution (Diebolt & Robert (1994)) (Figure

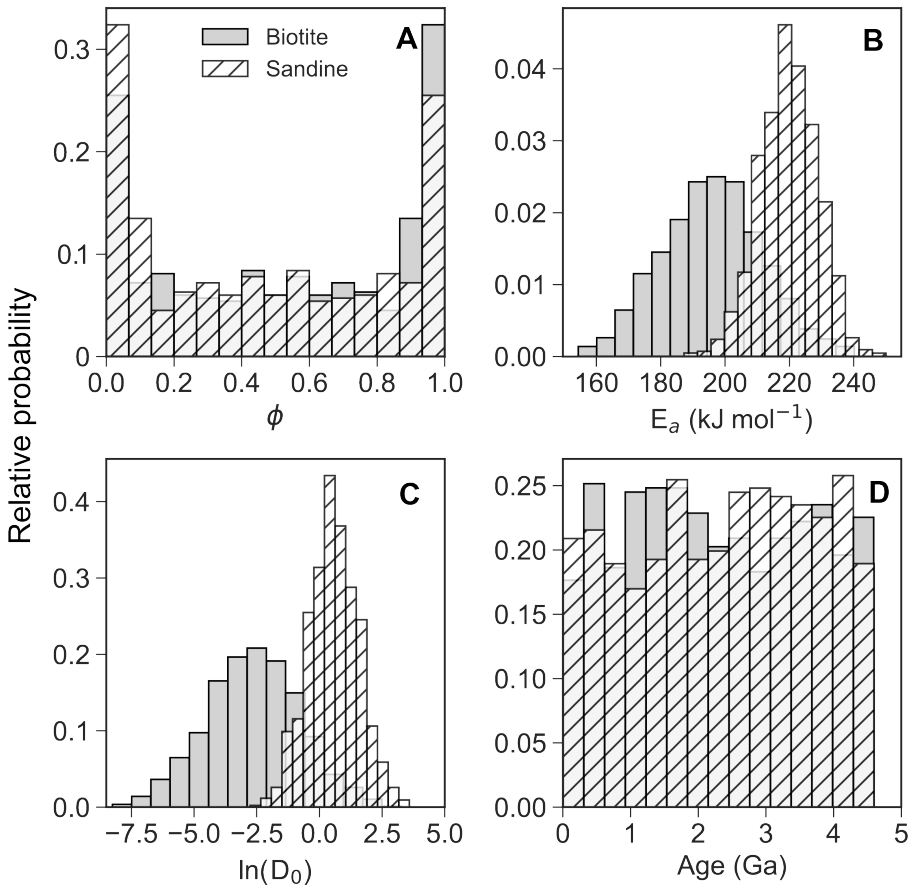

Figure 2.3: Prior information used in our Bayesian deconvolution of mixture 2, shown as relative probabilities. I assume to know the number (n = 2) and composition (biotite, shown in gray, and sanidine, shown in white stripes) of the components in the mixture. (**A** and (**B**)) Prior distribution of activation energies (E_a) and frequency factors (D_0), estimated from the diffusion kinetics reported in Cassata & Renne (2013) and Harrison et al. (1985). (**C**) Prior distribution of mixture fractions ϕ assuming a Dirichlet boundary condition. Note that the bin size for D_0 is held constant and therefore appears nonuniform in log space. (**D**) Prior distribution of component ages.

2.3A). I note that this is the fraction of ^{39}Ar contributed by each component, which is related but not equal to the mass of material from each component in the mixture. Figures 2.3B and C show the prior diffusion kinetics parameters I define using published experiments by Cassata & Renne (2013) and Harrison et al. (1985). In order to fully sample the kinetics parameters, I use the reported values from these experiments to construct distributions of the activation energies (E_a) (Figure 2.3B) and frequency factors (D_0) (Figure 2.3C), treating the reported 2σ value as 1σ in the prior distribution. Figure 2.3D shows the prior age distribution for each component. To be as unrestrictive as possible, I define the prior age distribution as a uniform distribution with a lower bound of 0 and an upper age bound given by the age of the Earth.

Given these priors, I then ran our MCMC sampler 300,000 times, each time predicting the age spectra and cumulative ^{39}Ar release spectra. I assess the goodness of fit

for each model result by comparing the model to the observations, which include both the age spectra and cumulative ^{39}Ar release spectra, via our likelihood function (Eq. 2.10). Good fits, which minimize the summed likelihood functions, suggests that the model, and therefore the parameters that build the model, may adequately describe the observation. The mean posterior model was then constructed from the model samples after the 'burn-in', which refers to the initial model samples that occur while the Markov chain explores parameter space widely before it reaches its equilibrium distribution. The mean posterior model from this post-burn-in sampling can then be compared directly with our observations. Figure 2.1 shows the mean posterior predictive models, also known as the expected models, from our Bayesian inversion of all four VanLaningham & Mark (2011) age spectra (solid black lines) and corresponding 95% credible intervals (white boxes, black outline). The expected models largely reproduce the complex age spectra observed in the laboratory experiments. The most significant differences typically occur during transition steps between 'pseudo' plateaus; nonetheless, most of these steps agree with the expected model within the credible interval, with the exception of Mixture 2, wherein steps during the transition are outside the model credible interval (Figure 2.1B). In Figure 2.4, I show the expected model for cumulative ^{39}Ar release for mixture 2 compared to the cumulative ^{39}Ar release observed. I provide expected models of cumulative ^{39}Ar release for all four VanLaningham & Mark (2011) mixtures in Figure A.2. Our fits to the cumulative release of ^{39}Ar are generally much poorer than our fits to ^{40}Ar/^{39}Ar age spectra. For each cumulative release model fit, we see deviations from the observed ^{39}Ar release for initial ^{39}Ar release at lower temperatures.

In addition to reproducing the mixtures' cumulative ^{39}Ar release and age spectra, our aim was to deconvolve the age of each component in a mixture by sampling for these desired parameters from the posterior. Figure 2.5 shows the MCMC samples, after the initial burn-in period of 200,000 iterations, for the age of each component in Mixture 2. Figure 2.5 demonstrates that after the burn-in period, our model converges on ages for the two components in the mixture that minimize the log likelihood function (Figure 2.5C). Figure 2.6 shows a pair plot of the posterior sampling of component ages and diffusion kinetics for mixture 2, where diagonal plots show histograms of a single parameter and off-diagonal plots show the correlations between parameters. Pair plots for the rest of the VanLaningham & Mark (2011) mixtures are shown in Figures A.3-5.

Overall, I found that our Bayesian inversion method successfully modeled the ages

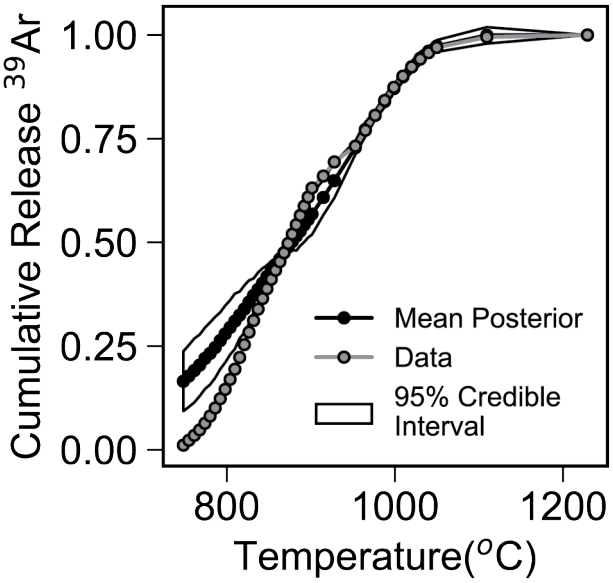

Figure 2.4: Comparison of cumulative argon release observed (dashed black line) and predicted (solid black line, grey 95% credible interval) by our Bayesian model for mixture 2, HDB1 (25%) and ACs (75%), of Vanlaningham and Mark (2011).

Component	Accepted Age ± 1σ (Ma)	Estimated Age ± 1σ (Ma)
Mixture 1: 75% Alder Creek sanidine (ACs), 25% Taylor Creek Rhyolite sanidine (TCRs)		
ACs	1.19 ± 0.014[1]	1.21 ± 0.15
TCRs	28.26 ± 0.28[2]	28.0 ± 1
Mixture 2: 75% ACs, 25% Heidelberg biotite (HD-B1)		
ACs	1.19 ± 0.014	1.24 ± 0.06
HD-B1	24.59 ± 0.24[3]	24.6 ± 1.1
Mixture 3: 50% HD-B1, 50% TCRs		
HD-B1	24.59 ± 0.24	24.8 ± 0.8
TCRs	28.26 ± 0.28	± 28.1 ± 0.6
Mixture 4: 50% ACs, 25% TCRs, 25% HD-B1		
ACs	1.19 ± 0.014	1.20 ± 0.12
TCRs	28.26 ± 0.28	28.0 ± 1
HD-B1	24.59 ± 0.28	25.0 ± 1

Table 2.1: Deconvolution model results for the VanLaningham & Mark (2011) mixtures, compared to known ages for mixture

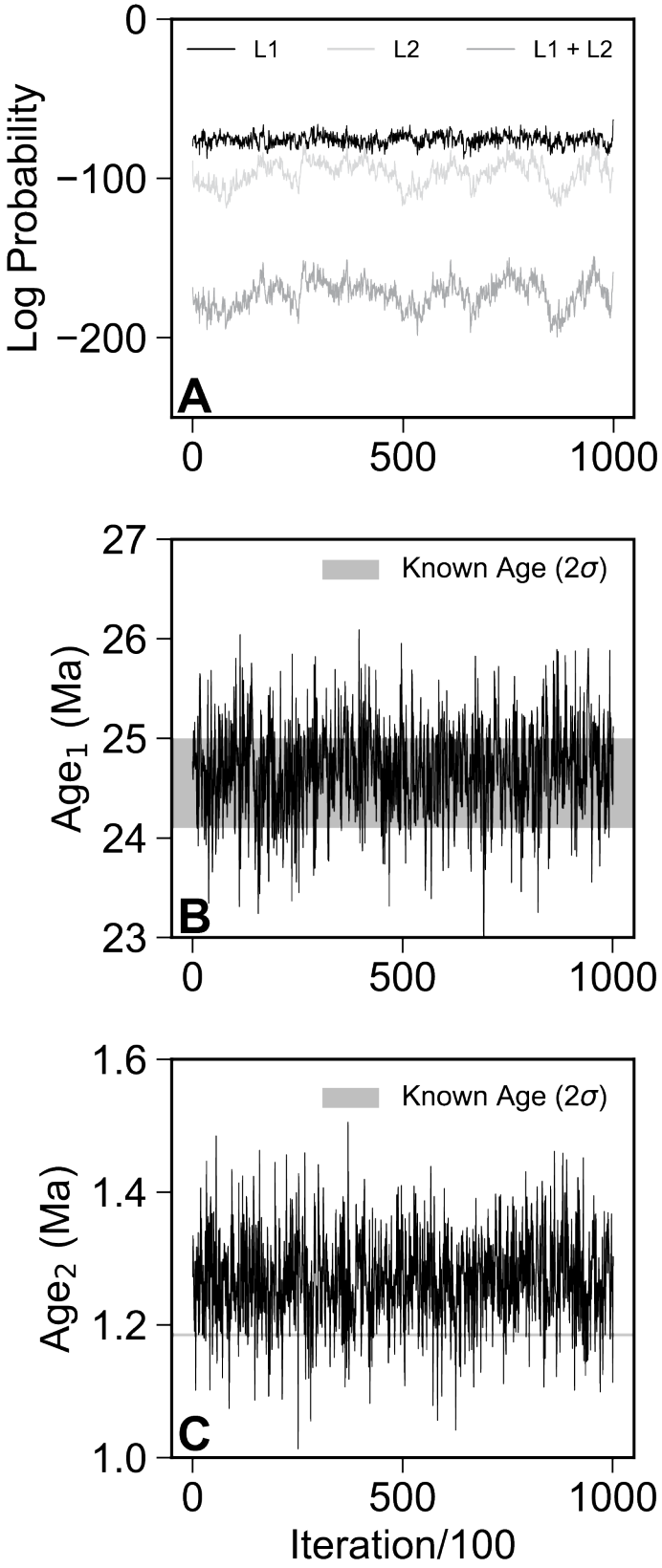

Figure 2.5: (**A**) Log likelihood of each model age spectra (L1) and cumulative release spectra (L2), as well as the summed log likelihood (L1 + L2), for mixture 2 of Vanlaningham and Mark (2011). Note that the summed log likelihood and L1 plot on top of one another. (**B**) and (**C**) are accepted sample ages of HDB1 and ACs in the mixture created by Vanlaningham and Mark (2011). Every 100th accepted sample for the post-burn-in iterations is shown.

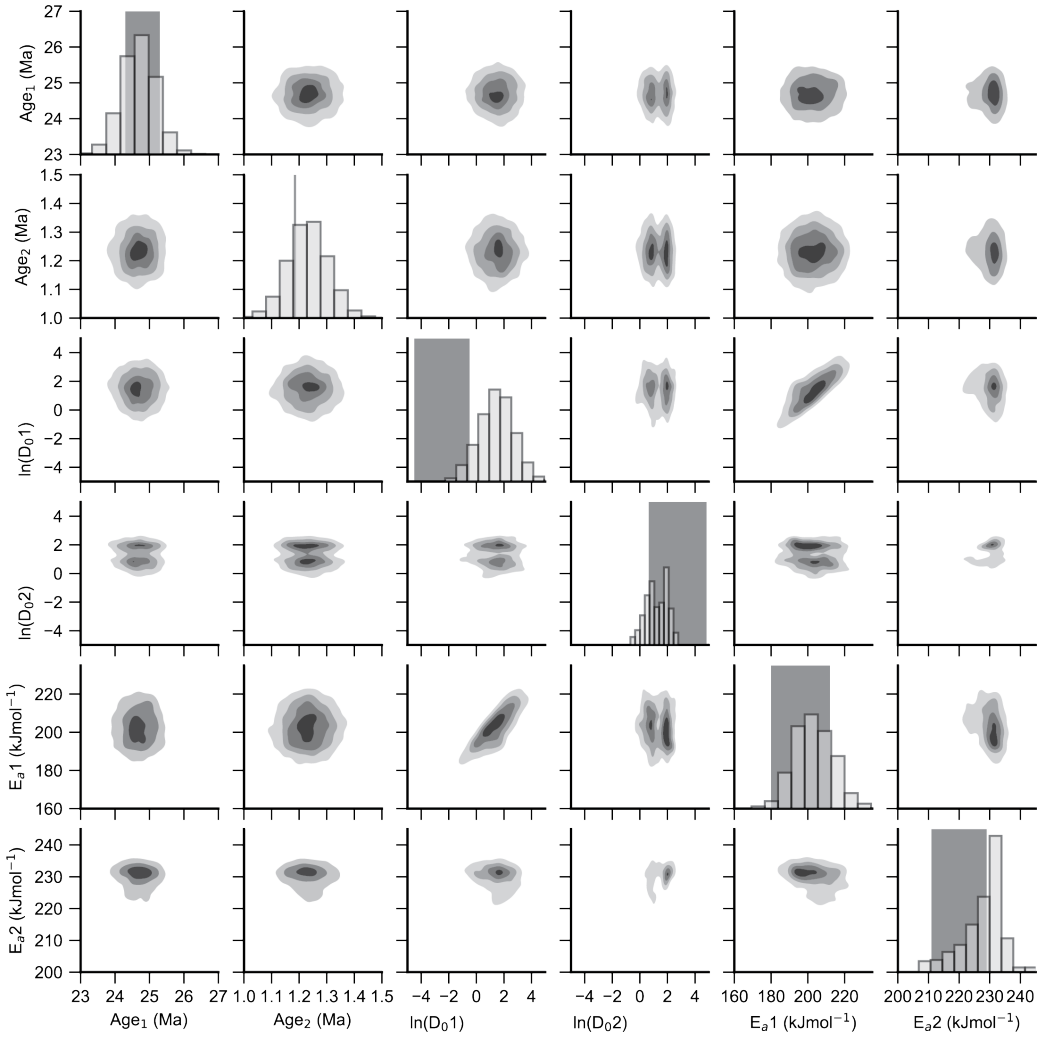

Figure 2.6: Pair plot showing the posterior sampling of each component's age (Ma), activation energy (Ea, kJ/mol) and frequency factor (cm^2s^{-1}) for mixture 2 (25% HD-B1 and 75% ACs by mass). In diagonal histogram plots, light grey boxes represent the 95% confidence bounds of the known parameter values from prior studies (**?**). I interpret component 1 as ACs (accepted age of 1.1848 0.0006 Ma; Niespolo et al. (2017)) and component 2 to be HD-B1 (accepted age of 24.7 ± 0.3 Ma; Fuhrmann et al. (1987)).

and diffusion kinetics for each component in the VanLaningham & Mark (2011) mixtures. This is illustrated in Figure 2.6 for Mixture 2 (on-diagonal histograms), as well as for all four mixtures in Table 2.1 and Figures A.3-6. The ages of the components I estimate from the posterior sampling are statistically indistinguishable from the known ages of the components in each mixture (Table 2.1), although, as expected, the age uncertainty from the posterior estimate is in most cases greater than the uncertainty on the known age. I do not observe any significant differences in the relative uncertainty of model-predicted ages as a function of the number of components, nor do we observe any significant differences in predicted age uncertainty as a function of which phases are present in a mixture. I find that the relative uncertainty in the predicted age for Alder Creek sanidine (ACs), which is by far the youngest component with an age of 1.19 ± 0.014 Ma (VanLaningham & Mark (2011)), is significantly greater (on the order of ∼ 3-6×) than the relative age uncertainty for the other three, older monitor standards. I also find that, although indistinguishable within the uncertainties reported, our estimated ages for ACs are nominally older than the known age; likewise, our estimated ages for the oldest components in a given mixture (either HD-B1 or TCRs) are nominally younger than the known age. I explore possible reasons for these differences in our Discussion section.

2.4 Case study 2: Kula et al. (2010)

In the first case study, specifically Mixture 1 and 4, I examined mixtures containing components of the same mineral, but did not observe this to have a significant effect on the model predicted ages or their relative uncertainties. Here, I reevaluate the muscovite and biotite mixture data presented by Kula et al. (2010) as an endmember, limiting case of mixtures with multiple components of the same mineral. Our expectation is that this scenario should be challenging for our model, since the individual components will have very similar and possibly even identical argon diffusion kinetics. In their study, Kula et al. (2010) created mixtures of two muscovite and biotite samples, respectively, that individually yield robust age plateaus (97-100% of the ^{39}Ar release). The individual muscovite components yielded $^{40}Ar/^{39}Ar$ plateau ages as follows: IV14, with an age of 148.8 ± 0.8 Ma (2σ), and NY25, with an age of 71.8 ± 0.4 Ma (2σ). Similarly, the individual biotite components yielded $^{40}Ar/^{39}Ar$ plateau ages as follows; IV8, with an age of 146.13 ± 0.82 (2σ), and PM1, with an age of 75.31 ± 0.40 Ma (2σ).

Kula et al. (2010) created three mixtures with different ratios of the muscovite or biotite samples by mass (3:1, 1:1, and 1:3 IV14 to NY25 and IV8 to PM1). The $^{40}Ar/^{39}Ar$ age and cumulative ^{39}Ar release spectra from incremental heating of these muscovite and biotite mixtures are reproduced in Figures 2.7 and 2.8, respectively. The muscovite mixtures show similar features to mixture 1 of VanLaningham & Mark (2011) in that, to a first order, they observe similar ages for most steps that are proportional to the mixing fractions (Kula et al. (2010)). The biotite mixtures show highly discordant spectra with an overall decrease in age toward the younger PM1 component but with localised undulation of step ages. I initially set up our Bayesian deconvolution model with priors analogous to those set up for case study 1. Specifically, I fixed the number of components in each mixture to 2, used the diffusion kinetics of argon in muscovite and biotite reported by Harrison et al. (2009) and Harrison et al. (1985) respectively, and allowed the component ages to be free parameters described by uniform distribution. I found that with these unrestrictive priors, our modeled step ages agree with essentially all of the steps in the observed age spectra, and generally have much larger credible intervals than the observed uncertaintes in step ages (Figures. A.6-7, A-C). In the muscovite models, the predicted age spectra are flat for 85% of the cumulative ^{39}Ar, whereas the observed age spectra exhibit an overall slight upward increase in age over this gas fraction, causing several of the initial observed step ages to be outside the modeled credible interval (Figures A.6, A-C). Over the last 15% of the cumulative ^{39}Ar release, the predicted step ages decrease and approach the age of the final observed step age. In the case of the biotite mixtures, while the undulations in the observed age spectra are technically within our model's very large credible intervals, our mean posterior age spectra exhibits a monotonic decrease in step ages with increasing ^{39}Ar release fraction that is notably different from the observed age spectra shape. I also found differences between the predicted and observed cumulative ^{39}Ar release for these mixtures when using a model setup with unrestrictive priors (Figures A.6, D-F). For the muscovite mixtures, I consistently predict higher ^{39}Ar release fractions at low temperatures than observed in experiments (Figure A.6, D-F). Conversely, for the biotite mixtures I predict lower ^{39}Ar release fractions at low temperatures than observed in experiments, although in this case the observed values are very close to the wide model credible interval (Figure 2.7, D-F).

While the predicted age spectra and cumulative ^{39}Ar release curves provide some insight about the model's performance with the unrestrictive prior, I am most interested

to know about the model's ability to resolve the ages of different components present in the mixture. For the muscovite mixtures, our model technically resolves the presence of two components. However, in all cases our model predicts that one component completely dominates the mixture and fails to predict the age of either component in the mixtures, with the exception of the younger component in the 1:3 IV14:NY25 mixture (Table 2). For example, in the 3:1 IV14:NY25 mixture, the older component carries 99% of the mixture weight. The ∼133 Ma modeled age of the older component is consistent with the apparent plateau age in the observed age spectrum (Figure A.6), but is inconsistent with the known age of IV14, the older component in this mixture, of ∼149 Ma (Table 2.2). Similarly, the modeled age of the younger component is ∼100 Ma, which is consistent with the youngest step ages observed at the end of the step heating experiment (Figure A.6) but inconsistent with the ∼72 Ma age of NY25, the younger component in this mixture (Table 2.2). For the biotite mixtures, the mixing fractions predicted for the biotite mixtures with the unrestrictive prior are also inconsistent with the known mixing fractions, although I do resolve the presence of two components. For example, in the 1:3 IV8:PM1 mixture, our model predicts mixing fractions of 57% IV8 and 48% PM1. With the unrestrictive prior I predict component ages that either 1) correspond to the initial and final step ages of the observed age spectra (Figure A.7 A-C), which do not correspond to either of the known ages of the individual components, or 2) have very large uncertainties, such that the ages of the individual components are indistinguishable (Table 2.3).

To attempt to successfully deconvolve the age components for Kula et al. (2010) mixtures, I imposed more restrictive priors. Specifically, I placed a tighter constraint on the prior for the mixture fraction of each component. For example, for a mixture with a known mixture fraction by mass of 1:3, I constrain one component to have a mixture fraction between 0.2 and 0.3 and the other to be between 0.7 and 0.8. Imposing this more restrictive prior ensures that there is a weight assigned to the fraction of each component that is within the known range of mixture weights for the prepared samples, which prevents the model from collapsing to a single component of intermediate age between the individual component ages, as I observed for the muscovite mixtures. Modeled component ages for both the initial model setup with unrestrictive priors and this setup with more restrictive mixture priors are given in Tables 2.2 and 2.3. I also report model results with these more restrictive priors as pair plots of the diffusion kinetics and ages of each component in the Kula et al. (2010) mixtures in Figures

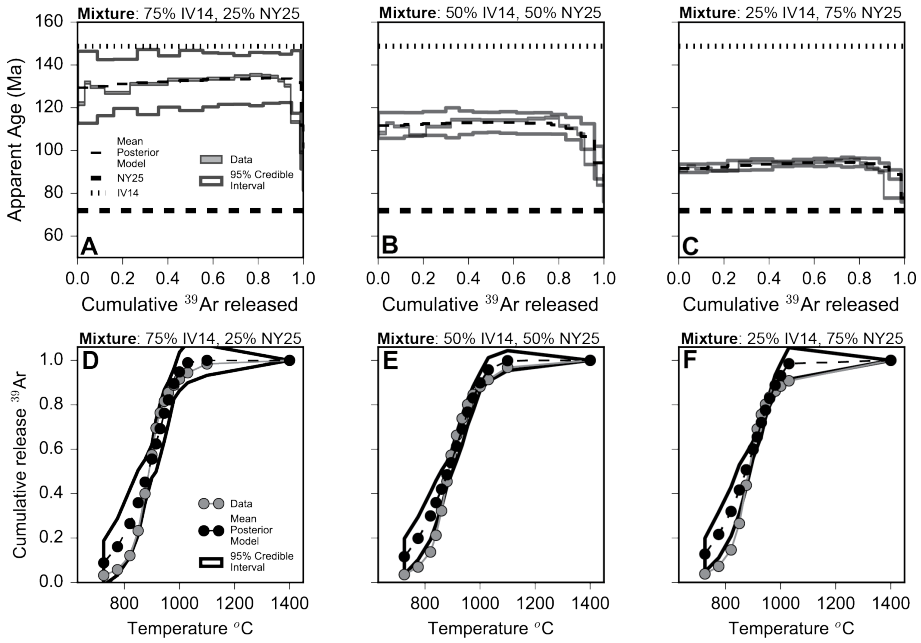

Figure 2.7: Age spectra (**A**, **B**, **C**) and cumulative release curves (**D**, **E**, **F**) of muscovite mixtures created by Kula et al. (2010). Each mixture contains grains from two muscovite samples, mixed in different proportions by mass: IV14 (grey stippled line, 148.8 ± 0.8 Ma), and NY25 (grey dashed line, 71.9 ± 0.4 Ma). The observed age spectra and fractional release data are shown in grey. The mean posterior age and fractional release models are given by a black dashed line, with the 95% credible interval is shown with a solid black line. Models shown are for the more restrictive priors on the mixing fraction of each component described in the text.

A.8–13. With a more restrictive prior on the mixing fractions, our model does a better job of reproducing the complexities of the observed $^{40}Ar/^{39}Ar$ age spectra of the muscovite mixtures. Specifically, our model predicts slightly increasing step ages by 80% or more of the ^{39}Ar release, followed by decreasing step ages in the last ∼20% or less of ^{39}Ar release (Figure 2.7 A–C). In contrast, our model is unable to predict the cumulative release curves for the muscovite mixtures; specifically, our model predicts an earlier ^{39}Ar release than observed in the experiments over the initial 50% of the ^{39}Ar release (Figure 2.7 D–F). I predict ages for the muscovite mixture components that, in all but one case, are within the 2σ confidence limit of the known ages of NY25 and IV14. The one case in which I do not predict the component age is for the younger component in the 3:1 IV14:NY25 mixture. The relative uncertainty of the component ages for these muscovite mixtures are larger than the relative uncertainties I obtained for component ages in case study 1 (Table 2.2). Imposing a more restrictive prior for the biotite mixtures enabled us to predict component ages that agree with the known component ages within the modeled credible interval for all three mixtures. However, like the muscovite mixtures I predict a much larger relative uncertainty in

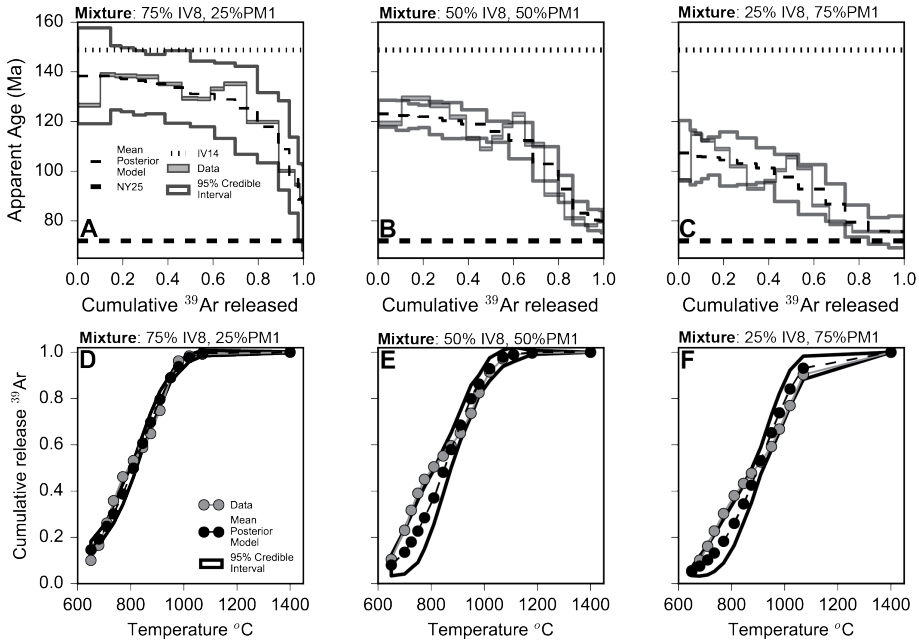

Figure 2.8: Age spectra (**A**, **B**, **C**) and cumulative release curves (**D**, **E**, **F**) of biotite mixtures created by Kula et al. (2010). Each mixture contains grains from two biotite samples, mixed in different proportions by mass: IV8 (stippled line, 146.13 ± 0.82 Ma), and PM1 (dashed line, 75.31 ± 0.4 Ma). The observed age spectra and fractional release data are shown in grey. The mean posterior age and fractional release models are given by a black dashed line, with the 95% credible interval is shown with a solid black line. Models shown are for the more restrictive priors on the mixing fraction of each component described in the text.

the estimated component ages than is observed for the individual biotite components (Table 2.3), and also much larger relative uncertainties compared to the results in case study 1. The posterior predicted age spectra for the biotite mixtures are similar to the overall observed age spectra, in that step ages decrease with increasing cumulative ^{39}Ar, with a much higher age gradient toward the end of the experiments. However, our modeled age spectra still lack the complexity in the age spectra observed for these mixtures, particularly the two 'undulations' observed over the first 60–80% of ^{39}Ar release. Unlike the muscovite mixtures, our modeled cumulative release curves exhibit a later ^{39}Ar release than observed in the experiments for the first 50% of the ^{39}Ar release.

	Accepted Age ± 2σ (Ma)	Estimated Age ± 2σ (Ma) unrestrictive prior	Estimated Age ± 2σ (Ma) restrictive prior
Known: 3:1 (IV14:NY25)			
IV14	148.85 ± 1.6	132.7 ± 2.5	144.6 ± 5.1
NY25	71.85 ± 0.8	106.4 ± 12.1	99.2 ± 2.8
Known: 1:1 (IV14:NY25)			
IV14	148.85 ± 1.6	112.43 ± 1.77	132.4 ± 15.2
NY25	71.85 ± 0.8	83.5 ± 2.84	82.7 ± 16
Known: 1:3 (IV14:NY25)			
IV14	148.85 ± 1.6	94.1 ± 0.9	140.8 ± 25.8
NY25	71.85 ± 0.8	78.47 ± 2.7	78 ± 6.3

Table 2.2: Modeled ages, using both nonrestrictive and restrictive priors for muscovite components in mixtures created by Kula et al. (2010), with comparison to known ages.

	Accepted Age ± 2σ (Ma)	Estimated Age ± 2σ (Ma) unrestrictive prior	Estimated Age ± 2σ (Ma) restrictive prior
Known: 3:1 (IV8:PM1)			
IV8	146.3 ± 1.6	139.6 ± 4.3	139.1 ± 8.8
PM1	75.31 ± 0.4	89.3 ± 2.5	77.9 ± 24.7
Known: 1:1 (IV8:PM1)			
IV8	146.13 ± 1.6	124.55 ± 7.6	138.6 ± 13.6
PM1	75.31 ± 0.4	79.42 ± 3.5	77.65 ± 7.7
Known: 1:3 (IV8:PM1)			
IV8	146.13 ± 1.6	103.2 ± 9.8	179.95 ± 52
PM1	75.31 ± 0.4	72 ± 16.5	68.2 ± 15

Table 2.3: Modeled ages, using both nonrestrictive and restrictive priors for biotite components in mixtures created by Kula et al. (2010), with comparison to known ages.

2.5 Case study 3: a hypothetical *in-situ* Martian experiment

While I use the previous two case studies to investigate the strengths and weaknesses of our Bayesian approach, it is also insightful to demonstrate our Bayesian framework for a geologically interesting case study. For this purpose, I created a hypothetical $^{40}Ar/^{39}Ar$ dataset for the Martian surface using compositional data from previous rover observations. The recent successes of rover-based missions to Mars, such as the Mars Science Laboratory (MSL) and Mars Exploration Rover (MER) missions, have pushed the development of an *in-situ* absolute dating package for future rover-based missions (Swindle (2000), Anderson et al. (2012), Cassata (2014), Cohen et al. (2014), Solé (2014), Cho et al. (2017), Morgan et al. (2017)). The ubiquity and dominance

of primary K-bearing silicate minerals (e.g., Ehlmann & Edwards (2014)), makes the K–Ar system one of the most promising radioisotopic systems for dating materials *in-situ* on the surface of Mars.

All existing *in-situ* K-Ar ages from Mars, obtained by the Curiosity rover in Gale Crater, are from multi-component mixtures of K-bearing minerals (Farley et al. (2014), Vaniman et al. (2013), Martin et al. (2017)). Interpreting these analyses requires a number of assumptions about the ages and distribution of Ar in individual components in the mixture. Assumptions about the distribution of Ar could potentially be addressed by putting a ^{251}Cf source on future rovers, which would be used to irradiate samples with neutrons and allow for *in-situ* $^{40}Ar/^{39}Ar$ rather than K-Ar (Morgan et al. (2017)). Nonetheless, *in-situ* measurements on future missions will still very likely be applied to mixtures, as mineral separation capabilities on rovers are currently limited to processes like simple sieving (e.g., Mahaffy et al. (2012), Farley et al. (2014)). Our Bayesian approach could therefore be important for interpreting future $^{40}Ar/^{39}Ar$ datasets from *in-situ* measurements on mixtures, and also for $^{40}Ar/^{39}Ar$ studies in future sample return missions (e.g., Williford et al. (2018)) where the amount of material is too small or the risk of losing material too great to carry out mineral separations.

I generated a hypothetical $^{40}Ar/^{39}Ar$ dataset based on existing mineralogical and age information from the Murray mudstone Formation explored by the Curiosity rover. Of the phases detected in the Murray Formation, jarosite, plagioclase, and sanidine contain sufficient K to contribute argon to an $^{40}Ar/^{39}Ar$ age spectra (Rampe et al. (2016)). A large amorphous fraction detected in the Murray Formation may also contain phases with nontrivial K abundances; however, because the exact composition and therefore diffusion kinetics of any K-bearing phase are not known, I ignore this component at present Rampe et al. (2017). Martin et al. (2017) carried out a two step K-Ar dating experiment at the Mojave 2 site in the Murray Formation. The first step at 500 °C yielded an age of 2.12 ± 0.36 Ga (2σ), which Martin et al. (2017) associate with low retentivity jarosite and possibly K-bearing salts present in the amorphous fraction. They attribute this relatively young age for secondary mineralization to the presence of fluids on the Martian surface at or slightly before this date. The second step at 930 °C yielded an age of 4.07 ± 1.36 Ga, which the authors ascribe to a detrital component of plagioclase, similar to the results obtained for bulk degassing of material in the Sheepbed mudstone (4.21 ± 0.71 Ga 2σ, Farley et al. (2014)).

For our hypothetical mixture, I use the mineral composition measured at Telegraph

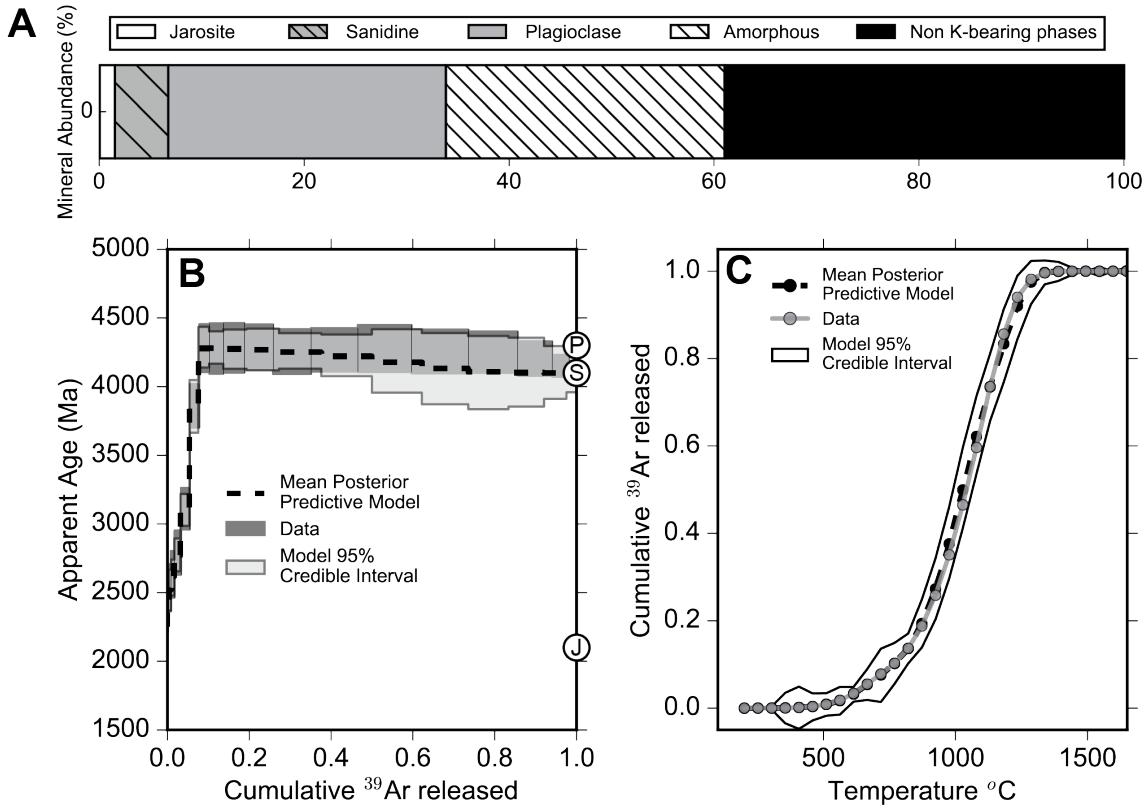

Figure 2.9: (**A**) Mineral abundances in weight % of the Murray mudstone formation measured by CheMin at Telegraph Peak, after Rampe et al. (2016). I use the relative abundances of K-bearing phases shown (jarosite, sanidine, and plagioclase), previously-determined *in-situ* K-Ar ages (Martin et al. (2017)), and published diffusion kinetics to generate (**B**) a hypothetical $^{40}Ar/^{39}Ar$ age spectra for a bulk sediment analysis at this site and (**C**) a hypothetical cumulative release ^{39}Ar spectra. Mean posterior models (solid black line) for both the age spectra and cumulative ^{39}Ar release spectra are shown in **B** and **C**.

Peak (Figure 2.8A; Rampe et al. (2016)) rather than the Mojave 2 site, as the latter lacks sanidine. I treat sanidine and plagioclase as separate components and assume both are Noachian in age, consistent with the existing *in-situ* chronology (Farley et al. (2014), Martin et al. (2017)), but give these two components slightly different ages (4.1 $\pm$ 0.05 and 4.30 $\pm$ 0.35 Ga for sanidine and plagioclase, respectively) in order to test whether our Bayesian approach can resolve the age difference. I ascribe an age of 2.10 $\pm$ 0.25 Ga to a jarosite component after the low-temperature degassing age obtained by Martin et al. (2017). Given these ages and compositions of components, I calculated an age spectra for the synthetic mixture (Figure 2.9B) assuming diffusion kinetics for the phases present that are reported in the literature (Kula & Baldwin (2011), Cassata & Renne (2013)) and a grain size of 100 μm for each component (chosen as CheMin drill samples are typically ¡ 150 μm,Rampe et al. (2017)).

The synthetic age spectra I generated (Figure 2.9B) shows patterns similar to that

Component	Input Age ± 2σ (Ga)	Estimated Age ± 2σ (Ga)
Jarosite	2.1 ± 0.025	2.09 ± 0.16
Sanidine	4.1 ± 0.05	4.10 ± 0.14
Plagioclase	4.3 ± 0.035	4.28 ± 0.26

Table 2.4: Estimated parameter values for a hypothesised Martian mixture.

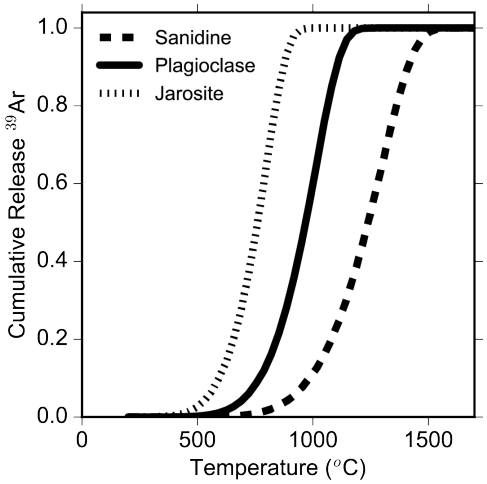

Figure 2.10: Individual cumulative release curves for the three K-bearing components in our synthetic Martian regolith dataset: jarosite, plagioclase, and sanidine. Calculations were carried out using the discretized solution of fractional loss for a sphere by Fechtig & Kalbitzer (1966) and using diffusion kinetics taken from literature studies on each of the components in the mixture (Cassata et al. (2009); Cassata & Renne (2013);Kula & Baldwin (2011)). The kinetics used in our model are scaled to a grain size of 100 μm.

expected from a sample that has undergone diffusive Ar loss, which manifests as monotonically increasing step ages with increasing cumulative ^{39}Ar release in the early part of the step degassing experiment. Unlike a case of thermally driven loss, our monotonically increasing step ages in the early to middle part of the experiment are due to the competing degassing of both jarosite, the youngest and least retentive component, and the oldest and intermediately retentive component plagioclase. To demonstrate this, Figure. 2.10 shows the cumulative ^{39}Ar release curves for the three mineral phases in this hypothetical mixture using the same diffusion kinetics as used to generate the age spectrum. Figure A.14 also shows the incremental ^{39}Ar release spectra from each component, as well as the incremental and cumulative ^{39}Ar release curves for the hypothetical mixture. I can see in Figure 2.10 that, by 800 °C, near complete degassing of jarosite has occurred, while only ∼20% and ≤ 5% of ^{39}Ar has degassed from plagioclase and sanidine, respectively. In the latter stages of release, both plagioclase and sanidine degas in concert, with plagioclase exhausting first (Figure 2.10), resulting in the small stepped decrease in age from the older plagioclase (4.3 Ga) to the younger sanidine (4.1 Ga) observed in our synthetic age spectra.

In our synthetic Martian dataset I assume diffusion kinetics priors from previous studies on the end-member K-bearing components (Cassata et al. (2009), Cassata & Renne (2013), Kula & Baldwin (2011)) and assumed a variance of 2σ for these values. I again assume a Dirichlet prior for the mixing fractions with no constraints for any component, like case study one, and set the prior for all age components to be a uniform distribution between 0 and 4.6 Ga to encompass the age of the Solar System.

Following our creation of this synthetic Martian regolith $^{40}Ar/^{39}Ar$ dataset I simultaneously invert both the fractional release and age spectra data with our Bayesian model. I report the estimated ages of each end member component in table 2.4 and show mean posterior models and confidence intervals for the age spectra and ^{39}Ar cumulative release spectra in figure 2.9. A pair plot showing the relationship between the posterior estimates of ages and diffusion kinetics for all components in the mixture is given in supplementary figure A.15. The posterior models of both the age spectra and cumulative ^{39}Ar spectra agree with the data within the 95% credible interval. The probability density estimates of age components in the mixture, which I draw from the posterior model, agree with the known input ages and have relative uncertainties of 1-7% (2σ).

2.6 Discussion

The aims of the Bayesian method developed here are to: (1) fit a posterior predictive model to $^{40}Ar/^{39}Ar$ datasets from mixtures of multiple components, and (2) estimate the values of model parameters, principally the $^{40}Ar/^{39}Ar$ ages of each component in the mixture. Below, I discuss what factors influence the degree to which our Bayesian approach was successful in meeting these aims for each of our case studies. I then compare our approach to existing approaches for interpreting $^{40}Ar/^{39}Ar$ datasets from mineral mixtures, and discuss ways in which our Bayesian model could be improved upon to yield better component age estimates as well as deal with more complex $^{40}Ar/^{39}Ar$ datasets. Finally, I outline several applications where I foresee our Bayesian approach being useful for answering geologic questions.

2.6.1 Model fits and parameter estimation

2.6.1.1 Case study 1

Our first case study, using stepwise heating experiments of mixtures of neutron fluence monitors created by VanLaningham and Mark (2011), is in many ways ideally designed to meet the assumptions set forth in our model framework. I know from previous work on the individual components in these mixtures that each component loses Ar by volume diffusion and experienced geologically instantaneous cooling, therefore exhibiting no evidence for diffusive loss of $^{40}Ar^*$. For TCRs and ACs, which consist of roughly equant grains, the assumption of a spherical diffusion geometry is also well-justified. Although an infinite sheet diffusion geometry may be more appropriate for HD-B1,this does not affect our model results in a statistically significant way. For example, if I assume an infinite sheet geometry for one component in Mixture 2, I obtain a similar fit to the age spectrum for early cumulative ^{39}Ar release fractions (Figure A.16) and results in a 1% difference in modeled age of HD-B1 and a 5% difference in the modeled age of ACs (Figure A.17). Importantly, both sets of modeled ages agree with the known component ages within their credible intervals. With these assumptions of our model framework about volume diffusion and geometry met, I find a good fit between our posterior models and the observed $^{40}Ar/^{39}Ar$ age spectra, with most step ages agreeing within the 95% credible interval of the expected model (Figure 2.1). This demonstrates that, when the assumptions of our model framework are valid, I can use our Bayesian approach to meet our first goal of fitting a posterior predictive model to $^{40}Ar/^{39}Ar$ datasets from mixtures of multiple components. This is the case even with essentially uninformed priors about the mixing fractions and ages of individual components (Figure 2.3). The fits to the cumulative ^{39}Ar release curves, shown in Figures 2.4 and A.2, are generally poorer than our fits to $^{40}Ar/^{39}Ar$ age spectra for this case study. For each cumulative release curve model fit, I see deviations from the observed cumulative ^{39}Ar release at low release fractions and low temperatures. The most likely explanation for this initial deviation in cumulative ^{39}Ar release is the inaccurate calibration of the furnace used to heat the samples at temperatures below $\sim$800 ^oC. Specifically, I think the furnace temperature for heating steps below 800 ^oC is overestimated. Our comparison of the VanLaningham & Mark (2011) apparent diffusivities to known diffusion kinetics for the individual components these mixtures (Figure 2.2, A.1) supports this hypothesis, as I observe much lower diffusivities and a greater rate of increase in diffu-

sivity than expected for the nominal temperatures below 800 ^{o}C in these experiments. This is also consistent with what we observe for the cumulative ^{39}Ar release curves, as our models consistently predict higher initial ^{39}Ar losses than observed experimentally (Figure 2.4, A.2). The nature of a cumulative quantity means that this overprediction of initial ^{39}Ar loss affects the predicted cumulative ^{39}Ar loss at all subsequent temperature steps, which for some of the cumulative ^{39}Ar release curves results in substantial misfits over as much as $\sim$50% of the cumulative ^{39}Ar. Further, we cannot predict more than 100% cumulative ^{39}Ar loss, which means that the model predictions will always converge with the observations at high temperatures and high cumulative ^{39}Ar release fractions. In spite of the misfit with the cumulative ^{39}Ar release curves, I was able to estimate component ages for the mixtures in case study 1 that agree with the known component ages within the model credible interval, (2σ), albeit with a much larger uncertainty on the model predicted age than the known age (Table 2.1, Figures. 2.6 and A.3-5). In general, the ability of my Bayesian model to accurately estimate the ages of individual components in the VanLaningham & Mark (2011) mixtures demonstrates that this approach can be used to extract geologically meaningful age information from $^{40}Ar/^{39}Ar$ mixture datasets, provided that assumptions about the individual components are consistent with our model framework. Moreover, these results are consistent with the fact that the cumulative ^{39}Ar release curve carries less weight in our summed log likelihood function than the $^{40}Ar/^{39}Ar$ age spectrum (Figure. 2.5). Our ability to deconvolve mixture component ages primarily from our model fits to $^{40}Ar/^{39}Ar$ age spectra indicates promise for the broad applicability of this model framework, as many labs generating $^{40}Ar/^{39}Ar$ datasets today heat samples with CO_2 lasers, which lack direct temperature information or control, and therefore cannot quantify cumulative ^{39}Ar release as a function of temperature. That said, temperature-controlled experiments are advantageous because they provide additional constraints for the inversion of datasets from mixtures, whether in our Bayesian framework or in a different inversion approach (e.g., Boehnke & Harrison (2016), Cassata et al. (2010)). Furthermore, although I have not done so here, accurate temperatures during step degassing can also reveal information about sample-specific diffusion kinetics that can be used to inform priors. I did not observe any systematic relationship between the uncertainty of our estimated component ages and either the total number of components or the number of mineral phases present. However, I did find that the relative uncertainty in our predicted ages for ACs, which is significantly younger than all other components in

case study 1, are ∼10% or greater (2σ), whereas the relative uncertainty on the ages of the other components are between 3 and 5% (2σ). I hypothesize the large uncertainty associated with the younger age component (ACs) is a result of this age component contributing a relatively small amount of $^{40}Ar^*$ to the overall $^{40}Ar^*$ budget.

I also find that, although indistinguishable within the uncertainties reported, our estimated ages for ACs are nominally older than the known age; likewise our estimated ages for the oldest in a given mixture (either HD-B1 or TCRs) are nominally younger than the known age. I hypothesize that this may result from the complexity of the dataset and the simplicity of model; specifically, the assumption that each component can be described by a single domain. Extending the model to account for a grain size distribution or MDD type behavior, as described later in this section, may provide a more realistic model and return the known ages without bias.

2.6.1.2 Case study 2

Our attempts to reanalyze the Kula et al. (2010) datasets may be consistent with our expectation about our Bayesian model's limits with regards to components of the same mineralogy. I was unable to deconvolve the individual known component ages with the same degree of prior information as I had in the VanLaningham & Mark (2011) case study and needed to impose a more restrictive prior on mixture fractions, in order to resolve two components. Although I was typically able to predict the known ages of the mixture components with this more restrictive prior on mixing fractions, our estimated ages are characterized by very large uncertainties, particularly in comparison to the estimated age uncertainties in case study 1. Furthermore, the fits to the mixture age spectra and cumulative release curves had very large credible intervals in comparison to our models of the VanLaningham & Mark (2011) mixtures and miss complexity present in the observed age spectra, particularly for the biotite mixtures. In the case of the muscovite mixtures, I argue that the model's difficulty in deconvolving component ages is attributable to the similarity in Ar diffusion kinetics characterizing NY25 and IV14. Below ∼930 ^{o}C, the similarity in Ar diffusion kinetics is demonstrated by the significant overlap between step degassing experiments of NY25 and IV14 individually both in cumulative ^{39}Ar release curves (Kula et al. (2010), their Figure. 2.3) and in an Arrhenius plot (Fig. A.18A). At temperatures $\geq$ 930 ^{o}C, Kula et al. (2010) observe earlier gas release from IV14 muscovite than NY25 muscovite in their cumulative ^{39}Ar release curves. For the muscovite mixtures, this change in

degassing behavior is reflected in the shape of the age spectra, first as upward curvature toward the age of IV14 at intermediate to high cumulative ^{39}Ar release fractions, and then as downward curvature at the highest ^{39}Ar gas release fractions, when Ar release from IV14 is exhausted. However, over most of the muscovite mixture age spectra, the diffusion kinetics parameters of the two components are similar, preventing our Bayesian model from differentiating these two components.

To demonstrate the effect of similar diffusion kinetics in a true endmember case, I generated a synthetic mixture consisting of two muscovite components with the same age, grain size and mixing fraction as the 3:1 IV14:NY25 mixture. In generating the synthetic dataset for this mixture, I assume that both muscovite components are characterized by identical Ar diffusion kinetics, using the kinetic parameters from Harrison et al. (2009). The resulting synthetic age spectrum is flat and featureless with an apparent plateau age of ∼130 Ma (Figure A.19A), while the resulting synthetic cumulative ^{39}Ar release curve has a sigmoidal shape consistent with volume diffusion from a single phase (Figure A.19B). Our mean posterior age spectrum and cumulative ^{39}Ar release curve match the synthetic data exceptionally well (Figure A.19). However, like the real muscovite mixtures in case study 2, I was unable to accurately estimate both component ages in the mixture (Table A.1), and the older component completely dominates the mixture with an estimated mixing fraction of 92%. Imposing more restrictive priors on the mixing fraction for the Kula et al. (2010) muscovite mixtures forced the model to discern two distinct component ages, but the predicted age for the younger component (NY25) is still in too old in the 3:1 IV14:NY25 mixture where it appears to be pinned to the final, youngest step age in the $^{40}Ar/^{39}Ar$ age spectrum. I hypothesize that these muscovite mixtures might be successfully deconvolved with less restrictive priors if a heating schedule with a greater number of short-duration, high-temperature steps was used. Such a heating schedule would lead to a more detailed picture of the structure of the $^{40}Ar/^{39}Ar$ age spectrum at high cumulative ^{39}Ar release, where the diffusion behavior of NY25 and IV14 differ the most, and therefore would increase the likelihood that our model would predict the presence of more than one component. Our challenge deconvolving the Kula et al. (2010) biotite mixtures may also point to issues with my initial assumptions in our model framework for these mixtures. The $^{40}Ar/^{39}Ar$ age spectra for the Kula et al. (2010) biotite mixtures are complex, exhibiting multiple large age undulations at low ^{39}Ar release fractions and an overall decreasing age trend toward the age of the younger component at high ^{39}Ar release fractions. A decreasing

age trend at high ^{39}Ar release fractions is consistent with volume diffusion from two components with different ages and slightly different Ar diffusion kinetics, with the younger component being more retentive than the older component. This decrease toward the younger age component at the end of the experiments is also consistent with the ^{39}Ar cumulative release curves observed for the individual biotite components, with the younger PM1 exhibiting greater Ar loss at higher temperatures than the older IV8. The large undulations in step age at lower ^{39}Ar release fractions, on the other hand, are unexpected.

I propose several factors that might produce such unexpected age spectra behavior for the biotite mixtures. These factors include the presence of multiple grain sizes in each component, multiple diffusion domain (MDD) behavior in one or both biotite samples, non-volume diffusion mechanisms, or syn-experiment structural breakdown of biotite. Effects associated with the presence of multiple grain sizes are possible, although I view this as unlikely to explain these undulations entirely as the range of sieve sizes used by Kula et al. (2010) was small(177–250 μm). Similarly, syn-experiment structural breakdown due to heating is unlikely to produce such undulations, as both biotite or muscovite samples would be expected to undergo crystal-chemical changes at similar temperatures and therefore steps in these experiments. A component of non-volume diffusion and/or MDD-like behavior remain possibilities and are consistent with the observed cumulative ^{39}Ar release curves and Arrhenius relationships for the individual biotite components, IV8 and PM1. Instead of exhibiting the characteristic sigmoidal shape diagnostic of volume diffusion (e.g., McDannell et al. (2018)), the cumulative ^{39}Ar release curves for IV8 and PM1 individually are relatively straight until high release fractions, whereby definition values have to approach 100%. The Arrhenius plots of diffusivities for these individual biotite components (Figure A.18C) exhibit a curvilinear pattern, indicative of the presence of multiple domains (e.g., Lovera et al. (1989)), rather than linear arrays as expected for thermally driven volume diffusion from a single domain, and as observed for most of the cumulative gas released from the muscovite samples.

For any of these potential explanations for the biotite mixture age spectra behavior, the initial assumptions of the current Bayesian model framework are violated. Specifically, I have assumed a single grain size and simple, single-domain volume diffusion with no structural transformations or changes in Ar diffusion kinetics for each component. Therefore, as I can see from the posterior age spectra (Figures. 2.7-2.8, A-C) our

models inability to capture the undulations, but it does predict the decrease toward the younger age components at high cumulative ^{39}Ar release fractions for all three biotite mixtures. These effects may also be affecting our model's ability to reproduce the muscovite mixture datasets, although this is likely to a smaller extent as the structure observed in the muscovite age spectra are much more subtle. In applications of our Bayesian model to geologic samples, it may be difficult to identify when the model's underlying assumptions about the individual components, such as only volume diffusion from a single domain, are violated, particularly if used to analyze mixtures with many more than two components. However, I also demonstrated that using additional constraints such as mixing fractions enabled us to nonetheless obtain reasonable estimates of the component ages in the biotite and muscovite mixtures in most cases, even if I were unable to entirely capture the complexity in the mixtures' age spectra. This additional constraint on mixture fraction may not be unreasonable for some geologic applications. For example, IV8 has higher Fe and much lower Mg than PM1 (Kula et al. (2010)). I therefore could have determined that there were two different biotite populations in the Kula et al. (2010) mixtures and in roughly what proportions they occur from compositional information independent of the Ar measurements. Therefore, although some real mixtures may have components that violate our model's underlying assumptions, we may still be able to extract meaningful geochronological information using our Bayesian approach, particularly if I have more prior information to incorporate into the model framework.

2.6.1.3 Case study 3

Case studies 1 and 2 highlight some of the strengths and weaknesses of our Bayesian approach to deconvolving ^{40}Ar/^{39}Ar datasets but lack geological significance in that the mixtures I deconvolved were laboratory-generated. Case study 3 is intended to provide a geologically interesting example: the analyses of bulk material from a planetary surface regolith. Although also artificial, I generated a hypothetical ^{40}Ar/^{39}Ar dataset for a Martian surface sample to highlight the complexity of estimating geologically relevant age information from potential *in-situ* planetary measurements, or measurements on bulk material from meteorites or returned samples. Although real datasets for lunar and Martian samples with multiple components exist, at present the model does not strictly accommodate MDD-type behavior for individual components, which is frequently exhibited in these datasets; therefore testing our models on these datasets

would probably not be informative without improvements to the model framework (see Section 2.6.2.2). The synthetic age spectrum in this case study shows monotonically increasing step ages to an apparent plateau encompassing the last 70% of the cumulative ^{39}Ar released. As discussed previously, this age spectrum pattern would conventionally be interpreted as reflecting partial diffusive loss of ^{40}Ar*, but for this mixture actually represents the simultaneous degassing of Ar from minerals (jarosite, plagioclase, and sanidine) with different ages and Ar diffusion kinetics. Like in case study 1, the very good fit we observe with the age spectrum for the synthetic Martian mixture reflects the fact that this mixture satisfies the assumptions underlying the Bayesian model setup. Unlike case study 1, for which I suspect issues with the furnace calibration at low temperature, I also observe good agreement between the synthetic Martian ^{39}Ar cumulative release curve, and the Bayesian mean posterior model (Figure 2.9C). These results are not unexpected for case study 3, as I have defined the diffusion kinetics grain size for each component in the mixture, and I do not introduce non-ideal behavior such as complex diffusion behavior (e.g., MDD) or non-volume diffusion. The idealised parameters I chose also enable us to deconvolve the component ages in this synthetic mixture within the uncertainty of the known component ages. However, as our synthetic muscovite mixture from case study 2 demonstrates (Figure A.19 and Table A.1), our ability to deconvolve the component ages is not a self-fulfilling outcome of generating a synthetic dataset and is dependent on the individual components of the synthetic mixture having non-identical Ar diffusion kinetics. One potential limitation of this case study is that I have not included a non-negligible amorphous K-bearing component (e.g., feldspathic glass), which has been observed in Murray Formation mudstones (Rampe et al. (2017)) and which may carry geologically relevant age information. It is possible to include an amorphous phase within this model as diffusion studies of glass have been carried out previously (e.g., Cassata et al. (2010), Gombosi et al. (2015)). However, the diffusion kinetics of amorphous materials have not been extensively studied and as such uninformative priors would need to be constructed for these parameters to reflect this limited knowledge.

2.6.2 Comparison to other approaches

Cassata et al. (2010) and Boehnke et al. (2016) have recently presented models for fitting and inferring information from age spectra from the degassing of multi-component mixtures. Our Bayesian approach is similar to theirs in that I assume each mixture

is comprised of multiple components characterized by different Ar diffusion kinetics, which is analogous way that MDD modelling assumes that crystals are comprised of multiple domains with distinct diffusion kinetics of individual components. However, both Cassata et al. (2010) and Boehnke et al. (2016) incorporate MDD-type behavior for individual components, which is an often-observed property of framework silicates (McDougall & Harrison (1999)). Our Bayesian framework can accurately represent MDD-type behavior: each domain in a particular mineral exhibiting MDD behavior will be represented as a component with a distinct age and Ar diffusion kinetics in the model posterior. However, because the framework as I implemented it here uses the number of components as a prior, I assume that MDD-type behavior is not occurring and that each component can be accurately represented with a single diffusion domain. Our assumption of simple diffusion behavior for individual components may contribute to our challenges in deconvolving age components for mica mixtures in case study 2. I describe in greater detail below how this assumption can be removed using a non-parametric framework in future work. There are several major advantages of our Bayesian approach over those of Cassata et al. (2010) and Boehnke et al. (2016). First, in contrast to Cassata et al. (2010) my approach allows parameters like diffusion kinetics to be constrained by the model inversion rather than imposed. Furthermore, the Bayesian approach enables us to directly quantify the uncertainty of all model parameters by their description as posterior probability distribution functions. This is distinct from the approach of Boehnke et al. (2016), which cannot quantify uncertainties of model parameters due to the computational complexity of the approach Boehnke et al. (2016). However, unlike Boehnke et al. (2016) I do not jointly optimize the Arrhenius plot and age spectrum, nor have I incorporated MDD-type behavior for individual components. As many samples exhibit Ar diffusion with MDD-type behavior, incorporating this type of behavior is one of the ways I can improve our model framework, which I discuss in more detail below.

2.6.3 Future work

2.6.3.1 Observational improvements

As previously mentioned, one potential reason why I was more successful in deconvolving the mixtures in case study 1 than in case study 2 may be the number of steps in the heating experiment and the resulting structure of the $^{40}Ar/^{39}Ar$ age spectra. The

age spectra in case study 1 are characterized by many more temperature steps than the age spectra in case study 2, which allows finer scale structure in the age spectra to be observed in case study 1. As noted by Gillespie et al. (1982) and Dong et al. (2000), differing diffusion kinetics between mixture components can allow Ar release from each component in the mixture to be unmixed via thermal separation, as the less retentive phases will experience greater degassing at lower temperatures than more retentive phases (e.g., Figure. 2.10). Degassing mineral mixtures over a greater number of steps and over smaller increments of temperature change should therefore enhance this thermal separation. I therefore suggest that, ideally, a very detailed heating schedule ($\geq$ 50 steps) coupled with our Bayesian approach has the greatest potential for success when deconvolving multi-component mixtures. In addition to degassing mixtures over many steps, other heating schedule strategies such as isothermal and retrograde heating steps, as noted by Harrison et al. (1991), should further help in unmixing the Ar contributed from each component in a mixture.

In addition to optimizing step heating experiments, I can pair mixture age spectrum data with other observations to place more informed constraints on priors in our model framework. Priors are one of the most important ingredients in the Bayesian framework, as they express our state of knowledge about a parameter before data is observed and constrain the posterior space of the model to a space smaller than that allowed by the likelihood itself. The age priors used in the case studies presented here are as uninformative as possible: a uniform distribution between 0 and 4.6 Ga. A uniform prior such as this does not affect the landscape of the posterior. By providing more informed priors in our model setup, it is possible to both increase model efficiency and yield better constraints on the posterior distributions of model parameters. For example, XRD information on mineral mixtures can be used to constrain the mineral phases that make up the mixture. This information about minerals present can be used to both optimize heating schedules for step heating experiments and use more informed priors for the diffusion kinetics characterizing each component in the inversion setup. Additionally, for real geological samples I can incorporate geologic context into our prior for mineral component ages. For example, if I have a sample from a terrestrial setting in a particular stratigraphic unit of known age, I can constrain the ages of components to be equal to or greater than the stratigraphic age. Similarly, in many cases I will have constraints on the range of potential source ages of sediment in a basin setting that can be used to better define age priors. Age priors such as this

are frequently utilized in Bayesian radiocarbon modelling (Ramsey (2009)) and can be readily incorporated into the Bayesian framework presented here.

2.6.3.2 Model improvements

Our three case studies highlight the advantages and shortcomings of our Bayesian approach and areas where implementing modifications to the model framework can improve fits to $^{40}Ar/^{39}Ar$ datasets as well as confidence in the estimated parameters of interest like component age. As discussed above, I think that one of the biggest challenges I faced modelling the age spectra, cumulative release curves, and component ages in case study 2 may be MDD-like behavior. In the current model framework, I cannot account for MDD-like behavior if it occurs within a component as I have defined it. In non-artificial mixtures, I will also likely need to account for grain size variation and its effect on diffusion kinetics, which will have a similar effect to MDD-like behavior. However, as discussed above, I may not have information about the presence of MDD-like behavior a priori, nor may we have detailed constraints on the grain size distribution in some mixtures (e.g., *in -situ* planetary measurements or bulk meteorite analyses).

Having a priori knowledge of either MDD-like behavior or the grain size distribution of a mixture component may not be necessary if I modify our Bayesian framework to be nonparametric. In such a modelling framework, the number of variables represents an unknown to be inferred (i.e., the underlying grain size distribution or the number of domains). Given that our datasets are both non-negative and compositional, I can utilize mixture models in which our observations are some linear combination of end member processes. Mixture models have been widely utilized in detrital geochronology (Sambridge & Compston (1995)) and grain size distribution studies (Yu et al. (2016)), which are also non-negative and compositional in nature. The Dirichlet process is one way to implement nonparametric statistics and is used primarily in Gaussian mixture models where the number of Gaussian distributions is unknown (Ferguson (1973), Sethuraman (1994)). Another nonparametric approach is to use a reversible jump Markov Chain Monte Carlo (RJMCMC) algorithm, where the number of model parameters is allowed to vary between model steps (e.g.,Gallagher (2012)). Both Dirichlet and RJMCMC methods can be readily implemented into our existing Bayesian framework, although both methods will make our Bayesian model substantially more computationally expensive (approximately an order of magnitude slower, based on preliminary

implementations). Regardless of implementation of a nonparametric Bayesian framework, I can also place additional constraints on the age prior for components using the method of asymptotes formulated by Forster & Lister (2004). In their interpretation, an upward-converging age asymptote, or partial pseudo plateau, represents the minimum age of one component, while a downward-converging asymptote represents a maximum age of another. Although the presence of asymptotes provides only lower or upper bounds on the age of components, I could potentially use this method of bounds to restrict the prior space for the age components. For example, Mixture 1 in case study 1 (Figure 2.1) exhibits a downward asymptoting plateau at ∼2 Ma which could be interpreted as a maximum age for the more retentive ACs component, thus allowing the age priors to be restricted between 0 and 2 Ma rather than 0–4.6 Ga. Similarly, the initial pseudo plateau at ∼12 Ma could be interpreted as a minimum age for the HD-B1 component, restricting the prior age for this component between 12 Ma - 4.6 Ga. Placing a narrower uniform distribution on the prior age for the ACs component may enable us to reduce the uncertainty in our posterior age estimate, which was elevated for this component relative to the other, older components in case study 1. In general, using asymptotes as a constraint may increase our model efficiency and potentially improve our estimates of posterior distributions of model parameters. A final improvement I envision for our Bayesian model framework is to fit additional parameters, such as the K/Ca ratios calculated from step heating experiments. K-bearing minerals have ranges of K/Ca ratios that can be included as prior information (e.g., McDougall & Harrison (1999)). Since K/Ca spectra will depend on many of the same model parameters as age spectra and cumulative release curves (e.g., a, E_a, D_0, ϕ), by including this observation I anticipate being able to better constrain the posterior distributions of these model parameters, as well as model parameters such as component ages. In summary, although our Bayesian framework as implemented here can be used to successfully deconvolve $^{40}Ar/^{39}Ar$ datasets from mineral mixtures, I can add additional model constraints to further improve our posterior estimates of model parameters, as well as make our model framework more flexible to accommodate $^{40}Ar/^{39}Ar$ datasets from more complex mixtures.

2.6.4 Applications

There are several geological applications for which obtaining $^{40}Ar/^{39}Ar$ datasets from polymineralic samples are useful or necessary. In these circumstances, the conventional

'plateau' criteria often used to interpret $^{40}Ar/^{39}Ar$ datasets is of limited or no value. Our Bayesian approach provides a quantitative interpretive framework that can yield geologically meaningful age information from multi-component samples. I envision the Bayesian approach being particularly useful for are (1) provenance studies of fine-grained sediments and (2) dating of terrestrial and extraterrestrial materials, both *in situ* by exploration vehicles or analysis of returned samples and meteorites.

In provenance studies, conventional sample preparation approaches may be undesirable for fine-grained sediment samples, especially in the case of silt sized material ($\sim$20–63 μm) whereby the processes of acid leaching or picking under an optical microscope could result in grain size biasing or loss of sample. In such a setting conventional K-Ar ages or $^{40}Ar/^{39}Ar$ fusion ages will reflect the integrated $^{40}Ar/^{39}Ar$ ages of all the sediment sources, and therefore not provide geologically meaningful information. Through the use of detailed stepwise heating coupled with our Bayesian approach, the ages corresponding to different sources could be estimated, and in cases where the potential source bedrock ages are known the presence or absence and possibly even the proportion of a particular provenance signal can be determined. Using our Bayesian approach could therefore be fruitful in provenance studies of loess (e.g., China Loess Plateau), submarine fan systems (e.g., Bengal Fan) and sediments that result from megaflood events (e.g., channeled scablands of North America) where fine-grained sediments will dominate. One important caveat is that application of $^{40}Ar/^{39}Ar$ dating to fine-grained material could be susceptible to recoil. It has been shown that ^{39}Ar can recoil ca. 0.08 μm (Onstott et al. (1995)) and therefore can be problematic for $^{40}Ar/^{39}Ar$ dating of fine-grained materials. There is no doubt that reactor-induced ^{39}Ar and ^{37}Ar recoil will limit the application of our approach. However, as identified by VanLaningham & Mark (2011) I do not expect recoil to be a major issue if samples are sonicated (to remove clay-sized particles adhered to coarser grains) and sieved at 10 μm and larger. Furthermore, I could build on knowledge from previous studies (e.g., Onstott et al. (1995), Paine et al. (2006), Jourdan et al. (2007)) and incorporate the effects of recoil on the initial distribution of ^{39}Ar and ^{37}Ar explicitly into our model framework, which would allow us to apply this framework to the finest grained provenance archives without resorting to micro-encapsulation techniques that allow for direct measurement of recoiled ^{39}Ar and ^{37}Ar (Dong et al. (1995)). Nevertheless, if possible, experiments designed to utilize our Bayesian model should interrogate a range of grain-sizes common to all samples of interest, including the coarsest fractions which

are not susceptible to recoil. In addition to the use as a provenance tool, our Bayesian approach could also be particularly useful for geochronology of planetary materials, both in the unlikely case of in situ planetary geochronology and, more prevalently, in the analysis of meteorites or mission-returned samples that are too fine-grained or valuable to carry out mineral separation. In the only in situ approach, the dating of the Martian regolith, the Curiosity rover SAM suite was used for analysis and the sample preparation was limited to simple sieving before SAM analysis. Detailed XRD analysis prior to the analysis revealed that in both cases multiple K-bearing components were constituents of the regolith (e.g., jarosite, and plagioclase). Given this limited sample preparation, by default, the samples must be of a polymineralic nature; however, what is not known is the geological age(s) of the K-bearing components. An attempt was made by Martin et al. (2017) to thermally separate K-components by employing a two-step heating method. In this analysis the low temperature step preferentially degassed the less retentive, younger component, inferred to be jarosite, and the high temperature step degassed a more retentive and older component, inferred to be detrital feldspar. However, despite the success of these applications the K/Ar ages inferred are only as accurate as the underlying assumptions that are coupled with them. Our Bayesian approach has the potential to interrogate extraterrestrial surfaces and more extract ages of the K-bearing components in the Martian surface. As mentioned above, the application of XRD priors to analysis would allow for the creation of prior probability density functions for mineral specific information (i.e., E_a, D_0, ϕ, K/Ca); furthermore the process of sieving will create bounds on the grain size priors. I highlight such an example in case study 3 which provides an idealised synthetic $^{40}Ar/^{39}Ar$ dataset of the Martian regolith of three different K-bearing components and ages; jarosite (2.1 Ga), plagioclase (4.3 Ga), and sanidine (4.1 Ga). This idealised case study highlights the applicability of our Bayesian analytical method to extract geologically meaningful ages from in situ rocky body settings.

2.7 Conclusions

Currently the $^{40}Ar/^{39}Ar$ dating system is most commonly applied to either single mineral phases or groundmass analysis. However, there are geological settings and problems where the analysis of mixtures with multiple components will be desirable or necessary, and such mixture data requires a nonconventional approach to estimate the

age (s) of each of the components that constitute the mixture. I have developed a Bayesian approach to address this problem, which first consists of constructing a multiple component age equation then inverting an $^{40}Ar/^{39}Ar$ dataset within this multi-component age framework to estimate the desired model parameters, i.e., the age of each component.

With our Bayesian approach, I find that there is more information available in mixture age spectra than previously realised, although our approach also has limitations. The reanalysis of the mixtures of monitor standards created by VanLaningham & Mark (2011) demonstrates that our model does a reasonably good job of fitting observed $^{40}Ar/^{39}Ar$ age spectra from mixtures, but generally does not reproduce cumulative ^{39}Ar release curves. The misfit with the latter is likely a consequence of inaccuracies in the calibration of the furnace used by VanLaningham & Mark (2011) at low temperatures. Of most significance, our reanalysis demonstrates that, with prior knowledge of the number of components and the mineral phases present, the ages of individual components can be inverted from $^{40}Ar/^{39}Ar$ datasets resulting from bulk mixtures. The ability of our model to invert individual component ages is a consequence of these mixtures meeting the assumptions I set forth in the model setup. Our reanalysis of the biotite and muscovite mixtures created by Kula et al. (2010) presents a limiting case for our modelling approach.Specifically, I was unable to resolve multiple components in the Kula et al. (2010) mixtures with the same degree of prior information used to invert the VanLaningham & Mark (2011) mixtures. In addition to prior knowledge of the number of components and mineral phases present, I also had to place narrower prior constraints on the mixing fractions in order to accurately resolve more than one component. With this additional prior information, I improved our estimates of the age components and resolved the known ages in all but one case, the younger component (NY25) in the 3:1 IV14:NY25 mixture. In all estimated ages I see an inflated uncertainty compared with both case study 1 and case study 3. I hypothesize that this is largely due to the similarity in Ar diffusion kinetics between the components in the Kula & Baldwin (2011) muscovite mixtures. There may also be issues associated with the assumptions in our model setup, including potential MDD-like or non-volume diffusion behavior, particularly for the biotite mixtures. It is also possible that, for these mixtures, a more detailed heating schedule that better resolves the structure of the $^{40}Ar/^{39}Ar$ age spectrum would improve the performance of our Bayesian model.

In addition to reanalyzing mixtures created in the laboratory, I also present an ex-

ample hypothetical application of our Bayesian approach for deconvolving an $^{40}Ar/^{39}Ar$ age spectrum from in situ measurements on Mars. This synthetic dataset, which I generated from existing Martian geochronological and mineralogical data, strongly resembles an $^{40}Ar/^{39}Ar$ age spectrum for a single component sample that has experienced diffusive loss. Nonetheless, I was able to use my Bayesian model to predict the $^{40}Ar/^{39}Ar$ age spectrum and cumulative ^{39}Ar release curve, as well as determine the component ages, of the synthetic dataset. Our example therefore highlights how our Bayesian approach could be used to distinguish between different possible interpretations of complex age spectra when multiple components are present. I propose that the Bayesian framework presented herein could allow the utilisation of $^{40}Ar/^{39}Ar$ as a provenance tool for finegrained sediments, as well as for geochronology studies of meteorites and mission-returned samples from rocky bodies in the inner Solar System.

Chapter 3

Stepwise heating of $^{40}Ar/^{39}Ar$ blind mixtures with applications to bulk sediment provenance studies

3.1 Introduction

In the previous Chapter I have shown that Bayesian modelling can be used successfully to infer the known ages of each mineral component in $^{40}Ar/^{39}Ar$ datasets of incrementally heated multiple mineral component mixtures. However, despite the success of this approach the model makes two assumptions that are oversimplifications, which need to be addressed: (1) that single domain behaviour is adequate to describe the loss of argon both in the geological history of a component and in the incrementally degassing of the sample during analysis and; (2) that the number of components is known prior to the analysis. In a natural geological setting any one, or combination, of these assumptions may be violated.

The first assumption, that single domain behaviour is adequate to describe the loss of argon, is shown to be violated in a number of studies (e.g., Zeitler (1987), Lovera et al. (1989), Harrison et al. (1991), Lovera et al. (2002), Cassata et al. (2010), Boehnke et al. (2016)). The violation of the assumption was first highlighted by Zeitler (1987) who noted that curvilinear behaviour in Arrhenius space was not behaviour expected from argon loss from a single domain, which would define a single line in Arrhenius space. Zeitler (1987) hypothesized that the curvilinear behaviour could be explained by the presence of sub-sample size diffusion length scales or an underlying domain size distribution of the sample. Lovera et al. (1989) then built on this idea to formulate

a more complex modelling approach; the Multi-diffusion domain (MDD) model. This model assumes that a sample contains a population of variably-sized non-interacting diffusion domains that form during crystallisation and remain intact throughout the geologic history and step heating of the sample. Coupled with this assumption, it is further assumed that loss of Ar occurs by thermally driven volume diffusion both over geological and laboratory time scales. Despite some researchers suggesting that (1) the mathematical construction of non-interacting domains is non-physical, (2) the loss of Ar could be controlled by other mechanisms in nature (e.g., fluid interactions), and/or (3) step heating modifies the bulk diffusive properties of a sample (e.g., Foland & Xu (1990), Lee (1995), Villa & Hanchar (2013), Parsons et al. (1999), Popov & Spikings (2020)), it has been shown that the MDD model has the ability to accurately reconstruct the thermal history of rocks over millions of years (e.g., Lovera et al. (2002)). Given this, and that multiple diffusion domains are likely a property of most framework silicates (e.g., McDougall & Harrison (1999)), it is therefore appropriate to include this behaviour into my modelling approach by modifying the mathematics to include MDD behaviour.

The second assumption, that the number of distinct age components is known, is most likely violated in most real world applications. To illustrate this, consider a fine-grained provenance study for which samples are collected from delta or fan sediments and are the mixture of multiple distinct sources. Prior to conducting $^{40}Ar/^{39}Ar$ analysis of bulk sediment, it is impossible to be able to force the constraint that the number of distinct age populations to be known. To remove the forced constraint of a known number of components, the modelling shown in Chapter 2 is extended from a parametric approach (one where the number of modelling parameters is known) to a non-parametric approach (one where the number of parameters is itself a parameter to be inferred in the model). This modelling set up is described in this Chapter.

Here I extend my Bayesian modelling approach by removing the constraints of a fixed number of components and single domain type behaviour. This model will then be used for a detailed analysis of more complex mixtures than the previous chapter to infer all parameters of the system: (1) the number of components; (2) the ages of each of these components; (3) the grain size distribution and/or MDD-type behaviour of each sample; (4) the activation energy (E_a) and frequency factor (D_0) of each component; and (5) the mixing fraction of each component. The model uses a nonparametric Bayesian framework using the stick breaking formulation of the Dirichlet process to

estimate the number of components and the properties of each estimated component. Unlike the previous chapter where the model was a joint inversion of the age spectrum and cumulative ^{39}Ar datasets, in this model iteration I jointly invert the age spectrum and Arrhenius array datasets. The cumulative release dataset of the previous Chapter is used to make the Arrhenius dataset following the equations of Fechtig & Kalbitzer (1966) so this change is arbitrary but, it does align the model with other recent studies (e.g., Lovera et al. (1989, 2002), Cassata et al. (2010), Boehnke et al. (2016)). The model framework is discussed in more depth in the methods section. The nonparametric approach presented here provides an initial state of ignorance considering the number of parameters and the possible range of those values to be unknown, except in cases where non-informative priors can limit the range to what is reasonable (e.g., minimum of age(s) >0 a).

The format of this chapter is as follows. In section 3.2, I review the expected observations of both the age spectra and Arrhenius arrays from the stepwise heating of mineral mixtures. In section 3.3 and 3.4 I introduce my Bayesian nonparametric modelling method and the mixture datasets. In sections 3.5 and 3.6 I show and discuss the results of the model on laboratory-generated blind mixtures. To conclude, I discuss applications of this method to different geological environments that contain materials with mixed mineral assemblages.

3.2 Expectation of Arrhenius and age spectra datasets from the stepheating of mineral assemblages

In the conventional ^{40}Ar/^{39}Ar technique incremental heating is used to gain information into the internal distribution of Ar within the sample. By this method, processes which affect the distribution of the parent (represented by ^{39}Ar) and radiogenic daughter ^{40}Ar* can then be interrogated, including metamorphic events, hydrothermal activity, episodic loss, impact heating, presence of extraneous (non-radiogenic daughter $^{40}Ar_{EX}$) or weathering. If the sample has remained a closed system, the internal distribution of the parent and daughter Ar isotopes should yield a uniform ratio across all regions of the sample and thus define a plateau in age spectrum space. In this study I apply the incremental heating technique, not to interrogate the geological process or the thermal history of the sample, but to use the valuable mineral and temperature dependent release kinetics of individual components coupled with my nonparametric model to

attempt to retrieve individual ages from a multi-age polymineralic mixture. Since the Ar I extract will be from a mixture of components with a range of ages and mineral compositions, detailed incremental heating schedules provide a means of determining the relative contributions of each mineral to the shape of the age spectrum. In the following section, I discuss the traditional features of an age spectrum diagram providing a framework for the modelling methods discussed to un-mix multi-age polymineralic age spectra.

Traditionally, in an age spectrum for the simplest case, which is a single mineral with a single pair of diffusion kinetics and single grain size (E_a, D_0, a), the main interpretive features are: (1) Cooling age (represented by the plateau age), (2) Ar loss (normally interpreted by a staircase pattern toward a pseudo plateau at higher temperature release steps), (3) Ar recoil (elevated initial steps as ^{39}Ar is lost from the outer regions of the sample during irradiation) and (4)inherited or excess $^{40}Ar_{EX}$ (normally characterised by a saddle shaped age spectra with high initial steps falling to a plateau then rising again at the higher temperature release steps; Lanphere & Dalrymple (1976)). However, by incrementally heating multi-age polymineralic mixtures the age spectra features can include all of the the above mentions for any of the components in the mixture. Ar will be released from all component over incremental heating. Individual age steps will be a mix from the contribution of all Ar from components that are thermally activated over the particular temperature and time step. To highlight the features of a multiage polymineralic age spectra I show blind mixture 1 (Figure 3.1, A) that is analysed later in this study. The blind mixture 1 age spectrum shows a pattern that is indicative of multiple age components; complex release patterns, staircase patterns similar to diffusive loss of ^{40}Ar (e.g., Turner (1968)) and pseudo plateau section at which time a particular component in the mixture is completely dominating the release. This pattern is similar to other bulk mixture degassing profiles which show erratic age spectra behaviour (e.g., VanLaningham et al. (2006, 2008), VanLaningham & Mark (2011), Villaseñor et al. (2016)).

Another distinct source of information in an incremental heating experiment is the Arrhenius array (Figure 3.1, B). The Arrhenius array is derived by plotting the natural log of the diffusion coefficient against the inverse of the laboratory heating temperature obtaining estimates of the activation energy (E_a; proportional to the gradient) and frequency factor (D_0; proportional to the intercept). The diffusion coefficient is calculated from the inverse of the ^{39}Ar release function assuming a single diffusion length scale

(Fechtig & Kalbitzer (1966)). In the degassing of a bulk sample, individual mineral diffusivities will be identifiable in Arrhenius space, for example the presence of multiple activation energies will be signified by a mixture of multiple slopes, the same is true for frequency factor derived from the intercept (D_0). Arrhenius arrays that result from the stepwise heating of an assemblage of mixtures can be thought of as a weighted average of a series of lines in Arrhenius space that define the linear array of diffusion characteristics of each component. This itself is the simplest example as each component may be composed of a range of effective diffusion length scales, which can itself be thought of as the weighted average of a series of parallel lines that define the dominant diffusion length scales of each domain within that component. The Arrhenius spectra (Figure 3.1, B), highlights the existence of multiple components diagnostic by the emphasised curvilinear pattern with the clear existence of multiple slopes and intercepts (therefore multiple activation energies (E_a) and frequency factors (D_0)). However, the observed non-linearity in this array could be further emphasised by the presence of multiple diffusion domains that are a characteristic of each component. By utilising both of these observations I can attempt to recover all of the systems parameters the describe these datasets.

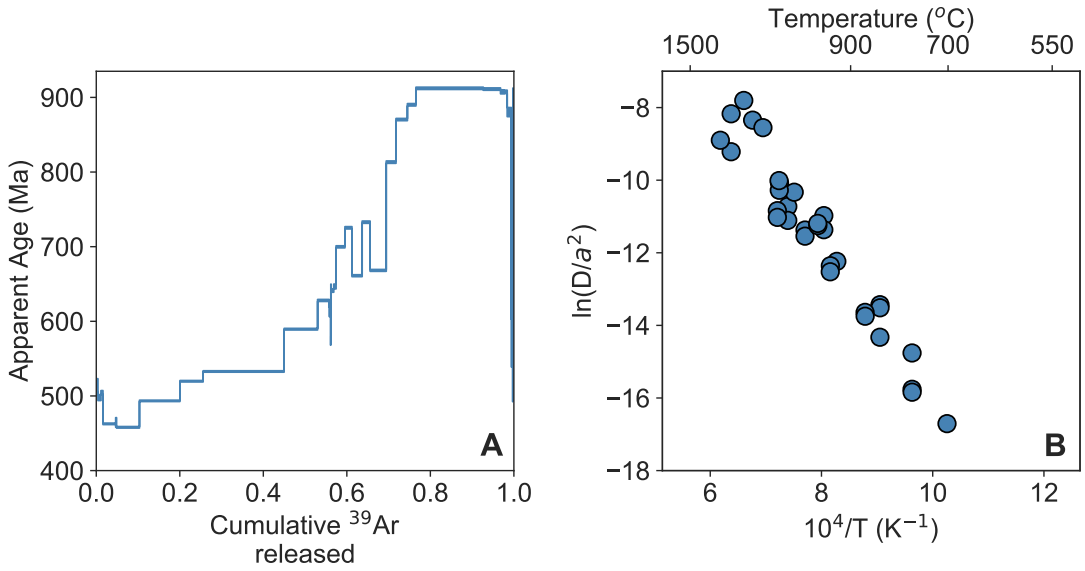

Figure 3.1: Panel A shows age spectra and panel B shows Arrhenius array of blind mixture 1. Note the discordant age step indicative of the presence of multiple ages of contrasting retentivity; with a younger age component that is less retentive dominating the early release and an older component that is more retentive dominating the latter high temperature steps. The presence of multiple components is further highlighted by the Arrhenius array (B) which shows multiple slopes and intercepts indicating the presence of multiple activation energies and frequency factors. However, the non-linearity observed could potentially be further heightened by the presence of multiple diffusion domains of varying length scales.

3.3 Model

In this section I describe the modelling set up to fit and infer desired parameters of the observed multi-age polymineralic age spectra and Arrhenius arrays. Unlike Chapter 2, I choose to fit the Arrhenius array rather than the cumulative release spectrum as an additional complementary dataset to the age spectrum. As the Arrhenius array is derived from the cumulative release this choice is arbitrary, but it aligns our model with the current literature (e.g., Lovera et al. (1989), Cassata et al. (2010), Boehnke et al. (2016)).

Firstly, I explain the assumptions of the model, which aim to maximise utility and be as least biasing as possible. The two main limiting assumptions are: (1) each component is described by a single age and (2) the loss of Ar is dominated by thermally

driven volume diffusion. Despite these constraints it is shown through the modelling of a series of blind mixtures that the behaviour need not be so simple but, just that volume diffusion dominates the loss. I further assume that each component is defined by a single set of diffusion kinetics and each component could potentially exhibit MDD type behaviour or is composed of multiple grain sizes. In the modelling set up this is implemented in a Bayesian framework, which allows for the number of domains to be 1 therefore describing Ar loss via a single length scale.

3.3.1 Bayesian inference

The use of Bayesian inference is ubiquitous across many fields of science (e.g., Koop (2003), Trotta (2008), Feroz et al. (2009), Ramsey (2009), Gallagher (2012) as a means of combining existing knowledge with new data to construct a better understanding, presented as a probability density function, of a given systems parameters. Prior knowledge is encoded in probability density functions that capture the most likely distribution of values that define the parameters in the model, these are known as Priors (P(θ)). In a general Bayesian model set up we first choose a set of hypotheses in the form of a vector of parameters, θ. Priors, (P(θ), are an important part of the Bayesian inference recipe, they reflect our state of ignorance about a physical parameter, for example, if we are in a complete state of ignorance with respect to the various ages of each mineral component in a mixture, our prior should reflect this (e.g., using a uniform distribution between 0 and 4.6 Ga). Specifically, in this case, the priors would define all physical parameters in the model e.g., the age, diffusion kinetics, mixing coefficient and grain size of each component in the model. Priors, P(θ), are then updated with respect to the likelihood, P(y | θ) the probability of the data with respect to the prior parameters, to form the posterior (P(θ | y)) from which all information is obtained. The updating of priors with respect to new observation to obtain the posterior is the foundation of Bayesian inference. Bayes' theorem is shown in Eq 3.1:

$$P(\theta|y) \propto P(y|\theta)P(\theta), \qquad \text{Posterior} \propto \text{Likelihood} \times \text{Prior} \tag{3.1}$$

Here, I take the proportional form of Bayes' theorem where the symbols corresponds to the word form of the equation, and y represents the observation. However, in the model I wish to accurately reflect prior knowledge that reflects what I would know or not know in reality: unknown number of components, unknown mineral phases, and

unknown ages of each component. Starting from this position of ignorance I want to infer the most likely number of components that describe the data. To avoid fixing the number of components and number of domains for each of the mineral components I use a non-parametric model in a Dirichlet process (DP) framework (Ferguson (1973), Antoniak (1974)). In the model set up, priors, (P(θ)), for each mixture parameter (component and domain mixture weights) are constructed using the stick-breaking form our the DP, shown in the next section.

3.3.2 Stick-breaking process

The Dirichlet process (DP) (Ferguson (1973)) is a powerful Bayesian non-parametric prior for mixing components (Hjort et al. (2010)). In the model I draw from our non-parametric DP prior by the stick-breaking process (Sethuraman (1994)), which is a full Bayesian construction of the DP. This can be constructed following Sethuraman (1994),

$$G = \sum_{i=1}^{\infty} V_i \prod_{j=1}^{i-1}(1 - V_j)\delta_{\theta_i} \tag{3.2}$$

$$V_i \overset{iid}{\sim} \text{Beta}(1, \alpha) \tag{3.3}$$

$$\theta_i \overset{iid}{\sim} G_0 \tag{3.4}$$

The stick-breaking process is so called because proportions of the stick, V_i, are sequentially broken from the remaining length, j = 1_{i-1}(1 - V_j), of a unit-length stick. In my model the proportions of the unit-length stick represent the mixture fraction of each component in the mixture. As i, the number of stick breaks increases, these weights stochastically decrease because smaller and smaller fractions of the unit stick remain, and so only a small number of weights contribute to the total sum. In theory this process is applied by implementing an infinite number of breaks, however, in practice for the $^{40}Ar/^{39}Ar$ model I truncated the number of breaks to 20. I show in the results section that this does not bias the output of the model.

In addition to this parent stick breaking process, above, I also create a daughter Dirichlet process to account for the possibility of the presence of multiple domains (Zeitler (1987), Lovera et al. (1989)) or grain size distributions (e.g., Harrison (1983)).

This is constructed in an analogous fashion. The Dirichlet process used for both the prior on the number of components and number of domains satisfies both the additive sum-to-one and non-negativity constraints (Lovera et al. (1989)).

3.3.3 Occam's Razor

In order to estimate the most likely number of components and the parameters which describe those components I rely Occam's razor which is a fundamental basis of Bayes Theorem (Eq 3.1). In scenarios where there are several competing theoretical models of an observed dataset, a Bayesian inference provides a formal way of comparison using the complexity of the data and any prior information that is available. The 'best' model is then one which strikes the delicate balance between the quality of the fit of the data and prediction. In any scenario, it is clear that a model with more free parameters will always fit data better as it has more parameters to tune and fit to the dataset. However, more free parameters also means a more 'complex' model. Through the formulation of Bayes equation a natural means of penalising complexity arises to determine the model that is the simplest but also fits the dataset without any redundant complexities. For example, consider the fitting of the age spectra and Arrhenius array shown in Figure 3.2.

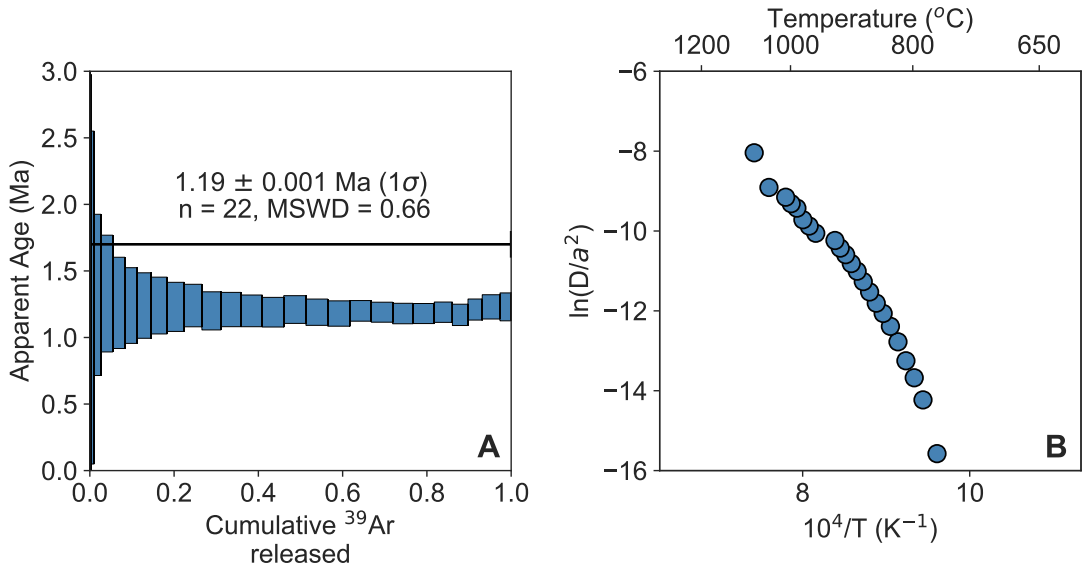

Figure 3.2: Panel A shows the age spectra of Alder Creek sanidine modified from Van-Laningham & Mark (2011). Blue boxes are the reported ages of each time temperature step, data in the figure is at 2σ. Panel B shows Arrhenius data of the Alder Creek sanidine using the ^{39}Ar release and the equation of Fechtig & Kalbitzer (1966) for loss from a sphere. Note that in this particular dataset aside from an initial low few steps due to small fractions of near background ^{39}Ar release and an upward inflection at very high temperature the data is highly linear.

It is clear that this age spectrum is the result of a single mineral component of a single distinct age (∼1.2 Ma). However, the same model fit would also be obtained for a two component mixture of two distinct ages that degas in concert to result in the plateau observed. Following equation 1, I can explicitly show how the Bayesian framework would compare these models.

Firstly, to simplify the expression I can assume that for both models the fit of the data is exactly the same effectively factoring out the likelihood from the expression. Now, I have a posterior probability ($P(\theta \mid y)$) dependent only on the product of the prior probabilities $P(\theta)$ of each variable. Consider the component of the simplest model which is described by the following priors on the parameters: age, activation energy, frequency factor, mixing fraction, and grain size. The second model will have double the number of parameters to describe the mixing of two components. Following that the probability of any prior, $P(\theta)$, is ≥ 0 and ≤ 1, the multiplication of all the priors in the second model must result in a lower posterior probability ($P(\theta \mid y)$) when compared to the simpler one component model. For this particular case, the Bayesian comparison

will choose the simplest model if more than one model fits the data equally well. This is the natural foundation of the Bayesian equation, which I exploit in the non-parametric model to fit the age spectra of more complex mixtures.

3.3.4 $^{40}Ar/^{39}Ar$ non-parametric Bayesian model

My $^{40}Ar/^{39}Ar$ model assumes that the observed age spectra and Arrhenius array dataset is the result of the mixing of Ar release from some K (where K is an integer K = 1, ..., n) number of mineral components. By using the stick breaking approach I estimate the number of components K and then assign each to the mineral component specific parameter: activation energy (E_a), frequency factor (D_0), grain size (a), age, mixing fraction (ϕ), number of domains (m), domain volume (ϕ_m) and domain length scales (a_d). I fit the Bayesian non-parametric model to the age spectra and Arrhenius array through the multiple component multiple domain (or grain size variation) models given by:

$$\text{Age}_{obs} = \frac{\sum_{i=1}^{k}\sum_{j=1}^{m}\phi_{i,j}\delta F_{i,j}\text{Age}_i}{\left(\sum_{i=1}^{k}\sum_{j=1}^{m}\phi_{i,j}\delta F_{i,j}\right)} \tag{3.5}$$

$$\ln\left(\frac{D}{a^2}\right) = \sum_{i=1}^{k}\left(\ln(D_{0i}) - 2\ln\left(\sum_{j=1}^{m}\frac{\phi_{i,j}}{a_{i,j}}\right) - \frac{E_{ai}}{RT}\right) \tag{3.6}$$

$$\phi_k = \sum_{i=1}^{k}\phi_i = 1 \tag{3.7}$$

$$\phi_m = \sum_{j=1}^{m}\phi_j = 1 \tag{3.8}$$

where δF is the derivative of the fractional release, F is the fractional release, Age is the age of each component, and ϕ_k, ϕ_m are the mixing fraction of the component and domains of each end-member. Both ϕ_k and ϕ_m are under additive sum-to-one constraints (shown in equations 3.7 and 3.8). I begin with the likelihood of my data, following Gallagher (2012) - I define the log likelihood of both the age spectrum and Arrhenius models following the sum of squares formulation shown below.

$$\chi^2 = \sum_{i=1}^{N}\left(\frac{d_i - m_i}{\sigma_i}\right)^2 \tag{3.9}$$

$$\mathrm{L} \propto \exp\left(\frac{-\chi^2}{2}\right) \tag{3.10}$$

where for the age spectrum model: d_i is the $^{40}Ar/^{39}Ar$ data, m_i is the model step ages, and σ_i is the observed uncertainty at each step i. For the Arrhenius model d_i is the Arrhenius data, m_i is the model, and σ_i is the observed uncertainty at each step i. Once the likelihood of each model has been constructed as shown above, the total log likelihood (L_T) is calculated by the summing of both individual log likelihoods with the addition of weights to each log likelihood:

$$L_2 = -\sum_{i=1}^{N} w_{2i}\left(\frac{d_i - m_i}{2\sigma_i}\right)^2 \tag{3.11}$$

$$L_T = L_1 + L_2 \tag{3.12}$$

Here, L_1 corresponds to log likelihood of the age spectrum part of the summation and w_2 and L_2 correspond to the weight vector and log likelihood of the Arrhenius part of the summation. The weight vector is included in the Arrhenius likelihood to prevent over fitting of the Arrhenius dataset. In the above equation I define a weight vector from the ratio of test log probabilities of each dataset for the mean model of each dataset. This is illustrated in Figure 3.3 using the dataset of the Heidelberg biotite (HD-B1) and Alder Creek sanidine (ACs) mixture from the previous chapter. Figure 3.3 shows the test log probabilities of each observation with the weight being described by the ratio of these. If this weight is not applied the model becomes anchored to the Arrhenius dataset as the likelihood, which is inversely proportional to the uncertainty, is far larger than the observed step age likelihood. This is only overcome with large excessive computation time on the order of days to weeks. However, with the application of the weights we scale the likelihood of the Arrhenius observable to be equal to the age spectrum. And both are fitted reasonably with good inference as illustrated in both the initial tests and the blind mixtures. By using the initial test log probability of each model I also have a unique weight vector for each case study, which is tuned for the particular pair of observed datasets.

Once this is constructed I can define the other part of the Bayesian equation; the priors. The priors for this nonparametric needs to reflect a level of ignorance of what is known for natural samples. Figure 3.4 shows the prior for the number of components. The prior chosen for this particular parameter is a gamma function; this is chosen

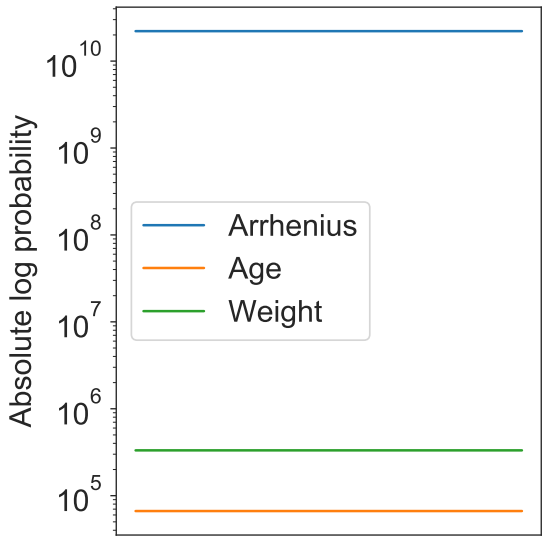

Figure 3.3: Absolute test log probabilities of the age spectrum and Arrhenius dataset of the HD-B1 and ACs mixture. The log probability of the age steps observation is shown in orange and the Arrhenius observation in blue. The weight is then described by the ratio of these and is shown in green.

with tuning parameters that preferentially sample mixtures with a fewer number of components than mixtures with a greater number of components. This particular parameter can be tuned for a particular application where prior knowledge dictates that mixtures with a greater number are more likely. For example, in Figure 3.4 the blue KDE and histogram favours a fewer number of components whereas orange and green KDE's and histograms show how this gamma function can be tuned.

The rest of the priors in the model: age (a), activation energy (kJmol^{-1}), frequency factor (cm^2s^{-1}), grain radii (μm), component and domain mixing fractions ϕ_k and ϕ_m are chosen to reflect the blind mixture problem, which is the purpose of this chapter. The activation energy, and frequency factor, and age priors are formed from two hyper-parameters that define both the mean and standard deviation for the chosen normal distribution of these parameters. These priors are shown in Figure 3.5 A - I. For all of these priors a uniform distribution is selected for the mean. Secondly, the standard deviation prior is constructed using a half-normal distribution satisfying the non-negativity constraint. Following this, these priors are combined to form a normal distribution with a mean from the uniform prior and a standard deviation from the half normal prior (Figure 3.5 A - I). The inclusion of the hyper-parameters for the age and diffusion kinetics is advantageous because if only a uniform distribution is selected, the log probability can either be 0 for values within the limits or negative infinity for

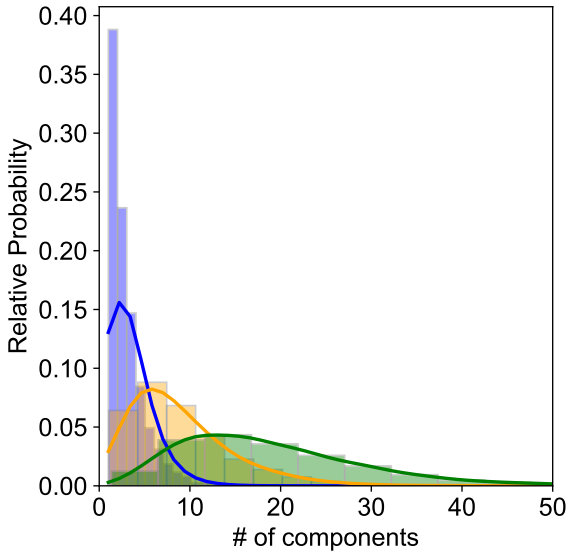

Figure 3.4: Prior for the number of components in the model. The prior is chosen as a gamma function with tuning parameters that preferentially sample a mixture with a lower number of components than one with a high number of components. This can be tuned when there is prior knowledge that suggests there are a greater number of components within a mixture, a fine-grained sediment derived from multiple source lithologies is a prime example of such a setting. The orange and green curves are an example of this tuning which give greater probabilities to mixtures with more components whereas the blue shows a prior in favour of fewer components.

values outside of the limits. Therefore, if this setup is used, there is no addition to the posterior and hence models of differing dimensions will be more difficult to compare. However, by using hyper-parameters for the mean and standard deviation, and then combining to form a normal distribution, I still remove any biasing but the log probability of the parameters are non-zero therefore making model comparison easier. A uniform prior is also selected for the grain radii (Figure 3.5 F) parameter to reflect that no single value in the ranges chosen has a greater probability than any other. Dirichlet priors are chosen for the mixing fraction satisfying the need for the non-negativity and sum-to-one constraint that is required for both of these parameters (Figure 3.5 G - H).

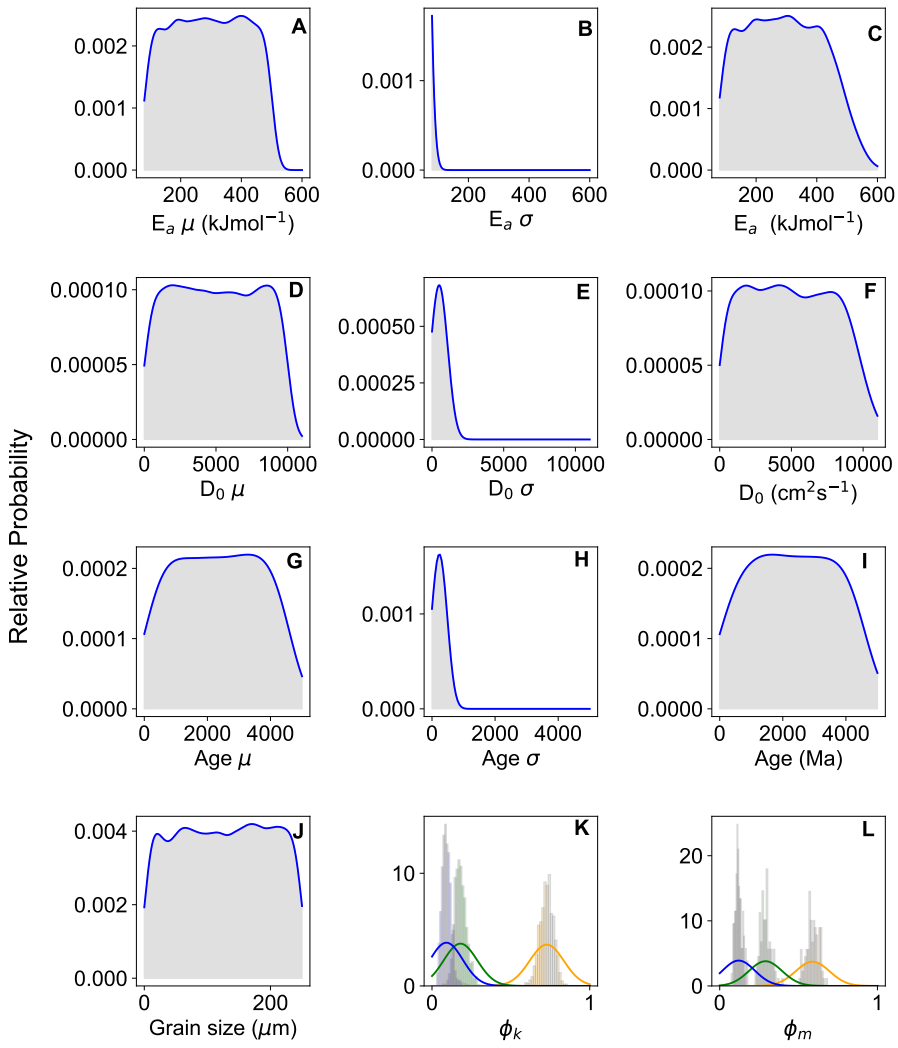

Figure 3.5: Priors used for parameters in this model. Panels A - F are the priors for the activation energy and frequency factor. Panels G and H are the mean and standard deviation hyperparameters of the age prior shown in panel I. Panel J shows the prior distribution for the grain size range. Panel K is an illustrated prior for the mixing fraction of each component in a mixture. For this particular illustrator value k, described above is chosen to be 3 and the relative mixing proportions of each of these components is shown by the orange, green, and blue histogram and KDE lines. Panel L is another illustration plot of the priors for the domain mixing proportions to illustrate the model; the value for m is again chosen as 3 with the priors for the mixing fraction shown by the orange, green, and blue histogram and KDE lines.

Following, the construction of the likelihood (Eq. 11) and the priors, a Markov Chain Monte Carlo (MCMC) is used to draw samples from the constructed posterior space and fitting both the age spectrum and Arrhenius array estimating the parameters that define the models. The sampling used is described in the next section.

3.3.5 Sampling

In my model I perform sampling in compound steps using both the Metropolis-Hasting (Metropolis et al. (1953), Hastings (1970)) for normal variables and a Categorical Gibbs Metropolis algorithm (Liu (1996)) for the categorical variables. The Categorical Gibbs Metropolis sampler allowing for stepping through dimensions at each iteration. For each blind mixture in these case studies, I use a burn-in of 1×10^6 samples; burn-in steps are an initial section of the chain that is discarded because it is a section of the chain that is searching for the equilibrium distribution and not sampling from it. Following this burn in, the chain is assumed to have reached equilibrium and I draw 1×10^5 samples from it. The 1×10^5 samples are then used to draw all inferences; model parameters and predictive posterior credible intervals of the model.

3.4 Blind Mixtures

I invert $^{40}Ar/^{39}Ar$ age spectra generated for this work from 'blind' mixture runs of samples with known ages. I refer to these as 'blind' mixtures because the number and composition of components in the mixture are not known *a priori*; unlike Carter et al. (2020) I infer the number of components through the DP mixture model. This case study has more realistic prior information than the first case study, analogous to the level of knowledge I might expect to have when applying my modelling approach to applications that require fine-grained sediment provenance or *in-situ* rover-based $^{40}Ar/^{39}Ar$ geochronology.

For these experiments I irradiated geological materials with neutrons for 50 hours at the Oregon State University TRIGA reactor in the Cadmium-Lined In-Core Irradiation Tube (CLICIT) facility. Irradiated materials included the neutron fluence monitor GA1550 biotite as well as Benson Mines orthoclase (BMO) (Foland (1994)), Madagascar orthoclase (MO) (Cassata & Renne (2013), and references therein), and three feldspars purchased on e-Bay: two labradorite samples, hereafter referred to as Oregon labradorite (OL) and Pennsylvania labradorite (PL) , and one anorthite sample, hereafter referred to as JC anorthite (JCA).

As the purchased samples have no existing $^{40}Ar/^{39}Ar$ data, I first conducted step degassing experiments on individual irradiated samples to establish whether they exhibit (1) continuous age plateaus consistent with geologically rapid cooling (and no heat treatment by the sellers), and (2) simple, linear Arrhenius diffusion behavior.

Single grains of each sample were loaded into packets made from high-purity platinum tubes and baked under vacuum for 36 hours. Sample packet temperatures did not exceed 180^{o}C during baking, as monitored by a K-type thermocouple in the center of the sample chamber. Samples were then sequentially degassed using a 75W diode laser in a PID-feedback control loop with a coaxially aligned optical pyrometer. To account for the temperature-dependent emissivity of the platinum tubes, pyrometer temperatures were calibrated against a thin-wire K-type thermocouple under identical conditions to my previous degassing experiments. My temperature calibration is valid for temperatures between 440 and 1100 ^{o}C to an accuracy of $\sim \pm$ 6 ^{o}C at lower temperatures, and $\pm \sim 1^o$C at higher temperatures. Argon isotopes released during each heating step were analyzed on an ARGUS V sector field mass spectrometer using a 5-faraday collector array in the Argon Isotope Facility at the Scottish Universities Environmental Research Centre. Details of the gas purification and measurement procedures are reported in Mark et al. (2009). Each heating step analysis was followed by measurement of an extraction line blank of the same duration as the heating step, then an air aliquot and a second extraction line blank with shorter purification durations (typically 5 minutes). I corrected time-zero signal intensities for ^{37}Ar and ^{39}Ar decay, interfering reactions, extraction line blanks, and mass spectrometer discrimination determined from air aliquot analyses. Results for step heating analyses on individual feldspars are reported in Table A.2 - A.6 and Figure 3.6.

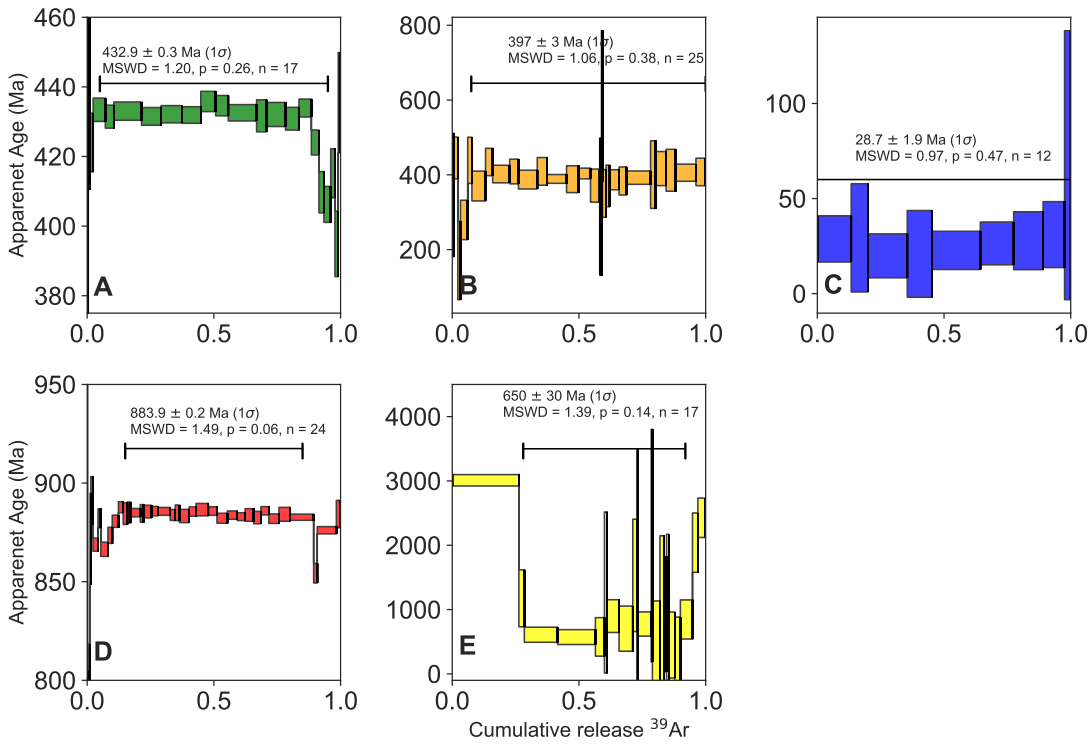

Figure 3.6: Age spectra of the individual components used to make the blind mixtures in this study. Panel A is the age spectrum of the sample of Madagascar orthoclase. Panel B is the age spectrum of the sample named Pennsylvania labradorite. Panel C is the age spectrum of the sample purchased on ebay named Oregon labradorite. Panel D shows the age spectrum of Benson mineorthoclase. Panel E is the age spectrum of the sample purchased from ebay named JC anorthite. All mixtures are assemblages of the samples shown above as well as the irradiation monitor GA1550 (McDougall & Wellman (2011)).

Component	Plateau Age ± 1σ (Ma)
Benson Mines orthoclase	883.9 ± 0.2
Oregon labradorite	29 ± 2
Pennsylvania labradorite	397 ± 3
JC anorthite	650 ± 30
Madagascar orthoclase	432.9 ± 0.3
GA1550	99.7 ± 0.1[a]

Table 3.1: Individual component age used in the blind mixture study.a Renne et al. (1998).

'Blind' mixtures were generated by my supervisor (Tremblay) by packing different

combinations of the irradiated mineral samples into platinum packets. The mixtures were kept small (6-8 grains) in order to ensure that uniform heating within the platinum packets was attained. When multiple grains from a single sample were utilized, grains were carefully chosen to be very similar in size in order to minimize the complexity that may be introduced by having multiple diffusion length scales for a single component, however each component may still exhibit MDD type behaviour. Sample heating and argon isotope analyses were carried out as described above. The heating schedule used for mixture experiments included multiple retrograde heating cycles, which is essential for assessing the presence of multiple diffusion domains (and, in our case, multiple components (e.g., Harrison et al. (1991))). The composition of each mixture was only revealed to me after Bayesian deconvolution of a mixture's $^{40}Ar/^{39}Ar$ age spectra. The results of the Blind mixture step heating are shown as age spectra in Figure 3.7 and KDE plots in Figure 3.8. From Figure 3.7 all blind mixtures show complex (unique) degassing patterns defined by both the specific mineral components and the heating schedule used for each mixture. For instance, figure 3.7 panel A shows blind mixture 1 with shows a complex age spectra of an overall increasing pattern from a likely lower age less retentive component degassing initially faster at lower temperature steps followed by the slower by increasing diffusivity of the older more retentive component that increasing dominates as temperature increases. Figure 3.7 panel D, shows a pattern that may be indicative of either extraneous ^{40}Ar in the less retentive regions or recoil loss from mineral edges resulting in the the elevate initial steps falling toward a subtly undulating plateau from $\sim$10 - 100% ^{39}Ar cumulative release (e.g., Onstott et al. (1995), Dalrymple & Ryder (1993)). However, if I assume that the grain sizes chosen effectively negate the effect of recoil and that extraneous ^{40}Ar is minimal, then these steps may hold geological relevant temporal information from an old component that is degassing within the low temperature steps of the experiment and is then dominated by a younger component resulting in the pseudo plateau in the mid to high temperature release. These age spectra show similar erratic patterns that have been observed in silt sized fractions of marine and terrigenous sediments (VanLaningham et al. (2006, 2008), Villaseñor et al. (2016)). Therefore these data present ideal test cases with potential applications to bulk sediment provenance studies.

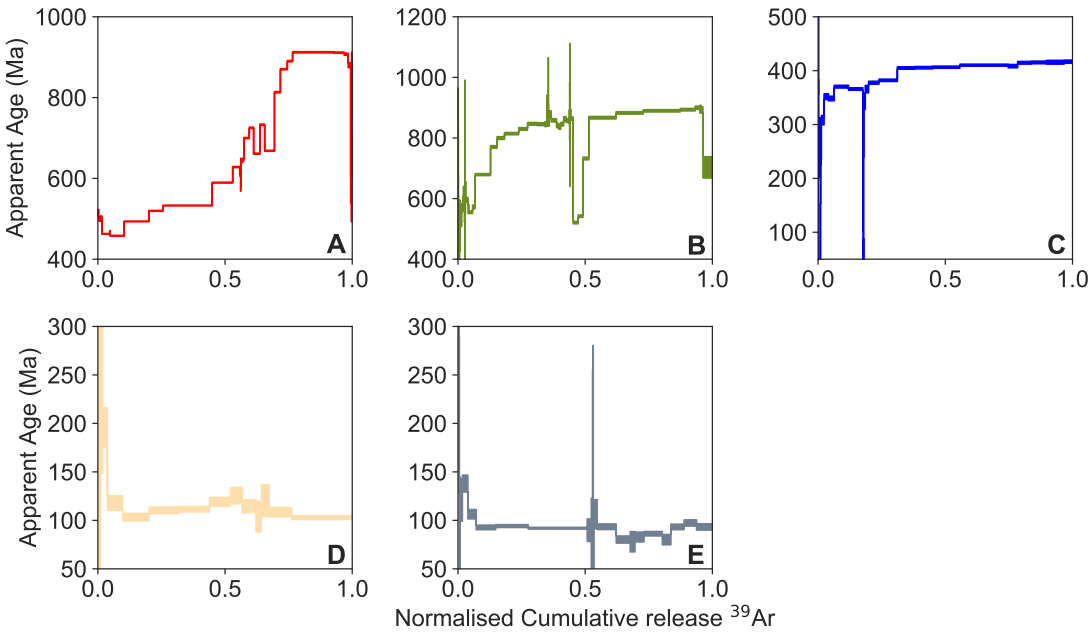

Figure 3.7: Age spectra of all step-heated blind mixtures analysed in this study. Note all age spectra and Arrhenius spectra are indicative of the presence of multiple different mineral phases and multiple age populations. In age spectra space the effect of multiple components is shown by undulating complex structures as various minerals dominate the Ar degassing budget.

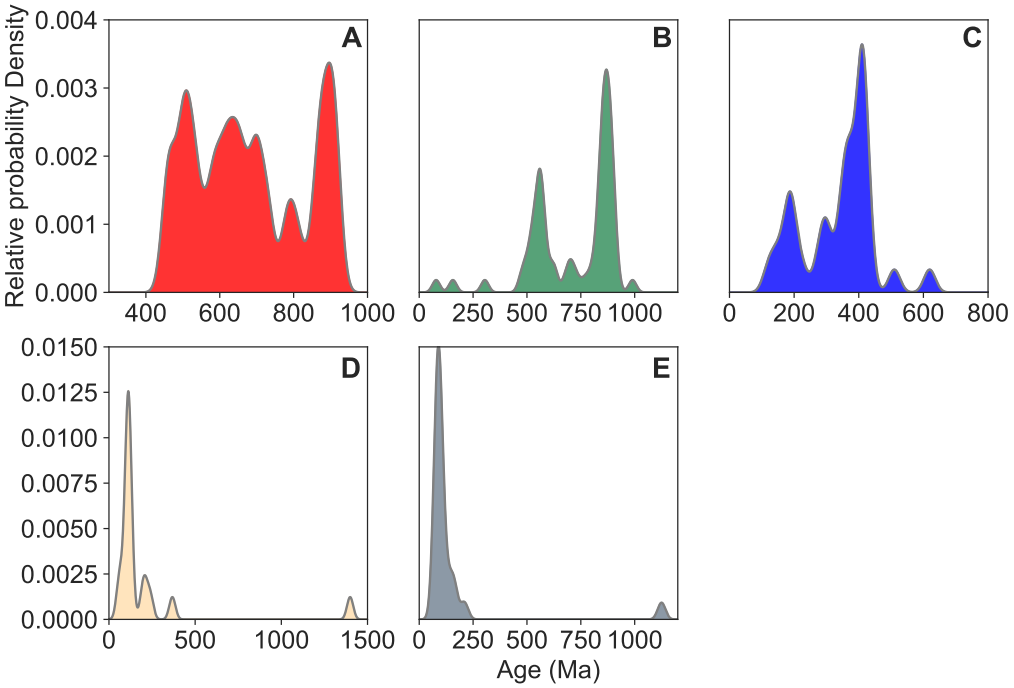

Figure 3.8: Visualisation of all blind mixture incremental heating dataset using probability density plots. These plots highlight the distribution of age steps that results from the heating of mixtures that are multiage and polymineralic. The ages on these plots are the result of mixing of the mineral phases that are present in the mixture and the time and temperature schedule of the incremental heating.

The other distinct source of information from the stepwise degassing experiments are the Arrhenius arrays, these are shown in Figure 3.9. In relation to their respective age spectra the Arrhenius datasets further emphasise the presence of multiple components of contrasting diffusion kinetics. All the Arrhenius arrays show, to varying degrees, curvilinear behaviour due to the presence of multiple and contrasting diffusion kinetics, this pattern is most likely compounded by the existence of multiple diffusion domains of each component. We include both the age spectrum and Arrhenius array in our model to infer the maximum amount of information possible.

3.5 Results

In order to gauge the quality of my model at inferring both the age and kinetics of each mineral component in the mixture I first analysed each component individually to estimate their ages via age spectrum analysis and diffusion kinetics by analysing

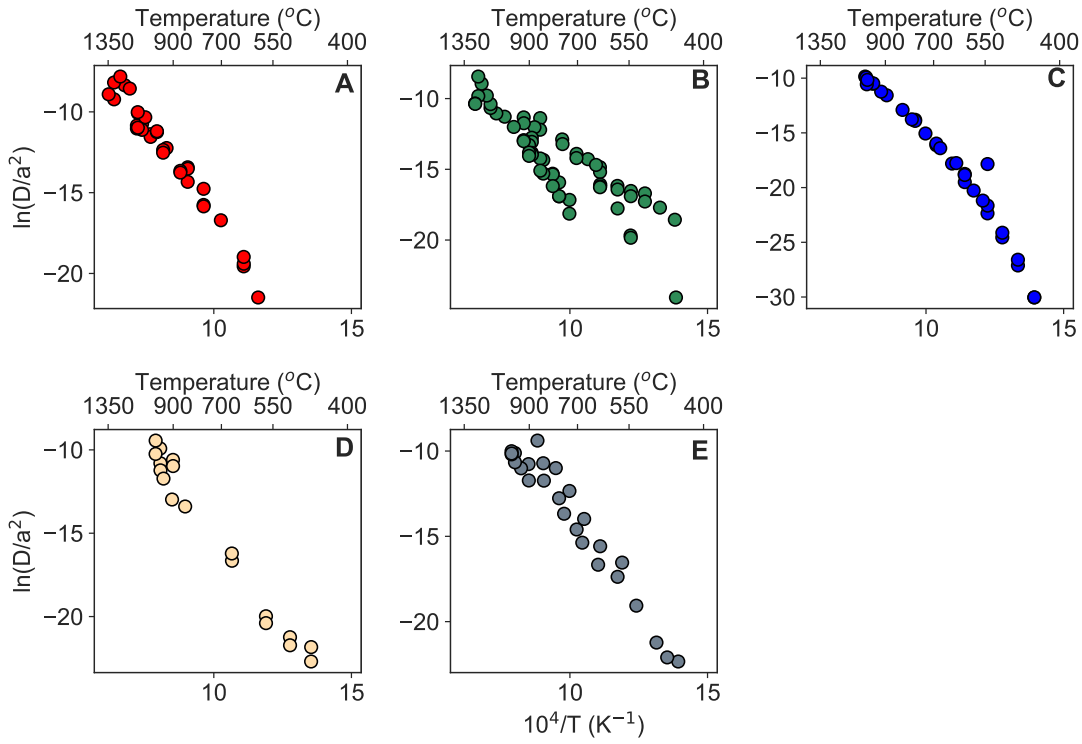

Figure 3.9: Arrhenius data of the blind mixtures. Letters correspond to the same components in Figure 6 and 7.

the accompanying Arrhenius datasets. Because, prior to analysis of the Pennsylvania labradorite, Oregon labradorite, and JC anorthite the degassing behaviour of these samples was unknown I conducted analysis of their Arrhenius arrays via my Bayesian model Dirichlet Process mixture framework, accounting for the possibility of MDD-type behaviour and providing further testing of this type of modelling approach. I also analysed the previously studied samples (Foland (1994), Cassata & Renne (2013)); Madagascar orthoclase and Benson Mine orthoclase by the same approach. Individual component age spectra are shown in Figure 3.6 and Arrhenius arrays for each individual component is shown in Figure 3.10. Each model run for these individual samples uses 1×10^5 burn in steps and 1×10^5 samples.

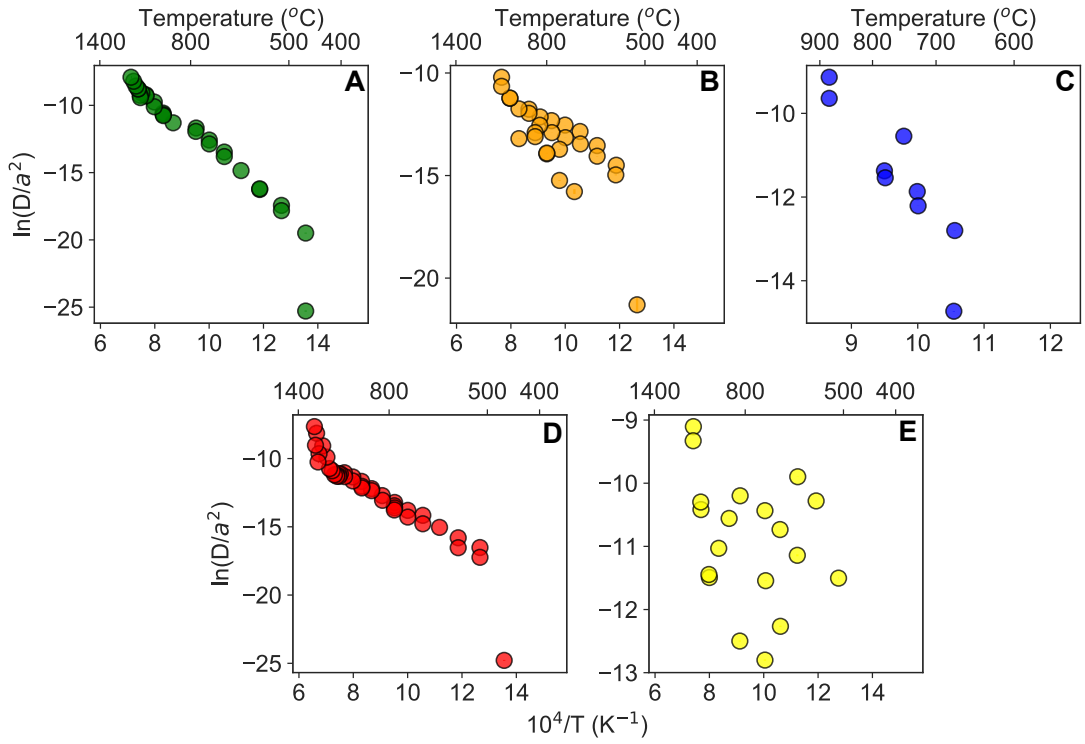

Figure 3.10: Individual component Arrhenius arrays of components used in the blind mixture study. Plots, lettering, and colours correspond to the age spectra shown in Figure 3.

3.5.1 Madagascar orthoclase

Madagascar orthoclase is an extensively studied alkali feldspar (Wartho et al. (1999), Arnaud & Kelley (1997), Parsons & Lee (2005), Cassata et al. (2010)). Interrogation of previously published data places the activation energy (E_a) in the range of 195 - 284 kJmol^{-1} with a number of studies noting low temperature activation energy of ∼195 kJmol^{-1} and higher temperature activation energy of ∼284 kJmol^{-1}(e.g., Wartho et al. (1999), Arnaud & Kelley (1997)). Conversely, Cassata et al. (2010) inferred a single activation energy of 272.8 ± 3.4 kJmol^{-1} at 1σ. I reanalysed the sample here using the same set up as described for the blind mixtures. Following Cassata & Renne (2013) I fit only the data below 800^{o}C at which temperature Madagascar orthoclase undergoes a phase change.

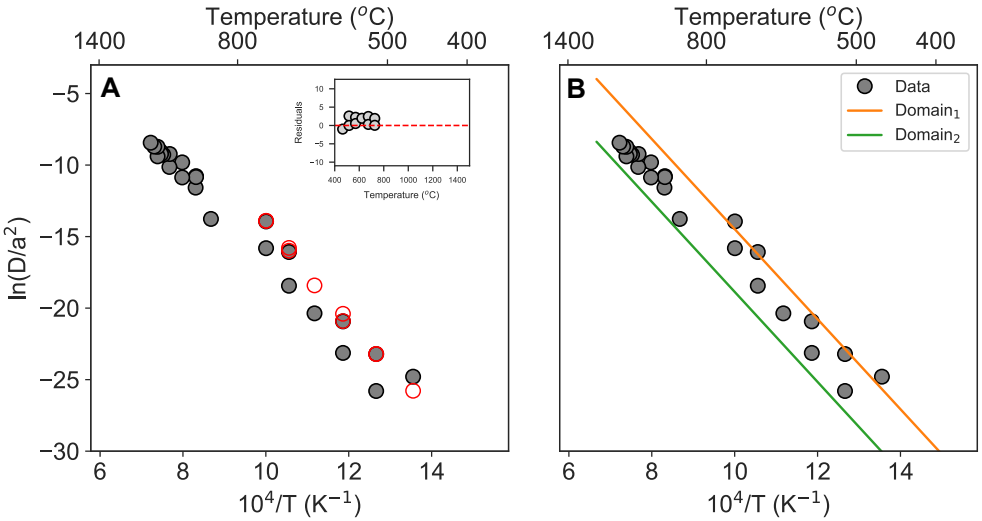

Figure 3.11: Model results for Madagascar orthoclase. Left panel shows the post posterior model output (red) and Arrhenius data (grey). Uncertainties in the data are shown but smaller than the markersize. Inset figure shows the residuals as a function of temperature for the model. The right panel shows the extrapolated Arrhenius arrays of the 2 domains from the model output; each domain has a color assigned shown in the legend.

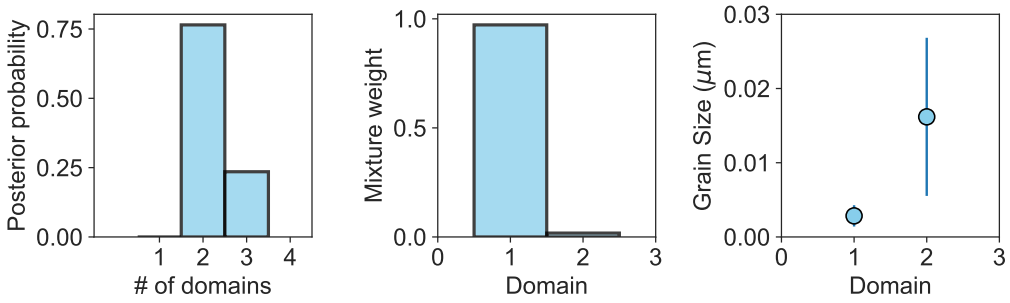

Figure 3.12: Left panel shows the inferred number of domains. The middle panel shows the mixture weights of the domains, also considered the volume of each domain and the right panel shows the domain size.

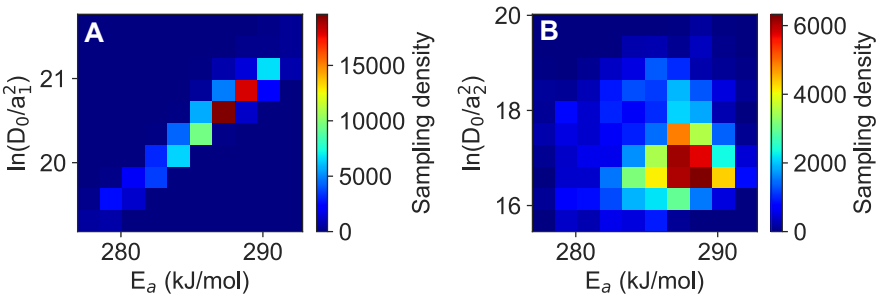

Figure 3.13: Each panel shows the inferred model activation energy against the natural log of the frequency factor over the domain length scale. Panels A and B show the natural log of D_0/a^2 against the E_a for both domains. Colour bars show relative sampling probability.

Like Cassata & Renne (2013) I infer a single activation energy of 286.4 ± 6 (2σ) kjmol^{-1} a value similar to the higher temperature array inferred by Wartho (1991) and nominally close but not overlapping at the 2σ level to Cassata & Renne (2013). I infer that these data are approximately within range of the prior studies, as expected.

3.5.2 Pennsylvania labradorite

Unlike the Madagascar orthoclase, Pennsylvania labradorite is an e-Bay purchase sample and hence presents a complete unknown in terms of both the age and kinetics of the material. Cassata & Renne (2013) provide a suite of 15 labradorite samples with kinetics that range from 160.4 ± 8.3 to 241.8 ± 26.6 kJmol^{-1} for activation energy and 0.6 ± 1.2 to 13.6 ± 4.0 for the natural log of the frequency factor. Other than this, studies of labradorite are limited; however I can use this range of diffusion kinetics for 15 samples as a guide for my model output. My data show large departures from the linear behaviour expected for single domain volume diffusion behaviour similar to a number of the Arrhenius arrays or Cassata & Renne (2013). The data here are indicative of a number of diffusion domains that are drastically different in size given the spread of the data in Arrhenius space. I analyse the data again with my Bayesian model. The results of the model are given below.

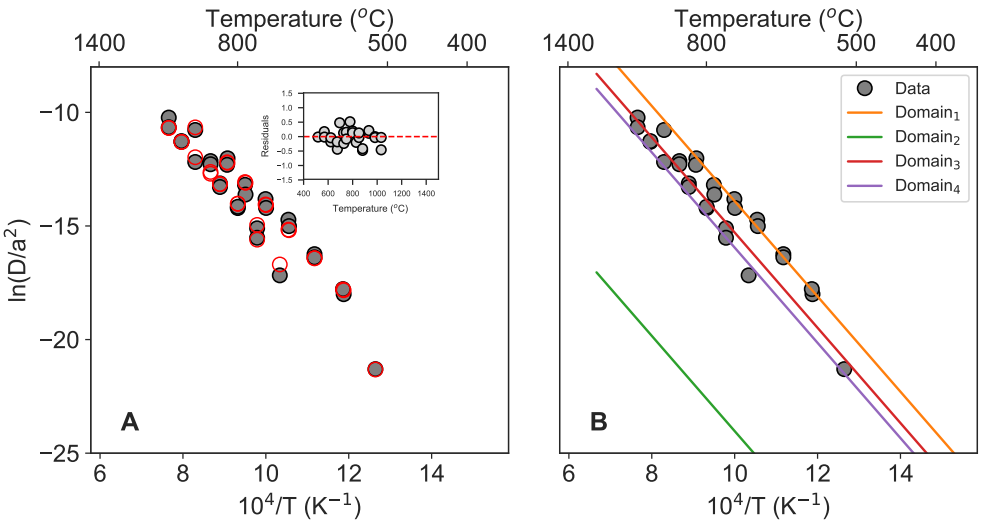

Figure 3.14: Left panel shows the post posterior model output (red) and Arrhenius data (grey). Uncertainties in the data are shown but smaller than the markersize. The inset figure shows the residuals as a function of temperature for the model. The right panel shows the extrapolated Arrhenius arrays of the 5 domains from the model output; each domain has a color assigned shown in the legend.

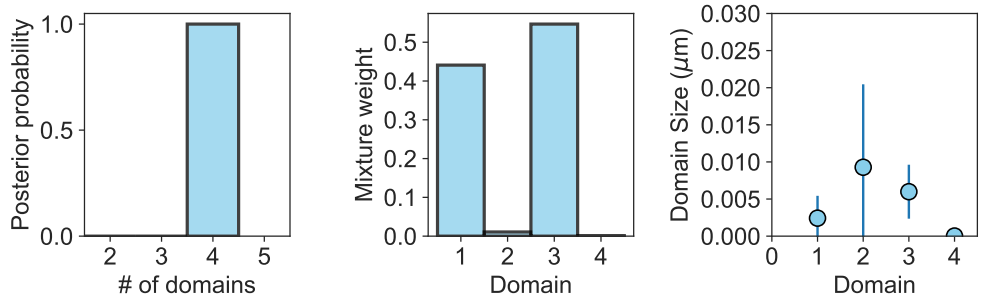

Figure 3.15: Left panel shows the inferred number of domains. The middle panel shows the mixture weights of the domains, also considered the volume of each domain and the right panel shows the domain size.

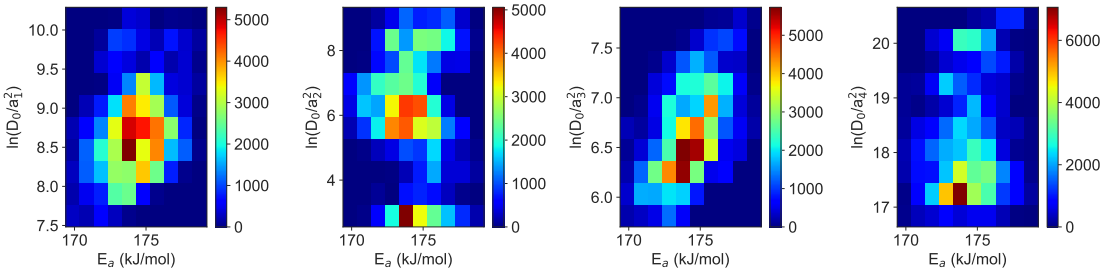

Figure 3.16: Each panel shows the inferred model activation energy against the natural log of the frequency factor over the domain length scale. Panels correspond to domains 1 - 4 inferred by the model. Colour bars show relative sampling probability.

The inferred kinetics of the Pennsylvania labradorite are 174.3 ± 1.7 kJmol^{-1} for the activation energy and 0.035 ± 0.03 for the natural log of the frequency factor. These values compare well with the, albeit large, range of diffusion kinetics reported by Cassata & Renne (2013).

3.5.3 Oregon labradorite

Similar to the previous sample, the Oregon labradorite is purchased from e-Bay and it also presents a similar unknown to its diffusive behaviour. Prior work on the labradorite, like the previous analysis on the Pennsylvanian sample is really limited to the study of Cassata & Renne (2013) and hence guide ranges highlighted earlier apply equally to this sample. The dataset of this sample shows linear-like behaviour and is similar to the labradorite from Pennsylvania, with likely MDD-type behaviour. I use a model to estimate the kinetics, number of domains and their characteristics which best describe this dataset.

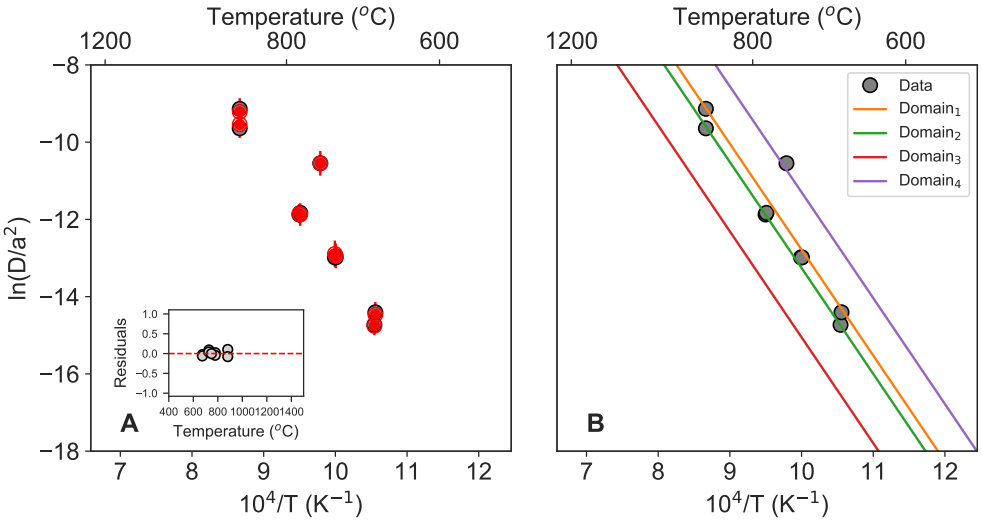

Figure 3.17: The left panel shows the model output (red) and Arrhenius data (grey). Uncertainties in the data are shown but smaller than the marker sizes. Inset figure shows the residuals as a function of temperature for the model. The right panel shows the extrapolated Arrhenius arrays of all domains found in the mixture each with a different colour shown in the legend.

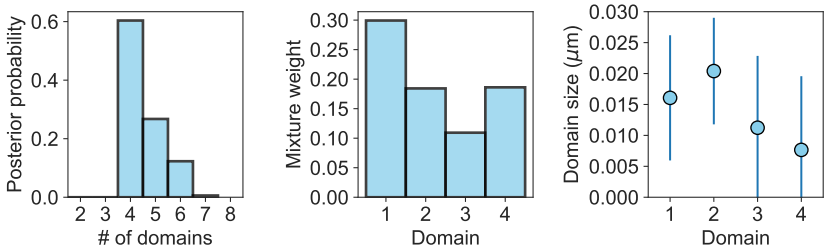

Figure 3.18: Left panel shows the inferred number of domains. The middle panel shows the mixture weights of the domains, also considered the volume of each domain and the right panel shows the domain size.

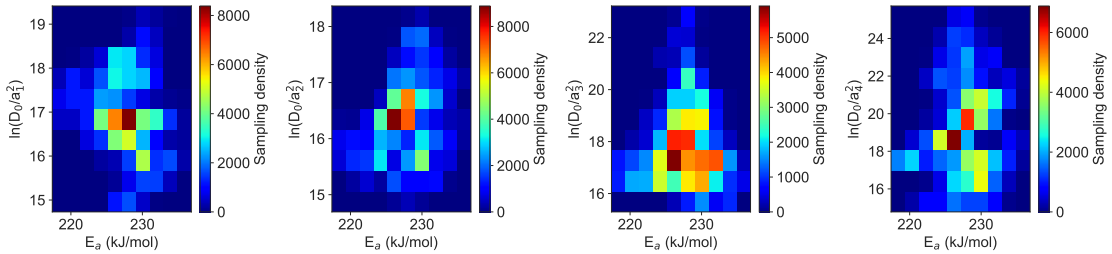

Figure 3.19: Each panel shows the inferred model activation energy against the natural log of the frequency factor over the domain length scale. Panels 1 - 4 correspond to domains 1, 2, 3, and 4 inferred by the model. The colourbar shows the relative sampling density

The inferred diffusion kinetics of this mineral are 227.7 ± 3.3 kJ/mol for the activation energy and 8.5 ± 0.5 for the frequency factor. These values like the previous Pennsylvania labradorite are within the large range of prior values for the labradorite feldspar (Cassata & Renne (2013)).

3.5.4 Benson Mine orthoclase

Benson Mine orthoclase is another extensively studied alkali feldspar (Foland & Xu (1990), Foland (1994), Cassata & Renne (2013)). Activation energy from prior studies range from 183.25 ± 4.1 to 229.9 ± 3 kJ/mol (Foland (1974), Cassata & Renne (2013)). Cassata & Renne (2013) present data from 6 single crystal Benson Mine crystals that show highly idealised linear behaviour in Arrhenius space. Our data show an initial low point due to the low temperature release and a ^{39}Ar release that is very close to the background level which is omitted in the analysis. Following this we see a mid to high temperature array that is linear and then like the Madagascar sample an upward inflection at high temperature release. Following Cassata & Renne (2013) I only fit the data below 1000^{o}C at which temperature Benson Mine orthoclase undergoes a phase change.

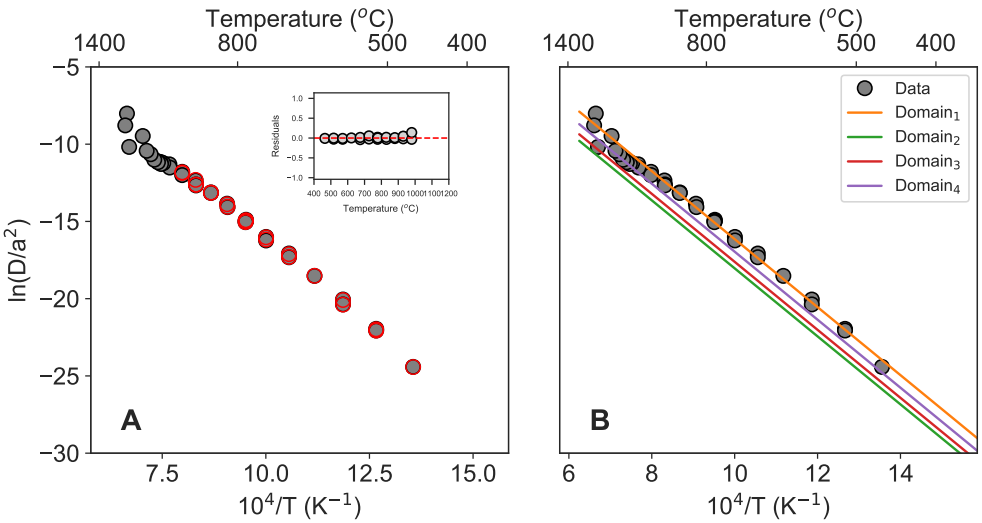

Figure 3.20: Model results for Benson Mine orthoclase. Left panel shows the post posterior model output (red) and Arrhenius data (grey). Uncertainties in the data are shown but smaller than the marker sizes. Inset figure shows the residuals as a function of temperature for the model. The right panel shows the extrapolated Arrhenius arrays of the 2 domains from the model output; each domain has a color assigned shown in the legend.

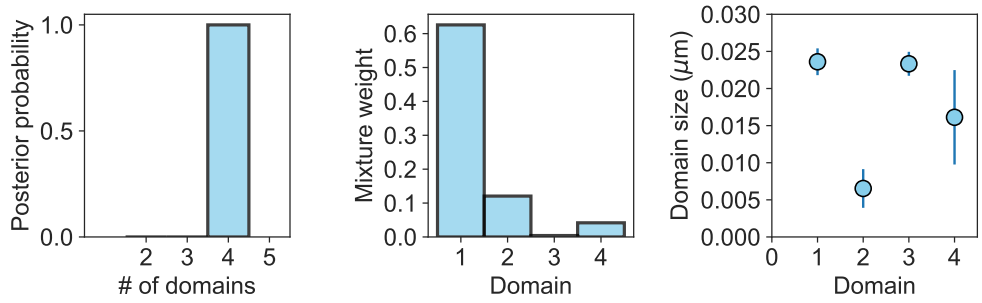

Figure 3.21: Left panel shows the inferred number of domains. The middle panel shows the mixture weights of the domains, also considered the volume of each domain and the right panel shows the domain size.

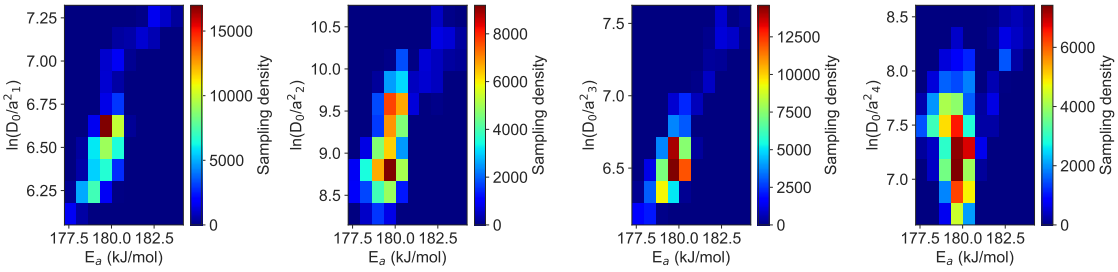

Figure 3.22: Each panel shows the inferred model activation energy against the natural log of the frequency factor over the domain length scale. A and B correspond to domains 1 and 2 inferred by the model. The colourbar shows the relative sampling density

We infer an activation energy of 180 ± 1 kJmol^{-1} (2σ) . This aligns our estimate with the previously determined values of Foland & Xu (1990), Foland (1994) but is outside the range estimated by Cassata & Renne (2013). Given the success of the previous estimate of the Madagascar orthoclase and other samples with past literature and known range of the type of K-bearing minerals, I believe this difference to be a sample dependent one.

3.5.5 JC anorthite

JC anorthite is the third purchased e-Bay sample and thus presents a sample with no prior analyses. However, the extensive diffusion study of feldspars by Cassata & Renne (2013) presented data for three anorthite samples with activation energies from 196.1 ± 20.4 to 236.8 ± 5.8 kJmol^{-1} and frequency factors ranging from 5.4 ± 2.9 to 16.9 ± 0.9. The dataset recovered from this sample is highly erratic with no defined linear behaviour or MDD-type structure (Fig 3.10 panel E and 3.23 panel A). However, to be consistent, I analysed the data is the same fashion as all of the other components used in the blind mixture experiments.

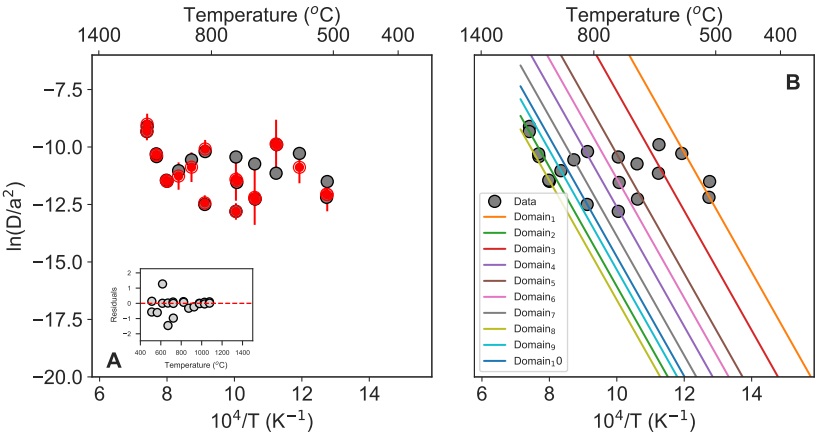

Figure 3.23: Left panel shows post posterior model output (red) and Arrhenius data (grey). Uncertainties in the data are shown but smaller than the markersize. Inset figure shows the residuals as a function of temperature for the model. This model shows clear signs of a poor fit this is due to the erratic nature of the dataset. The left panel shows the inferred domains extrapolated through Arrhenius space. Each of the 7 domains corresponds to a different colour shown in the legend.

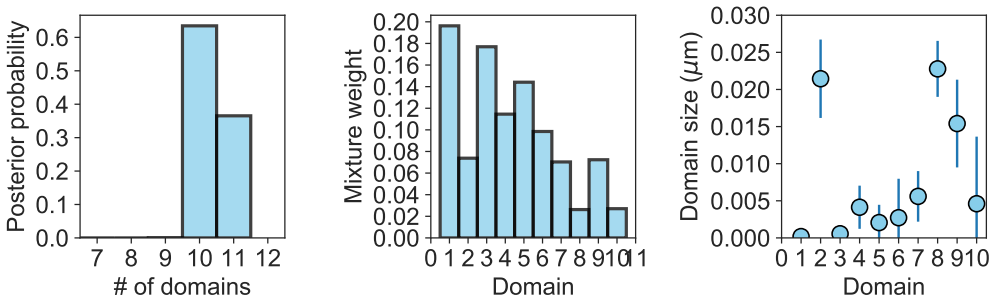

Figure 3.24: Left panel shows the inferred number of domains. The middle panel shows the mixture weights of the domains, also considered the volume of each domain and the right panel shows the domain size.

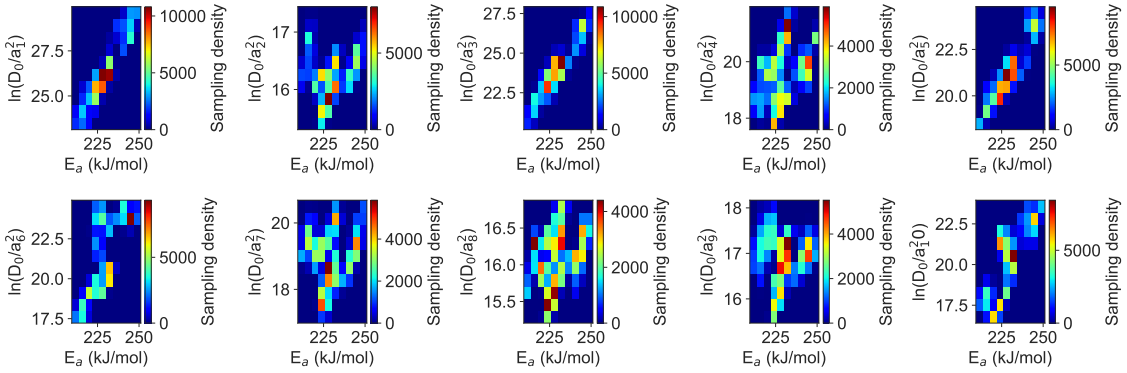

Figure 3.25: Each panel shows the inferred model activation energy against the natural log of the frequency factor over the domain length scale. Panels correspond to domains 1 - 10 inferred by the model.

The erratic characteristics are most likely due to complexities that are outside of the MDD-type modelling approach. Nevertheless, I show that I can reasonably fit the data when I consider the MDD to be the correct model for the data and from this I can infer diffusion kinetics for this sample. These are 229.6 $\pm$ 9.3 kJmol^{-1} for the activation energy and 8.5 $\pm$ 0.34 for the frequency factor. From Figure 3.19 it is possible to see that these values do not show the usual correlated sampling behaviour that is associated with how these parameters vary together. This observation highlights the potential non-volume diffusion artefacts that may be inherent in this particular sample dataset. The inclusion of a sample such as this to the blind mixtures pushes the model to a potential limit by an inability to fit data such as this. This provides a natural test of the possible incorporation of non-ideal samples, such as those samples that would be sampled in a real world geological setting.

I now have estimates of the kinetics and information on the behaviour of each sample in Arrhenius space. These data are also a test of the behaviour of the platinum packets in the vacuum heating within the laser cell of a mass spectrometer. The data show that the platinum packets do not cause any systematic offsets to the data as both the age spectra (Fig 3.6) and the Arrhenius arrays (Fig 3.10) determine ages and kinetics within the prior literature values for the known K-bearing mineral type.

3.6 Model testing

To test the modelling framework and mathematics, I analyse two datasets for which all parameters are known and defined. For this test the datasets are; (1) the Alder Creek

sanidine data shown in Figure 2 and (2) a slightly more complicated dataset of the Heidelberg Biotite and Alder Creek sanidine mixture analysed previously in Chapter 2. These datasets allow me to test both the fundamental assumptions of the model and the mathematics of using a tiered Dirichlet process mixing model that infers both the number of components and subsequent domains of each component as well as all other parameters for each component (e.g., diffusion kinetics, age, grain size(s) etc.).

3.6.1 Alder Creek sanidine

Alder Creek sanidine is a well-characterised material used as a neutron fluence monitor in $^{40}Ar/^{39}Ar$ dating. It produces a highly idealised and reproducible age spectrum and Arrhenius array (Figures 3.26 A and B). This makes it an ideal candidate to test the ability of this model to fit the most basic of datasets. I analyse the dataset with my Dirichlet process mixture model described above.

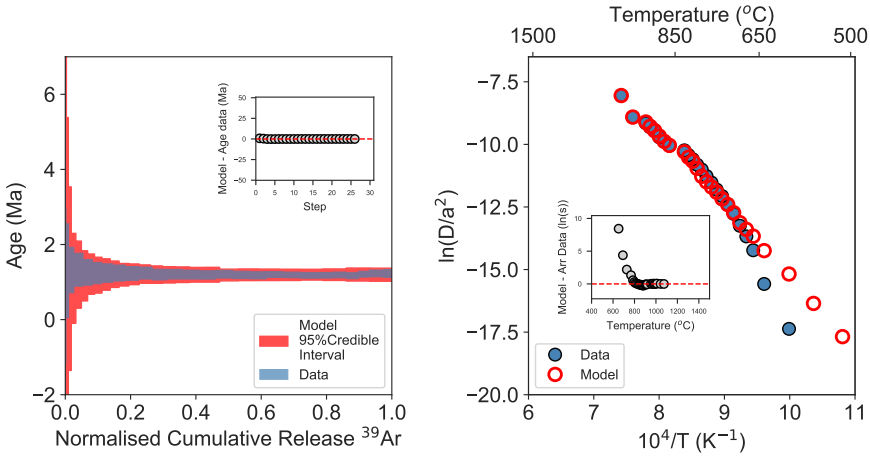

Figure 3.26: A Age spectra data (light grey) and the 68% model credible interval shown in red, figure indent shows the residuals (model - data) for each age step. B Arrhenius array data (dark grey) and modelled Arrhenius array (red circles unfilled), inset figure shows the residuals (model - data) for each temperature step. The differences in the fit between these two datasets is due to the penalising weight placed on the Arrhenius spectra.

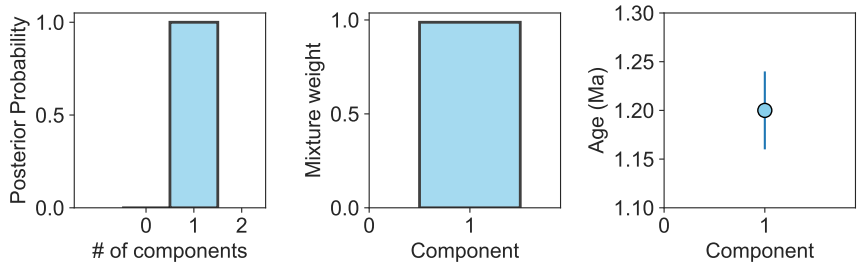

Figure 3.27: Left panel shows the inferred number of components, the model clearly favours a single component model. The middle panel then shows the mixing weight of the single component which by definition must be 1. The age of the component is shown in the right panel. The model age at 1σ is 1.19 ± 0.02 Ma, the reported age by VanLaningham & Mark (2011) using the conventional plateau method is 1.19 ± 0.007 Ma (1σ).

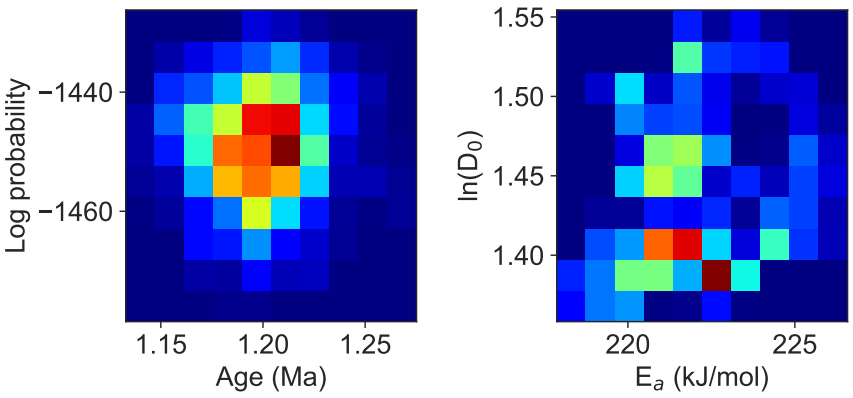

Figure 3.28: Left panel shows the log probability of the model against the sampled age and the right panel shows the inferred natural log of the frequency factor ($\ln(D_0)$) against the activation energy (E_a).The activation energy is 222 ± 5 kJmol^{-1} (1σ) and the frequency factor is $6^{-2.8}_{+17}$ cm^2/s where the quartiles are at the 68± credible interval. These samples are comparable to other inferred diffusivities of studied sanidines (typically ∼220 kJ/mol; Cassata & Renne (2013)). Colourmaps in both panels reflect sampling density from low (blue) to high (red). As a further note the sampling density plot of activation energy vs. the natural log of the frequency factor is highly correlated which is an expected result.

As expected, for this simple test, my model returns a simple single component mixture with an age statistically identical at the 1σ level to VanLaningham & Mark (2011). It also returns diffusion kinetics that are comparable to other sanidines that

have been previously studied by Cassata & Renne (2013). Although this test is simple, it highlights the basis of the Occam's razor framework, which will become more necessary as the datasets increase in complexity.

3.6.2 Heidelberg biotite and Alder Creek sanidine

In this section I present a second test of a dataset previously analysed by my parametric model in Chapter 2. However, here I used an extended nonparametric model to attempt to not only infer the correct ages but also the correct number of components, thus removing the need for it as a constraint in the modelling set up. This analysis is presented below.

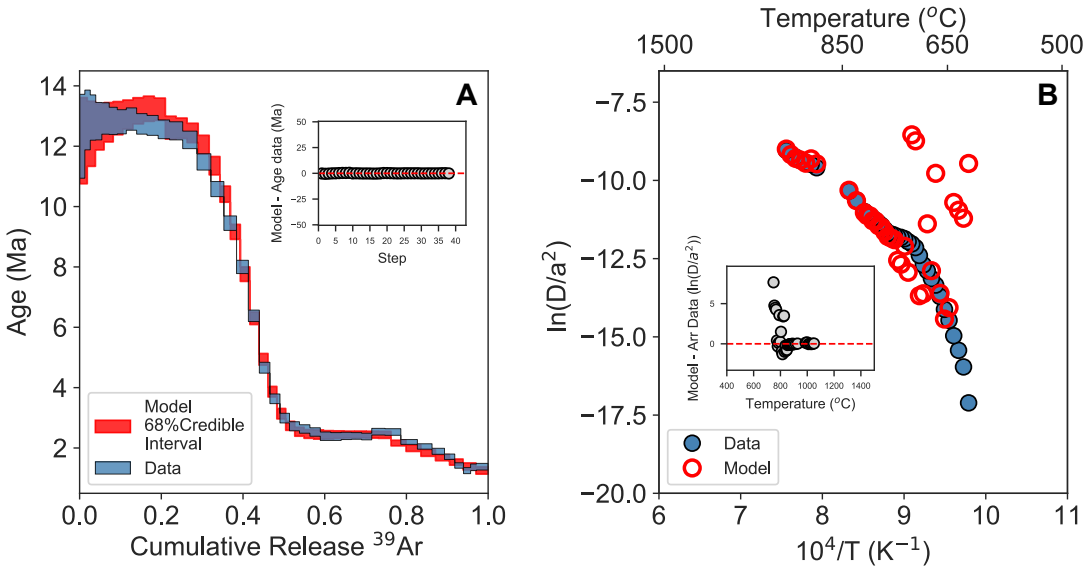

Figure 3.29: A Age spectra data (blue) and the 68% model credible interval (red), figure indent shows the residuals (model - data) for each age step. The cumulative release of ^{39}Ar is forward modelled from the inferred model parameters. B Arrhenius array data (dark grey) and modelled Arrhenius array (red circles unfilled), inset figure shows the residuals (model - data) for each temperature step. The differences in the fit between these two datasets is due to the penalising weight placed on the Arrhenius spectra.

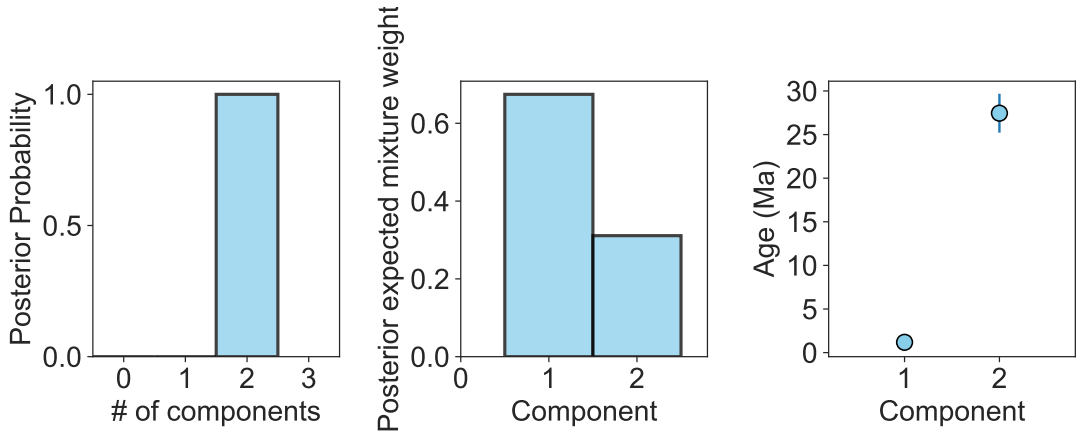

Figure 3.30: Left panel shows the inferred number of components, the model clearly infers a two components model with mixture weights shown in the middle panel. The ages of each component are then shown on the right hand panel.

Component	Model age ± 2σ (Ma)	Known age ± 2σ (Ma)
Alder Creek sanidine	1.23 ± 0.14	1.19 ± 0.007
Heidelberg biotite	25.2 ± 3.2	24.59 ± 0.12

Table 3.2: Model ages inference from the nonparametric model output compared to the individual component ages measured by VanLaningham & Mark (2011).

The results of this test define the expected features of the model inferences of the blind mixture datasets. The expectant features of the model output are therefore as follows; (1) the 95% credible interval of the inferred ages will be concordant with the known ages; (2) the uncertainty of the inferred ages will be greater than ages determined on individual components but will be relative the age of the specific components; (3) the poorer fit of the Arrhenius dataset indicates that the inferred kinetics will most likely be meaningless; (4) inferred model mixing fractions should be representative of the mixture; and (5) inferred number of mixture components will align with the known number of distinct components in the mixture.

I can also expand further conclusions from the previous Chapter by comparing our nonparametric model to the parametric model for this sample. In Chapter 2 I hypothesised that the generally greater relative uncertainty of the younger sanidine component and the biasing of its age toward an older age (∼1.25 Ma) could be due to the lack of inclusion of MDD type behaviour. By the addition of MDD behaviour I observe a number of features; (1) the fit the age spectra, in particular both the high temperature undulations and the point of transition from dominance of the older

biotite to younger sanidine is far improved;(2) the apparent biasing to an older age for Alder Creek sanidine has also been resolved by the inclusion of more complex behaviour and; (3) the discrepancy between relative uncertainties has been removed. In the nonparametric model the relative uncertainty of each component is ∼11% for ACs and ∼12% for HB-D1 making them approximately concordant compared to the 6× difference for the parametric model, which includes no MDD behaviour.

Following the success of the model applied in both parameter estimation and resolving previous model issues, I now interrogate the blind mixtures with the same model framework.

3.7 Blind Mixture Results

In this section I present the results of all blind mixture models and inferences. I use the modelling framework described in the previous sections. Namely, I use the non parametric model with the test log probability ratio as a penalising weight for the Arrhenius likelihood. This model is used to infer the ages of the components for all datasets, which are then compared to the known individual ages (Table 3.3) to make a prediction of which components are in the mixtures.

There are some notable model outputs that are highlighted with this modelling set up. Firstly, due to the favouring of fitting the age steps against the Arrhenius model I expect the age spectrum to be fitted better than the Arrhenius datasets. This is an expectation from the Heidelberg biotite and Alder Creek sanidine test and exhibited in all model outputs. This does not negate the results as in the previous Chapter, I show that geologically meaningful age information can be obtained with poor fits to the Arrhenius array.

3.7.1 Blind Mixture 1

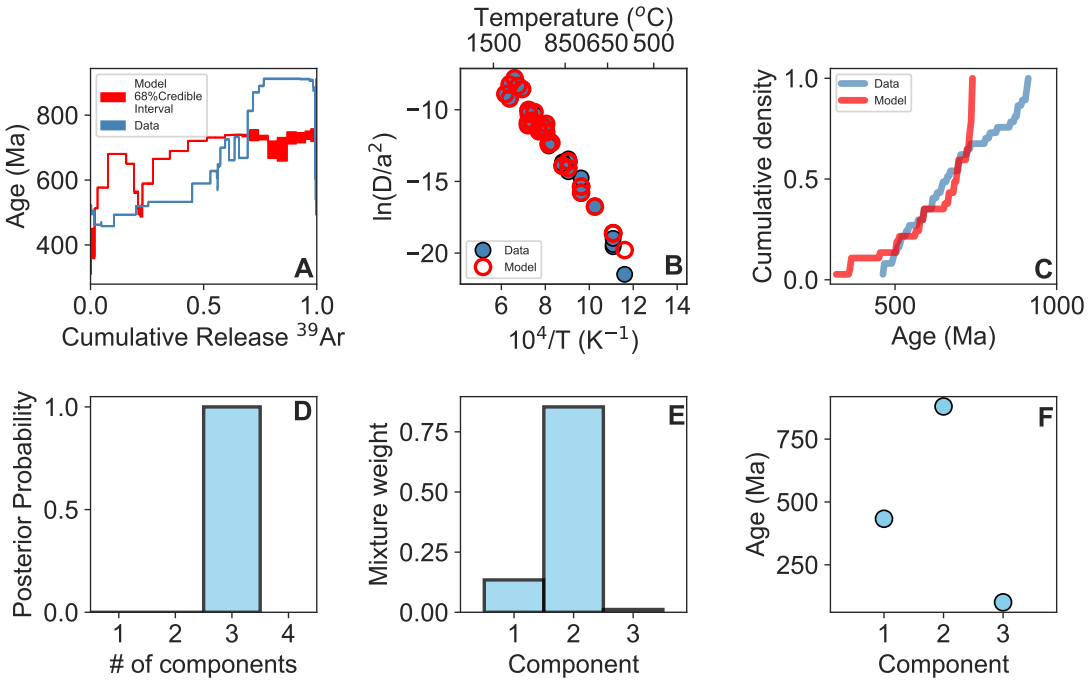

Figure 3.31: Model results for blind mixture 1. Panel A shows the posterior model age spectrum 68% confidence interval in red and the observed data set in blue, the inset figure shows the residual, the observed age of each step subtracted from the model step age. Panel B shows the observed Arrhenius array (blue circles with black outline) and the modelled Arrhenius array (red rings). Panel C shows the cumulative density plot of the step age data in blue against the model in red. Panel D is the inferred number of distinct age components in the model, E shows the mixture weight and F the ages of each component.

3.7.2 Blind Mixture 2

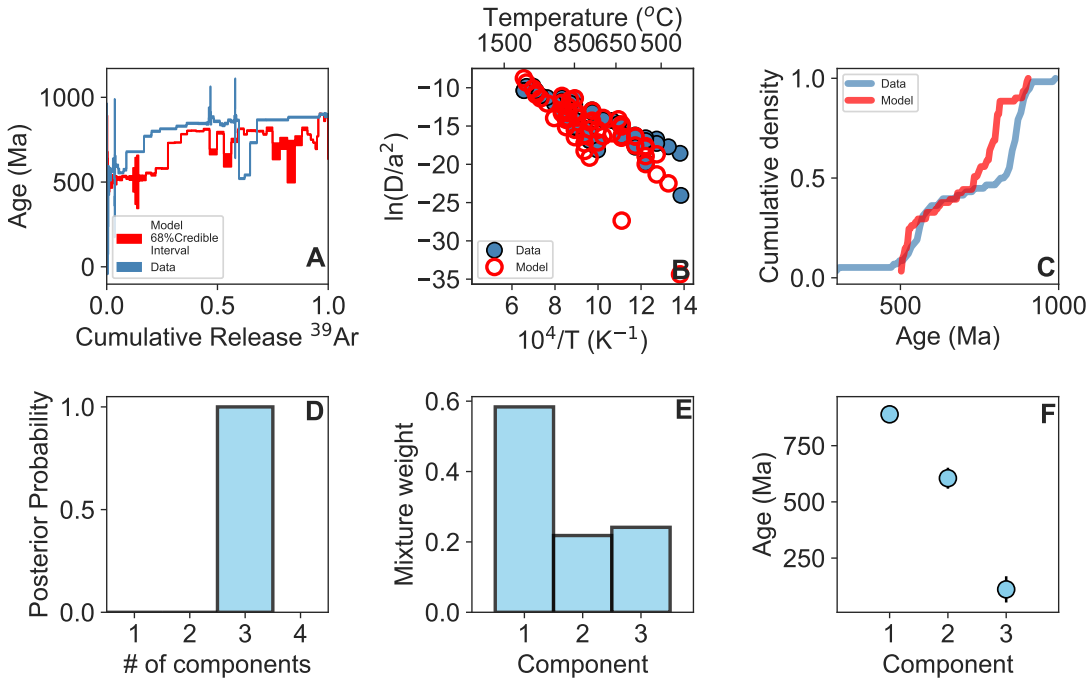

Figure 3.32: Model results for blind mixture 2. Panel A shows the posterior model age spectrum 68% confidence interval in red and the observed data set in blue, the inset figure shows the residual, the observed age of each step subtracted from the model step age. Panel B shows the observed Arrhenius array (blue circles with black outline) and the modelled Arrhenius array (red rings). Panel C shows the cumulative density plot of the step age data in blue against the model in red. Panel D is the inferred number of distinct age components in the model, E shows the mixture weight and F the ages of each component.

3.7.3 Blind Mixture 3

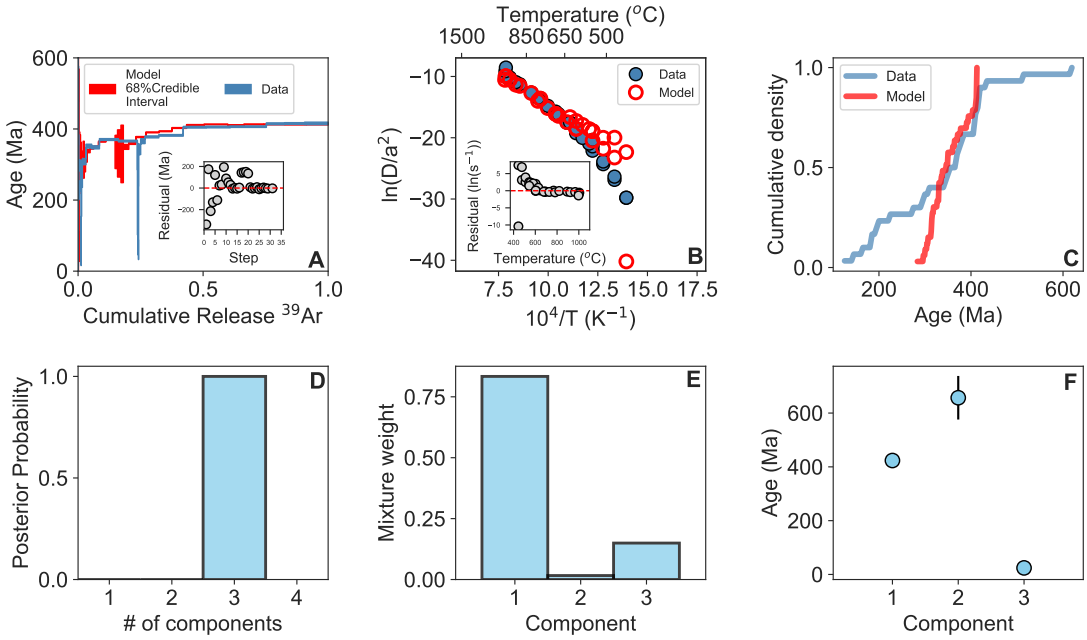

Figure 3.33: Model results for blind mixture 3. Panel A shows the posterior model age spectrum 68% confidence interval in red and the observed data set in blue, the inset figure shows the residual, the observed age of each step subtracted from the model step age. Panel B shows the observed Arrhenius array (blue circles with black outline) and the modelled Arrhenius array (red rings). Panel C shows the cumulative density plot of the step age data in blue against the model in red. Panel D is the inferred number of distinct age components in the model, E shows the mixture weight and F the ages of each component.

3.7.4 Blind Mixture 4

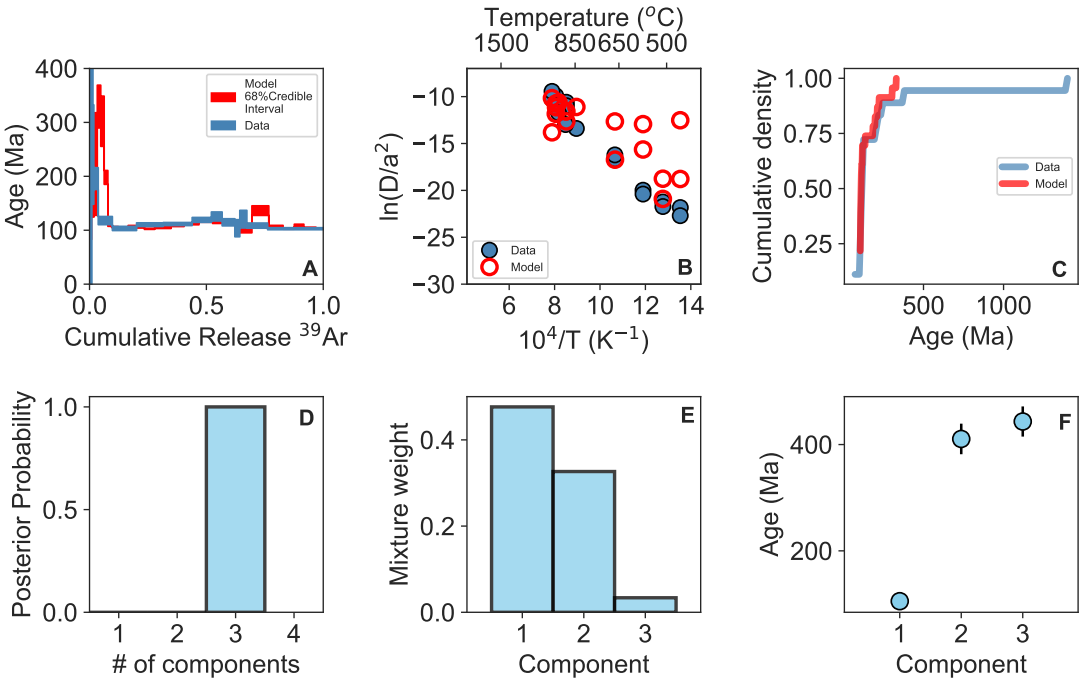

Figure 3.34: Model results for blind mixture 4. Panel A shows the posterior model age spectrum 68% confidence interval in red and the observed data set in blue, the inset figure shows the residual, the observed age of each step subtracted from the model step age. Panel B shows the observed Arrhenius array (blue circles with black outline) and the modelled Arrhenius array (red rings). Panel C shows the cumulative density plot of the step age data in blue against the model in red. Panel D is the inferred number of distinct age components in the model, E shows the mixture weight and F the ages of each component.

3.7.5 Blind Mixture 5

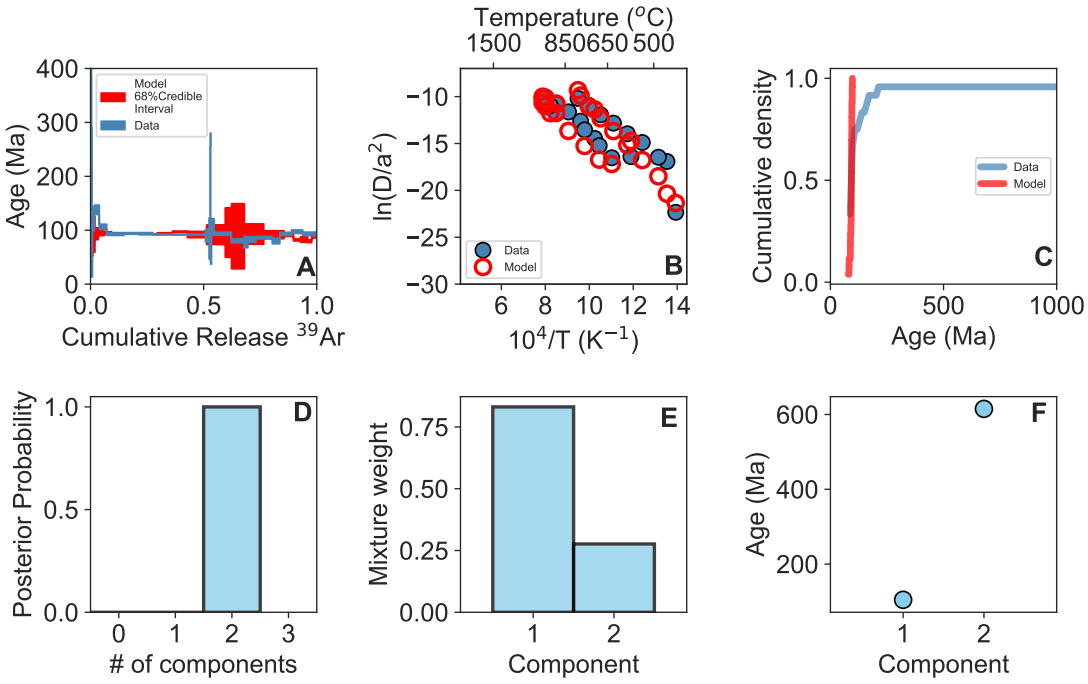

Figure 3.35: Model results for blind mixture 5. Panel A shows the posterior model age spectrum 68% confidence interval in red and the observed data set in blue, the inset figure shows the residual, the observed age of each step subtracted from the model step age. Panel B shows the observed Arrhenius array (blue circles with black outline) and the modelled Arrhenius array (red rings). Panel C shows the cumulative density plot of the step age data in blue against the model in red. Panel D is the inferred number of distinct age components in the model, E shows the mixture weight and F the ages of each component.

3.8 Discussion

The nonparametric Bayesian model used to fit both the age steps and Arrhenius array of a stepheating $^{40}Ar/^{39}Ar$ datasets has produced robust results that allow for straightforward interpretation of complex datasets. A summary of the results is shown in Figure 3.30. In this Figure, all five blind mixture datasets are shown as black KDE lines in panels A - E. The inferred components ages from the individual step analysis are shown as shaded regions which show the age and the 2σ uncertainty. These shaded regions correspond to the colours shown in the legend. Inferred component ages plotted as grey shaded KDE curves are then plotted for each blind mixture, which allows

for a straightforward determination of which components are in the blind mixture by comparison of the grey KDE plots to the shaded regions of the individual components ages and their respective uncertainty. I show here and in Table 3.3 that the inferred component ages match with the known component ages that were used to prepare the mixtures. This is a robust outcome showing that each blind mixture test was successful in recovering 'known' ages making this a tool applicable to complex geological settings.

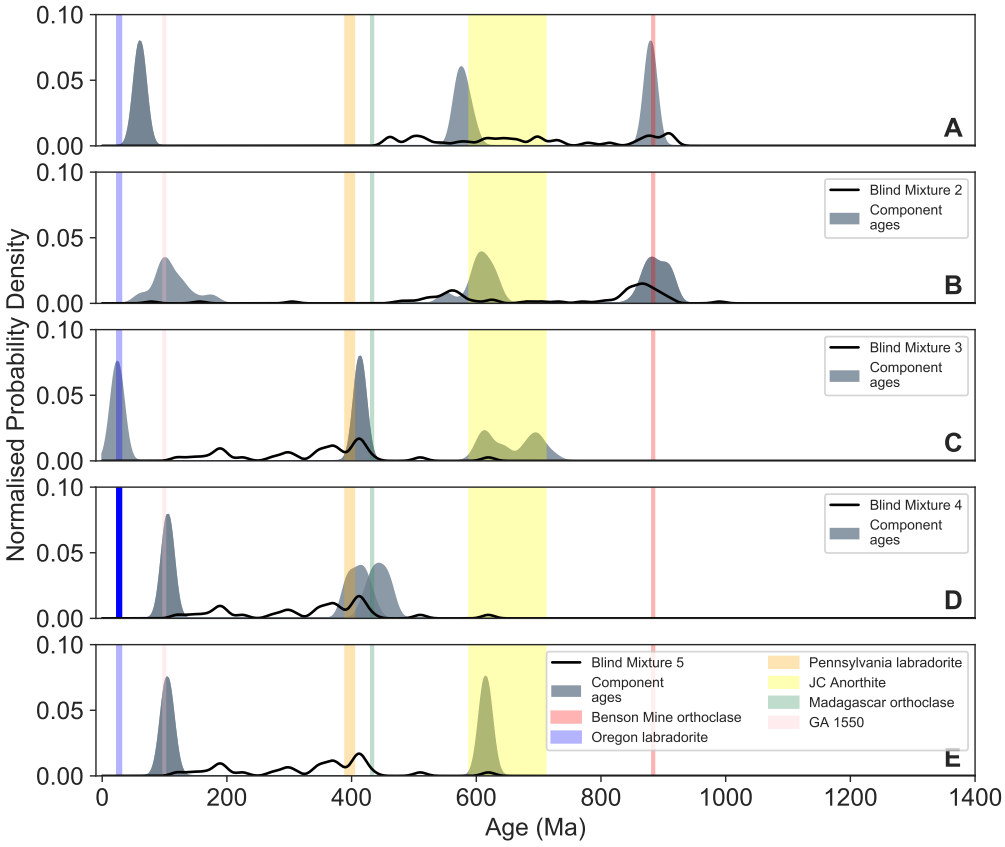

Figure 3.36: Figure showing the model output of the blind mixture datasets (A - E). Shaded regions of the figure show the ages and 2σ uncertainty of the potential mixture components. Black lines show the KDE of each dataset and gray distributions show the inferred model components of each dataset.

Mixture	# of Components	Age ± 2σ	Guess	Known
1	3	100 ± 1	GA1550	GA1550
		433 ± 0.6	MO	MO
		879 ± 2	BMO	BMO
2	3	110 ± 20	GA1550	GA1550
		605 ± 46	JCA	JCA
		889 ± 58	BMO	BMO
3	3	24 ± 7	OL	OL
		414 ± 1	MO/PL	MO
		657 ± 81	JCA	JCA
4	3	105 ± 4	GA1550	GA1550
		410 ± 28	PL	PL
		443 ± 28	MO	MO
5	2	104 ± 7	GA1550	GA1550
		615 ± 7	JCA	JCA

Table 3.3: Results of blind mixture study. Number of inferred components, ages of the components and then guess of the components are shown compared to the known mixture components.

These results show the potential of this non-parameteric Bayesian model to be applied to a range of complex geological settings. For example, in blind mixture 3 the component ages that comprise the mixture are ∼30, 430, and 650 Ma this mixture is particularly complex as the oldest component shows non-volume diffusion behaviour and potential extraneous ^{40}Ar both of which violate assumptions of the model. Furthermore, the relative differences in ages between oldest and youngest is ∼20 × which could be expected to complicate the inferred ages as the older mineral components ^{40}Ar budgets will dominate the younger components ^{40}Ar budget. Also, for mixtures that include JCA there are a number of additional complications. For example, the relative uncertainty of each age component is inflated relative to mixtures with no JCA, and more complex non-Normal age component distributions are also observed. Nonetheless, despite these complications the ages and the number of components were correctly determined. This at first seems like an unexpected result as the non-parametric model with the assumption that components in the model are defined as closed systems and follow volume diffusion, would most likely not be able to deal with a component as

complex as JC anorthite. However, I assume that components with excess ^{40}Ar will be treated similarly. For example, if I have a mixture which has a complex component that exhibits excess $^{40}Ar_{EX}$ I expect the model to deal with it in the same manner as it did for blind mixture 4. That is, the model will detect, if shown in the mixture, the excess ^{40}Ar and most likely infer the elevated age step as a component, this will add a component to the posterior calculation which will carry with it an additional 11 parameters at a minimum (assuming single domain behaviour). For transparency these parameters are as follows; Activation energy, frequency factor and age which are formed from 3 priors each totalling 9 with the addition of a diffusion length scale and volume which make it 11. The behaviour of extraneous ^{40}Ar has been well studied, with the archetypal age patterns exhibiting saddle shapes (Lanphere & Dalrymple (1976)). In a number of cases the effects of extraneous ^{40}Ar affect only a limited number of steps and the dominant step ages correspond to a pseudo plateau and the age of the sample as shown in Figure 3.6 panel E. In such a scenario the increased number of parameters needed to model a single elevated initial step (e.g., Figure 3.6 panel E) will reduce the posterior in such a fashion that a single age corresponding to the dominating pseudo plateau age will be inferred. Following from this I expect that in real world scenarios where components demonstrate complex behaviour, the model will behave accordingly and produce an age that is geological meaningful. This effect is further highlighted in all blind mixtures that contain JCA (Blind mixtures 2, 3, and 5). In these the age matches the inferred plateau age but there are variations between the mixtures to a far greater extent than any other component. This is most likely a by-product of the complexity of the individual sample.

The other model parameter inferences, such as the diffusion kinetics, cannot be used a diagnostic tool for distinguishing the mineral species of a component of differentiating between two components for which the age overlaps two individual component ages (e.g., blind mixture 3 and 4). The poorer fit to the Arrhenius data relative to the age steps is a product of the penalising model weight that is required for more straightforward inference. Thus, by this method, a unique solution for a mixtures individual component diffusion kinetics is not possible. Despite the poor quality of inferred kinetics, the ages of each component are correctly inferred which is the desired model output.

The components chosen for this blind mixture study represent differences in age: (ca. 30 to 900 Ma) and behaviour: (highly ideal samples such as the MO to the complex

behaviour of JCA). The choice of minerals, mostly feldspars with labradorite, anorthite, and orthoclase represent material that dominate the Martian surface (e.g., Ehlmann & Edwards (2014); Labradorite ∼60% of the K-bearing material on Mars).These components were specifically chosen such that the data presented here would be analogous to the Martian regolith. Although the mixtures presented here are most likely simplified in the number of components relative to Martian regoliths (e.g., NWA 7034), I show that my non-parametric model can deal with complex datasets that may be observed in samples return to Earth from Mars. I therefore foresee this model as being a tool to interpret and infer ages from complex multi-component-age K-bearing mixtures that may be recovered from geological settings both on Earth and on other terrestrial bodies in the Solar System.

3.9 Conclusion

I have shown that with an extension of the parametric model shown in Chapter 2 to a non-parametric model, the ability to infer real geological age information from complex multi-age polymineralic stepheating datasets is possible with little prior information. By initially testing the model on a simple mixture of Heidelberg biotite and Alder Creek sanidine I show the efficacy of this approach before analysis of complex blind mixtures. The materials chosen exhibit varying degrees of complexity and I show it is possible to extract geologically meaningful information regardless. These observations extends the applicability of this model for use in geological settings which will be naturally complicated due to a high number of mineral components (e.g., provenance studies with a large number of source areas). The flexibility of the model is also adapted to geological settings where there is no prior knowledge of the composition of the minerals. However, as shown with the differences in complexity between the test models and the blind mixtures, both good fits of the age spectrum and Arrhenius arrays were not achieved in the blind mixture analysis. Nonetheless, the model still provides meaningful age information. The overarching aim of this PhD was to develop an analytical framework that would allow for the interpretation of complex datasets that result from the stepwise heating of polymineralic multi-age mixtures. This non-parametric model provides a flexible framework that is as complex as the data require due to the nature of the Bayesian foundation.

Chapter 4

Reconstructing the source of Pleistocene glacial megafloods in North America

4.1 Introduction

The overarching aim of this PhD was to construct an analytical framework that could deal with complex $^{40}Ar/^{39}Ar$ stepwise heating datasets from polymineralic mixtures with applications to extra-terrestrial in-situ dating. Chapter 2 showed that in case studies where mixtures are composed of ideal components (neutron fluence monitors) the wealth of prior information makes it possible to unmix the datasets and recover the known ages of the components in the mixtures. Despite the success of the model in these particular case studies, it is clear that both the wealth of prior information and the ideal nature of the samples is not reflective of nature. Chapter 3 presents an extension of this model to be flexible enough to apply to geological settings where the sample is a complex assemblage of multi-age and multi-phase components which all have simple geologic histories. The parametric model of Chapter 2 is extended to a non-parametric modelling framework that removes the constraint of the number of components and introduces MDD-type behaviour, which is a likely property of framework silicates (e.g., Lovera et al. (1989, 1991)). Through the analysis of 'blind' mixtures I have shown that in geological settings with no prior information, similar to collecting sediment derived from multiple source lithologies, it is possible to estimate the most probable model from which the number of components and their particular set of parameters can be inferred. I show that the model set up in Chapter 3 is efficient at analysing synthetic

mixtures consisting of more complex materials. In this Chapter, I take the modelling framework and apply it to two natural datasets: (1) Moses Coulee and (2) Ephrata Fan sediments deposited by late Pleistocene glacial megafloods in Northwestern USA. This work aims to address the outstanding question: What is the source of the Moses Coulee flood sediments?

4.2 Glacial Lake Missoula megafloods

Glacial megafloods, defined as flows travelling at 10^6 m^3s^{-1}, occurred frequently during Pleistocene glaciations. Evidence of megafloods has been observed in North America (Bretz (1923, 1925)), Europe (Winsemann et al. (2016), Weckwerth et al. (2019)), Russia (Carling et al. (2009), Margold et al. (2018)), and the Himalayas (Lang et al. (2013), Turzewski et al. (2020)). Megafloods are associated both with large continental ice sheets in North America (e.g., O'Connor et al. (2020)) and also with mountain glaciers, such as the repeated outburst floods of the Yarlung-Tsango Gorge in the Eastern Himalayas (Lang et al. (2013), Turzewski et al. (2020)). Glacial megafloods occur when ice in alpine glaciers or ice sheets that temporarily block water behind them, acting as a dam and then fail. The resulting dam failing causes the release of a cataclysmic amount ($\sim$20 - 30 $\times$ 10^3 m^3s^{-1}; O'Connor & Baker (1992)) of freshwater. In North America, deglaciation and collapse of the Laurentide and Cordilleran ice sheets during the late Pleistocene (ca. 18.5 to 15 ka; O'Connor et al. (2020)) produced large volumes of freshwater that influenced the thermohaline circulation of the Pacific and Atlantic Oceans, causing abrupt changes in climate (Bond et al. (1993), Clarke et al. (2003)), and that also scoured and eroded the landscape and deposited huge amounts of sediment (Clarke et al. (2003)). The advancement of the Laurentide and Cordilleran ice sheets during cooling periods in the Pleistocene created a series of glacial lakes by damming natural pathways for water to flow from areas of high topography to the ocean. In essence, glacial advance primed the region for future glacial mega-floods. The full extent of the two great continental ice sheets are shown in Figure 4.1.

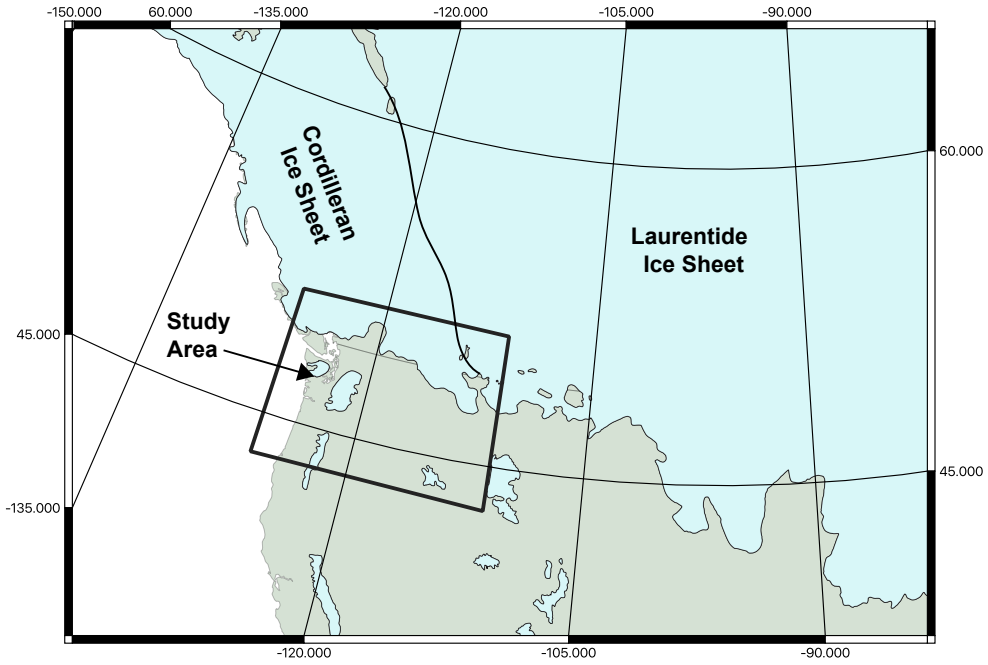

Figure 4.1: Maximum extent of the Laurentide and Cordilleran Ice Sheets across northwestern North America. Data are from Dyke & Evans (2003).

During the last glaciation, referred to locally as the Fraser Glaciation (29 - 14ka), the Purcell Trench lobe of the Cordilleran ice sheet advanced south into Idaho and dammed the Clark Fork River, impounding glacial Lake Missoula (Figure 4.2; Bretz (1923), O'Connor et al. (2020)). At approximately the same time, the Okanogan lobe, further west of the Purcell Trench lobe, dammed the Columbia River, creating glacial Lake Columbia in northeast Washington (Figure 4.2; Bretz (1923), Atwater (1984, 1986)). It is hypothesised that for several thousand years, between ∼18.2 and ∼14.7 ka (Lamb et al. (2008), Amidon & Farley (2011), Amidon & Clark (2015), Balbas et al. (2017)), glacial lakes Missoula and Columbia repeatedly filled and emptied. Floodwaters from glacial Lake Missoula are hypothesised to have entered glacial Lake Columbia, where deposits of an estimated 89 separate floods interbedded with glacial Lake Columbia sediments have been observed (Atwater (1986)). The floods then continued scarring the basalts of the Columbia Plateau creating the Channeled Scablands of central Washington, depositing giant bars, creating fan complexes and Coulees (large steep-walled troughs), and depositing fine-grained rhythmic bedded sediments (Bretz (1925), Waitt Jr (1980), Waitt et al. (2009), Waitt (2016)). The floods continued down the Columbia River, eventually washing into the Pacific Ocean through the Astoria

Fan (Figure 4.2).

Despite the landscape being extensively studied, there exist a number of controversies associated with the glacial Lake Missoula megafloods. The number of times that glacial lake Missoula drained and flooded the landscape is unknown with estimates ranging between 1 and 100 (Bretz (1925), Shaw et al. (1999)). Another source of controversy is the source of the floods. It is accepted that the most likely source of fresh water for the glacial megafloods was glacial Lake Missoula. However,other contributing sources are also hypothesised, such as glacial Lake Columbia (O'Connor et al. (2020)) or a source from subglacial reservoirs of the Okanogan Lobe (Shaw & Sharpe (1987), Shaw et al. (1999), Lesemann & Brennand (2009)). Recent modelling has also suggested that the volume of glacial Lake Missoula is not enough to account for the eroded landscape that is observed today (Komatsu et al. (2000), Miyamoto et al. (2006, 2007)). This anomaly could be explained by multiple flood pathways for different flooding events or a potential non-Missoula source of freshwater, such as the sub-glacial lakes under the Cordilleran Ice Sheet, as proposed by Shaw et al. (1999), or contribution from glacial Lake Columbia (Bretz et al. (1956), Gaylord et al. (2007), Lesemann & Brennand (2009)).

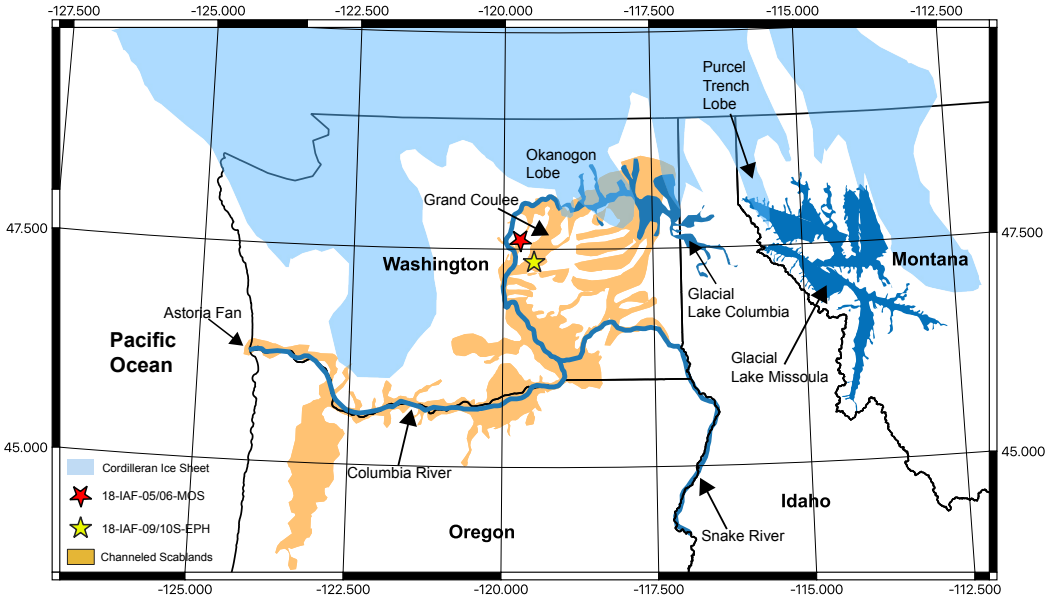

Figure 4.2: Overview map of U.S Pacific Northwest megaflood landscape, adapted from O'Connor et al. (2020) showing glacial Lake Missoula to the east, the Channelled Scablands in central Washington and the eventual outflow to the Pacific through the Astoria Fan in the west. The red and yellow stars show the sampling location of the Moses Coulee (18-IAF-05/06-MOS) and Ephrata Fan (18-IAF-09/10S-EPH) sediments.

In this Chapter I aim to identify the source of the Moses Coulee and Ephrata Fan flood sediments using detailed $^{40}Ar/^{39}Ar$ stepheating analysis. I apply this methods to bulk fine-grained sediment (20 - 125 μm), with particular focus on the silt sized fraction (20 - 64 μm). I then use my non-parametric Bayesian model detailed in Chapter 3 to interpret the resulting age spectra and Arrhenius datasets to identify the age components in these sediments. Connections between the sources and sediments are then made through the inferred model ages. Analysis of the bulk silt-sized sediments using this method has the potential to provide a integrated provenance signal, identifying the source regions, proximal age components and even flood pathways. The geologic map of the study area is shown in Figure 4.3. If Lake Missoula is the source of these floods, one definite component is the bedrock of this region which is dominated by Mesoproterozoic aged bedrock (~1000 - 1600 Ma). However, if the freshwater source is from glacial Lake Columbia I expect to find a component of Mesozoic age (~262 - 65 Ma). A third possibility is that both glacial Lakes Missoula and Columbia are both freshwater sources of these floods meaning both age components would be expected in the model inference. An expected component for all samples is the Columbia River

Basalts which is the Earth's youngest continental flood basalt province with volcanism beginning around 17 Ma. Previous age determinations place the age range of the province between 17 and 6 Ma (Baksi (1989), Tolan & Beeson (1984)), with the majority of the volcanism between ∼16.7 and 15.9 Ma (Kasbohm & Schoene (2018)). I therefore expect and ca. 16 Ma age component to be present in all mixtures and I modify the age prior accordingly.

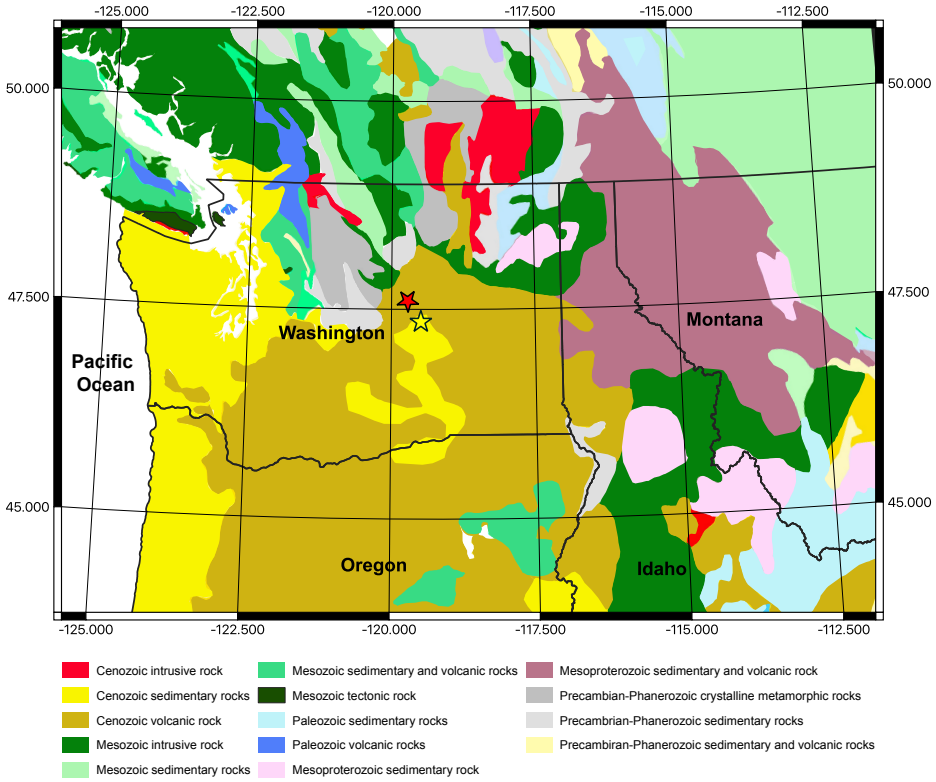

Figure 4.3: Geologic map of U.S Pacific Northwest megaflood landscape. Data is from the USGS database (Reed et al. (2005)). The red and yellow stars show the sampling location of the Moses Coulee (18-IAF-05/06-MOS) and Ephrata Fan (18-IAF-09/10S-EPH) sediments. Both Moses Coulee and Ephrata Fan sediments are deposited on top of the Columbia River Basalts (CRBs) which are Cenozoic in age and most recently dated to ca. 16 Ma (Kasbohm & Schoene (2018)).

4.3 Study areas

This study examines bulk fine-grained (0 - 125 μm) flood sediments from the Giant Bar of the Moses Coulee and from the Ephrata Fan complex. Two sites at each location were sampled. Figure 4.4 shows a digital elevation model of the samples sites, both are located in the Channeled Scablands (Figures 4.2 to 4.4) and are described in the next sections.

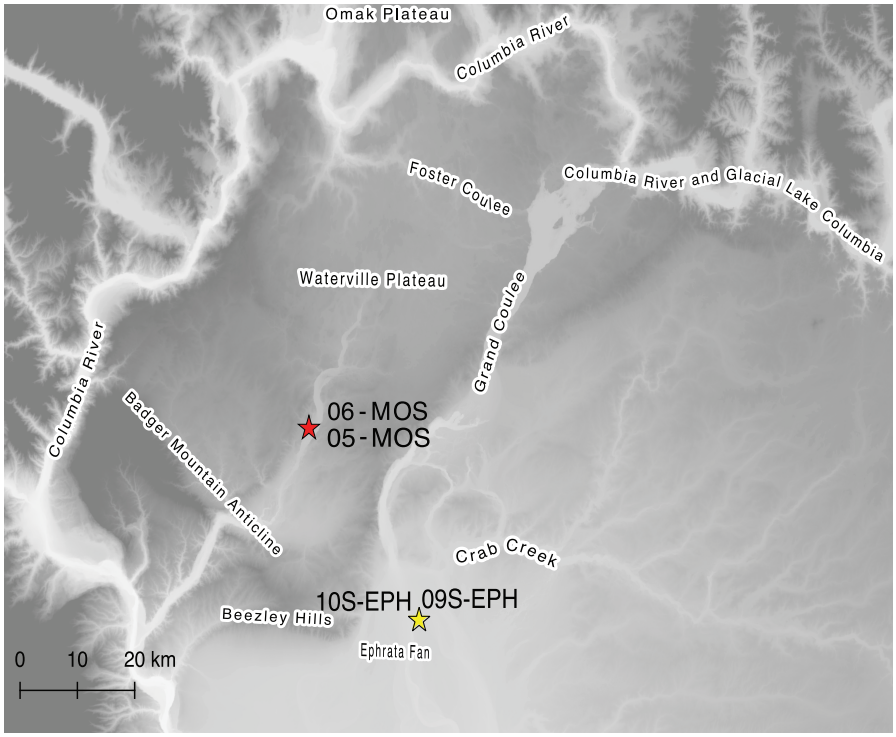

Figure 4.4: Digital elevtaion model of the study are labeled with the major physiographic features and locations of sampled sediment. The sites of Moses Coulee and Ephrata Fan samples are shown by red and yellow stars. The map is 1:8×10^5 scale.

4.3.1 Moses Coulee

Moses Coulee is the second-largest and farthest west canyon of the Channeled Scablands located ∼30 km to the west of and hanging several hundred meters above Grand Coulee. In this study I examine two gravel samples from the Great Bar within upper Moses Coulee (18-IAF-05-MOS and 18-IAF-06-MOS). The Great Bar accumulated at an inside bend in upper Moses Coulee, downstream of a bedrock protrusion. The Great Bar has an area of ∼4 km^2 and varies in elevation from 550m near the western canyon wall, to 500m in the middle of the canyon where it intersects valley fill sediment. Samples 18-IAF-05-MOS and 18-IAF-06-MOS were taken from the bar surface surface at 540 m elevation and 3 km downstream from the bedrock protrusion. Samples were extracted by digging a pit and removing sediment from the walls of the pit at 55-70 cm depth for 18-IAF-05-MOS and 65 - 80 cm depth for 18-IAF-06-MOS (Figure 4.5).

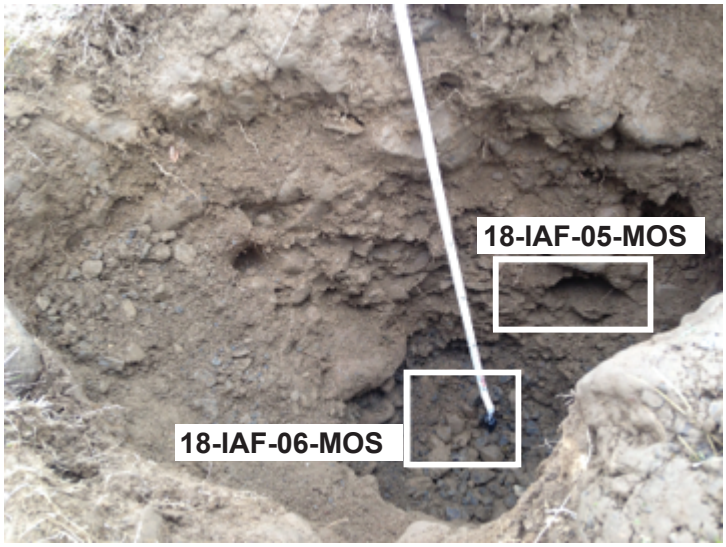

Figure 4.5: Photograph of the Moses Coulee samples from the Great Bar.

4.3.2 Ephrata Fan

In addition to the Moses Coulee samples, Ephrata Fan gravels were also sampled. The Ephrata Fan is the outwash of the Grand Coulee ∼30 km from Moses Coulee as it dispersed into a large basin (Figure 4.4). The Ephrata Fan complex is hypothesised to have formed from the Glacial megafloods that carved the Grand Coulee. The Ephrata Fan gravels (18-IAF-09S-EPH and 18-IAF-10S-EPH) were sampled from two points at a cut bank above the Trout Lodge Hatchery. The site is approximately 9 km downstream from the entrance of the Grand Coulee into the Quincy Basin (Figure 4.4). 18-IAF-09S-EPH was taken from 374 m elevation, near the surface of the terrace and 18-IAF-10S-EPH was taken from 355 m elevation, about 20 m above the level of Rocky Ford Channel (Figure 4.6, panel B). The upper sample (18-IAF-09S-EPH) is a clast-supported, rounded cobble gravel, with interstitial granules, sand, and silts (Figure 4.6, panel C). Cobbles within this sample are well rounded and are basalt or granite. The lower samples (18-IAF-10S-EPH) is a clast-support pebble-cobble gravel with a higher proportion of basalt than the upper sample and a lower degree of clast rounding (Figure 4.6, panel A).

Figure 4.6: Photographs of the Ephrata Fan samples. A shows the lower sample site 18-IAF-10S-EPH. B shows the field relationships of the sample sites and C shows the upper sample site 18-IAF-09S-EPH.

4.4 $^{40}Ar/^{39}Ar$ as a provenance tool

In provenance studies, the $^{40}Ar/^{39}Ar$ method can be applied to detrital K-bearing mineral grains or clasts because the temperature at which radiogenic Ar loss occurs is typically far above diagenetic conditions (e.g., the closure temperature of muscovite is $\sim 350^{o}$C ; McDougall & Harrison (1999)). Most commonly this is applied through single grain analysis, with the most common choice of material to date being white mica (e.g., Grimmer et al. (2003), Von Eynatten & Wijbrans (2003), Li et al. (2007), Carrapa et al. (2009), Najman et al. (2009), Van Hoang et al. (2010), Gemignani et al. (2017, 2019)). Muscovite is chosen since it is common in sandstones and siltstones and appears robust enough to survive one or multiple recycling episodes (e.g., Eide et al.

(2005)). The typical provenance method using $^{40}Ar/^{39}Ar$ applied to muscovite is as follows: Single grains of muscovite are analysed by laser fusion, which provides a single age inferred to represent the age of a unique source. The $^{40}Ar/^{39}Ar$ age distribution for the white mica is plotted as a cumulative or relative probability distribution and then compared to existing $^{40}Ar/^{39}Ar$ or K-Ar data from basement units to determine the provenance.

As well as single grain provenance analysis the $^{40}Ar/^{39}Ar$ method has be used to attempt to recover provenance information from silt sized bulk sediment (e.g., VanLaningham et al. (2006, 2008), Villaseñor et al. (2016)). This method analyses the bulk, multi-mineral silt fraction, that is potentially sourced from bedrock of different cooling ages. The focus on the silt sized sediment mean that the sediment is fine enough to reflect all source regions and large enough to avoid or reduce the effects of Ar recoil compared to finer size fractions (e.g., Clauer (2013)). In the previous bulk sediment $^{40}Ar/^{39}Ar$ provenance studies (VanLaningham et al. (2006), Villaseñor et al. (2016)) the authors assume that each mineral phase exhaust Ar at a time-temperature range specific to that phase, whereby the resulting age spectrum release will be indicative of the contributing minerals over specific time-temperature ranges. For, example if two components are degassing in concert, the resulting age step will be a weighted mean of the contributing components. In the provenance studies of bulk sediment by VanLaningham et al. (2006) the author uses the relationship between the age spectra and K/Ca spectra noting that concordance of both have the potential to infer an age of geological meaning, this technique is also used by Villaseñor et al. (2016). VanLaningham et al. (2006) use this method to link sediment contributions from 14 different river systems to the continental margin. Villaseñor et al. (2016) use this technique to determine the primary source of sediment in the Canterbury continental shelf in New Zealand. Despite the promise of this method the interpretation relies on defining ages from pseudo plateaus of both the age spectra and K/Ca spectra to assign ages of geological meaning. However, the degassing of two mineral components that are of different ages but the same phase would produce a weight plateau age proportional to the contribution of both of these phases that has no geological meaning (e.g., Kula et al. (2010)). Nonetheless, the method could relay ages of geological meaning if coupled with geologic evidence of the source area (i.e., an identifiable source that is indistinguishable from the plateau age). However, this interpretative method of bulk sediment analysis is purely qualitative and requires an interpretative model to formally infer the

ages present in a bulk fine-grained age spectra. Here, I use the non-parametric method detailed in the previous Chapter to interpret the age spectra and Arrhenius arrays of step-heated Ephrata Fan and Moses Coulee sediments. By fitting these two sources of information with my nonparametric Bayesian model I attempt to infer the number of components and their ages that best describe the datasets.

4.5 Methods

Bulk fine-grained sediments (0 - 125μm) from each sample site were initially cleaned following VanLaningham et al. (2006). Briefly, organic compounds were removed by initially adding 30 mL of 35% hydrogen peroxide to the samples for 8 hours. After, an additional 30 mL of hydrogen peroxide was added and the samples were shaken for 72 hours. I used two hydrogen peroxide steps as suggested by VanLaningham et al. (2006) due to high organic content in fresh water sediments. Three washes in distilled water followed. Carbonate was then removed by adding 200 mL of dilute acetic acid to each sample and then samples were shaken for a further 24 hours. Samples were then cleaned in 3 more washes with distilled water.

After cleaning, approximately 30mg of each sample were loaded into 5 11-well aluminium irradiation dics, wrapped in aluminum foil, and sealed in a glass cylinder for irradiation. Grains of the neutron fluence monitor GA1550 (age = 98.8 $\pm$ 0.96 Ma (1σ); Renne et al. (1998)) were loaded alongside the samples. The samples and GA1550 were irradiated for 30 hours in the Cadmium-Lined in-Core Irradiation Tube (CLICIT) facility a the Oregon State University TRIGA reactor. Following irradiation, approximately 10-15 mg of bulk fine grained sediment were loaded into packets made from high-purity platinum tubes. Samples were then sequentially degassed using a 75W diode laser in a PID-feedback control loop with a coaxially aligned optical pyrometer. To account for the temperature-dependent emissivity of the platinum tubes, pyrometer temperatures were calibrated against a thin-wire K-type thermocouple under identical conditions to the degassing experiments. Samples were degassed over very detailed heating schedules ($\sim$40 - 60 steps) including both isothermal and cyclic heating steps to aid in the interrogation of the presence of multiple mineral diffusion kinetics (Harrison et al. (1991)). I am confident that uniform heating of the grains within the packet is achieved because of the low sample mass loaded into each packet as well as the fine-grained nature of the sample.

Isotopes of argon were measured using an ARGUS V multi-collector noble gas mass spectrometer (Mark et al. (2009); Since the publication of Mark et al. (2009) there have been a series of system upgrades; the replacement of the 100 1×10^{11}ohm and 1 1×10^{12} GVI Faraday resisters (GVI generation) with TIA Systems 100 1×10^{11}ohm and 1 1×10^{12}ohm resistors). A sequence of a background, air and another background measurement were run following every sample measurement for the same duration as the laser degassing step to provide careful control on background corrections and mass spectrometer discrimination. The step heating of each mixture will produce a release pattern unique to the heating schedule, the mineral component composition and ages, and unique grain size distribution of the components in the mixture. Samples that are of the same mineral phase but from different bedrock sources will produce concordant steps and a weighted average $^{40}Ar/^{39}Ar$ step age. Here I couple a very detailed heating regime (∼40 - 60 steps) with isothermal and cyclic steps to highlight the presence of multiple components with differing retentivity (Harrison et al. (1991)).

4.6 Results

4.6.1 Ephrata Fan results

The results of the 20-63μm grain size fraction of the Ephrata Fan sediment are displayed below. Figure 4.7 panels A and B show the age spectrum and Arrhenius array of sample 18-IAF-09S-EPH.The pattern of both these datasets is indicative of the presence of multiple mineral phases and multiple distinct age populations. In sample 18-IAF-09S-EPH the age spectra is undulating with an initial release at ∼380 Ma followed by falling step ages over the first 30% of the gas release. Following this the age spectrum increase to a step age of ∼400 Ma before falling to a minimum age step at 90% the age step then increase to a maximum over the final number of age steps. All Ephrata Fan samples show no conventional plateau indicating that they record the degassing of multiple mineral phase components with different ages over the experiment. The Arrhenius array is curvilinear with multiple gradients and intercepts possibly indicating the presence of multiple phases with different retentivities.

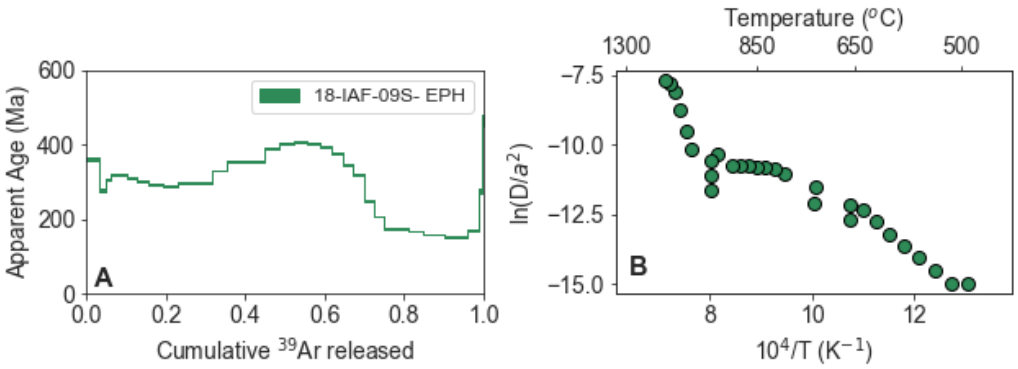

Figure 4.7: A Age spectrum and B Arrhenius array of the 18-IAF-09S-EPH sediment.

Figure 4.8 shows the age spectra and Arrhenius arrays of 18-IAF-10S-EPH. Panels A and B show the age spectrum and Arrhenius array of a more coarse sample. Panels C and D show the age spectrum and Arrhenius array of sample described as more silt like, hereafter labeled 18-IAF-10S-EPH (silt). Sample 18-IAF-10S-EPH and 18-IAF-10S-EPH (silt) show undulating patterns over all the Ar release steps with the final release steps rising to a maximum ages of ∼760 and ∼3.2 Ga. Similar to 18-IAF-09S-EPH the Arrhenius arrays of both of these samples show curvilinear behaviour with the presence of multiple intercepts and gradients. The difference in the release patterns of these samples (Figure 4.8, A and C) is most likely due to the different temperature schedules used (Figure 4.9 panel B). Additionally, the slightly different grain sizes of these samples mean that subtle differences in the heating schedule will cause large differences in the release of Ar from each sample.

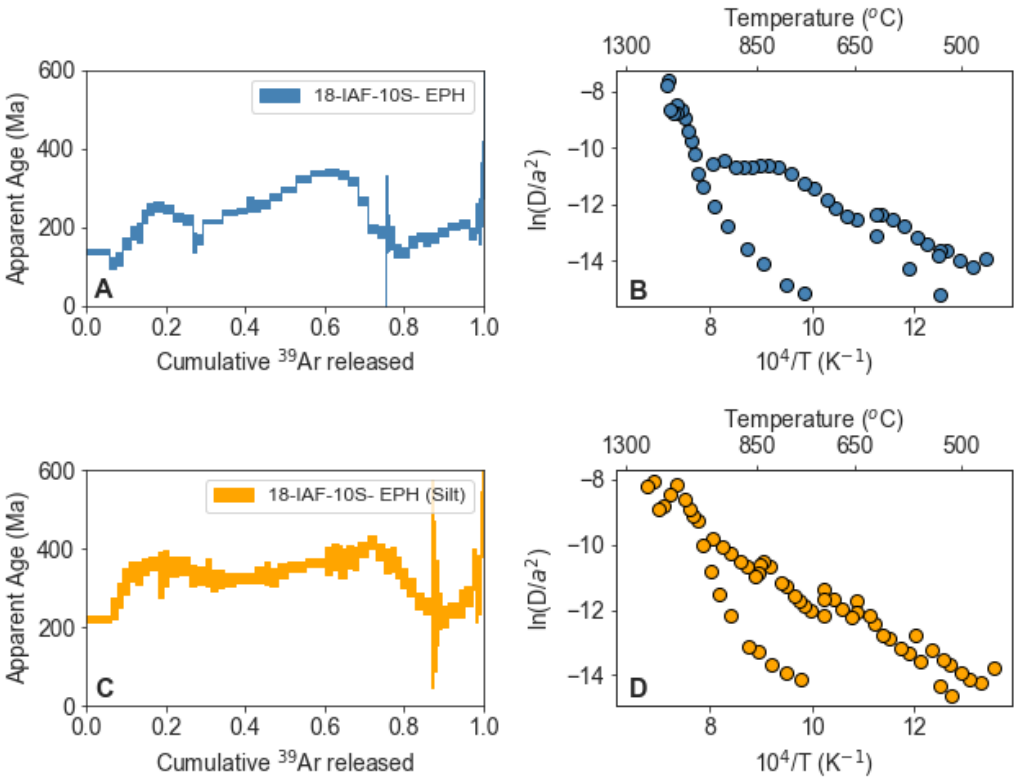

Figure 4.8: Panel A shows the Age spectrum and panel B Arrhenius array of 18-IAF-10S-EPH. Panels C and D are the age spectra and Arrhenius array and from the same site however the sediment is described as more silt like.

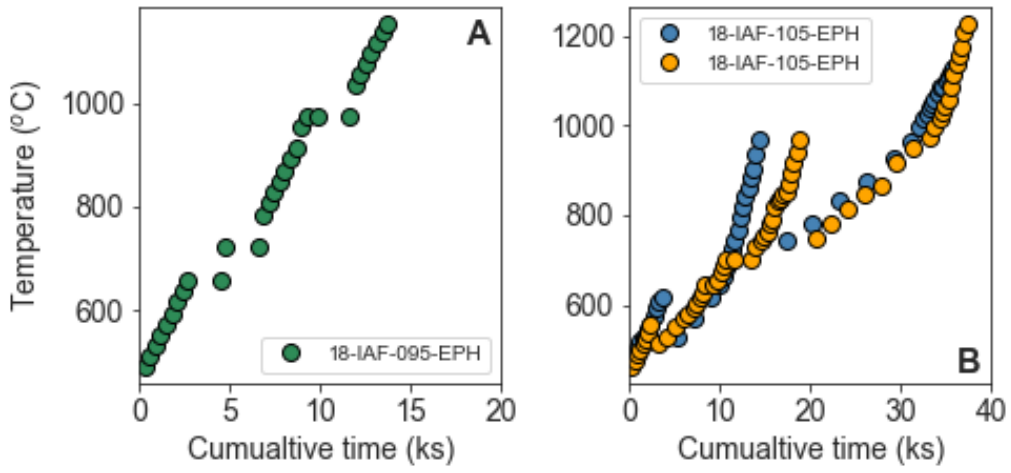

Figure 4.9: Panel A shows the temperature for each step against the cumulative time for the experiment on 18-IAF-09S-EPH. Panel B shows temperature for each step against the cumulative time for the experiment for both 18-IAF-10S-EPH samples.

4.6.2 Moses Coulee results

The results of the of the 20 - 63μm fraction of the Moses Coulee sample is shown below. Figures 4.10 and 4.11 show the age spectra and Arrhenius array of 18-IAF-05-MOS and 18-IAF-06-MOS. In both Figures panels C and D are described as more silt like material and will hereafter be named 18-IAF-05-MOS (silt) and 18-IAF-06-MOS (silt). Like the previous Ephrata Fan samples these age spectra show undulating release patterns (Figure 4.10, panels A and C). Both 18-IAF-05-MOS and 18-IAF-05-MOS (silt) show an initial age of ∼200 Ma followed by a hump at ∼10% of the ^{39}Ar releas. Following this inital release both age spectra slope down and the rise to a second hump at ∼50% of the gas release. Over the last portion of the release both age spectra show decreasing ages to ∼90% of the gas release before sharply rising age steps to exhaustion. Similar to both the 18-IAF-05S-MOS samples, 18-IAF-06S-MOS show similar release patterns. Both start with an initial higher age step followed by a short decrease over the first 10% of the gas release following this both age spectra so rising step ages to a mid release hump at ∼50% of the gas release. Next both show falling age steps before sharp rises in age as both sample are fully degassed. Similar to the age spectra of the Ephrata Fan samples none of the Moses Coulee age spectra show any conventional plateaus indicating that they also reflect a multiple mineral mixture of different phases and ages degassing in concert. Arrhenius arrays of both of these samples all show curvilinear behaviour with multiple gradients and intercepts likely due to multiple component phases. Also similar to the Ephrata Fan samples the subtle differences in heating schedule (Figure 4.12) and slightly different grain size distributions result in the difference between the age spectra of each sample.

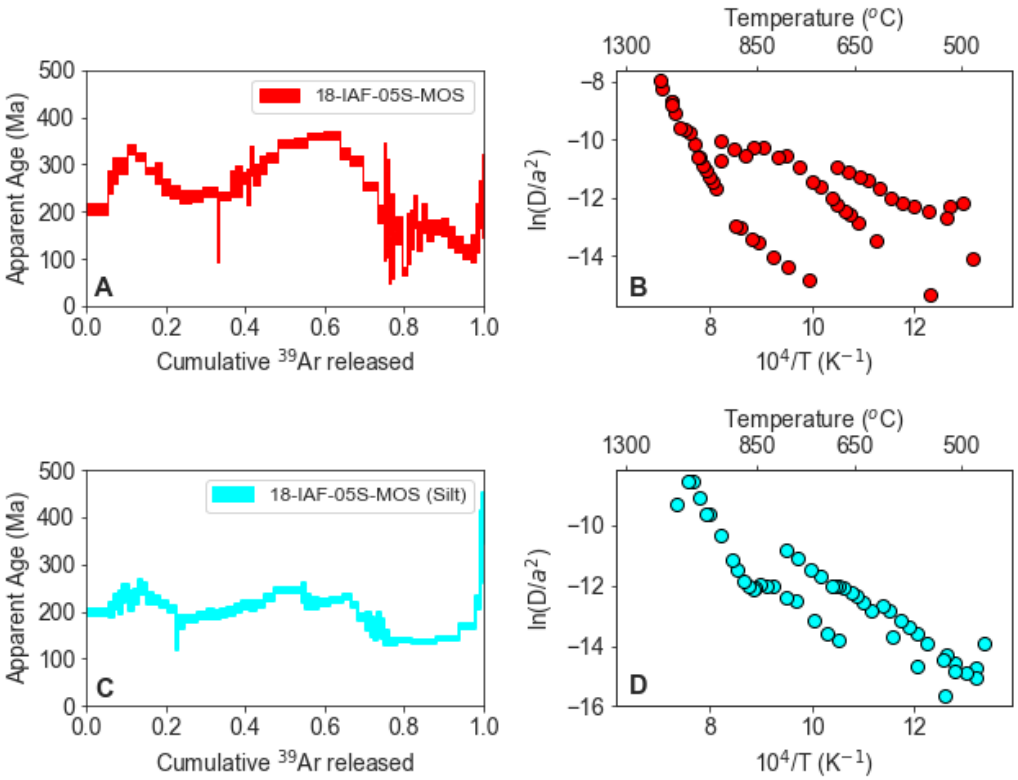

Figure 4.10: Panel A shows the Age spectrum and panel B Arrhenius array of the 18-IAF-05S-EPH sediment sampled from the Giant Bar of the Moses Coulee. This sample was taken from 50-65 cm below the surface. Panels C and D show the age and Arrhenius array from the same site however the sediment is described as more silt like.

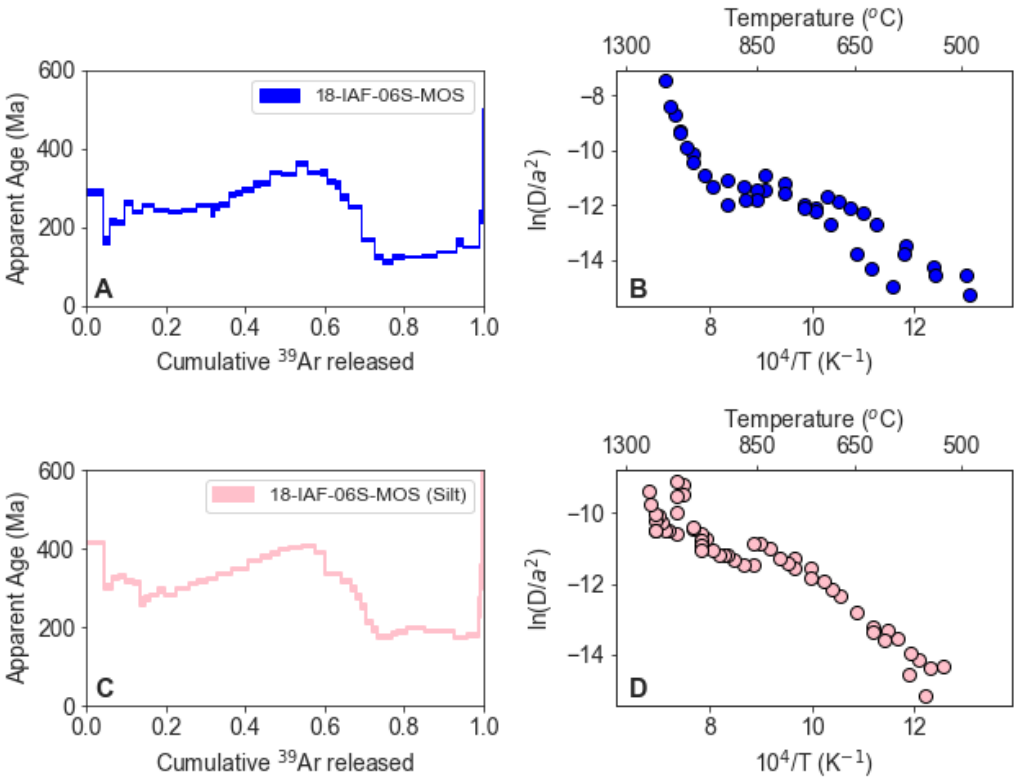

Figure 4.11: A age spectrum and B Arrhenius array of the 18-IAF-06S-EPH sediment sampled from the Giant Bar of the Moses Coulee.

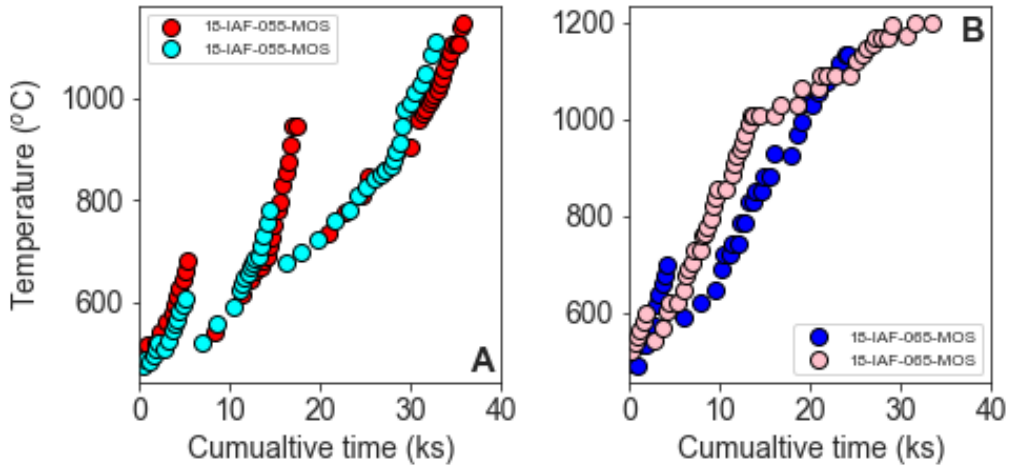

Figure 4.12: Panel A shows the temperature for each step against the cumulative time for the experiment on 18-IAF-05S-MOS. Panel B shows the temperature for each step against the cumulative time for the experiments for both 18-IAF-06S-MOS samples.

4.6.3 Data Summary

In Figure 4.13 I show the KDE of all step heating data; Ephrata Fan (panel A) and Moses Coulee (panel B). Similarities in the bulk of the ages are centred around ~250 Ma which does suggest that it is likely both Moses Coulee and Ephrata Fan are composite of the same minerals and age populations. Differences between the two samples can be observed at the most ancient ages. Both show ≥ 1000 Ga age steps but Moses Coulee has far more age steps in this range suggesting perhaps a higher abundance of the most ancient material in the sediment or the potential of a different flood pathway or source.

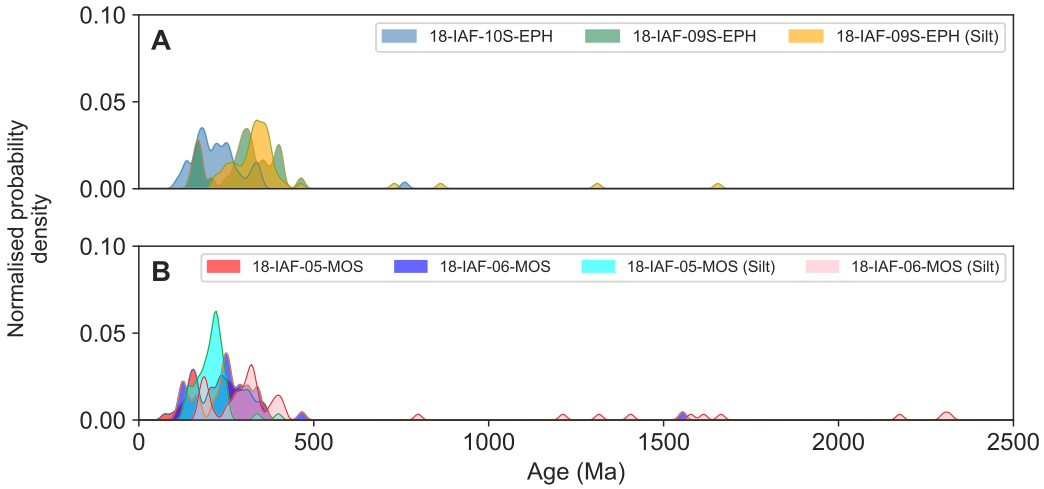

Figure 4.13: A KDE of the stepheating datasets of the Ephrata Fan sediments. B KDE of the stepheating datasets of the Moses Coulee sediments.

Like previous bulk sediment analyses (e.g., VanLaningham et al. (2006), Villaseñor et al. (2016)), the age of each step will be a mixture of the ages of each component within the sample that release Ar over the temperature and time of that step. Nonetheless, given that the age spectra presented here represent a mixing process, some basic inference can be drawn before applying the model. In particular for all age spectra the maximum age step is equal to or less than the age of the oldest component present and the minimum age step is greater than or equal to the youngest age component present. Figures 4.14 and 4.15 show the minimum and maximum ages of the Ephrata Fan and Moses Coulee silt sized sediment step healing data sets to illustrate these bounds. These plots are created using the age and 2σ uncertainty of both the maximum and minimum age step.

Figure 4.14 shows the minimum and maximum age bounds for the Ephrata Fan datasets. Panel A (18-IAF-09S-EPH) shows that there must be a component ≥(450

- 475 Ma) in this sample and ≤ (150 - 155 Ma). Panel B (18-IAF-10S-EPH) shows a similar younger component bound ≤(100 - 160 Ma) but a much higher upper limit of ≥(400 - 1000 Ma). Panel C (18-IAF-10S-EPH (silt)) shows the same lower bound again (100 - 150Ma) with a higher again upper bound and more spread (due to the large ∼750 Ma 1σ uncertainty on this age step) of ≥(1700 - 4700Ma).

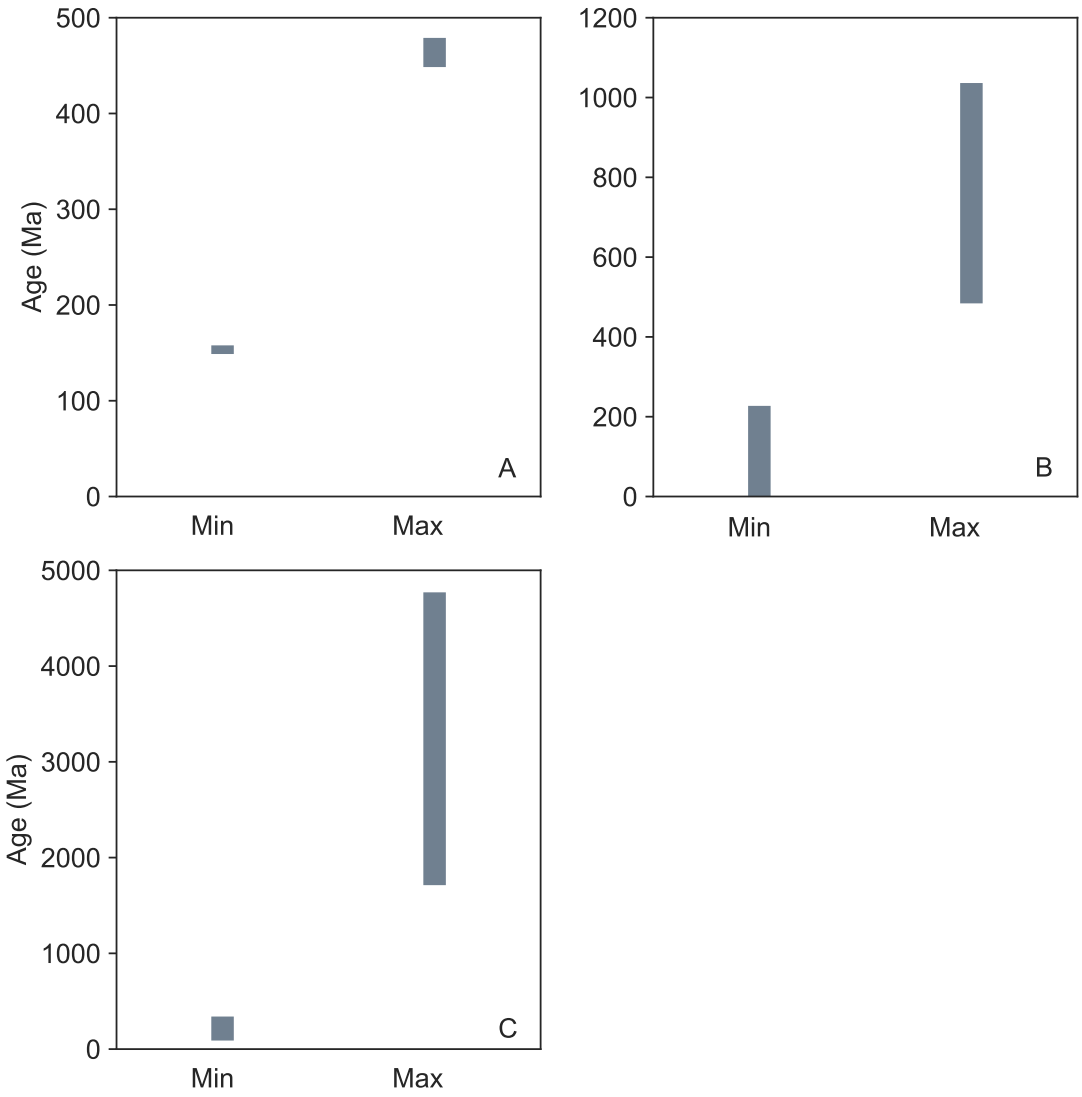

Figure 4.14: These plots are created from the minimum and maximum age step of each dataset and the 2σ uncertainty of these steps. Panel A shows the box plot of the 18-IAF-09S-EPH. Panels B and C show the box plots of the youngest and oldest steps and their uncertainty for 18-IAF-10S-EPH.

Figure 4.15 show minimum and maximum data for the Moses Coulee datasets. 18-IAF-05-MOS (panels A and B), the former showing minimum and maximum bound of ≤80 Ma and ≥750 - 2250 Ma and the latter is the more silt sized fraction have maximum ages of greater than or equal to ≥(360 - 460 Ma) and younger ages less than

or equal to ≤(150-160 Ma). 18-IAF-06-MOS (panels C and D), where the latter is the more silt sized fraction have maximum ages of greater than or equal to ≥(0 - 8000 Ma; due to the large uncertainty on the oldest age step) and younger ages less than or equal to (≤80-120 Ma). And the former shows a minimum bound of ≤80-90 Ma and ≥750 - 2250 Ma.

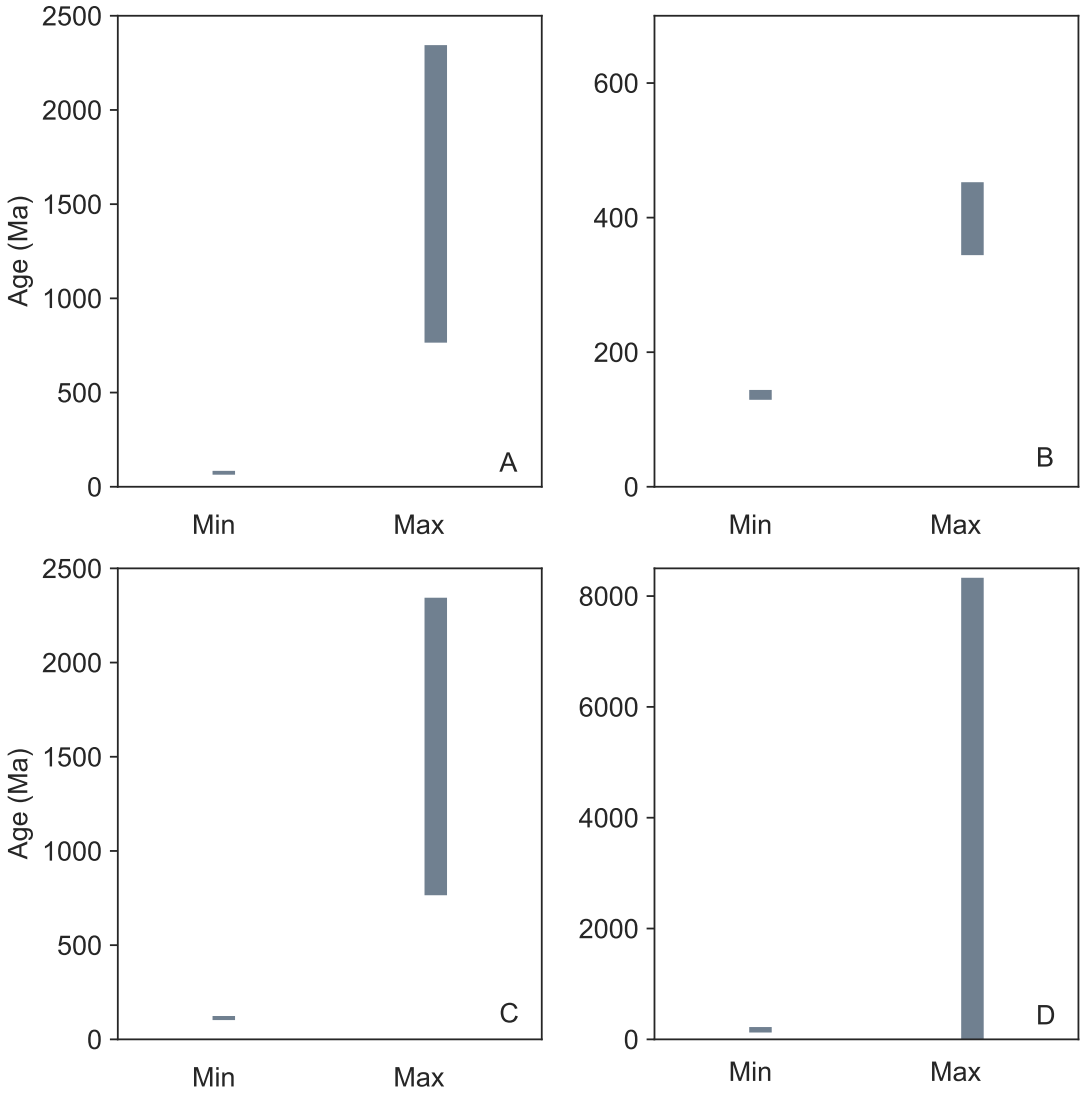

Figure 4.15: These plots are created from the minimum and maximum age step of each dataset and the 2σ uncertainty of each of these steps, panels A and B shows the box plot of the 18-IAF-05-MOS. Panels C and D show the plot of the youngest and oldest steps and their uncertainty for 18-IAF-06-MOS.

Although these are crude estimates they provide some broad implications for inferences of provenance in particular for the older components which in both the Ephrata Fan and Moses Coulee show ancient ages albeit with large spread that are similar to the glacial Lake Missoula age source (1000 - 1600 Ma). In the next section I use my

nonparametric Bayesian model to interpret these datasets with a far more detailed analysis.

4.7 Model

I interpret these datasets with the nonparametric Bayesian model described in detail in the previous Chapter. Briefly, I use a Dirichlet process mixture model, formatted to remove the fixing of the number of components, and a second Dirichlet prior to remove the constraint of single domain behaviour. I also make one change to the model to account for prior information available from the bedrock source ages. Previously a uniform distribution from 0 - 4600 Ma was used. Here I create an age prior by concatenating a uniform distribution from 0 - 2500 Ma (the maximum age range of the source ages) and a normal distribution centred at 16.3 Ma with a standard deviation of 0.3 Ma (the age range of the Columbia River basalt (ca. 15-17 Ma; Kasbohm & Schoene (2018)) and then interpolating the resulting array to obtain probability for points evenly spaced between 0 and 2500 Ma on a 1000 point grid. This prior is shown below (Figure 4.16).

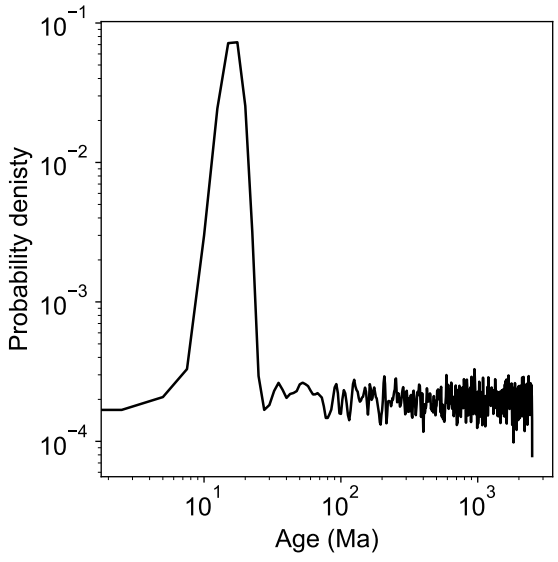

Figure 4.16: Age prior for both the Ephrata Fan and Moses Coulee sediments. Both x and y axes are shown in a log scale.

I fit the age spectra and Arrhenius array datasets inferring estimates of the number of components and the ages of each component. For each mixture I used a burn in of $\sim 1 \times 10^6$ steps (varied due to the differences in dataset size, larger dataset longer burn-

in). Following the burn in, another 1×10^5samples are taken from which estimates of all model parameters are drawn. The burn is necessary in Bayesian analysis as the initial steps are both highly correlated and dependent on the initial value. The Dirichlet process mixture model used here is particular difficult to obtain ideal sampling and convergence across all parameter so I use a particularly long burn to obtain convergence for the contributing parameters to the model.

4.8 Modelling results

Figure 4.17 shows the model results for the 18-IAF-09S-EPH sediment age spectrum fit (panel A), arrhenius fit (panel B) and cumulative density plot of the comparison of model age steps against data age steps (panel C). Panels D, E, and F show the inferred number of components, the component weights, and the age of each component.

There are some notable model outputs that highlight the modelling set up. Firstly, due to the favouring of fitting the age steps against the Arrhenius model I expect the age spectrum to be fitted better than the Arrhenius dataset. This is evident in Figure 4.17 Panels A - C: the Arrhenius array is poorly fit in the initial lower temperature steps. This does not negate the results as in the previous Chapter through the analysis of blind mixtures and the Heidelberg biotite and Alder Creek sanidine created by VanLaningham & Mark (2011), I show that good temporal information can be obtained with poor fits to the Arrhenius array.

As I treat all models the same, similar model fits, notably, the poorer fit to the Arrhenius, array are expected for all Ephrata Fan sediments. These are shown in Figures 4.18 and 4.19 (A - C) where similar posterior models are obtained, namely poorer fits to the Arrhenius array and better fits to the age spectrum. The number of components inferred vary across the samples (Figures 4.17 - 4.19) but all have broadly similar component ages that I summarise in table 4.1.

4.8.1 Ephrata Fan

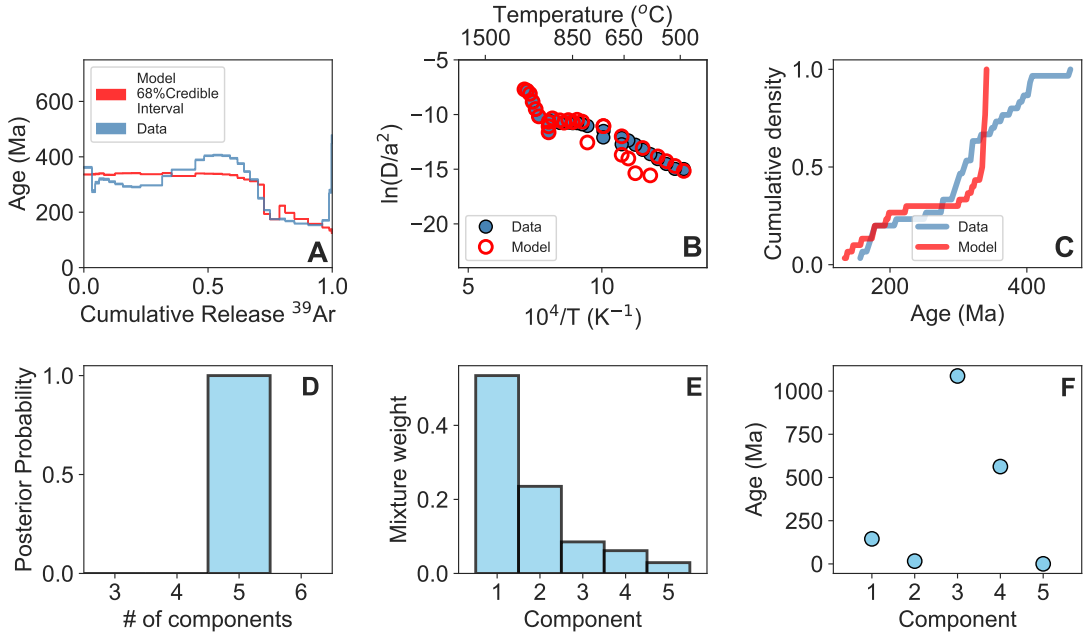

Figure 4.17: Model results for 18-IAF-09S-EPH. Panel A shows the posterior model age spectrum 68% confidence interval in red and the observed data set in blue. Panel B shows the observed Arrhenius array (blue circles with black outline) and the modelled Arrhenius array (red open circles). Panel C shows the cumulative density plot of the step age data in blue against the model in red. Panel D is the inferred number of distinct age components in the model, E shows the mixture weight and F the ages of each component.

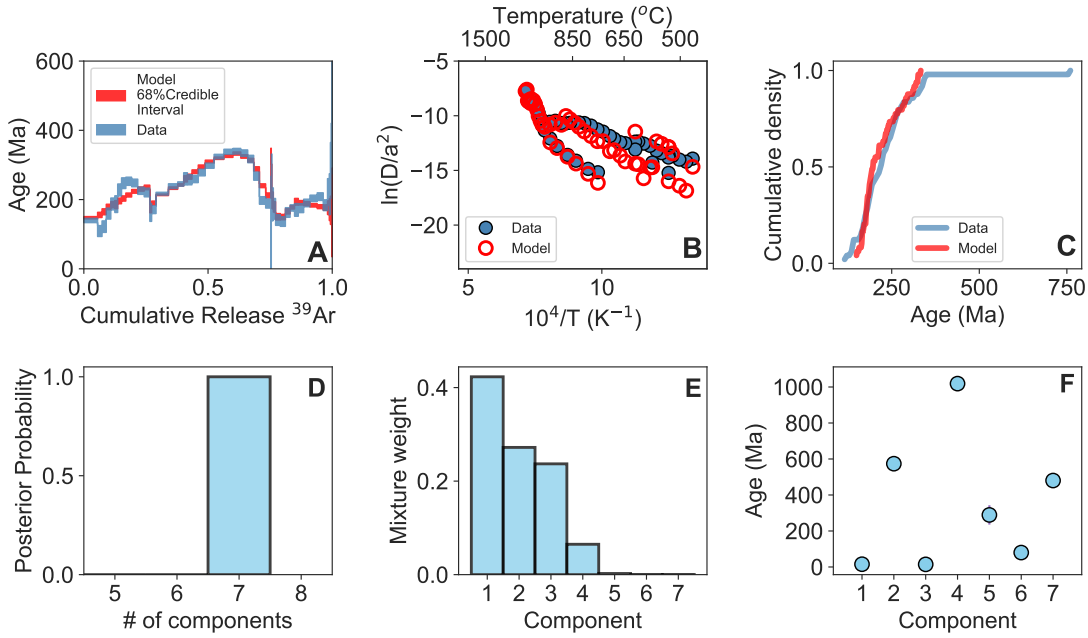

Figure 4.18: Model results for 18-IAF-10S-EPH. Panel A shows the posterior model age spectrum 68% confidence interval in red and the observed data set in blue. Panel B shows the observed Arrhenius array (blue circles with black outline) and the modelled Arrhenius array (red open circles). Panel C shows the cumulative density plot of the step age data in blue against the model in red. Panel D is the inferred number of distinct age components in the model, E shows the mixture weight and F the ages of each component.

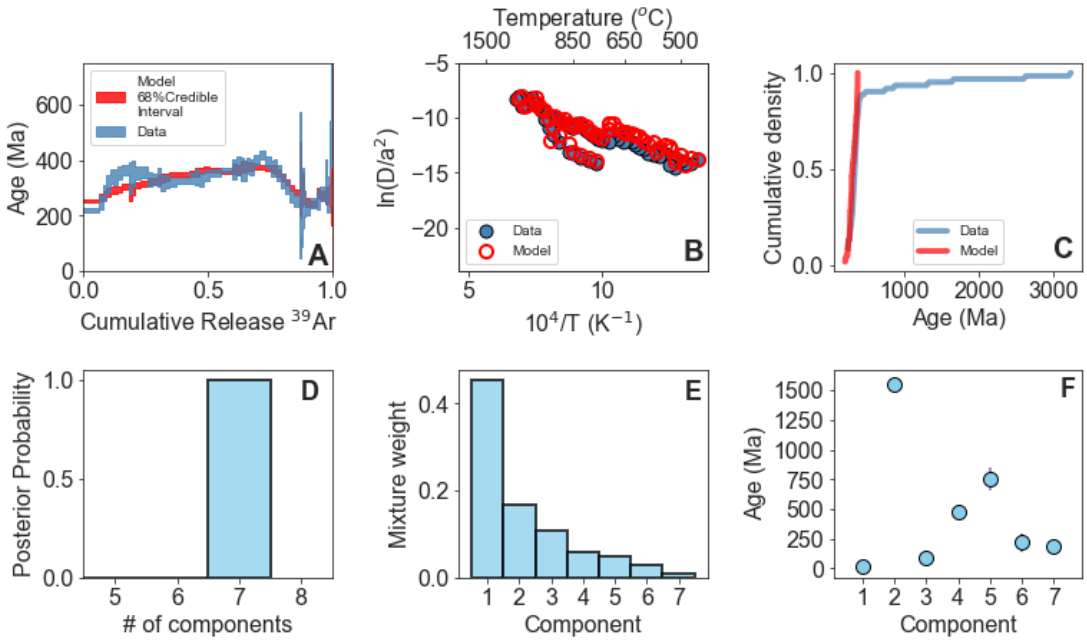

Figure 4.19: Model results for 18-IAF-10S-EPH (silt). Panel A shows the posterior model age spectrum 68% confidence interval in red and the observed data set in blue. Panel B shows the observed Arrhenius array (blue circles with black outline) and the modelled Arrhenius array (red open circles). Panel C shows the cumulative density plot of the step age data in blue against the model in red. Panel D is the inferred number of distinct age components in the model, E shows the mixture weight and F the ages of each component.

Table 4.1 shows the combined results for the three Ephrata Fan sediments. Common to all samples is the a component age derived from the Columbia River basalts (CRBs; ~16 Ma; Kasbohm & Schoene (2018)). This is an expected result as the samples are derived from the CRBs and I modify the prior for added probability of sampling from an age of ~16 Ma. Another common component is an age that is Mesozoic (~65 - 252 Ma) and associated with the age of glacial Lake Columbia. These age components differ between the sample 18-IAF-09S-EPH and both 18-IAF-10S-EPH/18-IAF-10S-EPH (silt). The final age component that is common across all components is ~1 - 1.6 Ga, an age associated with glacial Lake Missoula. The final expected result is the recovery of the most components for the silt sized sample that is expected to be the most integrated signal derived from all source areas.

Sample	# of Components	Component	Age ± 2σ
18-IAF-09S-EPH	4	1	13 ± 3
		2	131 ± 4
		3	563 ± 8
		4	1088 ± 12
18-IAF-10S-EPH	6	1	15 ± 4
		2	80 ± 36
		3	289 ± 54
		4	480 ± 20
		5	574 ± 16
		6	1019 ± 40
18-IAF-10S-EPH (silt)	7	1	16 ± 4
		2	95 ± 14
		3	183 ± 23
		4	218 ± 38
		5	476 ± 17
		6	751 ± 48
		7	1550 ± 24

Table 4.1: Summary of the model inferences for the Ephrata Fan sediments

4.8.2 Moses Coulee

Like the Ephrata Fan samples I observe similar modelling results for all Moses Coulee datasets. Specifically, these are reasonable but poorer fits to the Arrhenius array, an expected outcome of the penalising weight, and a better fit to the age spectra of all samples. I summarise the results in Table 4.2.

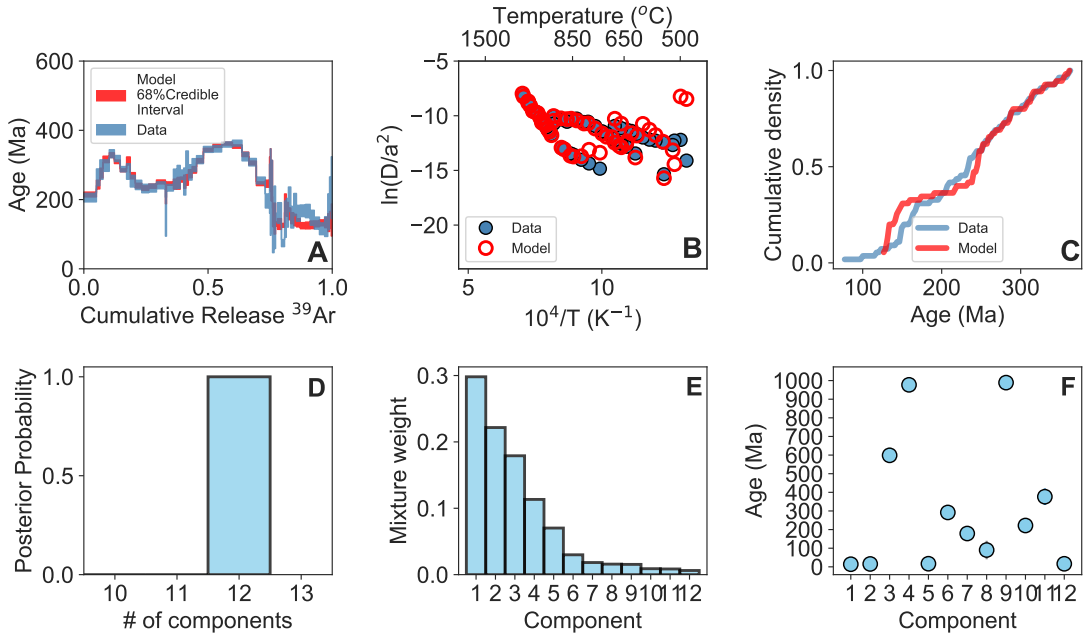

Figure 4.20: Model results for 18-IAF-05-MOS. Panel A shows the posterior model age spectrum 68% confidence interval in red and the observed data set in blue. Panel B shows the observed Arrhenius array (blue circles with black outline) and the modelled Arrhenius array (red open circles). Panel C shows the cumulative density plot of the step age data in blue against the model in red. Panel D is the inferred number of distinct age components in the model, E shows the mixture weight and F the ages of each component.

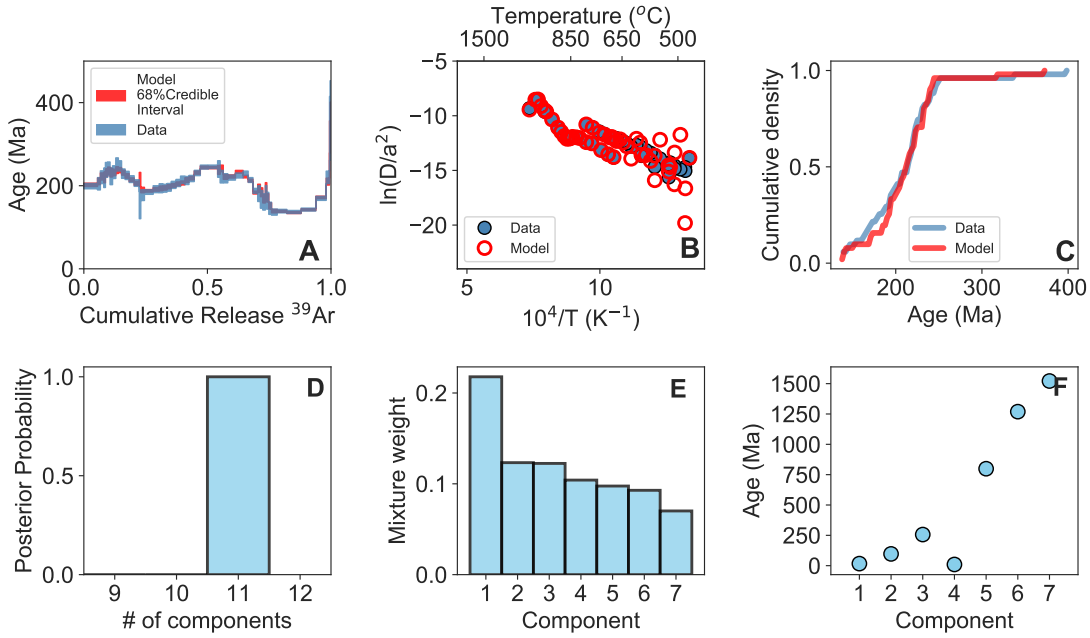

Figure 4.21: Model results for 18-IAF-05-MOS (silt). Panel A shows the posterior model age spectrum 68% confidence interval in red and the observed data set in blue. Panel B shows the observed Arrhenius array (blue circles with black outline) and the modelled Arrhenius array (red open circles). Panel C shows the cumulative density plot of the step age data in blue against the model in red. Panel D is the inferred number of distinct age components in the model, E shows the mixture weight and F the ages of each component.

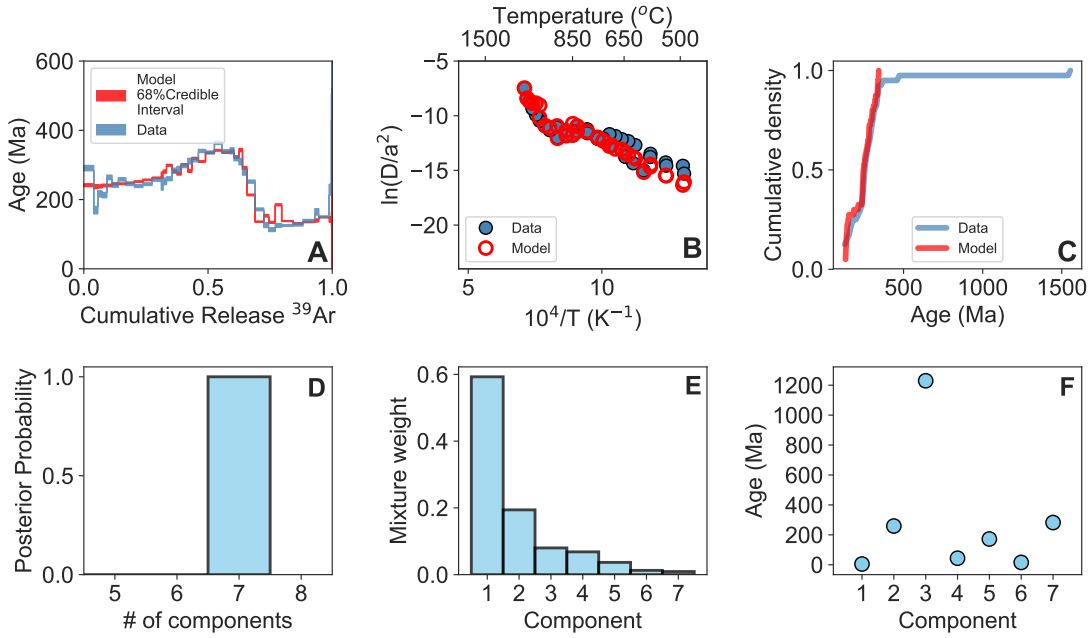

Figure 4.22: Model results for 18-IAF-06-MOS. Panel A shows the posterior model age spectrum 68% confidence interval in red and the observed data set in blue. Panel B shows the observed Arrhenius array (blue circles with black outline) and the modelled Arrhenius array (red open circles). Panel C shows the cumulative density plot of the step age data in blue against the model in red. Panel D is the inferred number of distinct age components in the model, E shows the mixture weight and F the ages of each component.

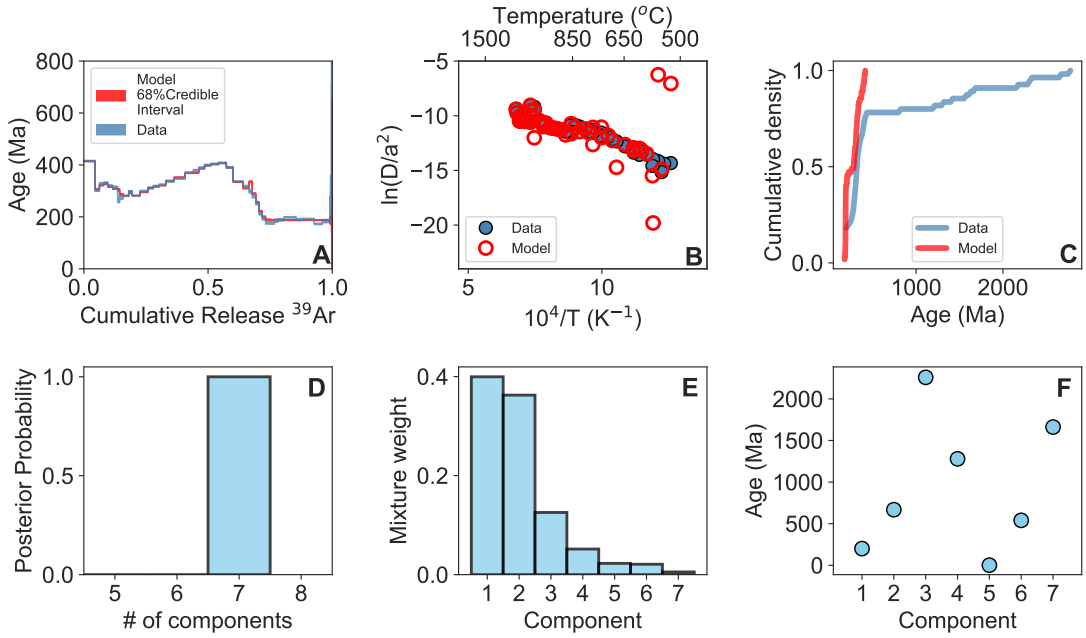

Figure 4.23: Model results for 18-IAF-06-MOS (silt). Panel A shows the posterior model age spectrum 68% confidence interval in red and the observed data set in blue. Panel B shows the observed Arrhenius array (blue circles with black outline) and the modelled Arrhenius array (red rings). Panel C shows the cumulative density plot of the step age data in blue against the model in red. Panel D is the inferred number of distinct age components in the model, E shows the mixture weight and F the ages of each component.

Table 4.2 shows the results for the four Moses Coulee sediments. Similar to the Ephrata Fan outputs all samples have age components corresponding to the CRBs (∼16 Ma), glacial Lake Columbia (∼65 - 252 Ma), and glacial Lake Missoula (∼1000 - 1600 Ma). Further similar to Ephrata Fan I see subtle differences between the age components for each of these age ranges.

Sample	# of Components	Component	Age ± 2σ
18-IAF-05-MOS	8	1	16 ± 5
		2	90 ± 50
		3	178 ± 30
		4	221 ± 26
		5	291 ± 22
		6	376 ± 44
		7	598 ± 40
		8	983 ± 32
18-IAF-05-MOS (silt)	6	1	13 ± 5
		2	91 ± 31
		3	256 ± 34
		4	797 ± 41
		5	1269 ± 40
		6	1522 ± 39
18-IAF-06-MOS	7	1	5 ± 8
		2	16 ± 4
		3	44 ± 6
		4	172 ± 10
		5	259 ± 10
		6	282 ± 13
		7	1230 ± 30
18-IAF-06-MOS (silt)	7	1	15 ± 3
		2	187 ± 4
		3	540 ± 5
		4	668 ± 11
		5	1279 ± 14
		6	1662 ± 15
		7	2259 ± 20

Table 4.2: Summary of the model inferences for the Moses Coulee sediments

4.9 Discussion

4.9.1 Provenance of the Moses Coulee and Ephrata Fan sediments

My approach to interrogate the sediment sources of the Moses Coulee and Ephrata Fan using $^{40}Ar/^{39}Ar$ analyses of bulk sediment has produced robust data that I am able to use to establish where the flood sediments in the Moses Coulee Great Bar and Ephrata Fan are derived from (Figure 4.24). The data from both sites require that material was sourced from glacial Lake Missoula, n.b., Mesoproterozoic age components were present at both sites and these are a distinctive aged sediment associated with the glacial Lake Missoula region. Another common age component, although of variable weight percentage in the sediments, is of Mesozoic age (∼252 - 65 Ma). This age range is dominantly associated with the bedrock of glacial Lake Columbia and confirms the observation of Atwater (1986) that at my study sites there are sediments from flood events interbedded with glacial Lake Columbia sediments. A final age component (ca. 16 Ma) that is common to all mixtures is, as expected, the age range of the Columbia River basalts (Kasbohm & Schoene (2018)). This particular result, owing to the sites being located within the Columia River Basalt province was a modified age prior for the modelling associated with these samples (Figure 4.16). A final age component that I infer to be sourced from material eroded en-route as the flood waters travelled down the regional topography is a Precambrian age component that is associated with the Columbia river (Figure 4.3), a known route for movement of the flood waters to the west of glacial Lake Columbia (Atwater (1984, 1986), Hanson & Clague (2016)). My data support models (Denlinger & O'Connell (2010), Benito & O'Connor (2003)) that suggest during periods of climate warming that induced retreat of the Cordileran Ice Sheet, glacial Lake Missoula breached. The flood waters then flowed into glacial Lake Columbia, flooded the lake before flood waters spilled out and travelled across the basalt plains of the Columbia Plateau. Depositing flood materials at both the Moses Coulee giant Bar and Ephrata Fan sites as the water lost energy on its journey west to the Pacific.

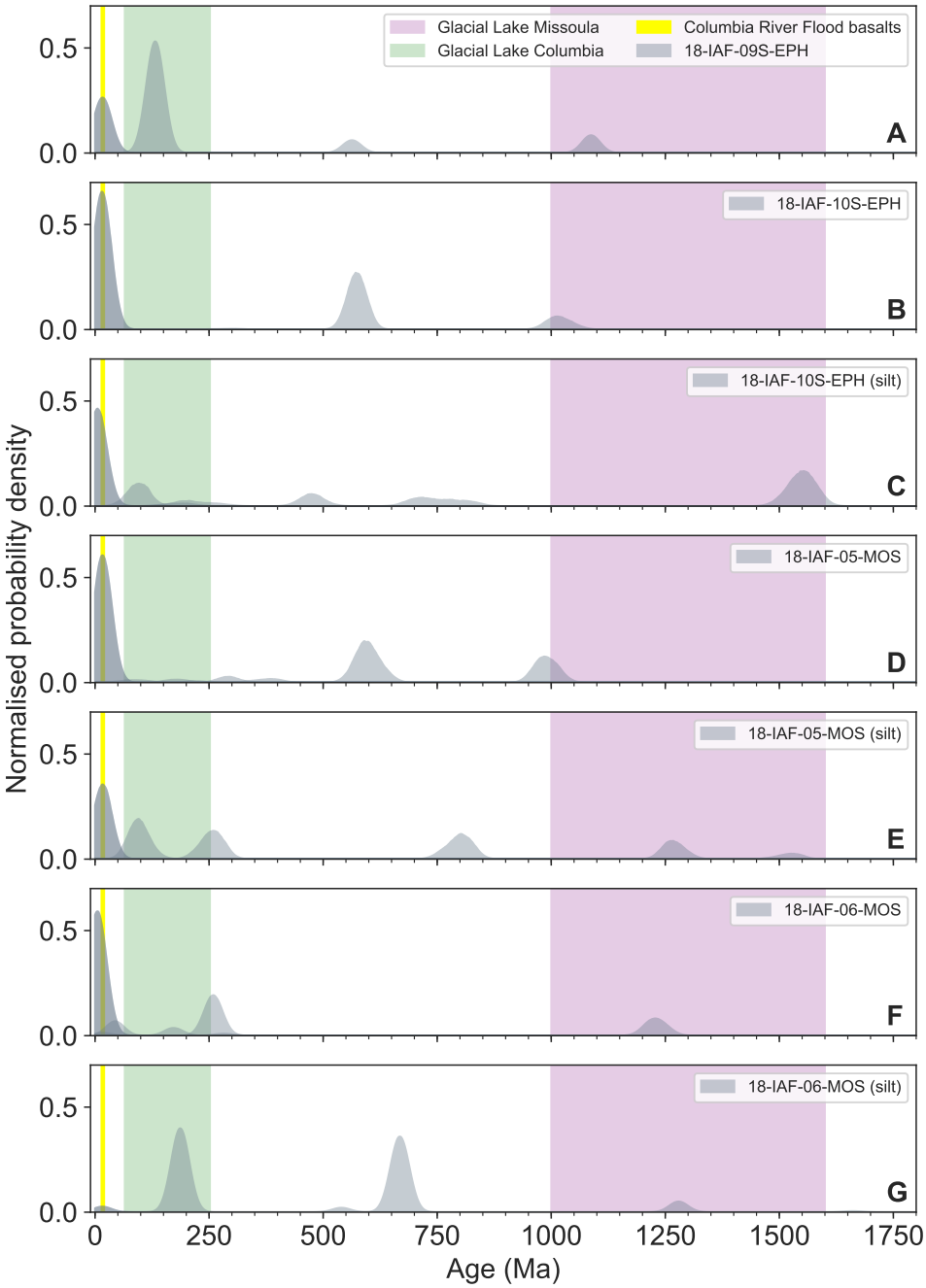

Figure 4.24: Figure showing the model output of all Ephrata Fan (A-C) and Moses Coulee Samples (D-G) Shaded regions of the graph show the most age range of the likely bedrock sources. Shaded blue regions show the age range of glacial Lake Missoula which is dominantly Mesoproterozoic. The yellow shaded region shows the age range of glacial Lake Columbia which is dominantly Mesozoic and the green region shows the age of the Columbia River flood basalts ca. 16 Ma (Kasbohm & Schoene (2018)). Age components are shown in grey and data sets of each sediment is shown in lighted shaded color shown in the legend of each panel.

4.9.2 Glacial megafloods of the Pacific NorthWest

The results of the provenance study show that the sources of both the Ephrata Fan and Moses Coulee flood sediments are the same with multiple age components indistinguishable at the level of uncertainty attained by my modelling approach. Given that data from both sites require Glacial Lake Missoula as a source, the data have major implications for the mechanics of the Pacific northwest megafloods.

A number of scenarios for the flooding of Moses Coulee exist in the literature; (1) Moses Coulee formed prior to the Grand Coulee (Figure 4.25 panel A; Larsen & Lamb (2016)) and/or; (2) Glacial Lake Missoula spilled into glacial Lake Columbia to the extent that water spilled into the Foster Coulee, which blocked from natural drainage pathways, would have entered Moses Coulee (Figure 4.25 panel B; Waitt (2016)); or (3) the floods were more voluminous than previously thought with flood waters flowing directly into the Grand Coulee and into Moses Coulee (Figure 4.25 panel C; Komatsu et al. (2000), Balbas et al. (2017)).

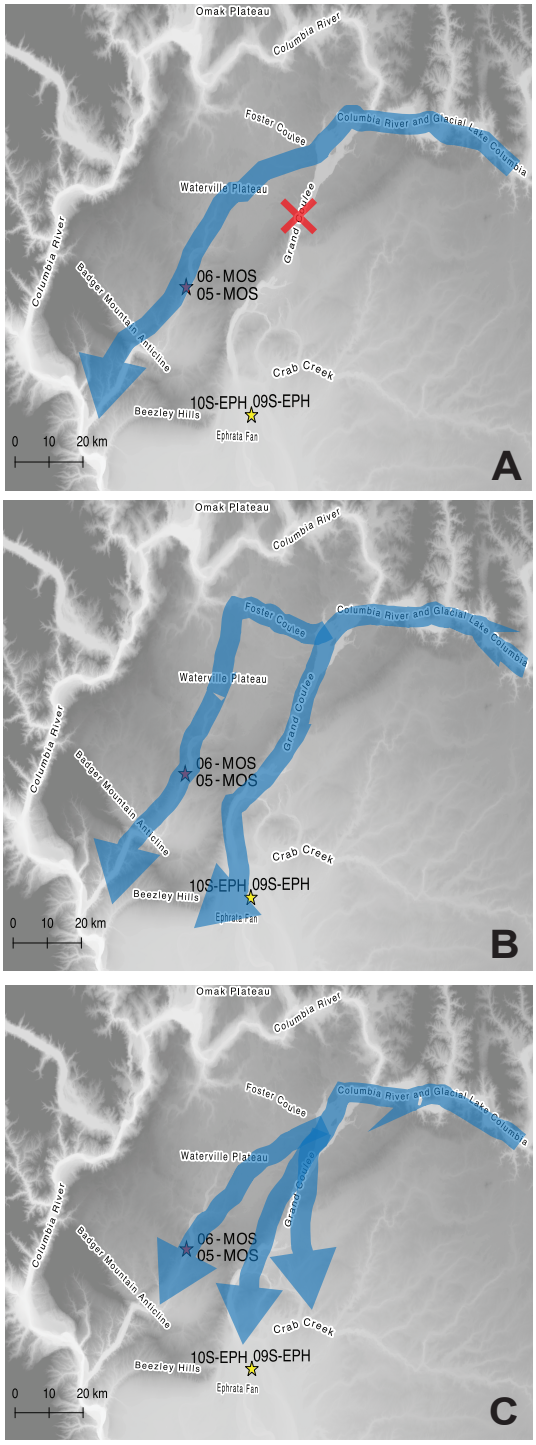

Figure 4.25: Potential flood pathways fulfilling the requirement that glacial Lake Missoula is a source of both Ephrata Fan and Moses Coulee flood sediments. (A) Moses Coulee formed prior to Grand Coulee which was formed in later flood episodes. (B) Glacial Lake Missoula flooded into Foster Coulee which drained across the Waterville Plateau and into Moses Coulle. (C) The flood waters were so great they flooded over the Grand Coulee and into the Moses Coulee.

My data and model outputs do not negate any of the scenarios shown above for the

glacial Megafloods of the Pacific Northwest. The model and data do require a glacial Lake Missoula source however, inferences do not dismiss the possibility of involvement of subglacial reservoirs (e.g., Shaw et al. (1999), Lesemann & Brennand (2009). Conversely the model output may require other freshwater source such as subglacial reservoirs to swell floodwaters to reach Moses Coulee. A possible inference such as this may reconcile the observations with the modelling inferences of Komatsu et al. (2000), Miyamoto et al. (2006, 2007) who all infer that the erosion of the Channeled Scablands requires more freshwater than just glacial Lake Missoula.

4.9.3 Broader implications for bulk sediment provenance studies

The model presented here has the potential to extract key provenance information from $^{40}Ar/^{39}Ar$ analyses of bulk sediments. Fitting both the age spectrum and Arrhenius array of incrementally heated bulk sediment has produced robust provenance information that considers all K-bearing mineral components within a sediment. As such, it produces an integrated provenance signal. Such information my be lost by adopting a conventional dating program that targets single crystals (e.g., muscovite) from more coarse grain size sediments (e.g., Gemignani et al. (2019)). Some source rocks, for example, may not contain the required mineral phase or the crystal size maybe below the selection limit of the technique utilised. In terms of application, this technique has the potential to be used to recover provenance information from fine-grained archives in a wide range of depositional settings that require identification of source changes through time. This method will be particularly useful in places which are dominated by silt and clay-sized sediment such as the Indus and Bengal Fans (Copeland & Harrison (1990), Najman et al. (2019), Rahman & Faupl (2003)) as well as fine grained sediment archives associated with retreat and advance of the Antarctic Ice Sheet. It could also be used on deep sea sediment to trace to track the contributions of continental margins as shown by, VanLaningham et al. (2006), but it would require less assumptions to be made concerning mineral components and not the requirement to conduct complimentary Nd-isotope studies.

4.10 Conclusion

The analysis of bulk sediment by $^{40}Ar/^{39}Ar$ incremental heating and subsequent modelling using a nonparametric Bayesian model has demonstrated robust provenance information can be recovered from real-world geological settings. The model fits the major features of both age spectrum and Arrhenius array datasets to infer the number of different components within a bulk sediment as well as their ages. The age components inferred in the Moses Coulee samples require that glacial Lake Missoula is a floodwater source. The ability of my model to infer ages from bulk sediment mixtures is a robust finding that extends the applicability of the $^{40}Ar/^{39}Ar$ technique to geological settings where the sample is fine-grained and potentially derived from multiple source rocks of various cooling ages. This could be used for any location where fine-grained sediments dominate both in terrestrial and extraterrestrial settings.

Chapter 5

Production of ^{40}Ar by an overlooked decay mode of ^{40}K with implications for K-Ar geochronology

5.1 Introduction

In this Chapter I reassess the K decay constant, specifically with regards to an unverified decay mode from ^{40}K to the ground state of ^{40}Ar. The decay mode is included in a convention for the decay constants by Steiger & Jäger (1977) but has subsequently been questioned by Min et al. (2000) due to the lack of experimental evidence. Here I theoretically calculate the decay mode strength and discuss the implication for ^{40}Ar/^{39}Ar and K/Ar geochronology by its inclusion.

5.2 ^{40}K decay

^{40}K is a naturally occurring radioisotope with atomic abundance of 0.0117% (Garner et al. (1975)). ^{40}K undergoes a branched decay to ^{40}Ar and ^{40}Ca with a total half-life of ca. 1.3 Ga, and is the basis of the K-Ca and the K-Ar geochronometers (Aldrich & Nier (1948), Wasserburg & Hayden (1955), Gopalan & Kumar (2008)). The K-Ar system is most often exploited using the variant ^{40}Ar/^{39}Ar method, wherein some of the ^{39}K in the sample, is transmuted to ^{39}Ar by irradiation with fast neutrons, thereby allowing both the parent and the daughter nuclides to be measured as isotopes of Ar

(Merrihue & Turner (1966)). The latter is widely used to date geological events that span Earth history, from volcanic eruptions recorded in historical texts (e.g., Preece et al. (2018), Renne et al. (1997)), to the earliest events in the solar system (e.g., Renne (2000)).

Advances in analytical precision have forced practitioners in geochronology to address systematic uncertainties that are inherent in all radioisotope dating methods (e.g., uncertainties in the measurement apparatus, prior assumptions made by the observer, or interference from environmental factors), including those that arise from imprecisely known decay rates of ^{40}K. In the geological literature, there have been two influential reviews of measurements of the ^{40}K decay rate. Beckinsale & Gale (1969) provided the first comprehensive review of measured and predicted decay rates, which became the basis of the convention adopted by Steiger & Jäger (1977) used by the geochronological community for the next 20 years. Subsequently, Min et al. (2000) provided a more lengthy, critical review of available specific activity data determined by direct measurements of decay, and updated the derived decay rates for newer physical constants. More recently, the ^{40}K decay parameters were estimated by Renne et al. (2010), and although direct measurements of the ^{40}K decay were incorporated into the estimate, it was heavily weighted to an intercomparison with ^{238}U decay. The decay rate determined by Renne et al. (2010), and the Min et al. (2000) decay rates are the most frequently used in $^{40}Ar/^{39}Ar$ geochronology. These evaluations, along with those from the nuclear physics community, have been summarized recently by Cresswell et al. (2018, 2019).

Despite decades of work and longstanding interest in ^{40}K decay, there remains uncertainty over the nature of the decay scheme. There is consensus that most ^{40}K decays by β^- to ^{40}Ca or by electron capture to ^{40}Ar via an excited state, and that a small amount ($\sim 0.001\%$) of ^{40}K decays to ^{40}Ar via β^+. The early but influential review of ^{40}K decay by Beckinsale & Gale (1969) included these decay modes, and also included a prediction of a second electron capture decay directly to the ground state of ^{40}Ar that would add an additional $\sim$2% to the rate of decay from ^{40}K to ^{40}Ar. Many workers in geochronology (e.g., those who use the Min et al. (2000) decay constants) have ignored this prediction, and some nuclear physics tabulations do not clearly include it (Audi et al. (2003)). The influential review by Min et al. (2000) described this decay mode as "unverified" and having a "questionable" existence.

However, the putative electron capture to ground state decay mode decay constant

is of the same order of magnitude as the uncertainties in the decay rate of ^{40}K to ^{40}Ar, and therefore is a non-negligible and potentially important part of the geochronological system. Here, I describe the theoretical basis of this predicted decay mode and demonstrate the robust nature of the prediction via an analogous calculation of ^{22}Na decay. I describe experiments that could be made to measure this decay mode and also identify observations from nuclear physics experiments that offer evidence for its existence. I conclude that the evidence for this decay mode is strong, and despite the large uncertainty, should be considered in evaluations of the ^{40}K decay rate.

5.3 Historical Overview

At the present time ^{40}K has three experimentally verified decay modes:
1) β^- decay to ^{40}Ca. This mode can be verified by direct measurement of β^- emission.
2) Electron capture to an excited isomer of ^{40}Ar, followed by decay to the ground state of ^{40}Ar accompanied by emission of a 1.46 MeV γ-ray, hereafter denoted EC*. This mode can be verified by direct measurement of the γ emission.
3) β^+ decay from the ground state of ^{40}K to the ground state of ^{40}Ar (Engelkemeir et al. (1962)). This is a very small component of the total decay rate and has been verified by direct measurement of the β^+ emission.

In their paper reporting the measurement of β^+/β^- Engelkemeir et al. (1962), through a private correspondence with Brosi and Kettle, proposed that an electron capture mode that goes directly to ground state also exists, with an electron capture to positron (β^+) ratio of 155. This decay mode is hereafter denoted EC$_{ground}$. This decay mode has not been detected, in part because the measurement is much more difficult than the others. It would contribute about 0.2% to the total decay rate of ^{40}K, or about 2% to the ^{40}Ar branch.

The EC$_{ground}$ decay mode was included in the review by Beckinsale & Gale (1969) and then subsequently in the influential convention published by Steiger & Jäger (1977). This decay mode is also included in the widely used ENSDF and DDEP evaluations (Chen (2017) and Mougeot (2018) respectively). However, evaluations by Endt & Van der Leun (1973, 1978), Audi et al. (2003), Endt (1990) do not explicitly include this decay mode, with Audi et al. (2003) giving a transition intensity which is the combined EC and β^+ intensities. Min et al. (2000) have questioned its validity because there is no experimental verification, and therefore do not include EC$_{ground}$ in their

estimates.

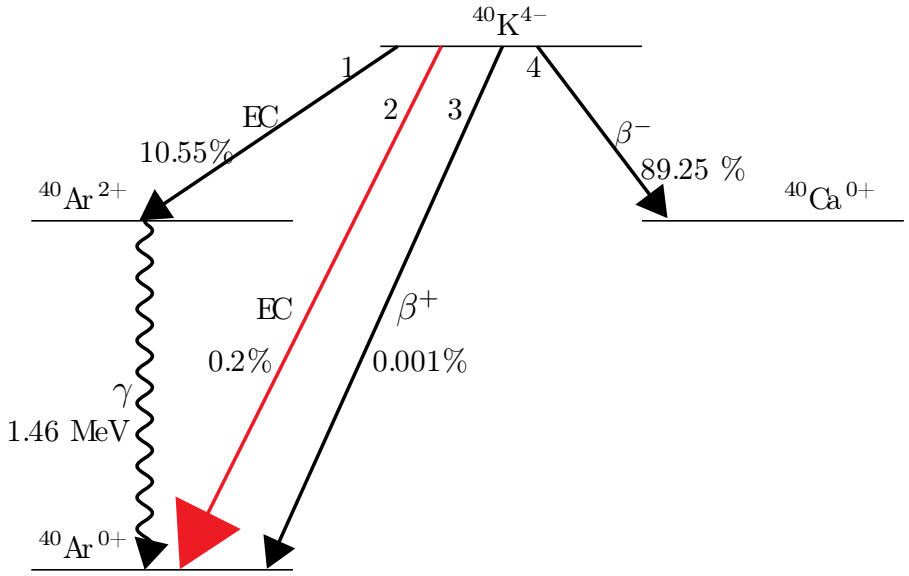

Figure 5.1: Decay scheme of ^{40}K after McDougall & Harrison (1999) and Leutz et al. (1965), where 1 is the electron capture branch to the excited state of ^{40}Ar with γ-ray emission (EC*), 2 is the electron capture direct to the ground state of ^{40}Ar (EC_{ground}), 3 is the positron decay to ground state of ^{40}Ar, and 4 is the beta decay to the ground state of ^{40}Ca. The disputed decay mode, EC_{ground}, is highlighted in red.

5.4 Why there must be an EC_{ground} decay mode

In nuclides that are relatively proton-rich, protons decay to correct this imbalance with two mechanisms. Either, (1) the nucleus can undergo electron capture (EC) wherein an orbital electron is captured by the nucleus, or (2) the nucleus can emit a positron ($\beta+$). Both processes are types of β decay result in the transformation of a proton to a neutron to conserve charge, and they also both emit a neutrino in order to conserve lepton number and energy. These two processes are typically paired: coupled EC-$\beta+$ is the second most abundant decay type on the chart of the nuclides, after β- decay (Audi et al. (2003)). They are linked because they are both processes have the same initial state and final nuclear states.

$\beta+$ decay is always accompanied by EC, but the converse is not always true (Bambynek et al. (1977)). This is because $\beta+$ decay, unlike EC, requires a minimum amount of energy($\sim$1022 keV, equivalent to the combined rest masses of both a positron and an electron) in order to produce the emitted positron and an electron (the latter to

satisfy charge conservation). The energy between initial and final nuclear states is the Q value, which is a function of the difference between the initial and final masses. This energy is shared between the outgoing neutrino, atomic excitation of the daughter system, recoil energy, and nuclear excitation of the daughter system. The energy which dictates if positron emission is possible is denoted Q_{EC}. In the decay of ^{40}K, the EC* branch has an energy difference (Q_{EC}) between the initial and excited isomer state of only 44 keV. In contrast, the energy difference between ^{40}K and the ground state of ^{40}Ar, is 1504.4 keV (Wang et al. (2017)), an energy greater than the combined rest masses of the positron and electron. Therefore, the EC* branch, with an energy difference of only 44 keV, *cannot* be the complement to the β^+ decay and the EC_{ground} *must* exist to provide the β^+ complement. The experimental observation of the β^+ decay mode comes from a single measurement by Engelkemeir et al. (1962). I rely on this measurement to make our argument for the existence the EC_{ground}. It is possible that the positrons observed arise from the pair production of the ∼1460 keV gamma; Engelkemeir et al. (1962) discuss this possibility in their experiment, calculating this as 55-60% of the total positron detection rate. However, positrons produced by this mode of pair production would be monoenergetic at 440 keV, whereas the observed positron energy spectra exceed this value, with a maximum of 491 keV. A reasonable fit is also observed between the measured β^+ energy spectrum and the theoretical 3rd forbidden unique energy spectrum, supporting the argument that these $\beta^+$are from a decay mode rather than arising from pair production.

5.5 Theory and calculation of EC_{ground}/β^+

The ^{40}K decay scheme itself is somewhat unusual because it's EC/β+ branch is the only known third order unique forbidden EC decay (explained below) known in nature. In the decay of ^{40}K, the nuclide can reach a more stable state (^{40}Ca or ^{40}Ar) only by violating selection rules. Decays which violate these selection rules undergo slow 'forbidden' unique transitions giving the long ∼ 1.3 Ga half life of ^{40}K. For ^{40}K, all decays undergo a parity reversal (where parity reversal is the flip of sign in one of the spatial coordinates (x, y, z)) between the initial parent state and final daughter state and so we can define the selection rules as

$$|\Delta - 1|^{st}\text{order unique forbidden decay} \tag{5.1}$$

where $\Delta J = J_i - J_f$, is the change in spin from initial to final state following Krane et al. (1987). For each decay mode of ^{40}K we can characterise it by degree of forbiddenness from the above selection rule. The electron capture to excited state of ^{40}Ar undergoes a spin change of and is classified as a first order unique forbidden decay. The three other decay modes of ^{40}K all undergone a spin change of and are classified as 3^{rd} order unique forbidden decays.

The EC process occurs because the atomic electrons have a finite probability to be in the nucleus with the likelihood of being captured highest for those closest to the nucleus. A theoretical description of emission was first given by Fermi (1934), while the possibility of electron capture which was first recognized by Yukawa & Sakata (1935) and later developed by Bethe and Bloch Bethe & Bacher (1936). Here I use Fermi theory of β^- decay to calculate the EC_{ground}/β^+ in the decay of ^{40}K.

I can use the ratio of orbital electron capture and positron emission to infer the existence of the overlooked decay mode. The ratio is defined as

$$br = \frac{\lambda_{ec}}{\lambda_{\beta^+}} \tag{5.2}$$

where λ_{ec} and λ_{β^+} and are the probability per unit time of electron capture of positron emission. In electron capture, orbital electrons can be captured from any orbital shell of the atom. The total capture-to-positron ratio is therefore the summation of the individual capture ratios from each shell. Following Bambynek et al. (1977), the total electron capture-to-positron ratio is:

$$\frac{\lambda_x}{\lambda_{\beta^+}} = \frac{\sum_x n_x C_x f_x}{f_{\beta^+} C(W)} \tag{5.3}$$

I initially simplify this equation to only consider the innermost K shell, the most dominant shell, and reduce the equation accordingly:

$$\frac{\lambda_k}{\lambda_{\beta^+}} = \frac{\sum_k n_k C_k f_k}{f_{\beta^+} C(W)} \tag{5.4}$$

where λ_K is now the probability of K-shell capture, n_K is the relative occupation number of the K-shell, C_k is similar to the shape factor in β decay, f_{β^+} is the integrated positron spectrum and is the integrated Fermi function in decay, C(W) is the theoretical shape factor for allowed or forbidden transitions, a review of past shape factors for ^{40}K

transitions is provided by Cresswell et al. (2019) and is defined as:

$$f_k = \frac{\pi}{2} q_k^2 \beta_k^2 B_k \tag{5.5}$$

where β_k is the Coulomb amplitude of the wave function, q_k is the momentum of the neutrino particle and B_k is the term for overlap and exchange corrections. is defined as

$$f_\beta^+ = \int_1^{W_0} F(-Z, W) W_p (W_0 - W)^2 dW \tag{5.6}$$

with $W = 1 + E_T/m_e$ the total energy of the positron from its kinetic energy E_T and rest mass, m_e , the momentum of the positron that corresponds with this is given by $p = \sqrt{W^2 - 1}$, and W_0 is the total normalised energy defined by $W_0 = 1 + E_{max}/m_e$, E_{MAX} is the upper limit of the positron energy (equal to the Q value of the decay), and F(-Z,W) is the Fermi function. I follow Bambynek et al. (1977) in the formula for which is given by

$$\frac{C_k}{C(\bar{W})} = [(2L-1)!]^{-1} q_k^{2(L-1)} \left(\sum_{n=1}^{L} \lambda_n p^{2(n-1)} q^{2(L-n)} ((2n-1)![2(L-n)+1]!)^{-1} \right)^{-1}$$

(5.7)

where $L = \Delta J$, and $L = 1$ for $\Delta J = 0$. The parameter λ_K cannot be calculated in a straightforward manner and therefore I follow a typical assumption that $\lambda_K = 1$, this reduces the above expression to

$$\frac{C_k}{C(\bar{W})} = \frac{q_K^6}{p^6 + q^6 + 7p^2q^2(p^2 + q^2)} \tag{5.8}$$

In a given decay the change in charge from initial to the final state can lead to an imperfect overlap of the wavefunctions of these states. Furthermore, given the indistinguishability of electrons, there is the possibility of an exchange effect wherein an electron does not necessarily need to come from the orbital where the vacancy appears. For instance, it is possible that a vacancy may appear in the K-shell but the captured electron from an outer shell then subsequent filled by the inner shell electron (Bahcall

(1962), Bambynek et al. (1977)). I follow Bahcall (1962) in implementing corrections for these effects, resulting in B_K= 0.979. Then using nuclear data given in Bambynek et al. (1977) I estimate an electron capture-to-positron ratio of 148.

First note that this value is in approximate concordance with the private correspondence value in Engelkemeir et al. (1962). However, this is only the capture ratio from the K-shell so I extend our model to a total electron capture ratio from all orbitals following Bosch et al. (1977), here the total electron-capture-to-positron ratio is given by

$$\frac{EC}{\beta^+} = \frac{K}{\beta^+}\left(1 + \frac{L}{K} + \frac{M}{L}\frac{L}{K} + ...\right) \tag{5.9}$$

where the total capture ratio is given as a sum of the separate shell captures. I can further simplify this equation by neglected shells that make a negligible contribution. In the case of ^{40}K I can omit all shell captures except L_1 capture and arrive at the total electron-capture to positron ratio:

$$\frac{EC}{\beta^+} = \frac{K}{\beta^+}\left(1 + \frac{L_1}{K}\right) \tag{5.10}$$

The ratio of each shell capture can be solved with the following equation:

$$\frac{x}{K} = \frac{\beta_x^2 (W_0 - W)^2 B_x}{\beta_K^2 (W_0 - W)^2 B_K} \tag{5.11}$$

where x = L_1 and the other symbols have the same definition as above. I calculate a total electron-capture-to-positron ratio of 164.

To further gauge the order of magnitude of the electron capture decay mode I can perform another calculation of $\frac{EC}{\beta^+}$ following Fireman (1949). The simplified form of the calculating $\frac{EC}{\beta^+}$ is dependent only on the Q value (the difference between the initial and final state energies). This is given by:

$$\frac{\lambda_{EC}}{\lambda_{\beta^+}} = \frac{(\eta + 2)^8}{0.450\eta^{6.5}} \frac{1}{0.0676 + 1.25\eta + 8.48\eta^2 + 12.5\eta^3 + 1.74\eta^4 + 0.079\eta^6} \tag{5.12}$$

where $\eta = \frac{Q}{m_e}$ - 2. I calculate an $\frac{EC}{\beta^+}$ of 272 using this method of Fireman (1949) and the updated Q-value of Wang et al. (2017). Note that despite discrepancies in these values for each method of evaluation, they are of the same order of magnitude. The differences in the values in these evaluations only heighten the need for experimental

verification for this decay mode.

5.6 Comparison with other evaluations

Other theoretical evaluations of EC_{ground}/β^+ for ^{40}K exist in the literature (Figure 5.2). Pradler et al. (2013) and Mougeot (2018) report ratios of 150 and 212 ± 0.15, respectively (uncertainties are reported where they have been estimated). These workers use broadly similar methods as us. Mougeot (2018) uses higher order corrections for both exchange and overlap and accounts for the dependence of $_K$, that I set equal to 1 in Eq5.9, on the energy of the decay. Pradler et al. (2013) use the Fermi method and data from Bambynek et al. (1977) but only perform the calculation for K-shell electrons, resulting in a slightly different calculated value than I report. Notably, all estimated values are of the same order of magnitude, similar to the ratio 155 reported in Engelkemeir et al. (1962), and our calculated value of 164. Currently, the most commonly-used EC_{ground}/β^+ value is calculated via the LogFT program, a program used in nuclear data evaluations (ENSDF Collaboration, LOGFT). However, the program is capable of only calculating first and second unique forbidden decay ratios, so the EC_{ground}/β^+ value from LogFT of 200 ± 100 is an extrapolation, with the assumption that the increase in the ratio from second to third order is by the same factor as the increase from first to second order. Finally, Chen (2017) evaluates the ^{40}K decay data and reports a EC_{ground}/β^+ value of 45.2 ± 1.4 without elaboration.

The variability between the modern estimates are driven primarily by choices when making the approximations necessary for these calculations to be tractable. Uncertainties on individual estimates which could be derived by propagating the uncertainties in the underlying experimental data are small and where uncertainties are estimated, are generally not explicated.

The value calculated by Mougeot (2018) of 212 ± 0.15 is currently the best estimate of the ^{40}K EC_{ground}/β^+. It is slightly higher than two other recent estimates, our value of 164 or that of Pradler et al. (2013) of 150. Given a broad consensus in calculated EC_{ground}/β^+ over several decades and via a variety of methods, it appears highly likely that it falls in the range 150-212 (Fig. 5.2).

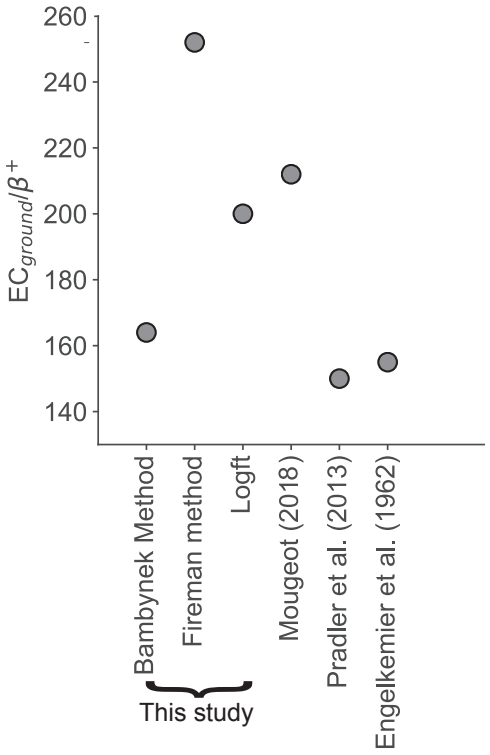

Figure 5.2: Comparison of theoretically calculated (EC_{ground}/β^+) ratios of ^{40}K in this study using three methods; (1) Bambynek Method (Bambynek et al. (1977))), (2) Fireman method (Fireman (1949)), and (3) Logft (LogFT, 2001). The value of Chen (2017) is not included in the figure as it is an extreme outlier and does not provide comment as to method used by the author to reach this value. Our calculated ratios are compared to previous evaluations in the literature (Engelkemeir et al. (1962), Pradler et al. (2013), Mougeot (2018)). Uncertainties in these valies are either intractable or in the case of Mougeot (2018) too small to plot. Note the consistency in the estimated ratio from all methods.

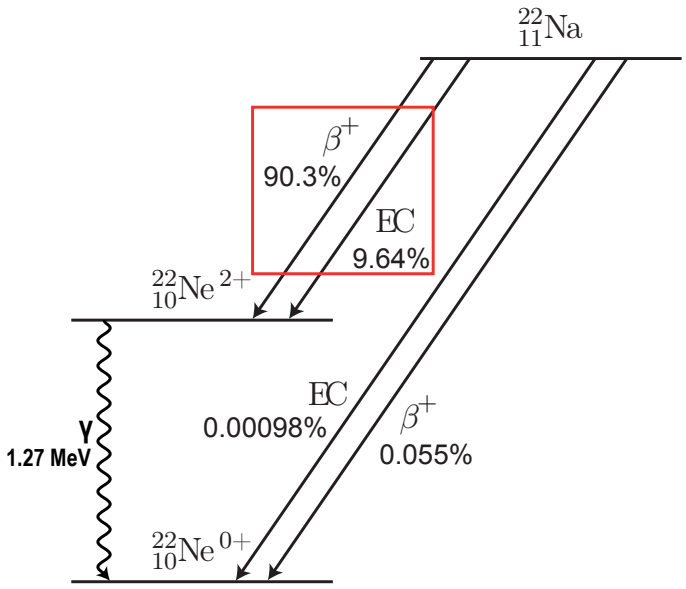

Figure 5.3: Decay scheme of ^{20}Na after Bé et al. (2006) and Leutz et al. (1965), where the calculated (EC/β^+) ratio is boxed in red, which I compare to experimentally measured values.

5.7 ^{22}Na

5.7.1 Comparison with ^{22}Na

To test the validity of our ^{40}K EC_{ground}/β^+ estimate, I use the same calculations to estimate the experimentally-constrained (EC/β^+)* value for ^{22}Na decay. ^{22}Na is radionuclide with a half-life of ~2.6 years, it occurs in nature as a low-abundance cosmogenic nuclide produced by spallation of ^{40}Ar and is also produced synthetically by proton irradiation for use in positron emission tomography. Like ^{40}K, it decays by electron capture and positron emission. The main EC-β^+ pair for ^{22}Na decays initially to the excited state of ^{22}Ne, followed by a 1.27 MeV γ emission (Figure 5.3; Bé et al. (2010)). This pair has a (EC/β^+)* of approximately 0.1 and accounts for >99.9% of the total decay. A second EC-β^+ pair decays directly to the ground state of ^{22}Na with an (EC/β^+)ground of ~0.02, but is a minor component. Here, I calculate the (EC/β^+)* for the main branch. Unlike ^{40}K, the dominant decay of ^{22}Na is the β^+ decay mode. This is due to the greater difference in energy between the initial and final states, as positron decay will have a greater possibility of occurring in decays with a greater mass differences between initial and final states (Emery (1975)). ^{22}Na is not a perfect analogue, however it is probably the best choice that has both a tractable theoretical calculation and a wealth of experimental data which can be used readily for verification.

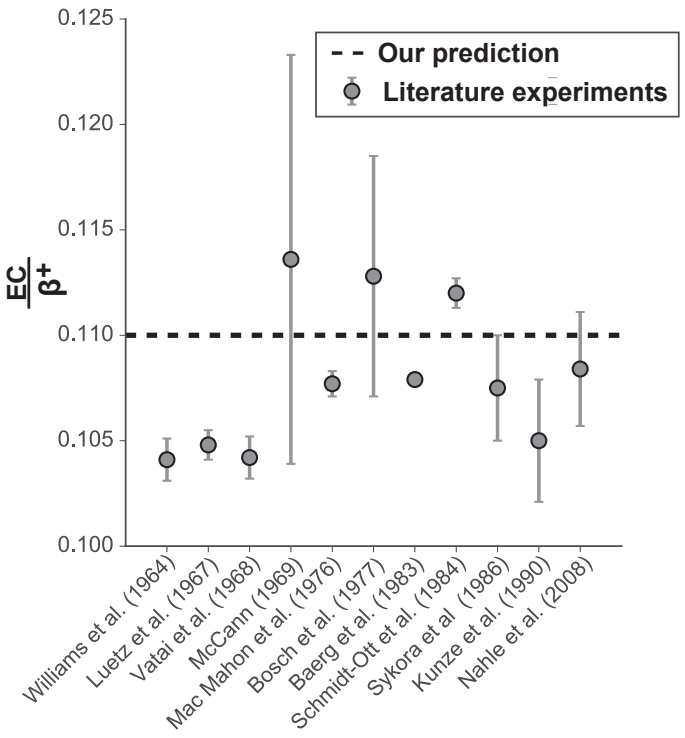

Figure 5.4: Comparison of experimentally measured (EC/β^+)* ratios of ^{22}Na (grey circles) adapted from Kunze et al. (1990) with our theoretically determined value (black solid line). Note the concordance of the theoretical and experimental determinations. The uncertainty in the Baerg (1983) determination is smaller than the symbol.

Unlike ^{40}K, there are numerous measurements of the electron capture to positron ratio for decay to the excited state of 22Na (Figure 5.4; Kreger (1954), Vatai et al. (1968), Williams (1964), McCann & Smith (1969), MacMahon & Baerg (1976), Bosch et al. (1977), Baerg (1983), Sỳkora & Povinec (1986), Kunze et al. (1990), Nähle et al. (2008)). Measurement of (EC/β^+)* for ^{22}Na is accomplished by measurement of both of the gammas (which come from both the EC* and the β^+*) and the x-rays (which only come from the EC branch). Relative to the ^{40}K EC$_{ground}/\beta^+$, the ^{22}Na (EC/β^+)* is a more straightforward measurement because of the higher activity (meaning higher count rate) and the higher energy of the x-ray emitted from the Auger electron, which an electron from the same atom that is emitted as a vacancy of an inner shell is filled. In a decay to the excited state of ^{22}Ne, the de-excitation 1.28 MeV γ will be associated with both electron capture and positron decay. However, those measured 1.28 MeV γ that are not accompanied by two 0.511 MeV annihilation photon's can be used to distinguish between both processes. I use the experimental measurements to verify our calculations described above for ^{40}K.

Following a similar calculation using the Fermi method, our preferred method, to that used for our proposed estimate of the ^{40}K EC$_{ground}/\beta^+$, I estimate an (EC/β^+)*

of approximately 0.11. This is within the range of measured values of 0.105-0.115 (Fig. 5.4), suggesting that our calculation strategy of the the ^{40}K EC$_{ground}/\beta^+$ is accurate, and lends further confidence to the existence of the current unmeasured ^{40}K electron capture to ground state decay.

5.8 Experimental verification of EC$_{ground}$ decay mode

In both β^- and β^+ decay, an electron or positron is emitted which allows for direct detection and verification of the decay process. In contrast, electron capture cannot be detected directly. Methods to experimentally verify electron capture rely on indirect processes associated with the rearrangement of the atom following the capture of the orbital electron. Once the electron is captured the atom will rearrange itself to fill the vacancy, resulting in the emission of a characteristic x-ray or Auger electron with an energy defined by the binding energy of the shell vacancy of the daughter nucleus. In the case of ^{40}K, verification of the EC$_{ground}$ decay can be achieved by measuring the characteristic x-rays (Di Stefano et al. (2020)). The orbital electron with the highest probability of capture is from the K-shell; if this electron is captured, the resulting vacancy in the K-shell may be filled by an electron from any of the other shells (e.g., L, M, ...), and a characteristic x-ray is emitted with an energy dependent on the particular shell that fills the vacancy. It is not necessary, however, that all K-capture processes result in the emission of an x-ray. By the Auger effect, a radiationless transfer may occur wherein the K-shell vacancy is replaced by two vacancies in the next outer shell, L, or one in the next two shells; L and M. The energies of the Auger electrons emitted in these transitions depend upon the ^{40}Ar product resulting from K-capture. Both electron capture decays to the ground and excited state of ^{40}Ar ($^{40}Ar^{2+}$) result in the same electron configuration and x-ray emissions. Di Stefano et al. (2020) suggested tagging x-rays with the de-excitation γ associated with electron capture to $^{40}Ar^{2+}$, which has a lifetime on the order of 10-12 $\times 10^{-9}$s (Di Stefano et al. (2020)). Measuring these tagged x-rays experimentally will be challenging since it requires identifying a low probability decay mode with x-ray signals present against a high background from the $^{40}Ar^{2+}$ state. Further, as illustrated in Di Stefano et al. (2020), it is expected that 50 EC* decays occur for every 1 EC$_{ground}$ decay; therefore a detector efficiency of $\geq 98\%$ is required to make sure that there is fewer than one mis-tagged EC* decay for each true EC$_{ground}$ decay. The experiment therefore requires an x-ray spectrometer able to

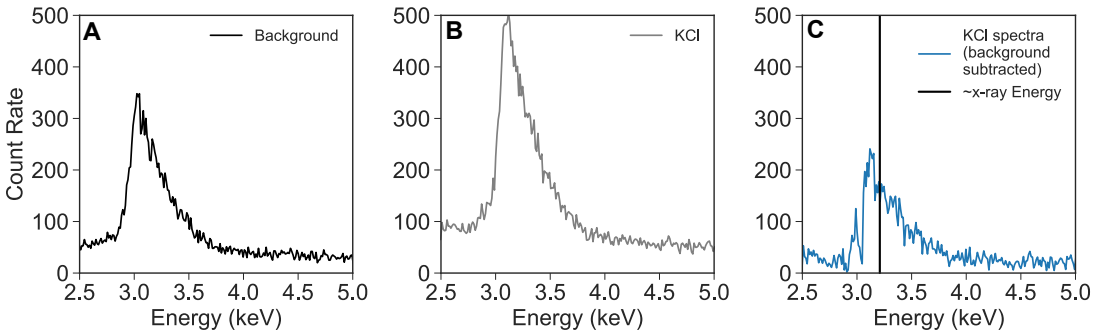

Figure 5.5: Spectra measured for the laboratory background (**A**), KCl spectra (**B**), and KCl with background subtracted (**C**).The potassium source is a potassium bearing KCl salt 600mg pressed to a 2" disc with an approximate 0.5cm thickness. Measurements for all spectra were over 250000s. The detector resolution in the 3keV region is approximately 50eV FWHM.

resolve the Ar-K x-ray from other x-rays in the background, and accurately account for the x-ray–γ-ray coincidence efficiency ($\geq$ 98%) to quantify x-ray emission rates in excess of those from the $^{40}Ar^{2+}$ state. Given the complexity involved in this experiment, a pilot study was conducted at SUERC to measure characteristic x-rays from a KCl source. The experiment was not successful because the detector was not able to resolve the Ar-K x-ray sufficiently but demonstrates the potential of this method to detect the x-rays, given a sufficiently high-resolution detector. Full details are provided in the next section

5.8.1 X-ray counting experiments

I attempted a pilot study to test whether the characteristic $\sim$ 3.2 keV x-ray emitted during both ground state and excited state electron capture of ^{40}Ar could be detected. In our experimental set-up, I used a 50 mm by 5 mm KCl disc as a ^{40}K source and a thin Be-window Ge detector (Ortec LoAx). The source and detector were housed in Pb brick containment to limit x-rays from the surrounding environment. Counts were taken over $\sim$ 250000 s (approximately 2.9 days) to test the possibility of detection. I show example spectra of the background, KCl, and KCl with background subtracted below (Figure 5.5, A - C).

The lower limit of x-ray energy detection is approximately 3 keV, resulting in an exponential noise pile across the energy region I are attempting to observe (Figure S1 A). Unfortunately, this noise pile-up dominates the region of interest during measurement (Figure 5.5B). The Ar-K x-ray is detected (Figure 5.5C), but is difficult to resolve from the noise pile up. Note that the characteristic x-ray does not appear at exactly

3.209 keV due to what I believe to be a non-linearity in the relationship between energy and channel number in the detector. I use this simple experimental set up to show that there is potential to detect the ^{40}K characteristic x-rays can be detected in our simple experimental configuration. I acknowledge that this set up cannot be used to distinguish between the x-rays of each electron capture decay mode of the ^{40}K decay scheme but use this set up as a pilot study to test the possibility to observe these x-rays and from this, make improvements and additions to move toward the experimental verification of the electron capture to ground state decay mode.

5.8.2 Conclusions and recommendations from SUERC counting experiment

The pilot study here shows the potential of determining the existence of the electron capture to ground state decay through the detection of characteristic $\sim$ keV x-rays associated with the relaxation of the daughter ^{40}Ar nucleus after decay. However, I acknowledge that this experimental set up cannot distinguish between x-rays that are from the electron capture to excited state and x-rays from the electron capture to ground state that is required for verification. The absolute verification requires the detection of excess x-rays that are not coincident with the -ray from the de-excitation of $^{40}Ar^{2+}$ to $^{40}Ar^{0+}$. Further, as illustrated in Di Stefano et al. (2020), it is expected that 50 electron capture to excited state decays (EC*) occur for every 1 electron capture to ground state decay (EC_{ground}); therefore, a detector efficiency of $\geq$ 98% is required to make sure that there is fewer than one mis-tagged EC* decay for each true EC_{ground} decay. The experiment therefore requires an x-ray spectrometer able to resolve the Ar-K x-ray from other x-rays in the background, and accurately account for the x-ray–-ray coincidence efficiency ($\geq$ 98%) to quantify x-ray emission rates in excess of those from the $^{40}Ar^{2+}$ state. In our experiment, a simple KCl source is used pressed to a thin disc to aid in the minimisation of self-absorption. However, this still results in a low count rate at the x-ray energy. Therefore, I recommend the use of a source enriched in ^{40}K, and a thinner sample to limit x-ray self-absorption. I also recommend the use of a NaI detector, with a detector efficiency of 98%, which offers both greater resolution at low energies and a much lower detection limit. Furthermore, counting over a very long period, on the order of months, is required to accumulate enough measurements to yield a precise result. The low activity of the potassium may also require long counting experiments in extremely low background environments, such as

the Boulby Dark Matter Laboratory.

5.9 Relevance for geochronology

Geochronology with the K-Ar system requires either both the branching ratio and the total decay constant, or in the case of an $^{40}Ar/^{39}Ar$ age wherein the fluence monitor age is constrained independently of its K-Ar systematics (Merrihue & Turner (1966)), only the total decay constant. Using lower and upper bound values of EC_{ground}/β^+ corresponding to 150 and 212 as described above, the decay constants calculated by Min et al. (2000) ($\lambda_{EC*} = 0.580 \pm 0.014 \times 10^{-10}$ a^{-1} and $\lambda_T = 5.463 \pm 0.107 \times 10^{-10}$ a^{-1}), and the β^+/β^- from Engelkemeir et al. (1962) ($1.12 \pm 0.14 \times 10^{-5}$), I calculate a β^+ decay constant of $5.47 \pm 0.69 \times 10^{-15}$ a^{-1}, and a range of EC_{ground} decay constants of 8.2 - 11.6 $\times 10^{-13}$ a^{-1}. Combining these values with the Min et al. (2000) quantities yields a new partial decay constant for ^{40}K to ^{40}Ar ($\lambda_{^{40}Ar}$) that ranges from 0.588-0.592 $\times 10^{-10}$ a^{-1} and total decay constant (λ_T) that ranges from 5.471-5.475 $\times 10^{-10}$ a^{-1}. These ranges are within the uncertainties calculated by Min et al. (2000) for decay constants that do not include the EC_{ground} decay mode. Existing and modified constraints on the decay modes are given in Table 5.1. Our preferred decay constants are those calculated with the $EC_{ground}/\beta^+ = 212$ from Mougeot (2018).

Parameter	Value ± 2σ	Relative Unc (%)	References
Previous values			
λ_{EC*}	$5.8 \pm 0.014^{1} \times 10^{-10}$ a^{-1}	2.4	Min et al. (2000)
λ_T	$5.463 \pm 0.107 \times 10^{-10}$ a^{-1}	2.0	Min et al. (2000)
$\lambda\beta^+$	$5.47 \pm 0.69 \times 10^{-15}$ a^{-1}	13	Engelkemeir et al. (1962)
Modified values with lower bound $EC_{ground}/\beta^+ = 150$			
$\lambda_{EC_{ground}}$	$8.2 \pm 1^{1} \times 10^{-13}$ a^{-1}	13	This work
$\lambda_{^{40}Ar}$	$0.588 \pm 0.014 \times 10^{-10}$ a^{-1}	2.4	This work
λ_T	$5.471 \pm 0.107 \times 10^{-10}$ a^{-1}	2.0	This work
Modified values with upper bound $EC_{ground}/\beta^+ = 212$			
$\lambda_{EC_{ground}}$	$11.6 \pm 1.5^{1} \times 10^{-13}$ a^{-1}	13	This work
$\lambda_{^{40}Ar}$	$0.592 \pm 0.014 \times 10^{-10}$ a^{-1}	2.4	This work
λ_T	$5.475 \pm 0.107 \times 10^{-10}$ a^{-1}	2.0	This work

Table 5.1: Evaluations of decay mode branches and total decay constant used in age determination. $\lambda_{^{40}Ar}$ is the partial decay constant for the ^{40}Ar branch, including both the EC* and EC_{ground} components. Uncertainties from the β^+/β^- and EC_{ground}/β^+ do not substantially change the uncertainties in $\lambda_{^{40}Ar}$ or λ_TT.

Consequently, K-Ar (and ^{40}Ar/^{39}Ar) ages calculated with these new decay constants will be younger than those calculated using the Min et al. (2000) decay constants. K-Ar dates are most sensitive to shifts in the decay constant because they incorporate the branching ratio, which is more strongly affected than the total ^{40}K decay constant. K-Ar ages will decrease by ∼ 1.4-2.0 % at 1 Ma, ∼ 1.1-1.5 % at 1 Ga, and ∼0.6-0.8 % at 4.5 Ga (Figure 5.6). Ages determined using the ^{40}Ar/^{39}Ar method, for which the fluence monitor age is independently constrained (e.g., Kuiper et al. (2008), Rivera et al. (2011)), are much less sensitive to the change in decay constant. Using equation 5.5 from Renne et al. (1998), and assuming calibration to a monitor with an age of 28.2 Ma, ages 28 Ma increase only slightly, by 0.002%. There is no age difference at 28.2 Ma, the fluence monitor age. Ages then decrease for ages 28.2 Ma, with ages decreased by 0.07-0.10 % at 2.5 Ga, and by 0.09-0.13 % at 4.5 Ga (Figure 5.6).

The age of fluence monitors such as the Fish Canyon tuff sanidine (e.g., Morgan et al. (2014)) determined by intercomparison with astronomically tuned ages of ash beds (Kuiper et al. (2008), Rivera et al. (2011)) is also sensitive to revision of decay

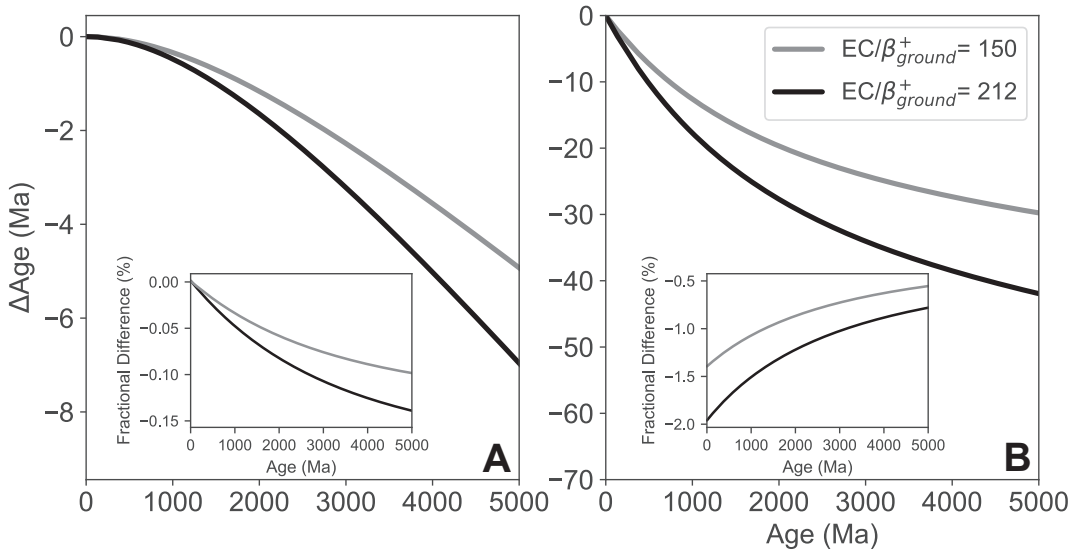

Figure 5.6: Change in age, Δage, is the age of a given sample with the decay mode to ground state included, subtracted from the age with the decay mode to ground state omitted. Panel A shows the change in age using the $^{40}Ar/^{39}Ar$ equation with independently calibrated standards using both the lower bound ($EC_{ground}/\beta^+ = 150$; grey) and upper bound ($EC_{ground}/\beta^+ = 212$; black). Panel B shows the change in age using the K-Ar equation using both the lower bound ($EC_{ground}/\beta^+ = 150$; grey) and upper bound ($EC_{ground}/\beta^+ = 212$; black). Inset figures in each panel show the fractional differences in age by the inclusion of both the upper and lower bound EC_{ground}/β^+ value. The larger difference in ages for the K-Ar system is due to the dependence on both the total decay constant and branching ratio.

constants. Using the data published by Kuiper et al. (2008), and incorporating an EC_{ground} decay mode, I calculate a new age for Fish Canyon sanidine of 28.200 ± 0.044 Ma, nominally lower, but indistinguishable from the published value of 28.201 ± 0.044 Ma. Overall, the effects of an EC_{ground} decay mode are unlikely to be significant for most current applications of $^{40}Ar/^{49}Ar$ geochronology. However, given the levels of analytical precision attainable by the K-Ar dating approach when dating geologically recent materials by K-Ar (e.g., Altherr et al. (2019)), the EC_{ground} decay mode will impact the accuracy of this chronometer.

5.10 Conclusion

Conservation of energy and the Fermi theory of Beta decay are theories that have decades of experimental support and are well established. I demonstrate this here by using this theory to accurately calculate the decay rate of a ^{22}Na, a nuclide with an experimentally-verified decay rate. I have used this information to demonstrate the high likelihood that the suspected second electron capture decay mode of ^{40}K exists. Based on the calculations of Mougeot (2018), the best estimate of the partial decay constant for ^{40}K direct to ground state ^{40}Ar is be 11.6 ± 1.5 × 10^{-13} a^{-1} (2σ), and other calculations are no lower than about 8.2 × 10^{-13} a^{-1}. Combining this with the decay constants published by Min et al. (2000) results in revised values of $\lambda_{^{40}_{Ar}}$ = 0.592 ± 0.014 × 10^{-10} a^{-1} and λ_T = 5.475 ± 0.107 × 10^{-10} a^{-1}. This addresses a longstanding question in K-Ar and $^{40}Ar/^{39}Ar$ geochronology and provides future workers with confidence that the ^{40}K EC_{ground} decay mode exists. Just as important as providing support for its existence, I also demonstrate that the magnitude of this decay mode is small enough that neglecting it has not yet resulted in significantly biased geochronological $^{40}Ar/^{39}Ar$ data. The same cannot be stated for the K-Ar dating approach, especially for geologically-young materials.

Despite the strong grounding in theory, the EC_{ground} decay mode has yet to be detected. The next step is experimental verification to determine the branching ratio. This will allow for a more complete evaluation of uncertainties associated with the decay mode and the branching ratio. This experiment is difficult, but not intractable.

Chapter 6

Final insights and further uses of Bayesian methods in $^{40}Ar/^{39}Ar$ geochronology

6.1 Introduction

In this chapter I reflect on the final insights and outcomes of this study and put forward some further uses of Bayesian inference in $^{40}Ar/^{39}Ar$ geochronology. I outline the main outcomes of my thesis and potential improvements to the model I have developed and future experiments, in particular, focusing on ways to increase the speed of both. I subsequently discuss two different applications of Bayesian modelling in $^{40}Ar/^{39}Ar$ geochronology. Firstly, I explore the inclusion of the K/Ca spectra that is collected as standard in the previously modelled datasets in an attempt to infer mineral phase dependent information coupled with age information. I use the Heidelberg biotite and Alder Creek sanidine mixture created by VanLaningham & Mark (2011) and analysed in Chapters 2 and 3 as a proof of concept. Second and finally, I discuss the use of a Bayesian crank method to determine the ages of components from multi-age and multi-mineral datasets with a greater degree of confidence.

6.2 Final thoughts and insights

- There is more geologically meaningful age information that can be recovered from multiple mineral component mixtures than previously realised. There is tremendous potential for applications of the $^{40}Ar/^{39}Ar$ step-heating and Bayesian

modelling methods to be extend to analysis of bulk sediments and multiple component assemblages. Examples include provenance reconstruction in fine-grained sediments, ancient soils and lunar and martian regolith. An interesting future application would be to sediments that contain authigenic minerals. For example, dating of fine-grained bulk sediment that contains the mineral glauconite would allow for resolution of sediment deposition ages.

- The extension of the initial Bayesian framework I developed to a non-parametric model removes fixed constraints making it flexible and applicable to geological settings that range in complexity.

- I expect the model to fail for the most complex sample that contains components that exhibit extreme behaviour individually (e.g., large loss of radiogenic ^{40}Ar*, age spectra that are disturbed by excess Ar ($^{40}Ar_{EX}$), recoil losses and redistribution of ^{39}Ar). But, these disturbances must be severe enough such that there is no pseudo-plateau evident in the age spectra. However, even in conventional single mineral phase step heating studies, generally no meaningful geological age information beyond maybe a maximum or minimum age would be recovered from such samples.

- Blind mixtures with the inclusion of JC anorthite which clearly exhibits $^{40}Ar_{EX}$ can still be estimated reasonably at the 95% confidence level. Excess Ar is not a significant limitation to the application of my model. The flexibility of the model has the potential to deal with such information and extract the broadest range of provenance information from bulk sediment.

- Mixtures with the same mineral phases with differing age present as an interesting problem in this type of modelling. For example the Kula et al. (2010) case studies present the need for extra prior information to un-mix this type of age spectra. However,

- With the right infrastructure (e.g., Morgan et al. (2017)) it is possible for remote planetary exploration platforms (e.g., Perserverance Rover) to use my approach to reconstruct provenance in extraterrestrial settings. This will be critical for where polymineralic multi-age samples are likely (e.g., sediments in Jezero Crater; Schon et al. (2012), Horgan et al. (2020)) and detailed sample preparation is not possible (e.g., Curiosity rover limited to simple sieving (Mahaffy et al. (2012)).

- My Bayesian model was used for a real geological application: unmixing the glacial megaflood deposits of both the Ephrata Fan and Moses Coulee sediments. The study showed that; (1) the maximal amount of provenance information is in the bulk fine-grained sediment 20 - 63 μm and; (2) Analysis of these sediments require that glacial Lake Missoula is the source of both Ephrata Fan and Moses Coulee.

- I show through the theory of Fermi (1934) and arguments based on energy conservation that there is an overlooked ^{40}K decay mode (^{40}K-^{40}Ar$_{groundstate}$) that has significant impact for the K-Ar dating of geologically young samples. Utilisation of this decay scheme results in an $\sim 2\%$ change in age $\leq$ 1Ga. This work further calls for experimental verification of this decay mode (e.g., Di Stefano et al. (2020)).

6.3 Model and experimental improvements

The Bayesian model I developed has evolved from a simple framework that required full parameterisation where the observers had a wealth of prior knowledge of the model parameters (i.e., number of components, kinetics, etc) to a non-parametric framework, which removed the need of prior information that would not likely be available in a natural samples. This increase in the complexity of the model has made the speed at which it runs drastically slower, approximately 10 times slower than the parameterised model (i.e., 50 model draws a second compared to 500). For future use on complex datasets, parallel computing would offer an opportunity to reduce the running time of the model from a day to approximately 2 - 4 hours. A further possibility to increase speed is to continue to different more efficient programming languages sucg as cython, C, C^{++}, or julia. Coupled with a more efficient programming language, moving from a Dirichlet process mixture model, which has proved effective, to a reversible jump Markov Chain Monte Carlo (rjMCMC) (e.g., Gallagher et al. (2009)), would be an improvement. In its current set up, the model can move through dimensions although all of the available parameter space is still sampled and it is only the contributing (non-negligible weight) components that are pulled out in the inference. Because the full component parameter space is still being sampled there are a large number of redundancies making the modelling inference process highly inefficient. Moving to an rjMCMC process would prevent this redundancy in parameter space. As well as

computation speeds, another issue is the length of time it takes to run the highly-resolved temperature-controlled step-heating experiments (several days on average). McDannell et al. (2018) present a continuous ramped heating approach as a means of screen samplings for (U-Th)/He dating. It may be possible to couple this analytical method with my detailed heating schedule approach to significantly increase the speed of the step-heating experiments. This has not been tried with respect to the $^{40}Ar/^{39}Ar$ technique.

6.4 Further uses of Bayesian inference in $^{40}Ar/^{39}Ar$ geochronology

Bayesian inference is an essential part of modern data analysis across a range of fields including astronomy, particle physics, radiocarbon dating and thermochronology (Koop (2003), Trotta (2008), Feroz et al. (2009), Ramsey (2009), Gallagher (2012)). Despite the widespread use, and in some cases reliance on Bayesian methods, its use in deeper time geochronology is infrequent. However, it is an increasing area of growth. Methods like radiocarbon dating are on reliant on Bayesian inference to extract meaningful calendar ages (Ramsey (2009)), thermochronology uses trans-dimensional Bayesian inference to infer the time temperature history of rocks (Gallagher (2012)), and Bayesian inference is also used to infer the eruption age from zircons (Keller et al. (2018)). The only applications of Bayesian modelling in $^{40}Ar/^{39}Ar$ geochronology is for construction of age-depth models, and this is a relatively recent development (e.g., Mark et al. (2017)).

The Bayesian framework presented offers possibility for more layers of complexity to be added that will help infer a greater wealth of information from complex $^{40}Ar/^{39}Ar$ data. I discuss possible further layers of complexity below.

6.4.1 Age spectrum, Arrhenius array, and K/Ca spectrum

Figure 6.1 shows the age spectrum, the Arrhenius array, and the K/Ca spectrum of the Heidelberg biotite and Alder creek sanidine mixture created by VanLaningham & Mark (2011). These three complementary data sets are recovered from the $^{40}Ar/^{39}Ar$ experiment and can be used along with my Bayesian framework to recover; (1) the age of each component in the mixture; and (2) the mineral component phases that are in

the mixture.

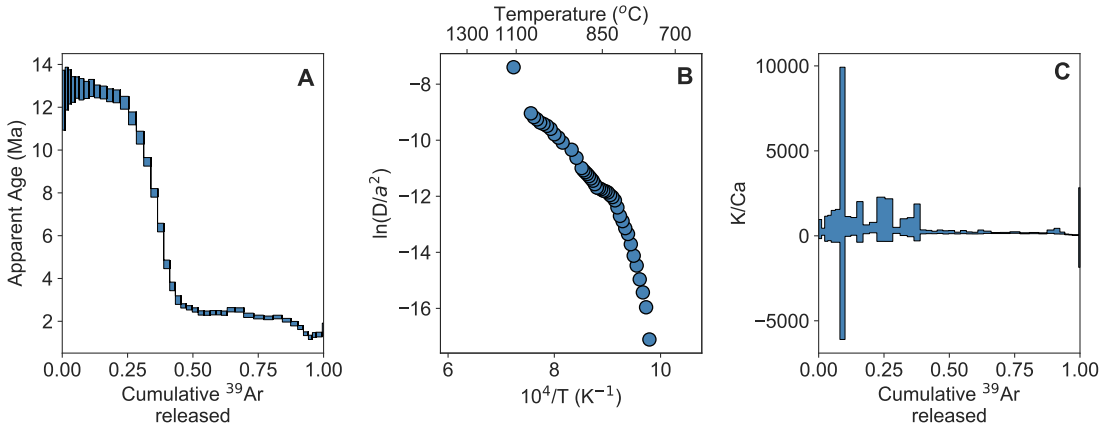

Figure 6.1: Panels A, B, and C show the age spectrum, the Arrhenius array, and the K/Ca spectrum of the Heidelberg biotite and Alder creek sanidine mixture created by VanLaningham & Mark (2011).

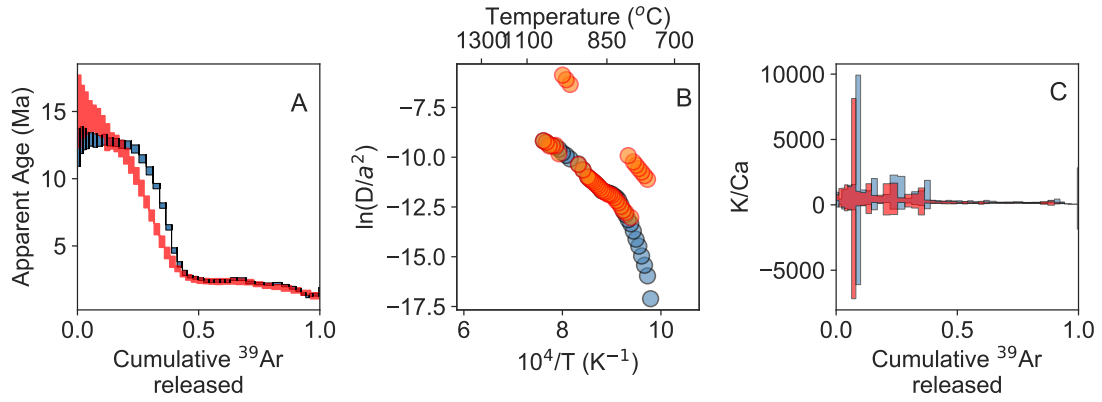

Figure 6.2: Model results of VanLaningham & Mark (2011). Panel A shows the age spectrum data (blue) and model (red), panel B shows the Arrhenius array data (blue) and model (red), and panel C shows the K/Ca spectrum data (blue) and model (red).

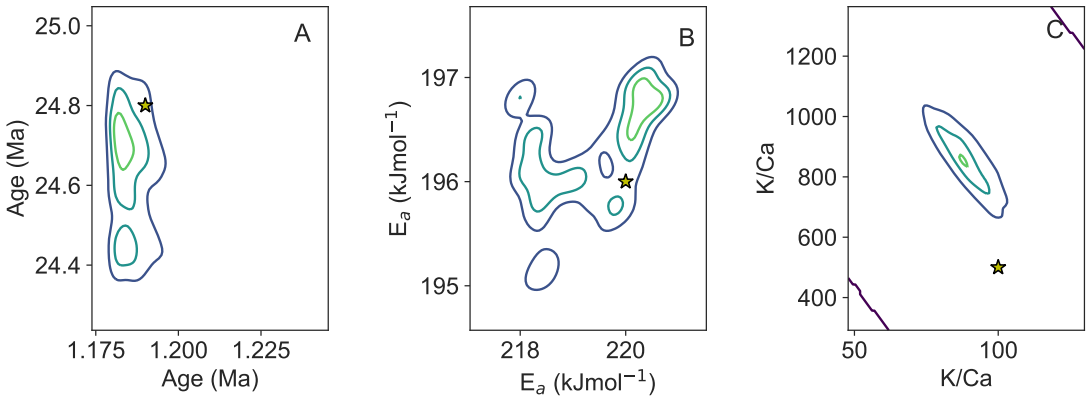

Figure 6.3: Panel A shows 50000 samples of the age (Ma) of component 1 vs. component 2. Panel B shows the activation energy (E_a kjmol^{-1}). Panel C shows the inferred K/Ca ratio of component 1 vs component 2. In all panels the accepted values of all parameters are shown by a yellow star. In panel A and C values are taken from VanLaningham & Mark (2011) and for panel B activation energy of both biotite and sanidine are taken from both Harrison et al. (2009), Cassata & Renne (2013).

Figures 6.2 and 6.3 show the modelling results for the fitting of the Arrhenius array and both the age and K/Ca spectra. Given that both the Arrhenius array and K/Ca are properties of mineral dependent parameters (i.e., the diffusion kinetics and K/Ca ratios) I expected that by fitting these three observations that both age and mineral dependent information could be inferred. I show in figure 6.3 a comparison of the inferred values produced by running the three datasets through my Bayesian model relative to the known values for each mineral component. The agreement at the 95% confidence level for all parameters shows that by including the K/Ca as an observation, mineral dependent information can be determined. This particular example points toward an extension of my Bayesian model to include more observations allowing for more information to be inferred.

6.4.2 Turning the Bayesian crank on provenance studies

In this section I describe a further improvement of the nonparametric model defined in Chapter 4 through the use of a Bayesian crank approach. Bayesian statistics is the natural process of updating prior distributions with observed data to produce a posterior distribution. Through the use of repeated analyses of a sample and the repeated updating of prior distributions through each new observation, there is potential to in-

crease the precision and accuracy with which each parameter can be estimated. In this modelling framework the non-parametric model described and used for deconvolving the age components of the blind mixtures in Chapter 3 and Missoula flood datasets in Chapter 4, can be evolved by the Bayesian crank method. To demonstrate this I consider one of the Moses Coulee mixtures analysed in Chapter 4. In this example it would be assumed that the observations (age spectra and Arrhenius arrays) are derived from the same sample. This means that although I have run multiple step-heating experiments of different aliquots of the same well-mixed sample such that generally, the distinct age populations and minerals are the same across all aliquots. Given that the aliquots were extracted from the same geological location and the grain size is small enough to ensure adequate mixing, this assumption is most likely a fair one. In this approach the model would be run on dataset one (aliquot 1) with an output of inferences for the parameters defining the model. These posterior outputs are then used as priors for the next dataset (aliquot 2). As this process is repeated numerous times (aliquot 3, 4, 5....) and after each iteration there will be an increase in the confidence of the inferred model parameters. As such, the process would output increasingly precise component ages and ultimately increase the resolution with respect to complex provenance histories.

These final sections show other applications of Bayesian inference in $^{40}Ar/^{39}Ar$ geochronology. I highlight this with two final examples shown above. However, there are considerably more situations where Bayesian inference would be applicable and useful (e.g., modelling recoil or analysis of isochrons). Through applications of models such as the nonparametric model shown in Chapter 3, the recoil model and the Bayesian crank method discussed above, the reach of $^{40}Ar/^{39}Ar$ dating can be potentially extended to more complex geological settings and samples that don't allow for conventional approaches of age assessment using plateau or isochron criteria.

Appendix A

Appendix

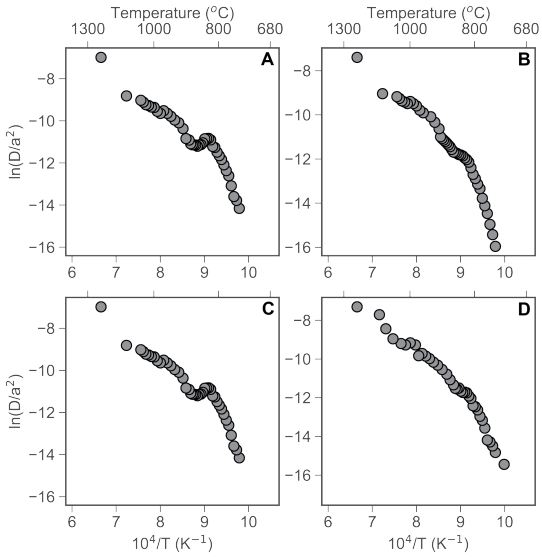

Figure A.1: Arrhenius plots for case study 1, wherein we re-analyze the mixtures of neutron fluence monitors reported by VanLaningham & Mark (2011)). The Arrhenius plots are ordered as follows; A - Mixture 1: 25% ACs and 75% TCRs, B - Mixture 2: 75% ACs and 25% HD-B1, C - Mixture 3: 50% HD-B1 and 50% TCRs and D - Mixture4: 50% ACs, 25 % HD-B1, and 25% TCRs.

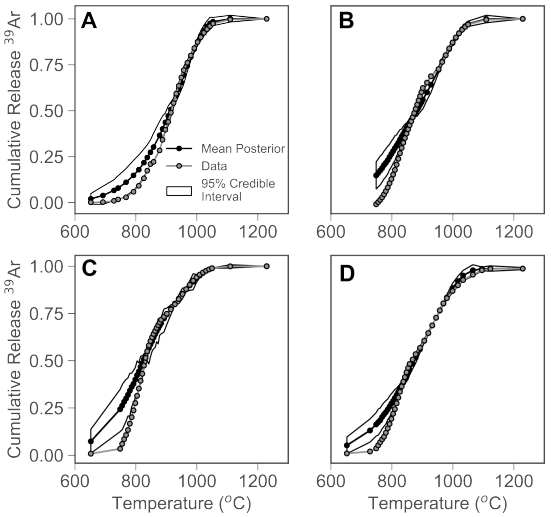

Figure A.2: Cumulative release spectra of all mixtures created by VanLaningham & Mark (2011) (black) compared to our mean posterior predictive model (dashed grey) given with its 95% credible interval (grey).

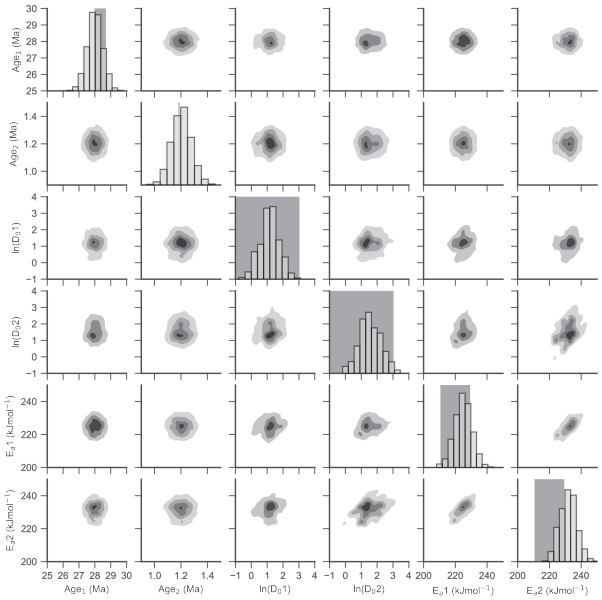

Figure A.3: Pair plot showing the posterior sampling of model parameters for mixture 1 (25% ACs and 75% TCRs by mass) of VanLaningham & Mark (2011). In diagonal histogram plots, dark grey boxes represent 95% confidence bounds of the known parameter values from prior studies. In the off-diagonal kernel density estimation plots, four contours are shown from light to dark gray representing 95, 68, 34 and 5% credible intervals.

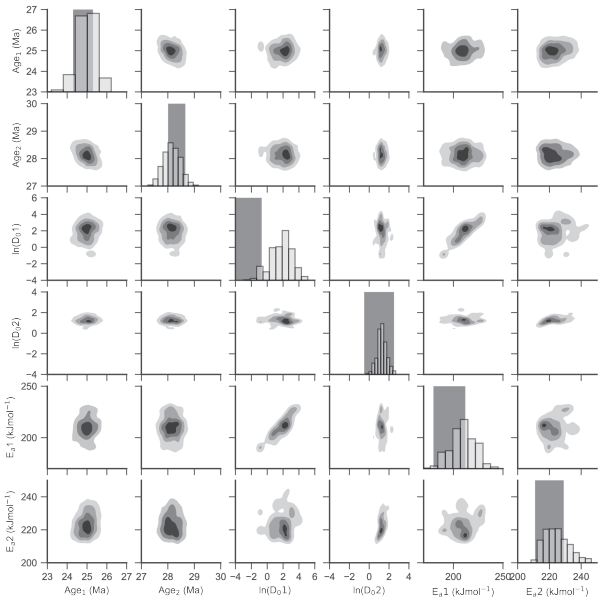

Figure A.4: Pair plot showing the posterior sampling of model parameters for mixture 3 (50% HD-B1 and 40% TCRs by mass) of VanLaningham & Mark (2011). In diagonal histogram plots, dark grey boxes represent 95% confidence bounds of the known parameter values from prior studies. In the off-diagonal kernel density estimation plots, four contours are shown from light to dark gray representing 95, 68, 34 and 5% credible intervals.

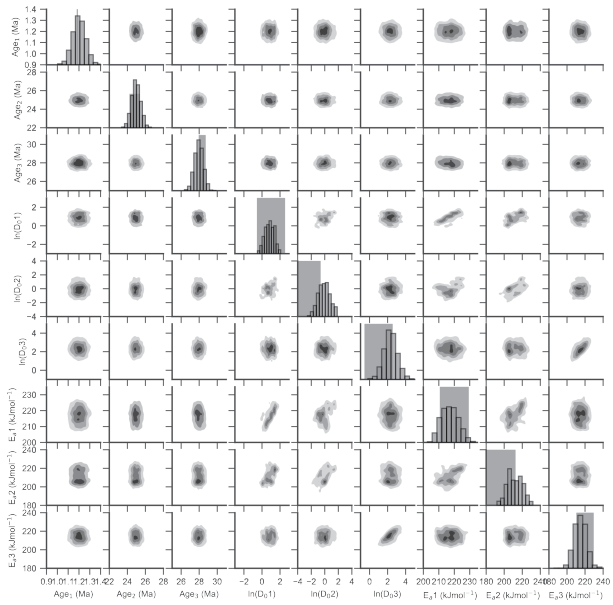

Figure A.5: Pair plot showing the posterior sampling of model parameters for mixture 4 (50% ACs, 25% HD-B1 and 25% TCRs by mass) of VanLaningham & Mark (2011). In diagonal histogram plots, dark grey boxes represent 95% confidence bounds of the known parameter values from prior studies. In the off-diagonal kernel density estimation plots, four contours are shown from light to dark gray representing 95, 68, 34 and 5% credible intervals.

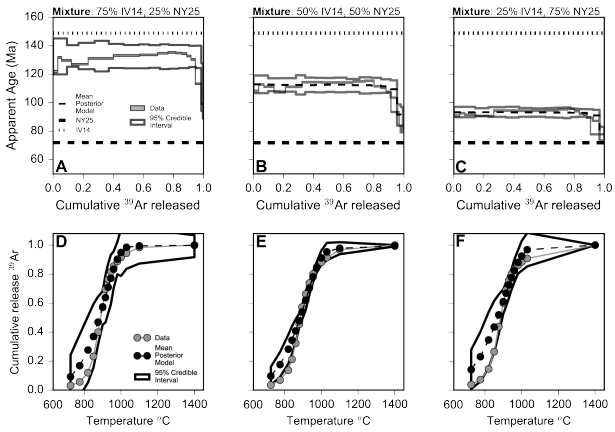

Figure A.6: Posterior age spectra (A-C) and cumulative release spectra (D-F) for case study 2 using the Kula et al. (2010) muscovite mixtures. These models use the same degree of prior information as in case study 1 on the VanLaningham & Mark (2011) mixtures.

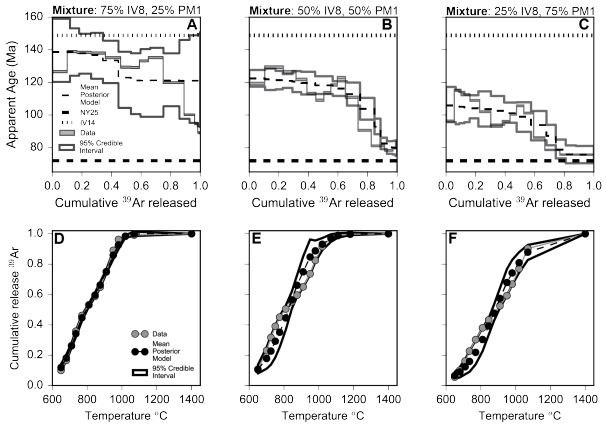

Figure A.7: Posterior age spectra (A-C) and cumulative release spectra (D-F) for case study 2 using the Kula et al. (2010) biotite mixtures. These models use the same degree of prior information as in case study 1 on the VanLaningham & Mark (2011) mixtures.

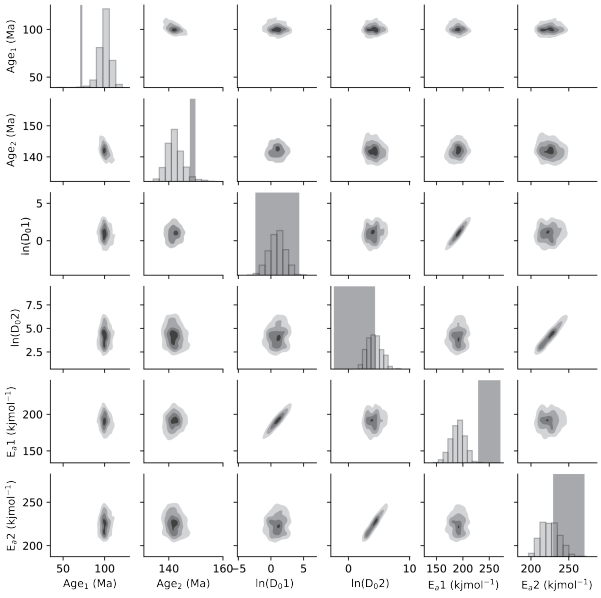

Figure A.8: Pair plot showing the posterior sampling of model parameters for the 3:1 IV18:NY25 muscovite mixture in case study 2. These models use more restrictive priors on the component mixing fractions than in case study 1.

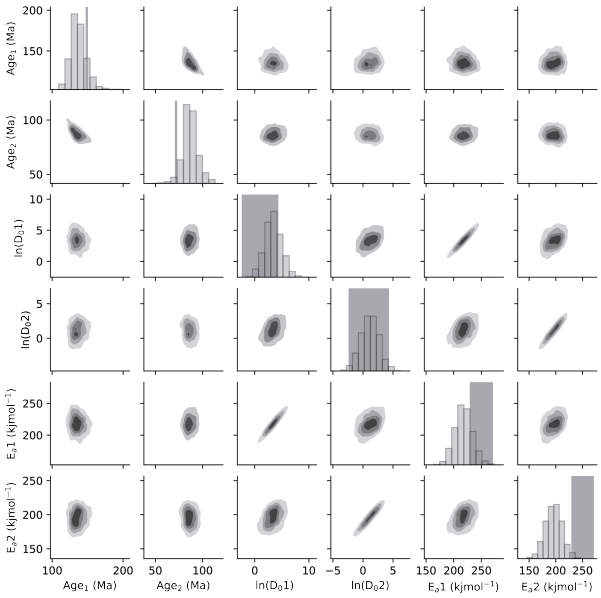

Figure A.9: Pair plot showing the posterior sampling of model parameters for the 1:1 IV18:NY25 muscovite mixture in case study 2. These models use more restrictive priors on the component mixing fractions than in case study 1.

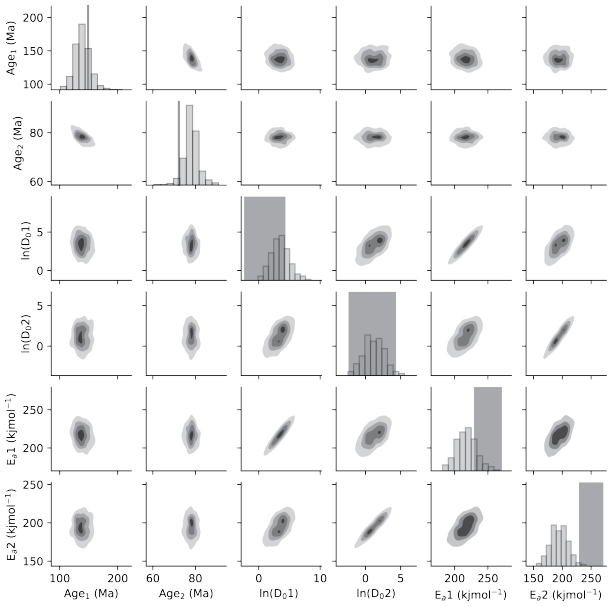

Figure A.10: Pair plot showing the posterior sampling of model parameters for the 1:3 IV18:NY25 muscovite mixture in case study 2. These models use more restrictive priors on the component mixing fractions than in case study 1.

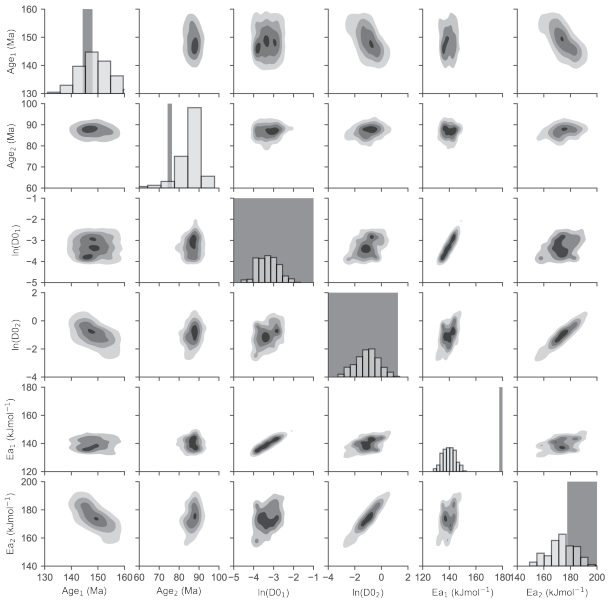

Figure A.11: Pair plot showing the posterior sampling of model parameters for the 3:1 IV8:PM1 biotite mixture in case study 2. These models use more restrictive priors on the component mixing fractions than in case study 1.

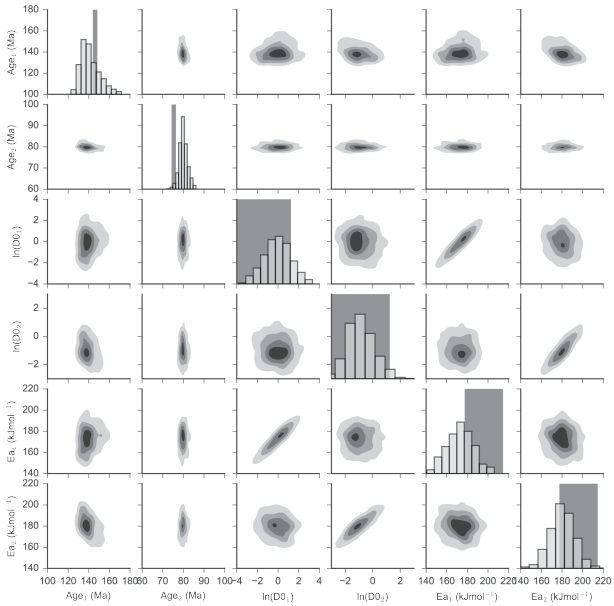

Figure A.12: Pair plot showing the posterior sampling of model parameters for the 1:1 IV8:PM1 biotite mixture in case study 2. These models use more restrictive priors on the component mixing fractions than in case study 1.

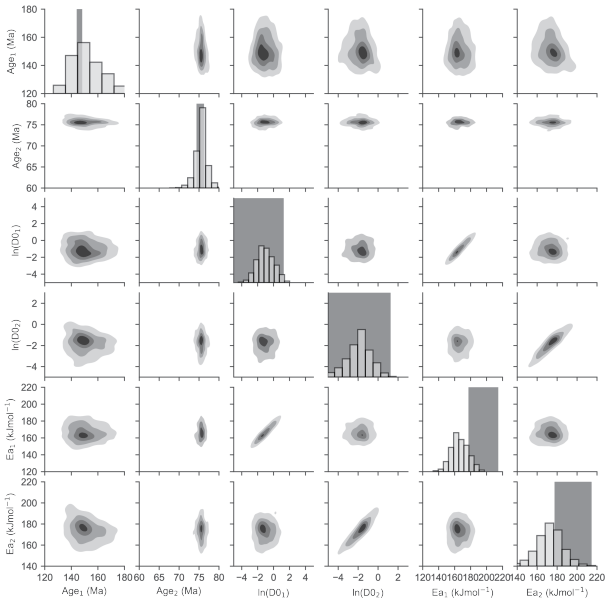

Figure A.13: Pair plot showing the posterior sampling of model parameters for the 1:3 IV8:PM1 biotite mixture in case study 2. These models use more restrictive priors on the component mixing fractions than in case study 1.

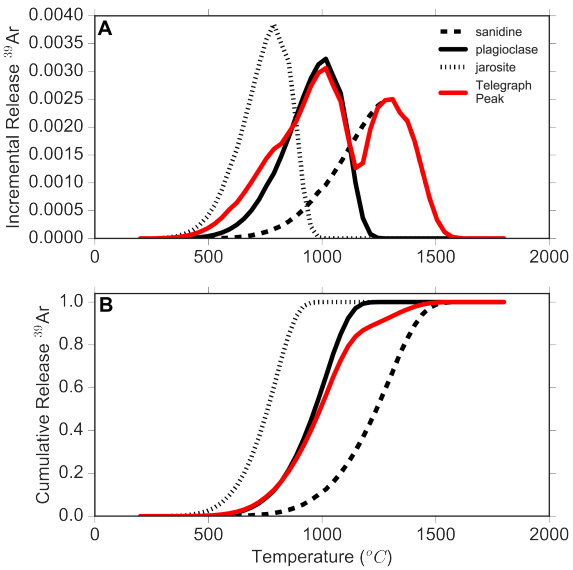

Figure A.14: Individual incremental (A) and cumulative (B) release spectra for a synthetic mixture of K-bearing minerals detected at Telegraph peak on Mars. Calculations use a monotonic 50 step heating schedule with temperatures increasing from 200 to 1600^{o}C and the discretised solution of fractional loss for a sphere by Fechtig & Kalbitzer (1966). We assume argon diffusion kinetics from the literature (for jarosite,Kula & Baldwin (2011); for sanidine, Cassata & Renne (2013); for plagioclase, Jourdan & Eroglu (2017)). The red curve corresponds to the modelled incremental and cumulative release for the combined release of argon from all K-bearing minerals in our synthetic mixture.

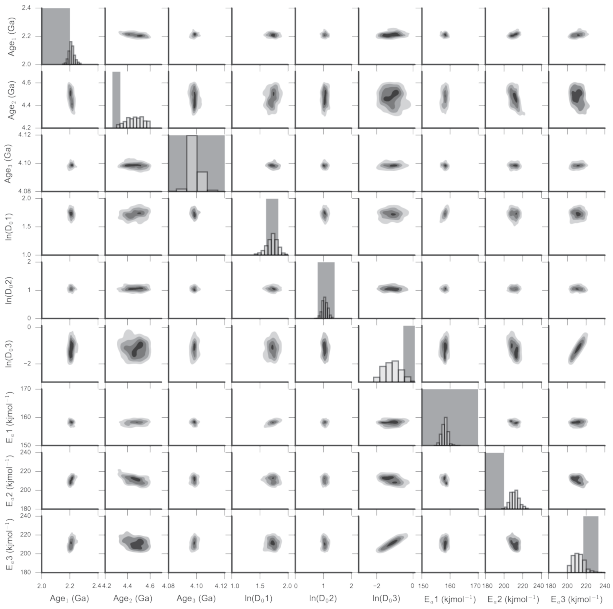

Figure A.15: Pair plot showing the posterior sampling of model parameters for the synthetic Martian mixture in case study 3.

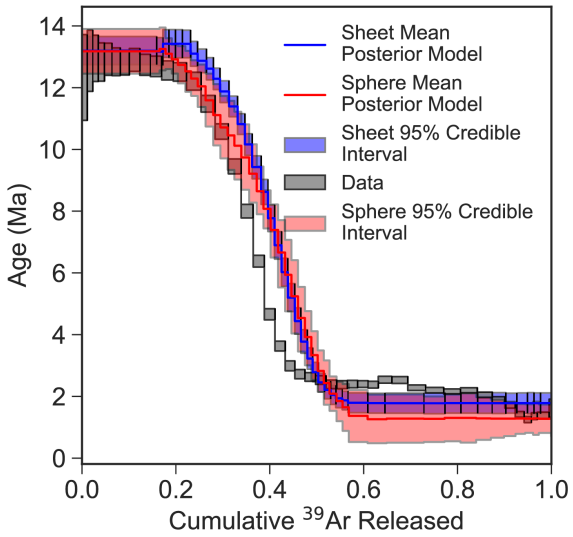

Figure A.16: Age spectrum for Mixture 2, case study 1, compared to posterior age spectra from two models. For model with the red posterior age spectrum, both components have a spherical diffusion geometry. The model with the blue posterior age spectrum has one component with an infinite sheet diffusion geometry and one with a spherical diffusion geometry; the component with an infinite sheet geometry has the older posterior age estimate, consistent with the age of HD-B1. We do not observe an improvement in model fit to the observed age spectrum with the inclusion of one component with an infinite sheet diffusion geometry.

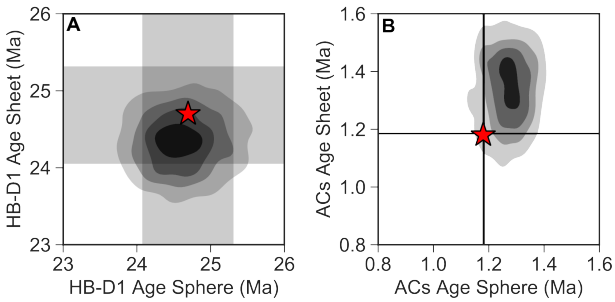

Figure A.17: Comparison of modeled component ages of HD-B1 (A) and ACs (B) in Mixture 2, case study 1, using either a spherical geometry (horizontal axis) or an infinite sheet geometry (vertical axis) for HD-B1. The red stars and grey or black bars represent the known component ages and 2 uncertainties. Model kernel density estimates of the ages are shaded as in the pair plots. For a spherical geometry of HD-B1, we predict ages of 24.6 ± 1.1 Ma and 1.27 ± 0.16 Ma for HD-B1 and ACs, respectively (2). For an infinite sheet geometry of HD-B1, we predict ages of 24.3 ± 0.8 Ma and 1.34 ± 0.28 Ma for HD-B1 and ACs, respectively (2).

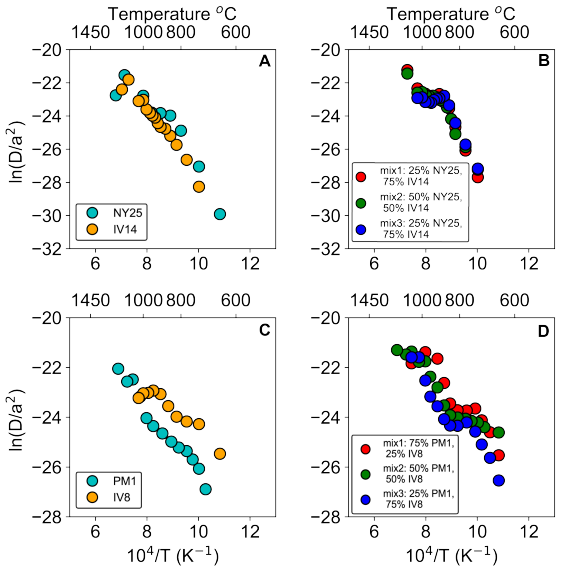

Figure A.18: Arrhenius plots from step degassing measurements Kula et al. (2010). (A) individual muscovite samples, (B) muscovite mixtures, (C) muscovite mixtures, and (D) biotite mixtures.

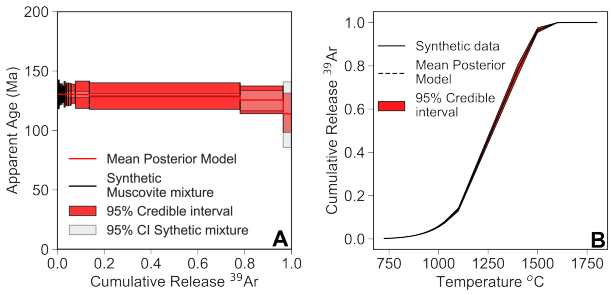

Figure A.19: Age spectrum for the synthetic two-component muscovite mixture (grey) and the mean posterior model from our Bayesian inversion of these synthetic data (red). The 95% confidence interval (grey) and credible interval (red) are shown, respectively. (B) Cumulative ^{39}Ar release spectrum for the synthetic two-component muscovite mixture (solid black) and mean posterior model from our Bayesian inversion of these synthetic data (dashed black). The model 95% credible interval is shown in red.

Input age $\pm$ 2σ (Ma)	Estimated age $\pm$ 2σ (Ma)
71.9 $\pm$ 0.8	108.4 $\pm$ 4.8
148.8 $\pm$ 1.6	144.0 $\pm$ 3.1

Table A.1: Ages assumed for the synthetic two-component muscovite mixture, and estimated ages of each component from our Bayesian inversion

J	± 1σ	Discrim	± 1σ	Temp (°C)	± 1σ (°C)	Heating duration (s)	^{40}Ar	± 1σ	^{39}Ar	± 1σ	^{38}Ar	± 1σ	^{37}Ar	± 1σ	^{36}Ar	± 1σ	^{39}Ar (Moles)	^{40}Ar/^{39}Ar	± 1σ	^{40}Ar*/^{39}Ar$_K$	± 1σ	% ^{40}Ar*	± 1σ	Age (Ma)	± 1σ
0.0131	0.000026	0.959706	0.0006593	487.2	4.5	2997.1	0.9520512	0.000061	0.031714	0.0000521	0.0005566	8.60E-06	-0.0423907	0.0024742	0.0005064	0.000025	2.21998E-15	30.01989	0.055382	25.12304	0.2427502	83.76778	0.7880437	514.4398	4.326184
0.0131	0.000026	0.959706	0.0006593	520.8	3.1	2997	1.42626	0.00034	0.0572353	0.0000411	0.0006982	0.0000011	-0.0249949	0.0022308	0.0001313	0.00002	4.00647E-15	24.91923	0.0299301	24.19182	0.1090149	97.11327	0.4200067	497.7674	1.96081
0.0131	0.000026	0.959706	0.0006593	520.6	7.6	2996.6	0.9205474	0.00031	0.0376696	0.0000401	0.0005087	0.0000015	-0.0093112	0.0029821	-0.0000198	8.20E-06	2.63687E-15	24.4374	0.0342582	24.56977	0.0737384	100.562	0.2708368	504.5527	1.321338
0.0131	0.000026	0.959706	0.0006593	578.9	8	2997.1	5.396322	0.0013	0.2415651	0.0000872	0.0029503	0.0000013	-0.0555565	0.0024647	0.000048	8.29E-06	1.69096E-14	22.33899	0.0238798	22.25721	0.0261813	99.6531	0.0557865	462.631	0.4801546
0.0131	0.000026	0.959706	0.0006593	520.8	5.7	2997	0.3781917	0.00019	0.0164528	0.0000361	0.0002589	8.90E-06	0.0492506	0.0029952	0.00005	9.11E-06	1.1517E-15	22.9865	0.0510709	22.36182	0.1742126	97.08309	0.7248137	464.5485	3.191597
0.0131	0.000026	0.959706	0.0006593	628.1	5.4	1997	9.523823	0.0021	0.4346004	0.0002305	0.00517	0.000028	-0.1416883	0.0097519	-0.0001781	0.0000173	3.0422E-14	21.91398	0.0245385	22.00479	0.0271032	100.4405	0.0619631	457.9958	0.4983362
0.0131	0.000026	0.959706	0.0006593	678.2	2.3	1996.5	18.30459	0.0036	0.7678287	0.0001703	0.0089044	0.000031	-0.1983889	0.0030069	-0.0003522	0.0000118	5.3748E-14	23.83942	0.0246076	23.95082	0.0246917	100.4884	0.0323043	493.4274	0.4451884
0.0131	0.000026	0.959706	0.0006593	678.1	1.5	1996.5	11.09832	0.0031	0.4388085	0.0000972	0.0049126	0.0000012	-0.1262815	0.0027601	-0.0002305	9.10E-06	3.07166E-14	25.29194	0.02645	25.42002	0.0267851	100.5294	0.0442038	519.7246	0.4759585
0.0131	0.000026	0.959706	0.0006593	781.1	1.3	997	39.99012	0.0054	1.586065	0.0002004	0.0170296	0.0000036	-0.4005575	0.0022378	-0.0007471	0.00001	1.07525E-13	26.04	0.0263713	26.15894	0.0260608	100.4778	0.0192831	532.8075	0.4597501
0.0131	0.000026	0.959706	0.0006593	781.1	1.3	996.9	18.64115	0.0042	0.6353258	0.0001403	0.0070444	0.00002	-0.1654576	0.0025167	-0.0002283	0.0000118	4.44728E-14	29.34108	0.0304047	29.42154	0.0306517	100.2949	0.0351634	589.4673	0.5240573
0.0131	0.000026	0.959706	0.0006593	755.2	1.1	997	6.949564	0.0015	0.2191979	0.0000882	0.0024567	0.00002	-0.0561761	0.003025	-0.0000146	0.0000146	1.53439E-14	31.70452	0.0341342	31.69753	0.0394851	99.99808	0.068739	627.9675	0.6608615
0.0131	0.000026	0.959706	0.0006593	678.3	1.6	997	0.8126055	0.00025	0.0256557	0.0000451	0.0003042	1.00E-05	-0.0177202	0.0022707	0.000069	0.0000155	1.7959E-15	31.67343	0.0590905	30.79973	0.1896771	97.29047	0.5701893	612.8783	3.201229
0.0131	0.000026	0.959706	0.0006593	628.1	4.1	996.9	0.184993	0.00016	0.0060847	0.0000261	0.0001248	0.000011	0.0069804	0.0024767	0.0000253	0.0000109	4.25929E-16	30.40279	0.1210763	29.27379	0.5507064	96.21207	1.769653	586.9395	9.428705
0.0131	0.000026	0.959706	0.0006593	628	3.3	997	0.178802	0.00017	0.0055785	0.000025	0.0000869	1.00E-05	0.0058578	0.0025295	0.000023	0.0000191	3.90495E-16	32.05209	0.1337142	30.92573	1.032571	96.41765	3.194675	615.0037	17.40648
0.0131	0.000026	0.959706	0.0006593	703.4	1.4	997	1.610794	0.00041	0.0497219	0.0000451	0.0006022	0.0000011	-0.0212952	0.002787	-0.0000235	8.92E-06	3.48053E-15	32.39608	0.0420939	32.49313	0.0682105	100.3317	0.1092647	641.2346	1.133292
0.0131	0.000026	0.959706	0.0006593	703.3	1.5	996.9	1.456509	0.00035	0.0437495	0.0000371	0.0005005	0.0000012	-0.0171372	0.0027895	0.0000632	0.0000127	3.06247E-15	33.292	0.0421351	32.81997	0.0971994	98.61117	0.263489	646.6568	1.610098
0.0131	0.000026	0.959706	0.0006593	767.9	3.8	1001	6.063973	0.0012	0.1687505	0.0000812	0.0018396	0.000016	-0.0656918	0.0018034	-0.0001032	9.10E-06	1.18125E-14	35.93454	0.039497	36.07573	0.0422859	100.4221	0.0518766	699.7996	0.6801741
0.0131	0.000026	0.959706	0.0006593	768.1	1.6	997	5.002467	0.00091	0.1328452	0.0000481	0.0014195	0.000023	-0.0698064	0.0048304	-0.0000324	0.0000118	9.29916E-15	37.65637	0.039948	37.67285	0.048029	100.0823	0.0749037	725.3086	0.7617303
0.0131	0.000026	0.959706	0.0006593	821.2	1.1	997	6.492932	0.0014	0.1931944	0.0000571	0.0022739	0.000014	-0.0694292	0.0023682	-0.0000813	0.00001	1.35236E-14	33.60828	0.0352636	33.69621	0.0382591	100.2889	0.0541296	661.1138	0.6287104
0.0131	0.000026	0.959706	0.0006593	821.2	1.3	997	5.738768	0.0017	0.1510595	0.0000601	0.0016754	0.000012	-0.0846386	0.0020385	-0.0001102	0.0000118	1.05742E-14	37.9901	0.0413743	38.14791	0.0471158	100.4564	0.0728943	732.8274	0.7441455
0.0131	0.000026	0.959706	0.0006593	861.2	1.4	497.4	10.39935	0.0028	0.3058351	0.0001002	0.0036385	0.000013	-0.116376	0.0025518	-0.0001703	0.0000118	2.14085E-14	34.00314	0.0362293	34.12951	0.0376581	100.4004	0.0490911	668.2202	0.6164079
0.0131	0.000026	0.959706	0.0006593	861.3	1.4	496.9	8.002991	0.0023	0.185035	0.0000741	0.0019915	8.80E-06	-0.0933285	0.0021705	-0.0000998	0.0000136	1.29525E-14	43.25122	0.0470642	43.35617	0.0516606	100.2795	0.0634253	813.2703	0.7804222
0.0131	0.000026	0.959706	0.0006593	887.2	1.2	497	10.1706	0.002	0.2164626	0.0000721	0.0021546	0.000013	-0.1326484	0.001969	-0.0002009	8.37E-06	1.51524E-14	46.98547	0.0495871	47.19289	0.0502813	100.4858	0.03572	870.3209	0.7359929
0.0131	0.000026	0.959706	0.0006593	887.2	1.3	496.9	7.829926	0.0014	0.161688	0.0000741	0.0016587	0.000013	-0.0840608	0.0030706	-0.0001013	8.28E-06	1.13182E-14	48.42615	0.0527491	48.55343	0.0545706	100.3006	0.0394856	890.1271	0.7900769
0.0131	0.000026	0.959706	0.0006593	955.1	1	497	63.70397	0.022	1.277726	0.0003206	0.0122125	0.000034	-0.6024171	0.0035874	-0.0012109	0.00001	8.94408E-14	49.85731	0.053098	50.08545	0.0524499	100.492	0.0456662	912.1727	0.7501698
0.0131	0.000026	0.959706	0.0006593	1023.2	1	296.6	16.27611	0.0049	0.3263714	0.0001102	0.0032133	0.000013	-0.164623	0.0021795	-0.0002216	9.10E-06	2.2846E-14	49.86991	0.0535614	50.0141	0.0537498	100.3258	0.0429494	911.152	0.7691964
0.0131	0.000026	0.959706	0.0006593	1023.2	0.9	297.7	3.18629	0.0017	0.0641873	0.0000751	0.0006424	0.000013	-0.051597	0.0030809	-0.0000447	0.0000118	4.49311E-15	49.64052	0.0748733	49.75581	0.0928535	100.2897	0.1313694	907.4519	1.331519
0.0131	0.000026	0.959706	0.0006593	1061.6	6.4	296.6	3.093076	0.0016	0.0622998	0.0000551	0.0006493	0.000017	-0.0490625	0.0038533	-0.0000407	8.65E-06	4.36099E-15	49.64822	0.0666677	49.75267	0.0785395	100.2667	0.1080654	907.4068	1.126284
0.0131	0.000026	0.959706	0.0006593	925.6	3.7	497	3.897098	0.0053	0.0776698	0.0002405	0.0013395	0.000058	0.0883236	0.0128604	0.0006308	0.0000364	5.43689E-15	50.17522	0.1572329	47.87803	0.2091688	95.34763	0.3293994	880.322	3.044825
0.0131	0.000026	0.959706	0.0006593	881.7	0.7	997	0.8393016	0.0046	0.0167246	0.0003507	0.0008967	0.000077	0.1444314	0.0198183	0.0012716	0.0000391	1.17072E-15	50.18379	0.9602744	28.34042	0.9246109	56.13512	1.510287	570.888	15.97152
0.0131	0.000026	0.959706	0.0006593	845.9	0.7	996.9	0.4295441	0.00036	0.0089307	0.0000361	0.0002373	0.000012	0.0281715	0.0036093	0.0003738	0.0000109	6.25149E-16	48.09738	0.1815692	35.92996	0.4008786	74.53989	0.7682981	697.4533	6.456555
0.0131	0.000026	0.959706	0.0006593	793.5	1.6	997	0.1504315	0.00041	0.0028402	0.0000261	0.0000694	0.000013	0.0056125	0.0022965	0.0002509	0.0000137	1.09811E-16	52.9645	0.4496636	26.78243	1.466626	50.49801	2.725602	543.7734	25.71694
0.0131	0.000026	0.959706	0.0006593	793.7	1.3	997	0.1284623	0.00014	0.0026367	0.0000361	0.0000656	8.00E-06	0.0172397	0.0031015	0.0000195	0.0000182	1.84569E-16	48.72117	0.5928883	35.86784	2.1211314	73.28517	4.235482	696.4526	34.18193
0.0131	0.000026	0.959706	0.0006593	882.3	1.2	496.9	0.1315864	0.00022	0.0028182	0.0000301	0.0000832	9.90E-06	0.0134019	0.0025869	-3.37E-06	0.0000109	1.9727 4E-16	46.6919	0.4476116	47.58366	1.25177	101.5747	2.492788	876.0318	18.26502
0.0131	0.000026	0.959706	0.0006593	882.9	0.6	497	0.1518575	0.00014	0.003028	0.0000381	0.0000164	0.000011	0.0013426	0.0028496	0.00004	9.11E-06	2.1196E-16	50.15055	0.5610312	46.25716	1.042468	92.20953	1.799827	856.5721	15.37561
0.0131	0.000026	0.959706	0.0006593	982	0.5	296.7	0.4343794	0.00045	0.008578	0.0000381	0.0001048	0.000013	-0.0049826	0.0028515	0.0002716	0.0000218	6.0046E-16	50.63901	0.2098035	41.12335	0.7827013	81.2428	1.506673	779.221	12.04882
0.0131	0.000026	0.959706	0.0006593	981.6	1.3	296.7	0.1770015	0.00037	0.0037221	0.0000261	0.0000959	0.000011	0.0172385	0.0028552	0.000076	0.0000146	2.6054 7E-16	47.55468	0.3097268	41.95728	1.207797	87.94692	2.472541	792.0132	18.46163

Table A.2: Blind mixture 1 data

J	± 1σ	Discrim	± 1σ	Temp (°C)	± 1σ (°C)	Heating duration (s)	^{40}Ar	± 1σ	^{39}Ar	± 1σ	^{38}Ar	± 1σ	^{37}Ar	± 1σ	^{36}Ar	± 1σ	^{38}Ar (Moles)	± 1σ	^{40}Ar/^{39}Ar	± 1σ	^{40}Ar*/^{39}Ar$_K$	± 1σ	% ^{40}Ar*	± 1σ	Age (Ma)	± 1σ
0.0131	0.000026	0.959706	0.0009593	366	6.2	2996.6	0.2310245	0.00061	0.0021126	0.00002	0.0003227	0.000013	0.0638409	0.00131	0.0004451	0.0000126	1.47882E-16	0.9553494	109.3542	0.95114	49.91101	1.918205	44.68332	1.653549	909.6761	27.47325
0.0131	0.000026	0.959706	0.0009593	365.8	6.3	1996.5	0.0125674	0.000083	0.0004892	0.0000019	0.0000419	6.10E-06	0.0125368	0.0025664	1.19E-06	0.0000112	3.42444E-17	25.69194	0.8958885	0.0178	27.49112	7.076477	105.0999	26.78656	556.1577	123.2374
0.0131	0.000026	0.959706	0.0009593	393.4	4.9	1996.4	0.0224697	0.000089	0.0007664	0.000022	-0.0000191	0.000012	-0.0106737	0.0028575	1.27E-06	9.50E-06	5.36485E-17	29.31886	0.7524889	0.0178	27.45119	3.748839	94.53848	12.67425	555.4621	65.31143
0.0131	0.000026	0.959706	0.0009593	422.5	3.6	1996.5	0.0593125	0.00014	0.0020946	0.000019	0.0000964	0.000014	0.0333166	0.0028614	0.0000114	0.0000114	1.46622E-16	28.31621	0.2361547	0.0178	14.00067	1.647939	48.89868	5.734223	304.4915	32.98476
0.0131	0.000026	0.959706	0.0009593	422.6	3.6	1996	0.0305097	0.00011	0.0011789	0.0000251	0.000116	9.30E-06	0.0328032	0.0034409	0.0000978	0.0000105	8.25233E-17	25.88046	0.4920901	0.0178	25.74254	1.107525	74.99997	3.030991	525.4466	19.61802
0.0131	0.000026	0.959706	0.0009593	451.3	3.2	1996.5	0.0849045	0.00024	0.0024795	0.0000401	0.0001064	0.000017	0.0085426	0.0045941	0.0000734	8.49E-06	1.73565E-16	34.24195	0.497279	0.0178	25.74254	1.107525	74.99997	3.030991	525.4466	19.61802
0.0131	0.000026	0.959706	0.0009593	451.3	3.7	1996.6	0.0458743	0.0001	0.0017144	0.0000261	0.0001274	0.000013	0.0034528	0.0001261	0.0000105	1.20008E-16	26.75747	0.3637805	6.884689	0.0178	27.79875	0.9746817	87.66049	3.031407	561.5071	16.92401
0.0131	0.000026	0.959706	0.0009593	480.2	3.5	1996.5	0.1122367	0.00029	0.0035424	0.0000523	0.0000795	0.000014	0.0045902	0.0037456	0.0000476	0.0000113	2.47968E-16	31.68401	0.1975484	0.0178	22.91663	1.355478	75.961	4.450607	474.6843	24.69373
0.0131	0.000026	0.959706	0.0009593	479.8	3.4	1996.6	0.0823649	0.0002	0.0027399	0.0000523	0.0000999 4	1.00E-05	0.0141599	0.0040422	0.0000701	0.0000122	1.91793E-16	30.06131	0.2338659	0.0178	22.91663	1.355478	75.961	4.450607	474.6843	24.69373
0.0131	0.000026	0.959706	0.0009593	520.5	3.1	992.4	0.2021217	0.00049	0.0065743	0.0001333	0.0000361	0.000013	0.0020811	0.0034695	0.0000561	9.56E-06	4.60201E-16	30.74403	0.1648497	0.0178	28.22768	0.4639951	91.79715	1.450187	568.9396	8.023589
0.0131	0.000026	0.959706	0.0009593	520.2	3.1	997	0.1333818	0.00027	0.0046896	0.0001261	0.0001536	1.00E-05	0.0356822	0.002896	0.0000496	9.51E-06	3.28272E-16	28.44183	0.1506642	0.0178	26.02405	0.6281445	91.01769	2.151303	530.4263	11.09597
0.0131	0.000026	0.959706	0.0009593	550.3	3.4	996.5	0.3553207	0.00095	0.0115901	0.0001511	0.0001227	0.000013	-0.0010852	0.0037691	0.0000934	0.0000105	8.11307E-16	30.65713	0.141598	0.0178	28.24082	0.3038194	92.12646	0.9461324	569.1667	5.253106
0.0131	0.000026	0.959706	0.0009593	549.9	3.4	997	0.2438502	0.00058	0.0076747	0.0000371	0.0000183	1.00E-05	-0.0019789	0.0046465	6.61E-06	0.0000113	5.37229E-16	31.77345	0.1533835	0.0178	31.48827	0.4682808	99.1225	1.423296	624.4617	7.852826
0.0131	0.000026	0.959706	0.0009593	519.7	2.8	1996.5	0.130446	0.00029	0.0038207	0.0000271	0.0001058	0.000013	0.0159846	0.0031974	0.0000967	9.05E-06	2.67449E-16	34.14175	0.2257803	0.0178	26.99789	0.7382037	78.84766	2.094873	547.5476	12.91723
0.0131	0.000026	0.959706	0.0009593	479.8	3.6	1996.6	0.0388332	0.00027	0.0070744	0.0000872	0.0000876	9.00E-06	0.0198008	0.0025342	0.0000763	9.55E-06	4.93088E-17	54.41631	1.474178	0.0178	24.81233	4.21057	44.70704	7.484147	508.894	75.26937
0.0131	0.000026	0.959706	0.0009593	451.9	3.6	2966.1	0.0253307	0.000075	0.0003333	0.0000251	-0.000021	0.000015	-0.0134927	0.0037918	0.0000611	3.93E-06	1.092E-17	162.38	23.0531	0.0178	36.37495	8.935649	23.74785	4.781281	704.6062	143.3495
0.0131	0.000026	0.959706	0.0009593	451.4	3.6	2996.5	0.0075923	0.000085	0.0001333	0.000019	6.63E-06	0.000012	-0.0112542	0.0035091	0.0000112	3.78E-06	9.331E-18	56.94844	7.209011	0.0178	23.80887	8.80209	44.26118	15.30965	490.8662	158.9254
0.0131	0.000026	0.959706	0.0009593	519.9	3	1996.6	0.1126558	0.00021	0.0033253	0.0000523	0.0000136	0.000011	0.0193158	0.0032225	0.0000622	0.0000104	2.32771E-16	33.87863	0.217701	0.0178	28.87133	0.9630006	84.87769	2.778339	580.0358	16.55071
0.0131	0.000026	0.959706	0.0009593	520.3	3.2	1997.1	0.1058697	0.00017	0.0031492	0.000021	0.0000777	1.00E-05	0.0128198	0.0035229	0.000026	9.13E-06	2.20444E-16	33.61823	0.2065247	0.0178	31.56369	0.897067	93.62502	2.59631	625.7261	15.03283
0.0131	0.000026	0.959706	0.0009593	549.3	4.1	996.5	0.5012889	0.001	0.0165267	0.0002555	8.40E-06	0.0007183	0.0028221	0.0009309	0.0000763	9.55E-06	1.15687E-15	30.33213	0.0906394	0.0178	29.81625	0.2235232	98.27218	0.7211566	596.2033	3.807408
0.0131	0.000026	0.959706	0.0009593	580.6	4.3	596.9	0.218971	0.00037	0.0073271	0.0000351	0.0001151	0.000013	0.0020634	0.002798	0.0000468	9.47E-06	7.41E-16	29.88513	0.1368017	0.0178	27.40906	0.1143392	99.0434	0.3744097	554.728	1.9928
0.0131	0.000026	0.959706	0.0009593	620.6	7.3	596.8	0.7490837	0.0013	0.0270527	0.0000681	0.000344	9.30E-06	-0.0214411	0.0041263	0.0000183	7.41E-06	1.89369E-15	27.68977	0.0789192	0.0178	27.40906	0.1143392	99.0434	0.3744097	554.728	1.9928
0.0131	0.000026	0.959706	0.0009593	619.7	7.9	596.8	0.5681334	0.00097	0.0191876	0.0000501	0.0003291	0.000011	0.0047024	0.0041323	0.0000764	9.51E-06	1.34313E-15	29.60942	0.0859388	0.0178	28.4442	0.1719196	96.05073	0.5482038	572.68	2.966759
0.0131	0.000026	0.959706	0.0009593	690.4	3.5	596.3	4.042264	0.0084	0.1156223	0.0002505	0.0015475	0.000013	-0.0277526	0.0041352	0.0000516	0.0000113	8.09356E-15	34.96093	0.09748	0.0178	34.8024	0.1017304	99.56524	0.2843752	679.2009	1.655094
0.0131	0.000026	0.959706	0.0009593	690.6	2.1	596.9	1.985648	0.0042	0.0486374	0.0001102	0.0006038	0.000011	-0.0079206	0.0035497	0.0000422	0.0000122	3.40462E-15	40.82556	0.1171308	0.0178	40.54828	0.138981	99.33384	0.3315573	770.3468	1.499985
0.0131	0.000026	0.959706	0.0009593	710.1	3.6	596.3	2.394592	0.0054	0.0561378	0.0001403	0.0006992	0.000011	-0.0100996	0.0024865	0.000033	0.0000113	3.92965E-15	42.65558	0.1317348	0.0178	42.45964	0.1488432	99.55483	0.3369492	799.6757	2.265502
0.0131	0.000026	0.959706	0.0009593	750.3	1.5	596.9	4.641371	0.0096	0.1068508	0.0002204	0.0011975	9.80E-06	-0.0531325	0.0028459	-0.0000149	0.0000121	7.47956E-15	43.43785	0.1181917	0.0178	43.42414	0.1229097	100.0047	0.2822465	814.2968	1.855708
0.0131	0.000026	0.959706	0.0009593	750	3.5	596.4	2.963297	0.007	0.0666653	0.0001603	0.0007711	0.000011	-0.0385246	0.0028479	-0.000015	9.41E-06	4.66657E-15	44.45038	0.1372481	0.0178	44.45297	0.143569	100.0477	0.3241224	829.7639	2.149163
0.0131	0.000026	0.959706	0.0009593	720.1	0.9	1996.5	3.459434	0.0083	0.0758188	0.0001904	0.0008756	0.000013	-0.0206462	0.0025847	2.48E-06	0.0000113	5.30732E-15	45.62765	0.1447784	0.0178	45.58688	0.1513902	99.93116	0.3291997	846.6588	2.245167
0.0131	0.000026	0.959706	0.0009593	720.1	1	1996.5	2.476345	0.0059	0.0540447	0.0001303	0.0006449	0.000011	0.0004797	0.0029749	0.0000543	0.0000131	3.78313E-15	45.82033	0.1421412	0.0178	45.52045	0.1594722	99.34652	0.3491243	845.6734	2.366314
0.0131	0.000026	0.959706	0.0009593	680.1	1.2	1996.6	0.6738045	0.001	0.0146613	0.0000331	0.000197	0.000011	-0.0006599	0.0028918	0.0000203	0.0000123	1.02629E-15	45.95796	0.1176978	0.0178	45.49868	0.2585694	99.03068	0.5364516	845.3503	3.837446
0.0131	0.000026	0.959706	0.0009593	630.2	2.4	1996.5	0.1413906	0.00026	0.0029577	0.00002	-0.0000353	0.000012	-0.0126921	0.0035823	-0.0000257	0.0000103	2.07039E-16	47.80469	0.2997033	0.0178	49.90547	1.092627	104.7075	2.203297	909.5968	15.6497
0.0131	0.000026	0.959706	0.0009593	650	2.2	2996.6	0.3866103	0.0008	0.0081867	0.0000927	9.90E-06	-0.0148577	0.0029616	-0.0000256	0.0000104	5.73069E-16	47.22438	0.1513584	47.95299	0.4093189	101.6725	0.8491949	881.4129	5.954772		
0.0131	0.000026	0.959706	0.0009593	599.8	5.1	2996.6	0.0696606	0.00014	0.0012848	0.0000223	-0.0000144	0.000013	-0.0276122	0.002967	-0.0000171	0.0000113	8.9936E-17	54.21744	0.8662921	0.0178	55.64744	2.739714	104.172	4.854268	990.0234	37.53373
0.0131	0.000026	0.959706	0.0009593	650	2.4	1996.6	0.2436237	0.00049	0.0051588	0.0000271	0.0000418	0.000011	-0.0257798	0.0033051	2.75E-06	0.0000121	3.61116E-16	47.2253	0.238009	0.0178	46.50772	0.7421226	98.8241	1.515468	860.2639	10.92342
0.0131	0.000026	0.959706	0.0009593	690.2	1.2	1996.5	0.7361537	0.0012	0.0157977	0.0000421	0.0001279	0.000011	-0.0332646	0.0039113	-0.0000893	9.15E-06	1.10584E-15	46.59866	0.14193	0.0178	48.04814	0.2260915	103.2631	0.4323962	882.7965	3.286664
0.0131	0.000026	0.959706	0.0009593	730.1	0.9	1996.5	1.848051	0.0039	0.0399626	0.0001002	0.0004092	0.000012	-0.0536602	0.0033173	-0.0000382	0.0000157	2.79738E-15	46.24456	0.139628	0.0178	46.37916	0.1826444	100.3863	0.3765797	858.3706	2.691189
0.0131	0.000026	0.959706	0.0009593	750.3	1	596.8	0.7376631	0.0012	0.0164156	0.0000421	0.0002119	0.000011	-0.0121145	0.0033218	-0.0000198	0.0000112	1.14999E-15	44.93659	0.1274096	0.0178	45.21481	0.2412301	100.6724	0.502598	841.1324	3.588473
0.0131	0.000026	0.959706	0.0009593	750.3	1	596.9	0.6754743	0.001	0.0151084	0.0000251	0.0001803	0.000014	0.0020027	0.0039315	-9.45E-06	0.0000121	1.05759E-15	44.70853	0.0971774	0.0178	44.90911	0.2598039	100.4411	0.5713956	836.5793	3.874516
0.0131	0.000026	0.959706	0.0009593	720.1	0.9	1997.1	0.9935762	0.0018	0.0217016	0.0000401	0.0002509	0.000012	-0.0222747	0.0030264	0.0000117	0.0000113	1.51911E-15	45.78348	0.1123912	0.0178	45.50738	0.1918162	99.46946	0.4136502	845.4795	2.846553
0.0131	0.000026	0.959706	0.0009593	720	1.2	1996	0.8707496	0.0015	0.0187949	0.0000471	0.000201	0.000011	-0.0215677	0.003336	-0.000036	0.0000112	1.31564E-15	46.32905	0.1313701	0.0178	46.77132	0.2221786	101.0368	0.4476991	864.1397	3.263281
0.0131	0.000026	0.959706	0.0009593	730.1	0.8	1996.5	0.9898938	0.002	0.0215428	0.0000631	0.000221	0.000012	-0.0158552	0.0036442	-0.0000325	0.0000103	1.508E-15	45.95005	0.149927	0.0178	46.31723	0.2081908	100.8523	0.4106008	857.4579	3.069153
0.0131	0.000026	0.959706	0.0009593	680.2	1.1	1997.1	0.2251386	0.00041	0.0047865	0.0000251	0.0000231	0.000011	-0.0201182	0.0036519	-9.63E-06	0.0000112	3.35055E-16	47.03664	0.2341824	0.0178	47.16416	0.7416766	100.5665	1.514761	869.9004	10.85883
0.0131	0.000026	0.959706	0.0009593	629.9	2.9	1996.5	0.0491561	0.00011	0.0009537	0.0000118	-0.0000569	0.000011	-0.0248009	0.0042663	5.50E-07	0.0000104	6.6759E-17	51.54188	0.8686869	0.0178	48.42571	3.317503	95.65355	6.329176	888.2769	48.08018
0.0131	0.000026	0.959706	0.0009593	630	2.7	2996.6	0.0718191	0.00013	0.0014514	0.0000419	-0.0000232	9.00E-06	-0.0182852	0.0029316	5.05E-06	0.0000104	1.01598E-16	49.48311	0.5808763	0.0178	47.0316	2.203713	95.87941	4.346239	867.9585	32.29907
0.0131	0.000026	0.959706	0.0009593	600.1	4.8	2997.1	0.0230448	0.000064	0.0004226	0.0000223	-0.0000168	0.000012	-0.0185474	0.0030593	2.84E-06	0.0000113	2.95828E-17	54.52545	2.631882	0.0178	47.58436	8.098064	89.93296	14.68217	876.042	118.1611
0.0131	0.000026	0.959706	0.0009593	649.8	4.2	1996.5	0.0898771	0.000096	0.0019658	0.0000251	0.0000105	1.00E-05	-0.0005711	0.0028831	1.01E-06	0.0000112	1.37606E-16	45.72021	0.5186828	0.0178	45.53302	1.791412	99.61227	3.747604	845.8598	26.57897
0.0131	0.000026	0.959706	0.0009593	690	1.8	1996.6	0.2763234	0.00054	0.0058357	0.0000251	-4.21E-06	8.70E-06	-0.0295648	0.0029485	-0.0000161	0.0000112	6.33E-06	47.3507	0.2017018	0.0178	47.6058	0.6096068	100.8943	1.243562	876.3548	8.893405
0.0131	0.000026	0.959706	0.0009593	730.1	1.8	1996.5	0.7614733	0.0013	0.0164223	0.0000411	0.0001015	0.000014	-0.0407924	0.0036933	-0.0000376	0.0000112	1.14956E-15	46.36822	0.1310387	0.0178	46.77339	0.1759965	101.0496	0.3373579	864.1701	2.584468
0.0131	0.000026	0.959706	0.0009593	730.3	1.1	592.3	0.9221237	0.0016	0.0366995	0.0000742	0.0004232	1.00E-05	-0.0568495	0.0036983	-0.0000606	0.0000112	2.56897E-15	25.1263	0.0633433	0.0178	25.46886	0.1110418	101.4754	0.429445	520.5923	1.972214
0.0131	0.000026	0.959706	0.0009593	830.4	1.1	296.6	0.9675439	0.0017	0.0365012	0.0000721	0.0004291	7.40E-06	-0.0350897	0.0029012	-0.0000315	0.0000112	2.55508E-15	26.50717	0.0663912	0.0178	26.66989	0.1132418	100.6839	0.4163233	541.7989	1.987837
0.0131	0.000026	0.959706	0.0009593	870.4	0.9	296.2	1.6705213	0.0036	0.0442124	0.0001102	0.0004682	0.000013	-0.0495555	0.003397	-0.000067	0.0000121	3.09487E-15	37.78385	0.1145885	0.0178	38.11679	0.1408749	100.9617	0.357141	732.3358	2.22558
0.0131	0.000026	0.959706	0.0009593	900.3	1	296.7	2.879662	0.0062	0.0614982	0.0001303	0.0007078	0.000013	-0.0360409	0.0034535	-0.0000407	0.0000103	4.30487E-15	46.82516	0.1311165	0.0178	46.95651	0.1403631	100.3229	0.3024104	866.8577	2.058506
0.0131	0.000026	0.959706	0.0009593	900.1	0.7	596.4	6.736619	0.015	0.1434109	0.0003307	0.0015821	1.00E-05	-0.0811894	0.0027015	-0.0000273	0.0000103	1.00388E-14	46.97244	0.138722	0.0178	46.96696	0.1403906	100.0254	0.2955962	867.011	2.057495
0.0131	0.000026	0.959706	0.0009593	920.5	1.4	596.3	9.764436	0.021	0.2037845	0.0004509	0.0020903	0.000011	-0.132693	0.0024223	-0.0001364	9.30E-06	1.42649E-14	47.9155	0.1368174	0.0178	48.04112	0.1374532	100.3091	0.2839741	882.6945	1.998252
0.0131	0.000026	0.959706	0.0009593	949.5	0.8	596.3	13.4752	0.027	0.2786951	0.0005912	0.0028096	0.000015	-0.170701	0.0037776	-0.0002217	0.0000102	1.95087E-14	48.35104	0.1315677	0.0178	48.51844	0.1322538	100.3905	0.2649089	889.6203	1.915315
0.0131	0.000026	0.959706	0.0009593	970.5	1.2	296.1	5.477648	0.012	0.1127161	0.0002505	0.0011391	8.10E-06	-0.0793231	0.0037831	0.0000102	7.89013E-15	48.59687	0.1401095	0.1427167	100.4304	0.2934049	893.425	2.062496			
0.0131	0.000026	0.959706	0.0009593	970.1	0.9	596.3	1.712826	0.0042	0.0351426	0.0000932	0.000311	0.000011	-0.0389052	0.0031229	-0.0000727	0.0000103	2.45998E-15	48.73934	49.23	0.0178	48.78143	0.1603248	100.1859	0.3699666	899.896	2.633782
0.0131	0.000026	0.959706	0.0009593	990.2	1	296.7	0.4116114	0.0012	0.0083953	0.0000192	0.0000111	0.000011	-0.0142981	0.0037907	0.0000134	0.0000103	5.87671E-16	49.56518	0.255726	0.0178	48.89545	0.4486207	98.76702	0.8339553	895.072	6.477418
0.0131	0.000026	0.959706	0.0009593	989.5	5.7	596.3	0.6971989	0.0018	0.014261	0.0000601	0.0001729	0.000011	-0.0237307	0.0030659	-1.38E-06	0.000013	9.9827E-16	48.88836	0.2168955	0.0178	48.72839	0.3485097	99.78956	0.6530665	892.6583	5.038686
0.0131	0.000026	0.959706	0.0009593	990	0.2	2996.5	3.043192	0.017	0.0708332	0.0022045	0.0041563	0.00051	0.9055534	0.1242263	0.0019033	0.0000778	4.95832E-15	42.96277	1.200088	0.0178	36.27973	1.096222	83.6957	1.0597	703.0779	17.60093

Table A.3: Blind mixture 2 data

J	± 1σ	Discrim	± 1σ	Temp (°C)	± 1σ (°C)	Heating duration (s)	^{40}Ar	± 1σ	^{39}Ar	± 1σ	^{38}Ar	± 1σ	^{37}Ar	± 1σ	^{36}Ar	± 1σ	^{39}Ar (Moles)	^{40}Ar/^{39}Ar	± 1σ	^{40}Ar*/^{39}Ar$_K$	± 1σ	% ^{40}Ar*	± 1σ	Age (Ma)	± 1σ
0.0131	0.000026	0.959706	0.0009593	360.1	5	2997	0.0102265	0.00016	0.000111	0.0000221	7.09E-06	0.000013	-0.0260579	0.0255661	0.000014	0.0000115	7.77E-18	92.48283	16.29485	31.18105	33.15111	39.21707	38.48207	619.3026	557.5153
0.0131	0.000026	0.959706	0.0009593	359.9	5	2996.5	0.0027754	0.00011	0.0000465	0.0000221	-9.40E-06	0.000011	-0.0303188	0.0130774	-1.73E-07	0.0000125	3.255E-18	59.74487	25.1605	6.307449	57.31907	15.34637	138.8668	143.5513	1254.085
0.0131	0.000026	0.959706	0.0009593	389.9	3.4	2996.5	0.0104924	0.00015	0.0003467	0.0000201	-0.0000123	0.000015	-0.0510926	0.0282898	-0.0000103	0.0000106	2.4269E-17	30.26163	1.590507	24.87625	10.7836	90.62522	36.38775	510.0362	192.649
0.0131	0.000026	0.959706	0.0009593	389.9	3.2	2996.5	0.0073496	0.00015	0.0002975	0.0000201	-9.61E-06	9.60E-06	-0.0336676	0.0309531	-6.42E-06	0.0000115	2.0825E-17	24.70283	1.533022	20.56697	13.81671	89.80836	56.70746	431.3639	257.8123
0.0131	0.000026	0.959706	0.0009593	420	2.6	2997	0.0279194	0.00025	0.0011012	0.0000231	0.0000668	0.000012	0.0624452	0.0240599	0.000081	0.0000125	7.7084E-17	25.35248	0.5079521	8.210972	3.986992	31.11177	14.88055	184.7261	85.26751
0.0131	0.000026	0.959706	0.0009593	419.9	2.7	2996.5	0.0201108	0.0002	0.0009598	0.0000191	0.000011	8.50E-06	-0.0126755	0.0254286	-1.05E-07	0.0000115	6.7186E-17	20.95204	0.408452	19.75769	4.267218	95.16842	19.6428	416.1998	80.29456
0.0131	0.000026	0.959706	0.0009593	450.1	3.1	1796.7	0.0408096	0.00026	0.0029659	0.0000281	0.0000452	9.10E-06	0.0399376	0.0260245	0.000056	0.0000134	1.44613E-16	19.75401	0.2609792	13.36864	2.254098	66.76877	10.97207	291.7966	45.43538
0.0131	0.000026	0.959706	0.0009593	499.9	2.1	1796.7	0.2070489	0.00069	0.0124986	0.0000501	0.0001634	0.000012	0.1937318	0.0286881	0.000179	0.0000125	8.749026-16	16.56575	0.0769291	13.66363	0.3678939	81.59625	2.123068	297.7328	7.391253
0.0131	0.000026	0.959706	0.0009593	449.9	2.8	2996.5	0.0229244	0.00018	0.0014968	0.0000231	0.0000306	7.90E-06	-0.0855345	0.0287494	0.0000267	9.60E-06	1.04776E-16	15.31533	0.232713	5.2513369	2.3580045	35.65186	15.73247	120.2964	52.25952
0.0131	0.000026	0.959706	0.0009593	459.9	3	2997	0.0500088	0.00027	0.0021533	0.0000241	5.99E-06	0.000014	-0.0966406	0.0289203	0.0000667	9.60E-06	1.50731E-16	23.22419	0.2539652	10.10449	1.688118	44.86704	7.24017	224.7749	35.31196
0.0131	0.000026	0.959706	0.0009593	479.9	3.7	2996.5	0.0709715	0.00038	0.0046233	0.0000341	0.0000736	0.000011	0.0184491	0.023996	0.0000502	0.0000125	3.23631E-16	15.35086	0.122925	12.45735	0.9255436	80.9296	5.874921	273.3339	18.84745
0.0131	0.000026	0.959706	0.0009593	530.1	2	1796.7	0.3385708	0.00085	0.0210392	0.0000622	0.0002651	0.000012	0.0530494	0.0317369	0.0001502	0.0000115	1.47274E-15	16.09236	0.0565714	14.18397	0.2157597	87.9906	1.278427	308.1568	4.30985
0.0131	0.000026	0.959706	0.0009593	570.2	1.7	956.9	0.5886625	0.0013	0.0340217	0.0000852	0.0004527	1.00E-05	0.0519671	0.0291543	0.0001194	0.0000115	2.38152E-15	17.30255	0.0530862	16.39213	0.1361522	94.64166	0.748554	351.7358	2.664908
0.0131	0.000026	0.959706	0.0009593	570.1	1.7	1796.7	0.7793848	0.0017	0.045773	0.0001003	0.0005811	0.000013	0.1676624	0.0260147	0.000175	0.0000125	3.20411E-15	17.02718	0.0486784	16.21587	0.1072349	94.99687	0.6086425	348.2956	2.095015
0.0131	0.000026	0.959706	0.0009593	630.1	1.1	957.4	2.028456	0.0038	0.1125345	0.0002306	0.0013694	0.000012	0.0538706	0.034583	0.0002713	0.0000135	7.87742E-15	18.02519	0.0470274	17.34835	0.0649113	96.21692	0.3372906	370.2862	1.252823
0.0131	0.000026	0.959706	0.0009593	630	1.1	1796.7	1.975986	0.0038	0.1123538	0.0002306	0.0013694	1.00E-05	0.0545234	0.029339	0.0001909	0.0000106	7.86477E-15	17.58718	0.0463757	17.1232	0.0588551	97.33307	0.3161292	365.9355	1.138671
0.0131	0.000026	0.959706	0.0009593	519.9	1.8	1796.7	0.0269572	0.00017	0.0019376	0.0000241	0.0000426	1.00E-05	-0.028218	0.0294019	0.0000263	0.0000115	1.35632E-16	13.9125	0.1704864	8.6164485	2.145305	62.56359	15.21543	193.3778	45.66139
0.0131	0.000026	0.959706	0.0009593	500	1.8	2996.5	0.0149316	0.00019	0.0011957	0.0000231	0.0000159	8.90E-06	0.0200006	0.0259827	0.0000229	0.0000106	8.3699E-17	12.48799	0.252324	8.185404	3.217384	64.78795	24.93729	184.1792	68.82914
0.0131	0.000026	0.959706	0.0009593	450	3.3	2996.5	0.0227751	0.00012	0.002933	0.0000221	0.0000182	9.90E-06	-0.051463	0.0404187	-9.30E-06	0.0000134	2.0531E-16	7.765013	0.0626917	7.233051	1.742335	94.29413	22.18015	163.69	37.69836
0.0131	0.000026	0.959706	0.0009593	500	1.8	2997	0.0219817	0.00015	0.0010722	0.0000191	0.000016	8.30E-06	-0.0617314	0.0351335	0.0000247	0.0000106	7.5054E-17	20.50173	0.3438244	8.710375	3.827987	44.18777	18.7958	195.3751	81.38622
0.0131	0.000026	0.959706	0.0009593	559.9	3.3	2997	0.1940798	0.00063	0.0121392	0.0000451	0.0001634	0.000011	0.0966699	0.027106	0.0000321	0.0000125	8.49744E-16	15.98785	0.0703818	15.91574	0.3713931	99.00249	2.232838	342.4225	7.279397
0.0131	0.000026	0.959706	0.0009593	600	2.9	1796.7	0.4558347	0.001	0.0262334	0.0000712	0.0000331	0.000011	0.1243009	0.0258271	0.0000611	0.0000125	1.86634E-15	17.37615	0.0555441	17.11131	0.1755622	98.15569	0.966146	365.7054	3.397038
0.0131	0.000026	0.959706	0.0009593	640	1	1801.2	1.47784	0.0025	0.0813521	0.0001605	0.0009947	0.000012	0.1382936	0.0242476	0.0001604	0.0000125	5.69465E-15	18.16598	0.044859	17.73205	0.6693991	97.49988	0.3563389	377.6767	1.333976
0.0131	0.000026	0.959706	0.0009593	669.5	1	1796.7	2.673966	0.005	0.1447093	0.0002908	0.0017667	0.000012	0.0300329	0.0302497	0.0000115	1.01297E-14	18.47819	0.0477258	17.99504	0.0563783	97.19662	0.2865317	382.0346	1.081083
0.0131	0.000026	0.959706	0.0009593	724.4	1.1	597.3	2.618242	0.0051	0.1346386	0.0002808	0.0016212	7.60E-06	-0.0118692	0.027361	0.0001253	9.25E-06	9.4247E-15	19.44644	0.0519182	19.15966	0.0586316	98.53503	0.2856246	404.9118	1.110156
0.0131	0.000026	0.959706	0.0009593	745.1	0.9	596.9	2.762061	0.0053	0.1431788	0.0002908	0.0017815	8.90E-06	0.0307899	0.0273968	0.0000579	0.0000115	1.00225E-14	19.29698	0.0505714	19.18939	0.0585263	99.46229	0.2900711	405.4747	1.107817
0.0131	0.000026	0.959706	0.0009593	778	0.5	596.9	4.174287	0.0078	0.214321	0.0004812	0.0025718	0.000014	-0.1797948	0.0266098	0.0001136	9.44E-06	1.50025E-14	19.4768	0.0503194	19.24008	0.0531016	98.84593	0.2572124	406.4339	1.004604
0.0131	0.000026	0.959706	0.0009593	776.5	0.6	1796.7	7.453327	0.013	0.3793138	0.000712	0.0045251	0.000015	-0.3416119	0.0236252	0.0001611	0.0000134	2.6552E-14	19.6495	0.0478956	19.43842	0.0493275	98.99137	0.2349357	410.1822	0.931271
0.0131	0.000026	0.959706	0.0009593	806.9	2.6	296	1.484722	0.0025	0.0748035	0.0001404	0.0008785	0.000011	-0.1736676	0.0253275	0.0000722	0.0000143	5.23625E-15	19.84829	0.0477672	19.34433	0.0802845	97.62183	0.3840499	408.4051	1.517208
0.0131	0.000026	0.959706	0.0009593	804.3	2.3	596	2.159187	0.0041	0.1084902	0.0002206	0.0013176	0.000012	-0.0649333	0.0237008	0.0000618	0.0000125	7.59431E-15	19.99214	0.0519938	19.67563	0.0652408	98.99665	0.3130574	414.6552	1.229866
0.0131	0.000026	0.959706	0.0009593	802.4	2.1	956	2.364498	0.0048	0.1179449	0.0002507	0.0014461	0.000012	-0.0583949	0.0275941	0.0001148	0.0000105	8.25614E-15	20.04748	0.054884	19.71007	0.0644069	98.35441	0.3083748	415.3036	1.212519
0.0131	0.000026	0.959706	0.0009593	799.6	1.4	1796	2.837274	0.0075	0.1395015	0.0004011	0.0017911	0.000019	0.0836322	0.0525113	0.0003113	0.000023	9.76511E-15	20.33866	0.07187728	19.72747	0.092962	96.95802	0.4407672	415.6311	1.74978
0.0131	0.000026	0.959706	0.0009593	809.8	1.8	956	1.313234	0.0024	0.0652812	0.0001404	0.0008394	0.000012	0.0230907	0.0257483	0.0000794	9.10E-06	4.56968E-15	20.11658	0.0532861	19.78544	0.0761988	98.33333	0.3483317	416.722	1.433388

Table A.4: Blind mixture 4 data

J	± 1σ	Discrim	± 1σ	Temp (°C)	± 1σ (°C)	Heating duration (s)	^{40}Ar	± 1σ	^{39}Ar	± 1σ	^{38}Ar	± 1σ	^{37}Ar	± 1σ	^{36}Ar	± 1σ	^{39}Ar (Moles)	^{40}Ar/^{39}Ar	± 1σ	^{40}Ar*/^{39}Ar$_K$	± 1σ	% ^{40}Ar*	± 1σ	Age (Ma)	± 1σ
0.0131	0.000026	0.959706	0.0000593	379.8	3.9	1796.7	0.4361974	0.0014	0.0021937	0.0000251	0.0002069	0.000012	0.0739383	0.0317395	0.0008409	0.000117	1.53559E-16	198.8394	2.089827	89.15528	2.850512	43.78769	1.018448	1399.104	31.14466
0.0131	0.000026	0.959706	0.0000593	379.9	4.1	2996.5	0.0161518	0.00024	0.0006686	0.0000231	-0.0000227	0.000012	0.122384	0.0318074	0.000068	1.18E-06	4.68029E-17	24.15903	0.7975645	9.452384	4.552386	34.14885	15.18262	211.0824	95.9504
0.0131	0.000026	0.959706	0.0000593	420.2	2.9	1996.7	0.0341515	0.00028	0.0013655	0.0000211	0.0000169	0.000011	0.0222113	0.0299015	0.0001074	0.0000134	9.5585E-17	25.01043	0.3835826	2.8469	3.413934	11.25449	13.4121	66.20698	77.95788
0.0131	0.000026	0.959706	0.0000593	420.1	3	2996.5	0.0188253	0.00023	0.0009503	0.0000271	0.0000236	9.80E-06	-0.0014783	0.0252853	0.0000546	0.0000106	6.6521E-17	19.80963	0.5398681	2.527272	3.910501	12.77206	19.63852	58.89345	89.65901
0.0131	0.000026	0.959706	0.0000593	470	2.8	1796.7	0.068303	0.0004	0.0023991	0.0000231	0.000014	0.000011	0.0324521	0.0349796	0.0001003	0.0000115	1.67937E-16	28.4708	0.2817058	17.2178	1.947885	59.90827	6.38929	367.7647	37.64767
0.0131	0.000026	0.959706	0.0000593	469.9	3	2997	0.0279559	0.00028	0.00197	0.0000201	0.0000349	0.000011	0.0089714	0.0321332	0.0000246	0.0000115	1.379E-16	14.1911	0.1762109	10.85416	2.222984	76.24749	15.12315	240.3888	46.10043
0.0131	0.000026	0.959706	0.0000593	549.8	2.1	597.3	0.1067198	0.00048	0.009816	0.0000612	0.000189	0.000013	0.1833353	0.0322285	0.0001227	0.0000125	6.87123E-16	10.87201	0.0736592	8.730472	0.4755998	79.26518	4.208173	195.8024	10.10926
0.0131	0.000026	0.959706	0.0000593	550.1	2.2	2996.5	0.2541203	0.00079	0.0314072	0.0001003	0.0005397	8.80E-06	0.0582825	0.0322708	0.0003262	0.0000154	2.1985E-15	8.091144	0.0322836	5.143488	0.1704655	63.4931	2.074662	117.9039	3.782896
0.0131	0.000026	0.959706	0.0000593	649.8	1	596.8	0.7576925	0.0017	0.1420918	0.000341	0.0024054	0.000012	-0.0153339	0.0282472	0.0003488	0.0000106	9.94643E-15	5.332414	0.0161043	4.590661	0.0315369	86.10798	0.5720553	105.594	0.7046331
0.0131	0.000026	0.959706	0.0000593	650	1	2996.5	0.9026034	0.0023	0.1836037	0.0004914	0.0030842	0.000011	0.084829	0.0412478	0.0002692	0.0000144	1.28532E-14	4.916042	0.0165025	4.5164	0.033614	91.8548	0.6704189	103.934	0.7517337
0.0131	0.000026	0.959706	0.0000593	689.8	0.7	296.7	0.1677072	0.00055	0.0356892	0.0001504	0.000606	0.000011	0.0991473	0.0233446	0.0000556	0.0000105	2.49824E-15	4.699106	0.022349	4.462253	0.1046924	94.79099	2.193985	102.7227	2.342876
0.0131	0.000026	0.959706	0.0000593	690	0.7	1797.7	0.6620216	0.0015	0.1396458	0.000361	0.0023421	0.000014	0.0564966	0.0325395	0.0001749	0.0000134	9.77521E-15	4.740721	0.0149282	4.400111	0.0371669	92.80343	0.7666451	101.3315	0.832387
0.0131	0.000026	0.959706	0.0000593	730	0.4	296.6	0.2566844	0.00068	0.0537505	0.0001605	0.0009066	0.000016	-0.0036416	0.0278648	0.0000508	0.0000134	3.76254E-15	4.775479	0.0172264	4.487609	0.086656	93.99072	1.796096	103.29	1.938637
0.0131	0.000026	0.959706	0.0000593	729.7	0.6	601.4	0.2937504	0.00069	0.0590619	0.0001605	0.0009853	0.000014	0.0832186	0.0287847	0.0000566	0.0000125	4.13433E-15	4.973603	0.0162968	4.803674	0.0757058	96.50296	1.500069	110.3471	1.687066
0.0131	0.000026	0.959706	0.0000593	779.9	0.3	296.7	0.3278375	0.00076	0.0643411	0.0001705	0.0010547	0.000011	0.0949302	0.0255528	0.0000765	0.0000115	4.51018E-15	5.088186	0.016359	4.855234	0.064007	95.33768	1.238803	111.4958	1.425458
0.0131	0.000026	0.959706	0.0000593	779.2	0.4	597.4	0.2322913	0.00058	0.0426124	0.0001203	0.0007193	6.60E-06	0.1435883	0.0327185	0.0000757	0.0000115	2.29828TE-15	5.451257	0.0186598	5.199873	0.1030262	95.17787	1.853319	119.1548	2.284732
0.0131	0.000026	0.959706	0.0000593	778.8	0.4	596.8	0.1316848	0.00043	0.0239518	0.0000983	0.0004063	0.000014	0.1720671	0.0357381	0.0000486	0.0000115	1.67663E-15	5.497906	0.0256859	5.488382	0.1889828	99.3415	3.353035	125.5415	4.176147
0.0131	0.000026	0.959706	0.0000593	799.4	0.5	296.6	0.1413338	0.00042	0.0281993	0.0001003	0.000483	9.60E-06	0.1391506	0.0289262	0.0000396	0.0000115	1.97395E-15	5.011957	0.0208077	5	0.1483968	99.43374	2.910193	114.7169	3.298966
0.0131	0.000026	0.959706	0.0000593	686.8	0.8	2996.5	0.0583248	0.0004	0.0110434	0.0000752	0.0001832	0.000014	0.0194823	0.0286584	0.000034	0.0000106	7.73035E-16	5.281433	0.0445301	4.50709	0.3542543	85.24554	6.619984	103.7258	7.923343
0.0131	0.000026	0.959706	0.0000593	733.4	0.9	2996.5	0.0884851	0.00061	0.0156684	0.0001103	0.000299	0.000017	0.2330346	0.0419157	0.0000848	0.0000153	1.09679E-15	5.647361	0.0485571	5.263444	0.3685351	92.25025	6.367379	120.564	8.166349
0.0131	0.000026	0.959706	0.0000593	766.6	0.5	2996.5	0.2356539	0.0008	0.0460452	0.0001605	0.0008121	0.000015	0.2709038	0.0273261	0.0001357	0.0000144	3.22316E-15	5.117877	0.0221792	4.723341	0.1072411	91.92671	2.071097	108.5561	2.392184
0.0131	0.000026	0.959706	0.0000593	799.1	0.8	1796.7	0.5734568	0.0013	0.123604	0.0003009	0.0020599	0.000015	-0.0025147	0.0301178	0.0000708	0.0000144	8.65228E-15	4.689467	0.0141685	4.46692	0.0421322	96.29741	0.8969938	102.8271	0.9428075
0.0131	0.000026	0.959706	0.0000593	819.9	0.3	296.7	0.1842781	0.00053	0.0401064	0.0001304	0.0006594	0.000015	0.0364692	0.0226366	0.0000116	0.0000115	2.80745E-15	4.594733	0.0179182	4.583409	0.0982011	99.70636	2.116958	105.432	2.19432
0.0131	0.000026	0.959706	0.0000593	818.8	1	1796.7	0.543938	0.0013	0.1127409	0.0002908	0.0018949	0.000011	0.0692172	0.0217542	0.000119	0.0000106	7.89186E-15	4.824674	0.0154909	4.560259	0.0353738	94.49351	0.7214298	104.9146	0.7906813

Table A.5: Blind mixture 5 data

J	± 1σ	Discrim	± 1σ	Temp (°C)	± 1σ (°C)	Heating duration (s)	^{40}Ar	± 1σ	^{39}Ar	± 1σ	^{38}Ar	± 1σ	^{37}Ar	± 1σ	^{36}Ar	± 1σ	^{39}Ar (Moles)	^{40}Ar/^{39}Ar	± 1σ	^{40}Ar*/^{39}Ar$_K$	± 1σ	% ^{40}Ar*	± 1σ	Age (Ma)	± 1σ
0.0131	0.000026	0.959706	0.0009593	359.9	6	2996.5	0.3898184	0.001	0.0040775	0.0000221	0.0001752	0.000012	0.0534401	0.0364586	0.0004286	0.0000111	2.85425E-16	95.60193	0.5113726	65.855	1.42405	68.25767	1.144659	1124.722	18.10878
0.0131	0.000026	0.959706	0.0009593	379.9	4.2	2996.5	0.0233503	0.00021	0.0020678	0.0000261	0.0000373	8.90E-06	-0.0778425	0.0365653	-9.16E-06	9.16E-06	1.44746E-16	11.2926	0.1529521	1.919744	85.34885	16.72646	209.8037	40.49097
0.0131	0.000026	0.959706	0.0009593	400	3.4	2996.5	0.0259925	0.00022	0.00225	0.0000331	0.0000427	0.000012	-0.165746	0.0400077	4.78E-06	0.0000125	2.275E-16	7.997779	0.0924345	3.402273	1.448313	44.05222	18.52863	78.84478	32.84217
0.0131	0.000026	0.959706	0.0009593	439.8	2.9	1796.7	0.0711361	0.00036	0.0093608	0.0000481	0.0001846	0.000013	0.0866811	0.0334387	0.0000967	0.0000125	6.55256E-16	7.599392	0.0481185	5.283236	0.4942572	69.08101	6.366861	121.0025	10.94956
0.0131	0.000026	0.959706	0.0009593	479.8	4	1797.7	0.1656479	0.00055	0.0234396	0.0000923	0.0003995	0.000013	0.123047	0.033175	0.0001141	0.0000125	1.64077E-15	7.066998	0.0324151	6.05086	0.1984567	85.31778	2.746869	137.9286	4.355122
0.0131	0.000026	0.959706	0.0009593	519.9	2.1	896.6	0.1826626	0.00062	0.0355947	0.0001203	0.0006358	9.10E-06	0.1493513	0.0335817	0.0001018	8.93E-06	2.49163E-15	5.131737	0.0219057	4.623276	0.1081782	89.84187	2.063815	106.3226	2.416069
0.0131	0.000026	0.959706	0.0009593	559.9	3.7	896.6	0.395706	0.00092	0.0832085	0.0002307	0.0014049	1.00E-05	0.0459967	0.0336326	0.0002188	0.0000106	5.8246E-15	4.755594	0.0156959	4.01604	0.0518325	84.42927	1.063646	92.70935	1.166383
0.0131	0.000026	0.959706	0.0009593	599.7	3.4	596.9	0.6387273	0.0013	0.1387956	0.000331	0.0023196	0.000012	0.0531138	0.0306521	0.0002579	0.0000115	9.71569E-15	4.601928	0.0133556	4.078691	0.0330882	88.62053	0.6975721	94.11863	0.7440017
0.0131	0.000026	0.959706	0.0009593	639.9	1	597.3	1.184863	0.0019	0.2519029	0.0004714	0.004181	0.000014	-0.1591618	0.0300177	0.000566	0.0000107	1.76332E-14	4.70365	0.0111163	3.981081	0.0194858	84.68845	0.3834215	91.9225	0.4386795
0.0131	0.000026	0.959706	0.0009593	699.8	0.8	296.6	1.389105	0.0024	0.3038625	0.0005817	0.0050563	0.000018	0.2712568	0.033772	0.0005657	0.000013	2.12704E-14	4.571491	0.0112076	4.088912	0.0192442	89.40252	0.3971619	94.34846	0.4326586
0.0131	0.000026	0.959706	0.0009593	680.1	0.7	596.9	0.4586152	0.00099	0.1034047	0.0002507	0.0017166	0.000014	0.0514277	0.0301427	0.0000683	0.0000134	7.23833E-15	4.435147	0.0132655	4.278961	0.0470585	96.46098	1.045976	98.6162	1.0655
0.0131	0.000026	0.959706	0.0009593	629.9	1.1	901.2	0.0790754	0.00031	0.0174418	0.0000913	0.0002959	0.000014	-0.0542544	0.0440059	0.0000228	9.58E-06	1.22093E-15	4.533676	0.0262213	3.888791	0.2578224	85.97498	5.584411	89.84361	5.810966
0.0131	0.000026	0.959706	0.0009593	579.9	3	1796.8	0.0304564	0.00019	0.0054366	0.0000371	0.0001109	7.00E-06	-0.0265501	0.033902	0.000028	0.0000124	3.80562E-16	5.602051	0.0453055	3.664784	0.8384874	65.64925	14.86282	84.78775	18.95128
0.0131	0.000026	0.959706	0.0009593	469.8	5.6	2996.6	0.0113412	0.00001	0.0012906	0.0000201	-8.48E-06	0.000013	-0.0000326	0.0339605	7.26E-06	2.31E-06	9.0342E-17	8.787803	0.1212249	7.100974	2.191358	80.81303	23.54035	160.83	47.48877
0.0131	0.000026	0.959706	0.0009593	524.9	3.8	3001.2	0.0062958	0.0001	0.0011378	0.0000201	8.88E-06	0.00001	0.0447848	0.0374673	6.69E-06	1.61E-06	7.96466E-17	5.533286	0.1141215	7.084666	2.768762	124.5507	45.9021	160.4766	60.01339
0.0131	0.000026	0.959706	0.0009593	564.8	5.2	3001.2	0.0195236	0.00021	0.0041123	0.0000311	0.0000753	0.000012	0.0636061	0.0317709	0.0000371	8.54E-06	2.87861E-16	4.7476	0.0539045	3.310062	0.8761277	68.98176	18.01783	76.75257	19.80021
0.0131	0.000026	0.959706	0.0009593	615.1	1.8	1796.7	0.0591377	0.00032	0.0131698	0.0000772	0.0001772	0.000012	0.1131207	0.03789	0.000025	0.0000106	9.21886E-16	4.490413	0.0314118	4.629696	0.3329879	102.5029	7.240044	106.466	7.436416
0.0131	0.000026	0.959706	0.0009593	678	0.7	1796.8	0.3677205	0.00084	0.0815311	0.0002206	0.0013312	0.000014	0.0253747	0.0446379	0.0001331	0.0000125	5.70718E-15	4.510185	0.0145982	4.048266	0.0644525	89.75343	1.399655	93.43439	1.449789
0.0131	0.000026	0.959706	0.0009593	731.9	0.6	596.9	0.2819149	0.00064	0.0596705	0.0001605	0.0010841	1.00E-05	0.0666662	0.0344102	0.0002687	0.000013	4.17694E-15	4.724529	0.0152055	3.463275	0.0806358	73.26366	1.679544	80.22753	1.827111
0.0131	0.000026	0.959706	0.0009593	730.9	3.4	596.9	0.1045146	0.00035	0.0204873	0.0000772	0.0004217	0.000012	0.3396072	0.0379008	0.000212	0.000012	1.43411E-15	5.101425	0.0229113	3.362905	0.2309108	65.17068	4.417817	77.95184	5.238755
0.0131	0.000026	0.959706	0.0009593	760.6	1	596.9	0.1887539	0.00053	0.0384945	0.0001304	0.0006842	0.000013	0.3854147	0.0331204	0.0002764	0.000011	2.69462E-15	4.903403	0.013899	3.576895	0.1112756	72.45032	2.218412	82.80021	2.51779
0.0131	0.000026	0.959706	0.0009593	785.9	0.4	597.4	0.375658	0.0008	0.078091	0.0001906	0.0014028	0.000012	0.2337401	0.0414548	0.0003469	6.60E-06	5.46637E-15	4.810514	0.0143632	3.729005	0.0509306	77.36827	1.019426	86.23866	1.150197
0.0131	0.000026	0.959706	0.0009593	785.5	0.7	596.9	0.1823911	0.00045	0.0367523	0.0001304	0.0006539	9.50E-06	0.3231167	0.0335532	0.0002733	0.000011	2.57266E-15	4.962714	0.0193561	3.45944	0.1167601	69.29284	2.298444	80.14065	2.644414
0.0131	0.000026	0.959706	0.0009593	800	0.3	596.9	0.2686328	0.00059	0.0566283	0.0001404	0.0009686	8.40E-06	-0.0187483	0.0256308	0.0001284	9.61E-06	3.96398E-15	4.743792	0.0144462	4.039874	0.063513	85.194	1.317353	93.24562	1.428807
0.0131	0.000026	0.959706	0.0009593	799.7	0.3	896.6	0.2466366	0.00062	0.0528249	0.0001504	0.0008896	0.000013	0.0794183	0.0343348	0.0001013	8.55E-06	3.69774E-15	4.66895	0.0160949	4.219754	0.0722227	90.29875	1.512129	97.28772	1.621114
0.0131	0.000026	0.959706	0.0009593	799.4	0.7	1797.7	0.3177108	0.00079	0.0676425	0.0001805	0.0011092	1.00E-05	0.0326689	0.0382077	0.000158	0.0000125	4.73498E-15	4.696911	0.0155874	4.039333	0.0724809	85.98429	1.518	93.23344	1.630562
0.0131	0.000026	0.959706	0.0009593	798.6	1.3	2997	0.3173858	0.00089	0.0671582	0.0002006	0.0011259	0.000013	-0.063206	0.0348085	0.0001672	0.0000107	4.70107E-15	4.725944	0.0174461	3.905514	0.0640249	82.76681	1.35109	90.22049	1.463015

Table A.6: Blind mixture 6 data

J	± 1σ	Discrim	± 1σ	Temp (°C)	± 1σ (°C)	Heating duration (s)	^{40}Ar	± 1σ	^{39}Ar	± 1σ	^{38}Ar	± 1σ	^{37}Ar	± 1σ	^{36}Ar	± 1σ	^{39}Ar (Moles)	^{40}Ar/^{39}Ar	± 1σ	^{40}Ar*/^{39}Ar$_K$	± 1σ	% ^{40}Ar*	± 1σ	Age (Ma)	± 1σ
0.00915	0.000018	0.959706	0.0009593	386.9	2.9	296.6	1.193814	0.0027647	0.0549132	0.0001975	0.0011484	0.0000328	0.0145358	0.0000135	0.0023857	0.0000352	5.49E-14	21.74001	0.0929952	8.769257	0.2001914	40.33605	0.9141268	139.5571	3.066072
0.00915	0.000018	0.959706	0.0009593	399.3	2.9	296.6	0.182034	0.0014469	0.0177509	0.0001499	0.0002842	0.0000282	0.0003891	0.0000708	0.0002057	0.0000294	1.78E-14	10.25493	0.1189191	6.795774	0.5044356	66.26834	4.915324	109.0763	7.857127
0.00915	0.000018	0.959706	0.0009593	413.0	3.0	296.6	0.173734	0.0014469	0.0169539	0.0001223	0.0002553	0.0000275	0.0055275	0.0007869	0.0001494	0.0000299	1.70E-14	10.24743	0.1128886	7.616053	0.5360148	74.32157	5.239877	121.8081	8.290425
0.00915	0.000018	0.959706	0.0009593	427.4	2.5	296.7	0.218984	0.0018557	0.0181083	0.0001593	0.0002338	0.0000295	0.0036162	0.0007726	0.000122	0.0000306	1.81E-14	12.093	0.147704	10.08172	0.5223357	83.36821	4.314833	159.5475	7.911982
0.00915	0.000018	0.959706	0.0009593	435.0	2.5	296.6	0.208844	0.0015243	0.0160108	0.0001313	0.0002092	0.0000291	0.0033394	0.0007591	0.0000597	0.0000299	1.60E-14	13.04397	0.1432291	11.93045	0.5736832	91.4633	4.384704	187.3361	8.557231
0.00915	0.000018	0.959706	0.0009593	435.3	2.4	296.6	0.153191	0.0013652	0.0115261	0.0001003	0.0001706	0.0000286	0.0035966	0.0007676	0.0000539	0.0000306	1.15E-14	13.2908	0.1655383	11.89368	0.8078628	89.48803	6.08079	186.7875	12.05398
0.00915	0.000018	0.959706	0.0009593	449.8	2.1	297.7	0.238354	0.0016042	0.0154192	0.0001133	0.0002505	0.0000282	0.0043028	0.0007252	0.0000408	0.0000296	1.54E-14	15.4583	0.154047	14.66956	0.5917099	94.89762	3.817514	227.7388	8.631092
0.00915	0.000018	0.959706	0.0009593	461.0	2.0	296.6	0.292674	0.0016042	0.0171336	0.0001133	0.0002265	0.0000286	0.0068223	0.0007761	0.000061	0.0000296	1.71E-14	17.08191	0.146731	16.01912	0.5342215	93.77822	3.108987	247.3179	7.708603
0.00915	0.000018	0.959706	0.0009593	475.6	1.6	296.7	0.400114	0.0016863	0.0232336	0.0001223	0.0002304	0.0000291	0.007357	0.0007922	0.0000635	0.0000306	2.32E-14	17.22133	0.1160997	16.40508	0.4089732	95.26026	2.355761	252.8787	5.883198
0.00915	0.000018	0.959706	0.0009593	490.2	2.2	296.6	0.388524	0.0016863	0.0245122	0.0001313	0.0002983	0.0000282	0.0089855	0.0007634	0.0000158	0.0000299	2.45E-14	16.25819	0.111004	16.06568	0.3802367	98.81592	2.316062	247.9896	5.484625
0.00915	0.000018	0.959706	0.0009593	503.0	2.0	297.7	0.394394	0.0016863	0.0257267	0.0001313	0.0003592	0.0000276	0.0100952	0.0007459	0.0000705	0.0000296	2.57E-14	15.33014	0.1020877	14.5126	0.3570792	94.66707	2.314233	225.4477	5.215209
0.00915	0.000018	0.959706	0.0009593	510.3	1.7	296.6	0.325014	0.0016042	0.0224237	0.0001313	0.0003276	0.0000291	0.0105381	0.0007796	0.0000243	0.000031	2.24E-14	14.49424	0.1110227	14.1706	0.4268219	97.76712	2.928575	220.4459	6.251083
0.00915	0.000018	0.959706	0.0009593	435.1	2.3	1796.7	0.079836	0.0009405	0.0072491	0.0000722	-0.0000108	0.0000291	0.0047089	0.0006896	0.0000173	0.0000204	7.25E-15	11.01326	0.1698729	10.30146	0.8546125	93.53604	7.782152	162.8729	12.9213
0.00915	0.000018	0.959706	0.0009593	470.3	2.2	1796.7	0.215425	0.0012828	0.0176086	0.0001042	0.0002214	0.0000291	0.008752	0.0007127	0.0000083	0.0000213	1.76E-14	12.23408	0.1027294	10.82613	0.3741105	88.49155	3.058452	170.7883	5.631649
0.00915	0.000018	0.959706	0.0009593	510.0	1.8	1796.7	0.721865	0.0016388	0.0496392	0.0001431	0.0005912	0.0000274	0.0271185	0.0006803	0.0001006	0.0000208	4.96E-14	14.54223	0.053372	13.93735	0.1355625	95.84051	0.9164803	217.0265	1.989159
0.00915	0.000018	0.959706	0.0009593	535.0	2.0	897.0	0.58212	0.0017804	0.0369257	0.0001343	0.0004617	0.0000512	0.0253963	0.000744	0.0000424	0.000028	3.69E-14	15.76461	0.074925	15.42155	0.2383245	97.82384	1.499436	238.6746	3.455405
0.00915	0.000018	0.959706	0.0009593	548.0	2.0	597.3	0.3950544	0.001201	0.0239257	0.0001189	0.0002784	0.0000236	0.0167443	0.0011335	0.000053	0.0000157	2.39E-14	16.51172	0.0961768	15.8508	0.2171435	95.99725	1.25982	244.8875	3.137537
0.00915	0.000018	0.959706	0.0009593	564.1	2.6	296.6	0.256434	0.0014469	0.0149813	0.0000952	0.0001889	0.0000282	0.0098894	0.0008046	0.0000111	0.0000299	1.50E-14	17.11692	0.1455036	16.89628	0.6127056	98.71099	3.567822	259.931	8.779638
0.00915	0.000018	0.959706	0.0009593	575.6	2.3	296.7	0.317554	0.0014469	0.0181516	0.0000986	0.000215	0.0000286	0.0138566	0.0008055	0.0000482	0.0000299	1.82E-14	17.49453	0.1240363	16.70215	0.5060899	95.47072	2.879031	257.1471	7.263085
0.00915	0.000018	0.959706	0.0009593	595.1	3.3	296.7	0.452074	0.0015243	0.0258892	0.0001003	0.0003312	0.0000282	0.0206158	0.0007762	0.0000973	0.0000299	2.51E-14	18.0187	0.0942316	16.86102	0.3670038	93.57514	2.026856	259.4256	5.260375
0.00915	0.000018	0.959706	0.0009593	611.4	3.6	296.7	0.521504	0.0014469	0.0280042	0.0001029	0.0003429	0.0000277	0.0190661	0.0008238	0.0000423	0.0000306	2.80E-14	18.62238	0.0857189	18.17136	0.3368794	97.57808	1.793692	278.1102	4.778954
0.00915	0.000018	0.959706	0.0009593	631.1	2.9	296.7	0.712484	0.0015243	0.0353675	0.0001133	0.0004315	0.0000286	0.026915	0.0008247	0.0000676	0.0000299	3.54E-14	20.14514	0.0776117	19.57471	0.2634475	97.16838	1.287184	297.9093	3.696939
0.00915	0.000018	0.959706	0.0009593	652.3	2.0	296.7	1.293744	0.0017702	0.0391867	0.0000936	0.000736	0.0000282	0.0286059	0.0007639	0.0001569	0.0000294	3.92E-14	33.01484	0.0908748	21.45786	0.2344021	64.99461	0.6984952	324.1415	3.241632
0.00915	0.000018	0.959706	0.0009593	669.9	1.0	296.6	0.837834	0.0015243	0.0361808	0.0001063	0.0004386	0.0000279	0.0254543	0.00081	0.000082	0.0000299	3.62E-14	23.15689	0.0880271	22.47978	0.2587304	97.076	1.094612	338.219	3.550327
0.00915	0.000018	0.959706	0.0009593	685.0	0.8	296.7	0.733834	0.0014469	0.0312647	0.000102	0.000389	0.0000282	0.0220652	0.0007953	0.0000927	0.0000295	3.13E-14	23.47163	0.0894729	22.58605	0.2951714	96.22701	1.232441	339.6766	4.047112
0.00915	0.000018	0.959706	0.0009593	701.1	0.7	296.7	0.630504	0.0015243	0.0277063	0.0000961	0.0003117	0.0000282	0.0176317	0.0007652	0.0000538	0.0000302	2.77E-14	22.75666	0.0962021	22.17629	0.339129	97.44966	1.470411	334.0497	4.66831
0.00915	0.000018	0.959706	0.0009593	715.9	0.5	296.6	0.567784	0.0015243	0.0238747	0.0000994	0.0003211	0.0000282	0.0153886	0.0007597	0.0002266	0.0000296	2.39E-14	23.78179	0.1178516	20.94786	0.3853697	88.08836	1.595971	317.0747	5.350288
0.00915	0.000018	0.959706	0.0009593	733.2	6.9	301.2	0.413654	0.0014469	0.0228715	0.0000986	0.0003195	0.0000286	0.0169128	0.0007545	0.0000498	0.0000306	2.29E-14	18.086	0.1004066	17.43632	0.4112373	96.40781	2.260769	267.6527	5.867629
0.00915	0.000018	0.959706	0.0009593	757.1	0.4	297.6	0.345754	0.0014469	0.02499	0.0001223	0.00035	0.0000282	0.0273805	0.0008672	0.0001027	0.0000299	2.50E-14	13.83568	0.0890715	12.60903	0.3669109	91.13417	2.641841	197.4298	5.442486
0.00915	0.000018	0.959706	0.0009593	780.0	0.4	296.7	0.264356	0.0013294	0.0206175	0.0001124	0.0003298	0.0000282	0.0342537	0.0008155	0.0000561	0.0000296	2.06E-14	12.8219	0.095112	12.0098	0.4378662	93.66831	3.409259	188.5193	6.52707
0.00915	0.000018	0.959706	0.0009593	610.0	3.4	2996.6	0.044694	0.0039345	0.001955	0.0000578	1.20E-06	0.0000376	0.0031442	0.0007708	0.0000952	0.0000253	1.96E-15	22.86123	2.122875	8.327302	4.358414	36.42544	19.30245	132.7755	67.003
0.00915	0.000018	0.959706	0.0009593	640.0	2.4	2996.6	0.055792	0.00394	0.0026404	0.0000606	0.0000293	0.0000379	0.0017445	0.0008036	0.0000528	0.0000261	2.64E-15	21.13043	1.569085	15.15576	3.325152	71.72479	16.4492	234.8168	48.31349
0.00915	0.000018	0.959706	0.0009593	679.9	0.9	2997.0	0.094376	0.0039571	0.0054686	0.0000639	0.0001061	0.0000379	0.0030674	0.0008225	0.0000987	0.0000257	5.47E-15	17.25791	0.7513876	11.87173	1.583277	68.79009	9.583283	186.46	23.62808
0.00915	0.000018	0.959706	0.0009593	710.0	0.6	2996.6	0.130775	0.0039959	0.008941	0.000106	0.0000367	0.0000655	0.0038743	0.0007655	0.0001083	0.0000261	8.94E-15	14.62649	0.4647717	11.00921	0.9842124	75.26901	7.080767	173.5421	14.79323
0.00915	0.000018	0.959706	0.0009593	750.0	0.5	2996.6	0.27311	0.0042154	0.0189013	0.0001495	0.0003367	0.0000386	0.0107133	0.0009015	0.0003542	0.0000281	1.89E-14	14.44925	0.2566119	8.854323	0.5018166	61.27879	3.56665	140.8594	7.680141
0.00915	0.000018	0.959706	0.0009593	778.0	1.8	1797.7	0.597325	0.0022013	0.0203265	0.0001139	0.0005564	0.0000305	0.0270159	0.0008136	0.0014171	0.0000297	2.03E-14	29.38648	0.197087	8.57147	0.45177	29.16807	1.532399	136.5253	6.930786
0.00915	0.000018	0.959706	0.0009593	801.9	0.4	896.5	0.23374	0.0017029	0.0188438	0.0001434	0.000248	0.0000512	0.0398898	0.0009025	0.0001334	0.000028	1.88E-14	12.40408	0.1306591	10.29027	0.459617	82.95873	3.700903	162.7036	6.949821
0.00915	0.000018	0.959706	0.0009593	813.0	0.3	596.8	0.2288344	0.0007018	0.0177247	0.0001026	0.0002346	0.0000213	0.0260861	0.0011522	0.0001037	0.0000172	1.77E-14	12.91046	0.0845585	11.164	0.300218	86.47247	2.286319	175.8672	4.506636
0.00915	0.000018	0.959706	0.0009593	821.0	1.0	296.7	0.185915	0.0012279	0.0159051	0.0001046	0.0001913	0.0000291	0.02405	0.0008536	0.0000775	0.0000302	1.51E-14	12.31628	0.1178861	10.78325	0.6079167	87.55284	4.932475	170.1426	9.154504
0.00915	0.000018	0.959706	0.0009593	830.1	2.8	296.6	0.274209	0.0013365	0.0214863	0.0001089	0.0002856	0.0000286	0.0232638	0.0007866	0.0001183	0.0000302	2.15E-14	12.76203	0.089745	11.11828	0.4283266	87.12001	3.354054	175.1808	6.432142
0.00915	0.000018	0.959706	0.0009593	837.4	3.8	296.6	0.328765	0.0013579	0.0249312	0.0001133	0.00032	0.0000286	0.0213455	0.0008222	0.0000889	0.0000299	2.49E-14	13.18688	0.0809888	12.12271	0.3661455	91.93007	2.771101	190.2017	5.452887
0.00915	0.000018	0.959706	0.0009593	846.9	1.5	296.7	0.388572	0.0013724	0.0290834	0.0001223	0.0003542	0.0000286	0.0155394	0.0008231	0.0000832	0.0000294	2.91E-14	13.36062	0.0733561	13.02008	0.3107775	97.45122	2.315436	203.5168	4.594352
0.00915	0.000018	0.959706	0.0009593	855.4	1.5	296.7	0.344635	0.0013724	0.0241374	0.0001133	0.0002973	0.0000291	0.0157707	0.000824	0.0000744	0.0000294	2.41E-14	14.27802	0.0878985	13.35745	0.3729816	93.55249	2.601263	208.4973	5.497446
0.00915	0.000018	0.959706	0.0009593	867.1	1.2	296.6	0.214747	0.0012151	0.0170163	0.0000969	0.000222	0.0000271	0.0149753	0.0008412	0.0000534	0.0000292	1.70E-14	12.62009	0.1013211	11.68295	0.5209707	92.57428	4.127661	183.6406	7.786853
0.00915	0.000018	0.959706	0.0009593	867.1	1.4	296.7	0.107437	0.0010379	0.0070861	0.0000659	0.0001051	0.0000278	0.0063146	0.0007964	0.0000198	0.0000302	7.09E-15	15.1616	0.2032845	14.32844	1.288611	94.50477	8.502777	222.756	18.84844
0.00915	0.000018	0.959706	0.0009593	878.4	2.0	296.7	0.076234	0.0010255	0.0044903	0.0000659	0.0000464	0.0000282	0.0065959	0.0007747	0.0000474	0.0000299	4.49E-15	16.97751	0.3379563	13.8247	2.010061	81.42949	11.82993	215.3728	29.52135
0.00915	0.000018	0.959706	0.0009593	884.0	1.4	296.6	0.061679	0.0010066	0.0031104	0.0000615	0.0000552	0.0000282	0.0051628	0.0008125	0.0000128	0.0000292	3.11E-15	19.83008	0.5082809	18.59989	2.844478	93.79638	14.30607	284.1792	40.21641
0.00915	0.000018	0.959706	0.0009593	889.3	1.8	296.6	0.089143	0.0010465	0.0034843	0.0000663	0.0000552	0.0000282	0.0049405	0.0008287	0.0000284	0.0000306	3.48E-15	25.58387	0.5518214	23.15135	2.671328	90.49199	10.36683	347.411	36.47039
0.00915	0.000018	0.959706	0.0009593	896.2	1.5	296.6	0.048512	0.0009996	0.0007623	0.0000591	-0.0000173	0.0000286	0.0023009	0.0008815	0.0000167	0.0000302	7.62E-16	63.64311	5.106373	57.11587	12.70635	89.74399	18.804	760.1354	138.0666

Table A.7: 18-IAF-09S-EPH step heating data

J	± 1σ	Discrim	± 1σ	Temp (°C)	± 1σ (°C)	Heating duration (s)	^{40}Ar	± 1σ	^{39}Ar	± 1σ	^{38}Ar	± 1σ	^{37}Ar	± 1σ	^{36}Ar	± 1σ	^{39}Ar (Moles)	^{40}Ar/^{39}Ar	± 1σ	^{40}Ar*/^{39}Ar$_K$	± 1σ	% ^{40}Ar*	± 1σ	Age (Ma)	± 1σ
0.00915	0.000018	0.959706	0.0009593	404.2	2.8	296.7	7.797344	0.0084345	0.1843483	0.0003636	0.0043462	0.0003305	0.0203177	0.0002728	0.0111645	0.0000431	1.84E-13	42.29682	0.0978139	24.21547	0.0985816	57.25127	0.2085855	361.8808	1.335161
0.00915	0.000018	0.959706	0.0009593	422.0	2.7	296.6	2.120513	0.004272	0.0774814	0.0002353	0.001379	0.0000274	0.0076744	0.0002582	0.0024217	0.0000356	7.75E-14	27.36804	0.1024602	18.03656	0.1589737	65.90375	0.5585961	276.197	2.25758
0.00915	0.000018	0.959706	0.0009593	440.0	2.3	296.7	2.225641	0.0044598	0.0887229	0.0002746	0.0013088	0.0000291	0.0083748	0.0002734	0.0014524	0.0000343	8.87E-14	25.08531	0.0949996	20.19767	0.1419153	80.51594	0.5294875	306.6293	1.981698
0.00915	0.000018	0.959706	0.0009593	458.3	2.4	296.7	2.558019	0.0047434	0.1053752	0.0002943	0.0014328	0.0000286	0.0100604	0.0002659	0.0010993	0.0000347	1.05E-13	24.27535	0.0836125	21.1608	0.124606	87.16992	0.4764347	320.0286	1.72714
0.00915	0.000018	0.959706	0.0009593	475.0	2.1	296.6	2.765891	0.0044598	0.1206521	0.0002943	0.0015425	0.0000278	0.0121	0.0002626	0.0007855	0.0000344	1.20E-13	23.01993	0.0694344	21.06654	0.1077476	91.51433	0.4332836	318.7216	1.494554
0.00915	0.000018	0.959706	0.0009593	492.4	1.9	296.6	3.046164	0.0040853	0.1397709	0.0003141	0.0017032	0.0000291	0.0157433	0.0002626	0.0006289	0.0000341	1.40E-13	21.79398	0.058612	20.45046	0.0919708	93.83534	0.3833627	310.1557	1.281774
0.00915	0.000018	0.959706	0.0009593	509.9	1.7	296.7	3.594215	0.004272	0.1739197	0.0003636	0.0020626	0.0000276	0.022107	0.0002885	0.0004636	0.0000347	1.74E-13	20.66595	0.0510826	19.87006	0.0774958	96.14879	0.3331945	302.0487	1.084893
0.00915	0.000018	0.959706	0.0009593	527.1	2.0	296.6	4.008949	0.0048384	0.2020399	0.0004331	0.0024297	0.0000282	0.0310864	0.0002622	0.0004129	0.0000353	2.02E-13	19.84236	0.0501675	19.23222	0.0715822	96.92508	0.313494	293.0973	1.00708
0.00915	0.000018	0.959706	0.0009593	544.0	2.3	296.6	3.944174	0.0048384	0.2026701	0.0004331	0.002404	0.0000295	0.0372911	0.0003305	0.0002592	0.0000334	2.03E-13	19.46105	0.0492859	19.07913	0.0698263	98.03749	0.3113067	290.9421	0.9835469
0.00915	0.000018	0.959706	0.0009593	544.0	2.1	1796.7	9.867875	0.0088012	0.4988093	0.0009117	0.0055791	0.0000161	0.1082207	0.0003311	0.0004611	0.0000137	4.99E-13	19.78286	0.0413708	19.50684	0.0417312	98.60474	0.1338496	296.9567	0.5858578
0.00915	0.000018	0.959706	0.0009593	593.6	2.8	296.6	4.673277	0.0052011	0.2114466	0.0004225	0.0024139	0.0000132	0.0589147	0.0003061	0.0001106	0.0000158	2.11E-13	22.10145	0.0519676	21.94529	0.0562826	99.29346	0.1885157	330.8698	0.7754614
0.00915	0.000018	0.959706	0.0009593	594.2	2.9	1796.7	12.96069	0.0110006	0.5448438	0.0009117	0.0061504	0.000019	0.1695228	0.0004382	0.0003209	0.0000128	5.45E-13	23.7879	0.0459214	23.61202	0.0461941	99.26063	0.1250256	353.6893	0.628481
0.00915	0.000018	0.959706	0.0009593	642.4	2.7	296.7	5.386308	0.0058941	0.2927065	0.0004033	0.002316	0.0000295	0.0741239	0.0003376	0.0002071	0.0000344	2.03E-13	26.54235	0.0619721	26.23722	0.0796128	98.85038	0.2467502	389.0575	1.062168
0.00915	0.000018	0.959706	0.0009593	659.0	2.2	296.7	5.69401	0.0057974	0.2967987	0.0004033	0.0023764	0.0000295	0.0771447	0.0003076	0.0001268	0.0000338	2.07E-13	27.53407	0.0622713	27.35095	0.0788478	99.33494	0.2294304	403.8559	1.043387
0.00915	0.000018	0.959706	0.0009593	676.3	1.1	296.6	5.618267	0.0058941	0.2025345	0.0004033	0.0023478	0.0000282	0.0791756	0.0003257	0.0001417	0.0000343	2.03E-13	27.7398	0.0641778	27.53092	0.0814313	99.247	0.2362557	406.2358	1.076158
0.00915	0.000018	0.959706	0.0009593	691.0	0.8	296.6	4.959135	0.005412	0.1796263	0.0003537	0.0020949	0.0000286	0.0754133	0.0003261	0.0001474	0.0000356	1.80E-13	27.60807	0.063896	27.36303	0.0868147	99.11242	0.2653287	404.0157	1.148711
0.00915	0.000018	0.959706	0.0009593	707.1	0.6	296.6	4.573973	0.0048384	0.1695559	0.000324	0.001978	0.0000275	0.0844371	0.0003327	0.0001851	0.0000343	1.70E-13	26.988	0.0605987	26.66198	0.0851325	98.792	0.2698167	394.7157	1.132262
0.00915	0.000018	0.959706	0.0009593	722.9	0.6	296.6	3.840026	0.0041785	0.1503924	0.0002943	0.0018144	0.0000291	0.0912155	0.0003461	0.0001555	0.0000339	1.50E-13	25.53338	0.0587832	25.22457	0.0890564	98.79056	0.3061958	375.4963	1.197106
0.00915	0.000018	0.959706	0.0009593	739.0	0.5	296.6	3.180192	0.0022672	0.1350997	0.0001867	0.0016367	0.0000286	0.0863442	0.0002884	0.0001961	0.0000341	1.35E-13	23.53959	0.0377176	23.10624	0.0839794	98.15904	0.3355761	346.7949	1.146922
0.00915	0.000018	0.959706	0.0009593	769.1	0.3	296.6	3.917956	0.0033541	0.1823407	0.0003438	0.0023065	0.0000282	0.1336905	0.0003674	0.000277	0.0000353	1.82E-13	21.48701	0.0457364	21.03351	0.0732112	97.88944	0.2951803	318.2634	1.015761
0.00915	0.000018	0.959706	0.0009593	785.1	0.4	301.2	2.274207	0.0031765	0.1352965	0.0003141	0.001716	0.0000286	0.0944646	0.0003822	0.0002597	0.0000343	1.35E-13	16.80906	0.0467965	16.23607	0.0884364	96.5912	0.4919335	250.4457	1.273896
0.00915	0.000018	0.959706	0.0009593	785.0	0.4	596.8	1.96918	0.0025014	0.1411078	0.0003132	0.001871	0.0000133	0.0825135	0.0003162	0.0003206	0.0000138	1.41E-13	13.95515	0.0366754	13.27682	0.0458448	95.13918	0.2746919	207.3082	0.6763227
0.00915	0.000018	0.959706	0.0009593	785.0	0.4	1796.7	2.565659	0.0031081	0.2150164	0.0004723	0.0027316	0.0000196	0.1050326	0.0003905	0.0006102	0.0000142	2.15E-13	11.93239	0.0307595	11.08513	0.0351752	92.89951	0.2356798	174.6829	0.5283684
0.00915	0.000018	0.959706	0.0009593	829.1	0.2	296.6	1.587579	0.0025	0.1320007	0.0003042	0.0016839	0.0000286	0.157999	0.000478	0.0003941	0.0000337	1.32E-13	12.02704	0.0345071	11.13558	0.0830564	92.58785	0.6708652	175.4406	1.247071
0.00915	0.000018	0.959706	0.0009593	844.1	0.2	296.6	2.40708	0.0030017	0.2103089	0.0004431	0.0026221	0.0000291	0.1447416	0.0004302	0.0005631	0.0000347	2.10E-13	11.44545	0.0288015	10.64611	0.0563176	93.0161	0.4636316	168.0763	0.8490467
0.00915	0.000018	0.959706	0.0009593	859.0	0.3	296.7	3.388653	0.003265	0.3152305	0.0005726	0.0038888	0.0000276	0.1587737	0.0004152	0.0007453	0.0000344	3.15E-13	10.74976	0.0227296	10.0439	0.0391037	93.43365	0.3314887	158.9744	0.5925039
0.00915	0.000018	0.959706	0.0009593	873.1	0.2	296.6	3.305915	0.0031765	0.3226557	0.0005925	0.0039167	0.000027	0.1443748	0.0003929	0.0006209	0.0000347	3.23E-13	10.24505	0.0218361	9.671411	0.0383003	94.39251	0.3407741	153.3217	0.5821483
0.00915	0.000018	0.959706	0.0009593	888.0	0.2	296.7	1.81878	0.0025807	0.1567649	0.000324	0.0019242	0.0000282	0.1237262	0.0003033	0.0004119	0.0000342	1.57E-13	11.60196	0.0299075	10.81754	0.0711783	93.23894	0.5954883	170.659	1.071554
0.00915	0.000018	0.959706	0.0009593	902.0	0.2	296.7	0.9812534	0.0020518	0.0504725	0.000139	0.0006763	0.0000274	0.0784264	0.000351	0.000245	0.000036	5.05E-14	19.44134	0.069102	17.9919	0.2229736	92.54455	1.133288	275.5627	3.167551
0.00915	0.000018	0.959706	0.0009593	916.0	0.2	296.7	0.6378565	0.0019849	0.0181679	0.0000847	0.0002853	0.0000282	0.0498713	0.0003138	0.0001923	0.0000343	1.82E-14	35.10903	0.2020335	31.94934	0.5946508	91.00033	1.661282	463.7045	7.612777

Table A.8: 18-IAF-10S-EPH step heating data

J	± 1σ	Discrim	± 1σ	Temp (°C)	± 1σ (°C)	Heating duration (s)	^{40}Ar	± 1σ	^{39}Ar	± 1σ	^{38}Ar	± 1σ	^{37}Ar	± 1σ	^{36}Ar	± 1σ	^{39}Ar (Moles)	^{40}Ar/^{39}Ar	± 1σ	^{40}Ar*/^{39}Ar$_K$	± 1σ	% ^{40}Ar*	± 1σ	Age (Ma)	± 1σ
0.00915	0.000018	0.959706	0.0009593	377.5	3.3	297.6	1.430845	0.004334	0.0441699	0.0001669	0.0010937	0.0000344	0.0107808	0.0006203	0.0026915	0.0000429	4.42E-14	32.39412	0.1569008	14.2221	0.3106419	43.89689	0.9536458	221.2	4.547655
0.00915	0.000018	0.959706	0.0009593	390.9	3.1	296.7	0.3412261	0.0023971	0.0126598	0.0000763	0.0002627	0.0000351	0.002197	0.0006192	0.0004634	0.0000377	1.27E-14	26.95353	0.2494853	16.04094	0.9149959	59.50775	3.401171	247.6328	13.20072
0.00915	0.000018	0.959706	0.0009593	390.9	3.1	296.7	0.3412261	0.0023971	0.0126598	0.0000763	0.0002627	0.0000351	0.002197	0.0006192	0.0004634	0.0000377	1.27E-14	26.95353	0.2494853	16.04094	0.9149959	59.50775	3.401171	247.6328	13.20072
0.00915	0.000018	0.959706	0.0009593	402.5	2.4	296.6	0.2890298	0.002496	0.0109718	0.0000869	0.0001833	0.0000355	0.0024077	0.0006404	0.0002895	0.0000376	1.10E-14	26.34308	0.3087142	18.48419	1.058902	70.15841	4.026364	282.5425	14.98476
0.00915	0.000018	0.959706	0.0009593	411.5	2.1	296.7	0.2794233	0.0024888	0.0105018	0.0000869	0.0001944	0.0000342	0.0022463	0.0006411	0.0001976	0.0000388	1.05E-14	26.60705	0.323505	21.00764	1.141837	78.94559	4.298791	317.9044	15.84545
0.00915	0.000018	0.959706	0.0009593	423.0	2.2	296.6	0.3661572	0.0026624	0.0120123	0.0000972	0.0002087	0.0000351	0.0023903	0.0006344	0.0003105	0.0000373	1.20E-14	30.48186	0.3316704	22.78313	0.9710653	74.73471	3.174206	342.3768	13.29446
0.00915	0.000018	0.959706	0.0009593	431.3	2.1	296.6	0.361361	0.0026557	0.0116369	0.0000912	0.0001976	0.0000355	0.0021339	0.0006594	0.0003342	0.0000369	1.16E-14	31.05304	0.3335651	22.49458	0.989111	72.43172	3.178798	338.4221	13.57117
0.00915	0.000018	0.959706	0.0009593	431.3	2.1	296.6	0.361361	0.0026557	0.0116369	0.0000912	0.0001976	0.0000355	0.0021339	0.0006594	0.0003342	0.0000369	1.16E-14	31.05304	0.3335651	22.49458	0.989111	72.43172	3.178798	338.4221	13.57117
0.00915	0.000018	0.959706	0.0009593	443.9	2.0	296.7	0.4144349	0.0027143	0.0141063	0.0000938	0.0002438	0.0000351	0.0030511	0.0006323	0.0002684	0.0000376	1.41E-14	29.37943	0.2741352	23.71914	0.8339887	80.72373	2.836832	355.1461	11.33745
0.00915	0.000018	0.959706	0.0009593	461.3	1.7	296.6	0.5116689	0.0027753	0.0183788	0.0001106	0.0002407	0.0000355	0.0027831	0.000644	0.0002155	0.0000376	1.84E-14	27.84022	0.2255642	24.35243	0.6457748	87.46523	2.308115	363.7348	8.737226
0.00915	0.000018	0.959706	0.0009593	421.9	1.7	896.6	0.2134328	0.002453	0.0079245	0.0000859	0.0001384	0.0000326	0.0028934	0.0006448	0.0001247	0.0000546	7.92E-15	26.93344	0.4254992	22.26847	2.095985	82.6609	7.786689	335.317	28.80754
0.00915	0.000018	0.959706	0.0009593	434.9	2.1	896.6	0.2749748	0.0025008	0.0100403	0.00009	0.0001319	0.0000326	0.0028963	0.000654	0.0001326	0.0000548	1.00E-14	27.38719	0.3496682	23.47215	1.663674	85.68997	6.075009	351.7854	22.65848
0.00915	0.000018	0.959706	0.0009593	457.0	1.7	896.6	0.5157868	0.0026816	0.018764	0.000101	0.0003091	0.000034	0.0062068	0.0006639	0.0002399	0.0000549	1.88E-14	27.48808	0.2056625	23.70194	0.8938118	86.20874	3.248755	354.9123	12.15228
0.00915	0.000018	0.959706	0.0009593	469.9	1.7	897.1	0.5335487	0.0026718	0.0208441	0.0001106	0.0002519	0.0000326	0.004996	0.0006481	0.000126	0.000055	2.08E-14	25.5971	0.1867518	23.81402	0.8085884	93.0212	3.154229	356.4355	10.98432
0.00915	0.000018	0.959706	0.0009593	480.2	1.6	596.9	0.3543207	0.0023529	0.0139872	0.0000938	0.0001808	0.00003	0.0044607	0.0007985	0.0001568	0.0000443	1.40E-14	25.33176	0.2391356	22.01395	0.9714625	86.88582	3.833273	331.8155	13.37781
0.00915	0.000018	0.959706	0.0009593	492.8	1.3	596.9	0.4230169	0.0025223	0.0175111	0.0001218	0.0002379	0.0000286	0.006367	0.0008147	0.0001229	0.0000445	1.75E-14	24.1571	0.2213206	22.0945	0.7877769	91.4414	3.243783	332.9244	10.84166
0.00915	0.000018	0.959706	0.0009593	500.8	1.4	296.8	0.221891	0.0022798	0.0090681	0.0000795	0.0001545	0.0000355	0.0033506	0.000634	0.0000586	0.0000378	9.07E-15	24.4693	0.330474	22.57299	1.285267	92.2293	5.274527	339.4975	17.62411
0.00915	0.000018	0.959706	0.0009593	511.1	1.0	296.6	0.2821928	0.0022723	0.0118365	0.0000946	0.0001961	0.0000351	0.0052592	0.0006601	0.0001121	0.0000381	1.18E-14	23.84095	0.270507	21.05558	0.994968	88.2923	4.173012	318.5696	13.80224
0.00915	0.000018	0.959706	0.0009593	518.8	1.1	296.6	0.3316168	0.0022649	0.0138229	0.0000811	0.0002128	0.0000343	0.0054105	0.0006526	0.0001197	0.0000381	1.38E-14	23.99046	0.2160228	21.44182	0.8489992	89.35487	3.551764	323.9196	11.74256
0.00915	0.000018	0.959706	0.0009593	535.1	1.3	296.6	0.4646308	0.0024303	0.0200638	0.0001052	0.0002789	0.0000355	0.0092412	0.0006534	0.0001335	0.0000375	2.01E-14	23.15765	0.1715186	21.21396	0.5825729	91.58025	2.514682	320.7653	8.071671
0.00915	0.000018	0.959706	0.0009593	534.9	1.2	896.6	1.097875	0.0024866	0.037314	0.0001106	0.0005831	0.0000326	0.0178635	0.0006408	0.0009791	0.0000555	3.73E-14	29.42256	0.1097546	21.6324	0.4537347	73.50057	1.535224	326.5537	6.266498
0.00915	0.000018	0.959706	0.0009593	541.8	1.6	596.9	0.5110566	0.0023522	0.0183509	0.0000938	0.0003018	0.0000288	0.0098991	0.0008132	0.0003451	0.0000441	1.84E-14	27.84906	0.1916087	22.28422	0.7376298	79.98996	2.641696	335.5335	10.13688
0.00915	0.000018	0.959706	0.0009593	555.5	1.4	296.6	0.2776829	0.0022294	0.0111973	0.0000787	0.0001412	0.0000348	0.0047573	0.0006734	0.0000851	0.0000378	1.12E-14	24.79909	0.2645966	22.56912	1.039981	90.98366	4.207314	339.4445	14.26107
0.00915	0.000018	0.959706	0.0009593	566.8	1.4	296.7	0.3423347	0.002222	0.01399	0.0000861	0.0001874	0.0000351	0.0078702	0.0006652	0.000125	0.0000381	1.40E-14	24.47	0.2188457	21.85455	0.8399741	89.27938	3.436334	329.6191	11.58117
0.00915	0.000018	0.959706	0.0009593	580.1	1.4	296.6	0.4313186	0.0022704	0.0174762	0.0000811	0.0002224	0.0000345	0.0101706	0.0006385	0.0001017	0.0000372	1.75E-14	24.68033	0.1732035	22.997	0.6581647	93.14458	2.675731	345.3025	8.9961
0.00915	0.000018	0.959706	0.0009593	579.9	1.2	896.5	0.8654826	0.0023838	0.0347757	0.0001018	0.0004619	0.0000326	0.0204465	0.0006757	0.0001322	0.0000556	3.48E-14	24.88754	0.1000438	23.80799	0.4878168	95.62602	1.957014	356.3536	6.627079
0.00915	0.000018	0.959706	0.0009593	580.1	1.3	1796.7	0.9467644	0.0024379	0.0362265	0.0001115	0.0004457	0.0000351	0.0206137	0.0005081	0.0002074	0.0000381	3.62E-14	26.13461	0.1048673	24.47946	0.3300951	93.63243	1.252663	365.4527	4.461891
0.00915	0.000018	0.959706	0.0009593	599.9	3.1	596.8	0.3154062	0.0009927	0.0124253	0.0000758	0.0001394	0.0000326	0.0069798	0.0007909	0.0000311	0.0000552	1.24E-14	25.38424	0.1743068	24.69055	1.337455	97.23208	5.242291	368.3037	18.04988
0.00915	0.000018	0.959706	0.0009593	611.0	2.7	596.9	0.354277	0.0009519	0.0132367	0.0000729	0.0001648	0.0000329	0.0061974	0.0008127	0.0000555	0.0000547	1.32E-14	26.76469	0.164048	25.55802	1.243364	95.46309	4.621363	379.9731	16.67211
0.00915	0.000018	0.959706	0.0009593	618.9	1.8	296.6	0.1992781	0.0007063	0.0073177	0.0000564	0.0000984	0.0000348	0.0037308	0.0007932	0.0000641	0.0000373	7.32E-15	27.23222	0.2309085	24.66637	1.535951	90.54823	5.604158	367.9773	20.73245
0.00915	0.000018	0.959706	0.0009593	627.2	2.0	296.7	0.2451949	0.0007846	0.0082863	0.0000593	0.0000825	0.0000345	0.0046054	0.0007658	0.0001463	0.0000375	8.29E-15	29.59053	0.2318755	24.37033	1.367932	82.32879	4.591022	363.977	18.50542
0.00915	0.000018	0.959706	0.0009593	639.7	1.9	296.6	0.3309906	0.0008853	0.0106977	0.0000687	0.000129	0.0000344	0.0046283	0.0007733	0.0001952	0.0000378	1.07E-14	30.94041	0.2152483	25.5343	1.07241	82.50448	3.431385	379.655	14.38233
0.00915	0.000018	0.959706	0.0009593	647.7	1.6	296.6	0.3315441	0.0008724	0.0111111	0.0000593	0.0001309	0.0000341	0.0054963	0.0007866	0.000172	0.0000381	1.11E-14	29.83908	0.1774898	25.2632	1.036852	84.63779	3.451379	376.0156	13.93348
0.00915	0.000018	0.959706	0.0009593	667.3	1.0	297.7	0.4856798	0.000987	0.0165262	0.0000702	0.0001791	0.0000348	0.0058508	0.0008069	0.0001332	0.0000371	1.65E-14	29.38848	0.1383458	27.01627	0.6836413	91.90778	2.300284	399.4216	9.068789
0.00915	0.000018	0.959706	0.0009593	678.2	0.8	296.6	0.5374222	0.0009559	0.018	0.0000702	0.0001772	0.0000345	0.0077425	0.0007693	0.0000874	0.0000381	1.80E-14	29.85675	0.1279422	28.44862	0.6440801	95.25759	2.131133	418.3233	8.455143
0.00915	0.000018	0.959706	0.0009593	684.1	0.9	296.7	0.4233259	0.0008701	0.0148348	0.0000702	0.0002128	0.0000348	0.006379	0.0008195	0.0000983	0.0000375	1.48E-14	28.53594	0.1471787	26.59986	0.76826	93.18984	2.662024	393.8894	10.22252
0.00915	0.000018	0.959706	0.0009593	688.9	1.6	296.6	0.2775026	0.0008848	0.0103547	0.000068	0.0000942	0.0000345	0.0034815	0.0008096	0.0000707	0.0000371	1.04E-14	26.79967	0.1955859	24.79302	1.085816	92.4933	4.01578	369.6861	14.64263
0.00915	0.000018	0.959706	0.0009593	694.3	1.0	296.7	0.2911386	0.0008265	0.0092089	0.0000611	0.0001448	0.0000345	0.0038504	0.0007911	0.0002028	0.0000372	9.21E-15	31.61503	0.2282996	25.07852	1.221158	79.30348	3.832049	373.5321	16.43279
0.00915	0.000018	0.959706	0.0009593	708.0	1.0	296.7	0.2757723	0.0007866	0.0112209	0.0000624	0.0001209	0.0000345	0.0050441	0.0007867	0.0000382	0.0000372	1.12E-14	24.57661	0.1536844	23.60182	1.001609	96.00653	4.048341	353.5506	13.62815
0.00915	0.000018	0.959706	0.0009593	723.1	0.5	296.7	0.2781628	0.0004957	0.0122954	0.0000581	0.0001542	0.0000341	0.0067879	0.0007885	0.0000485	0.0000373	1.23E-14	22.62334	0.1142118	21.4964	0.91179	94.98528	4.007358	324.6743	12.60576
0.00915	0.000018	0.959706	0.0009593	741.0	0.5	296.6	0.3062745	0.0008435	0.0142656	0.0000709	0.0001881	0.0000343	0.0086844	0.0008031	0.0000804	0.0000375	1.43E-14	21.46945	0.1220188	19.84357	0.7941182	92.39107	3.677512	301.6778	11.11944
0.00915	0.000018	0.959706	0.0009593	760.0	0.4	296.6	0.2954964	0.0008125	0.0155196	0.0000687	0.0002029	0.0000345	0.0165357	0.0008251	0.0000854	0.0000378	1.55E-14	19.04025	0.099223	17.49387	0.733824	91.81386	3.838109	268.4737	10.46562
0.00915	0.000018	0.959706	0.0009593	780.0	0.4	296.6	0.3013593	0.0008651	0.0168873	0.0000795	0.0002147	0.0000348	0.0253039	0.0008151	0.0000811	0.0000373	1.69E-14	17.84535	0.0983941	16.54611	0.6662351	92.62671	3.713524	254.9062	9.573245
0.00915	0.000018	0.959706	0.0009593	615.1	2.0	1797.8	0.0353014	0.0004	0.0012483	0.0000551	0.000014	0.0000355	-0.0000964	0.0006479	0.0000325	0.0000394	1.25E-15	28.28039	1.288219	20.48724	9.464071	72.44902	33.32478	310.6682	131.861
0.00915	0.000018	0.959706	0.0009593	640.1	1.1	1796.7	0.0389313	0.0004145	0.0014762	0.0000555	0.000016	0.0000351	0.0003666	0.0006212	0.0000346	0.0000388	1.48E-15	26.37212	1.031096	19.38666	7.879479	73.50131	29.75562	295.2687	110.7222
0.00915	0.000018	0.959706	0.0009593	665.1	0.9	1796.7	0.0475213	0.0004252	0.001877	0.0000575	-0.0000137	0.0000355	-0.0002289	0.0006512	0.0000358	0.0000388	1.88E-15	25.31763	0.8082625	19.61042	6.198332	77.46637	24.37946	298.4103	86.94756
0.00915	0.000018	0.959706	0.0009593	689.0	0.7	1796.8	0.0601691	0.0004135	0.0026864	0.0000551	0.0000604	0.0000358	0.0015736	0.0006076	0.000078	0.0000382	2.69E-15	22.39806	0.4843014	13.78299	4.265198	61.5135	18.99837	214.7602	62.66332
0.00915	0.000018	0.959706	0.0009593	705.0	0.6	1796.7	0.0679143	0.0004368	0.0030722	0.0000555	0.0000547	0.0000351	0.0012645	0.0006082	0.0000502	0.0000388	3.07E-15	22.106	0.4241469	17.26399	3.783877	78.07663	17.06163	265.1922	54.06274
0.00915	0.000018	0.959706	0.0009593	743.0	0.6	1796.7	0.1437272	0.0005368	0.0072524	0.0000621	0.0001129	0.0000345	0.0036009	0.0006563	0.0001004	0.0000388	7.25E-15	19.8178	0.1850875	15.72825	1.604346	79.33979	8.06983	243.1159	23.20393
0.00915	0.000018	0.959706	0.0009593	767.0	0.4	1796.7	0.2344572	0.0010054	0.0127327	0.0000864	0.0002278	0.0000341	0.0128857	0.0006184	0.0001604	0.0000385	1.27E-14	18.4138	0.1477724	14.74157	0.9130081	80.00405	4.937058	228.7888	13.31004
0.00915	0.000018	0.959706	0.0009593	784.0	0.4	1796.7	0.3656895	0.0009922	0.0196234	0.0000939	0.0002743	0.0000362	0.022892	0.0006344	0.0001911	0.0000388	1.96E-14	18.63536	0.1025302	15.83249	0.5979636	84.89384	3.188705	244.6229	8.641245
0.00915	0.000018	0.959706	0.0009593	802.0	0.3	596.9	0.1872045	0.0006053	0.0107164	0.0000715	0.0001332	0.00003	0.0127961	0.0010119	0.0000228	0.0000453	1.07E-14	17.46891	0.1295676	16.94159	1.270135	96.90492	7.24293	260.58	18.1936
0.00915	0.000018	0.959706	0.0009593	815.0	0.3	596.9	0.3074793	0.000835	0.0154824	0.0000751	0.0002699	0.0000309	0.0155321	0.0010048	0.0000897	0.0000448	1.55E-14	19.85997	0.1103553	18.22269	0.8700002	91.69527	4.362203	278.8383	12.33681
0.00915	0.000018	0.959706	0.0009593	826.0	0.5	296.6	0.1365843	0.000378	0.0057161	0.0000575	0.0000476	0.0000342	0.0040574	0.0008264	0.0000141	0.0000371	5.72E-15	23.89446	0.2492757	23.22501	1.952304	97.15336	8.112399	348.4164	26.63908
0.00915	0.000018	0.959706	0.0009593	834.0	0.4	301.2	0.109523	0.0003429	0.0049599	0.0000558	0.0000495	0.0000348	0.0048981	0.0008273	0.0000672	0.0000371	4.96E-15	22.08189	0.257974	18.12589	2.248194	82.03123	10.13567	277.465	31.90415
0.00915	0.000018	0.959706	0.0009593	847.0	0.3	296.7	0.088605	0.0003055	0.0042237	0.0000553	0.0001069	0.0000345	0.0048676	0.0008065	9.04E-06	0.0000381	4.22E-15	20.97809	0.2839876	20.44663	2.708591	97.39191	12.84268	310.1024	37.75007
0.00915	0.000018	0.959706	0.0009593	868.0	0.3	296.6	0.1260233	0.0003737	0.0034879	0.0000528	9.87E-06	0.0000338	0.005896	0.0008292	0.0000518	0.0000373	3.49E-15	36.13133	0.5577125	31.86831	3.231774	88.09949	8.837471	462.6668	41.39723
0.00915	0.000018	0.959706	0.0009593	887.0	0.3	296.7	0.0784123	0.0003469	0.0012023	0.0000528	0.0000555	0.0000344	0.0032866	0.0008406	0.0000449	0.0000375	1.20E-15	65.21743	2.88044	54.37982	9.640925	83.22487	14.297	730.2185	106.5091
0.00915	0.000018	0.959706	0.0009593	903.0	0.3	296.6	0.0617866	0.0003419	0.0005028	0.0000511	0.0000125	0.0000343	0.0019474	0.0008214	0.0000953	0.0000375	5.03E-16	122.8863	12.51715	66.78045	23.37199	54.19734	18.14691	862.274	240.019
0.00915	0.000018	0.959706	0.0009593	918.0	0.2	296.6	0.0598235	0.0003481	0.0003039	0.0000524	0.0000113	0.0000348	0.0015267	0.0008538	0.0000828	0.0000378	3.04E-16	196.8789	33.96287	116.2958	42.37706	58.86368	18.87942	1310.365	339.6686
0.00915	0.000018	0.959706	0.0009593	934.0	0.2	296.7	0.0763591	0.0003707	0.0003721	0.0000524	0.0000222	0.0000362	0.0015608	0.0008041	0.0000527	0.0000378	3.72E-16	205.1889	28.90254	163.6838	38.21154	79.54002	14.79142	1655.136	253.1103
0.00915	0.000018	0.959706	0.0009593	956.0	0.2	296.7	0.0594904	0.0004034	0.000131	0.0000515	0.0000428	0.0000355	0.0009092	0.0008339	0.000043	0.0000375	1.31E-16	454.2811	178.8152	358.4717	165.8276	78.52903	18.84844	2628.979	641.015
0.00915	0.000018	0.959706	0.0009593	972.1	0.2	297.7	0.07592	0.0004305	0.0001093	0.0000511	-0.0000201	0.0000343	0.0002992	0.0008251	0.0000545	0.0000388	1.09E-16	694.4146	324.8367	546.9329	277.434	78.61203	15.25827	3241.115	764.4414

Table A.9: 18-IAF-09S-EPH (silt) step heating data

J	± 1σ	Discrim	± 1σ	Temp (°C)	± 1σ (°C)	Heating duration (s)	^{40}Ar	± 1σ	^{39}Ar	± 1σ	^{38}Ar	± 1σ	^{37}Ar	± 1σ	^{36}Ar	± 1σ	^{39}Ar (Moles)	± 1σ	^{40}Ar/^{39}Ar	± 1σ	^{40}Ar*/^{39}ArK	± 1σ	% ^{40}Ar*	± 1σ	Age (Ma)	± 1σ
0.00915	0.000018	0.959706	0.0009593	398.9	2.6	296.6	4.7091196	0.0056246	0.0379535	0.0001025	0.0031333	0.0000349	0.0112594	0.0008147	0.0140987	0.0000496	3.80E-14	1.24E-13	124.0781	0.3863313	13.17138	0.4190714	10.61539	0.3367666	205.7521	6.187651
0.00915	0.000018	0.959706	0.0009593	410.5	2.3	296.7	0.4948546	0.0010841	0.0103655	0.0000702	0.0003566	0.0000332	0.0030143	0.0007774	0.0010603	0.0000285	1.04E-14	4.74E-14	47.74068	0.3617511	17.20105	0.8454467	36.03018	1.758313	264.2929	12.08546
0.00915	0.000018	0.959706	0.0009593	423.0	2.8	296.6	0.378053	0.0014953	0.009554	0.0000717	0.0002046	0.0000332	0.0036618	0.0007902	0.0006658	0.0000311	9.55E-15	3.36E-14	39.57011	0.3355885	18.76496	0.9940525	47.42206	2.493871	286.5115	14.03621
0.00915	0.000018	0.959706	0.0009593	432.6	2.5	806.6	0.6798891	0.0015156	0.0188638	0.0001019	0.0003896	0.0000286	0.0043163	0.0006871	0.0010394	0.0000363	1.89E-14	8.09E-14	36.04196	0.2107002	19.59171	0.5902051	54.35806	1.615533	298.1478	8.280348
0.00915	0.000018	0.959706	0.0009593	447.0	2.1	596.9	0.488877	0.0015259	0.0154675	0.0001002	0.0002962	0.0000339	0.0058092	0.0006316	0.0004482	0.0000165	1.78E-14	7.58E-14	31.60677	0.2068482	22.05774	0.4165586	69.78802	1.27416	332.4184	5.734809
0.00915	0.000018	0.959706	0.0009593	463.2	2.2	597.4	0.5092207	0.0015259	0.0178285	0.0001002	0.0002962	0.0000339	0.0058092	0.0006316	0.0004947	0.0000165	1.78E-14	7.58E-14	28.56139	0.1819763	21.05603	0.3123909	73.72202	1.035981	318.5759	4.333486
0.00915	0.000018	0.959706	0.0009593	476.8	2.1	596.9	0.4831227	0.0014277	0.0189398	0.0000921	0.0003403	0.0000338	0.0073158	0.00066	0.0004221	0.0000153	1.89E-14	8.05E-14	25.5085	0.145169	18.85526	0.2682237	73.91758	1.012398	287.7861	3.786111
0.00915	0.000018	0.959706	0.0009593	492.0	1.7	296.6	0.2623978	0.0013096	0.0112304	0.0000787	0.0001351	0.000034	0.0049688	0.000784	0.0001874	0.00002	1.12E-14	4.78E-14	23.36488	0.2010077	16.38305	0.7901358	78.67812	3.359505	281.1107	11.19024
0.00915	0.000018	0.959706	0.0009593	506.2	1.6	296.6	0.3257864	0.0013096	0.0151779	0.0000903	0.0002642	0.0000329	0.0075221	0.0007738	0.0002559	0.0000294	1.52E-14	6.49E-14	21.46457	0.1541406	16.43972	0.5851008	76.65819	2.705114	253.2474	8.415129
0.00915	0.000018	0.959706	0.0009593	519.3	1.6	296.7	0.3982048	0.0013095	0.0194736	0.0001017	0.00027	0.0000336	0.0103774	0.0008107	0.0003113	0.0000294	1.95E-14	8.32E-14	20.44843	0.1261596	15.6754	0.4624475	76.65819	2.240071	242.3514	6.691286
0.00915	0.000018	0.959706	0.0009593	531.2	2.2	297.6	0.4043233	0.0013095	0.0211918	0.0000938	0.0003083	0.000032	0.0121005	0.0007755	0.0002927	0.000029	2.12E-14	9.07E-14	19.07925	0.1046133	14.95525	0.4184541	78.3849	2.180474	231.9012	6.089827
0.00915	0.000018	0.959706	0.0009593	545.4	1.7	297.7	0.4331017	0.0013094	0.0232498	0.0001034	0.0002972	0.0000326	0.0146168	0.0007743	0.000278	0.0000302	2.32E-14	9.91E-14	18.62823	0.1002	15.0587	0.397094	80.83804	2.115285	233.4061	5.774162
0.00915	0.000018	0.959706	0.0009593	562.2	2.9	296.6	0.5000402	0.0014016	0.0269837	0.0000964	0.0004113	0.0000324	0.0170749	0.000772	0.0002655	0.0000302	2.70E-14	1.15E-13	18.53117	0.0841319	15.59367	0.3342303	84.14833	1.837758	241.1685	4.966121
0.00915	0.000018	0.959706	0.0009593	577.9	2.3	2996.6	0.1020234	0.0013113	0.0032054	0.0001153	0.0001447	0.0000404	0.0018843	0.0008159	0.00024	0.0000189	3.21E-15	1.37E-14	31.82817	1.2155	9.480261	1.840786	29.78575	5.696313	150.4139	28.02416
0.00915	0.000018	0.959706	0.0009593	444.9	2.3	2997.1	0.4482652	0.0010885	0.0208893	0.0001141	0.0003146	0.0000395	0.0043264	0.0008566	0.000444	0.0000208	2.69E-14	1.15E-13	21.45912	0.1658256	15.11264	0.3245356	70.42326	1.459842	234.1902	4.717041
0.00915	0.000018	0.959706	0.0009593	509.9	1.7	896.5	0.2213209	0.0007279	0.0111926	0.0000907	0.0001339	0.0000279	0.0085429	0.0006282	0.0001093	0.0000368	1.12E-14	4.78E-14	19.77382	0.1729637	16.85816	0.9945437	85.25495	4.989781	259.3846	14.25542
0.00915	0.000018	0.959706	0.0009593	532.2	2.0	597.3	0.1860882	0.0005938	0.0095098	0.0000861	0.0000986	0.0000282	0.0066804	0.0006668	0.0000727	0.0000366	9.51E-15	3.98E-14	19.56807	0.1878309	17.2842	1.160129	88.32859	5.881264	265.481	16.57289
0.00915	0.000018	0.959706	0.0009593	545.4	1.7	597.3	0.4331017	0.0013094	0.0232498	0.0001034	0.0002972	0.0000326	0.0146168	0.0007743	0.000278	0.0000302	2.32E-14	9.91E-14	18.62823	0.1002	15.0587	0.397094	80.83804	2.115285	233.4061	5.774162
0.00915	0.000018	0.959706	0.0009593	562.4	2.7	297.5	0.131744	0.0006699	0.0063873	0.0000612	0.0001215	0.0000329	0.0076187	0.0009859	0.0000914	0.0000287	6.30E-15	2.69E-14	20.62585	0.2235954	16.35257	1.352638	79.28192	6.526361	252.1231	15.96623
0.00915	0.000018	0.959706	0.0009593	569.9	2.4	297.1	0.1600006	0.0006636	0.0076569	0.0000587	0.0001299	0.0000329	0.005657	0.0009583	0.0000147	0.000029	7.66E-15	3.27E-14	20.89614	0.1820734	20.32472	1.114297	97.26544	5.440128	308.4025	15.96325
0.00915	0.000018	0.959706	0.0009593	585.1	2.4	297.6	0.2364741	0.0007899	0.0112867	0.0000709	0.0001175	0.0000336	0.008705	0.0009881	0.0001041	0.000029	1.13E-14	4.82E-14	20.95162	0.1491088	18.19785	0.7785127	86.85651	3.686883	278.4859	11.04165
0.00915	0.000018	0.959706	0.0009593	597.5	3.9	297.1	0.2855105	0.0009173	0.0134137	0.0000673	0.0001588	0.0000323	0.0111488	0.0009743	0.0000716	0.0000294	1.34E-14	5.71E-14	21.28502	0.1267662	19.69127	0.6642683	92.51233	3.10043	299.544	9.312232
0.00915	0.000018	0.959706	0.0009593	618.0	2.6	297.1	0.463201	0.0010018	0.0208271	0.0000836	0.0002786	0.0000332	0.0185457	0.0009903	0.0000991	0.0000291	2.08E-14	8.85E-14	22.24027	0.1013989	20.82013	0.4141877	93.61456	1.835233	315.3004	5.756029
0.00915	0.000018	0.959706	0.0009593	640.2	2.9	297.1	0.6870685	0.0008052	0.0289255	0.0000853	0.000334	0.0000326	0.0248055	0.0009765	0.0000758	0.0000294	2.89E-14	1.23E-13	23.75099	0.0753358	22.96834	0.3116835	96.70476	1.28597	344.9107	4.261157
0.00915	0.000018	0.959706	0.0009593	653.3	2.8	297.1	0.6392539	0.0010888	0.026019	0.0000844	0.0003359	0.0000329	0.0223781	0.0009926	0.0001283	0.0000284	2.60E-14	1.11E-13	24.56876	0.0900335	23.09673	0.3371035	94.00853	1.347293	346.6651	4.604216
0.00915	0.000018	0.959706	0.0009593	677.9	2.6	297.1	0.8314124	0.0012141	0.0326563	0.0000861	0.0004493	0.000034	0.0280013	0.0009649	0.0001586	0.0000287	3.27E-14	1.39E-13	25.45944	0.0767275	24.00915	0.2720945	94.30353	1.048498	359.0844	3.690874
0.00915	0.000018	0.959706	0.0009593	696.8	1.8	297.6	0.7327759	0.0011154	0.0288783	0.0000853	0.0003877	0.0000323	0.027903	0.0010109	0.0001042	0.000029	2.89E-14	1.23E-13	25.37458	0.0842825	24.29749	0.3105994	95.75523	1.199849	362.9914	4.204086
0.00915	0.000018	0.959706	0.0009593	711.9	1.7	297.1	0.4872313	0.0010537	0.0202718	0.0000774	0.0002994	0.0000321	0.0235672	0.0009809	0.000175	0.0000294	2.03E-14	8.71E-14	24.03497	0.1019517	21.4574	0.4424406	89.27576	1.822021	324.1351	6.118695
0.00915	0.000018	0.959706	0.0009593	735.0	0.5	297.1	0.504399	0.0010538	0.0230158	0.0000895	0.0002966	0.0000329	0.0299587	0.0010303	0.0001249	0.0000287	2.30E-14	9.87E-14	21.91536	0.0967181	20.29651	0.382765	92.60865	1.719966	307.995	5.340878
0.00915	0.000018	0.959706	0.0009593	763.9	0.4	297.1	0.4943365	0.0010713	0.0270438	0.0000929	0.000358	0.0000325	0.0358097	0.0009832	0.0001561	0.0000302	2.70E-14	1.16E-13	18.27908	0.0742442	16.55535	0.3400731	90.56993	1.844716	255.0391	4.886209
0.00915	0.000018	0.959706	0.0009593	764.0	0.4	297.6	0.1942389	0.0007382	0.0127031	0.000074	0.0001541	0.0000332	0.0141268	0.0009843	0.0001182	0.0000287	1.27E-14	5.46E-14	15.29064	0.1063252	12.51177	0.6799308	81.8263	4.432028	195.9865	10.09365
0.00915	0.000018	0.959706	0.0009593	604.1	3.2	3597.4	0.0542876	0.0012402	0.0024128	0.0001125	0.0000703	0.0000427	0.0031064	0.0011014	0.0000614	0.0000183	2.41E-15	1.03E-14	22.49999	1.168444	14.90604	2.42904	66.24907	10.45426	231.1848	35.3642
0.00915	0.000018	0.959706	0.0009593	637.0	1.1	1797.1	0.027731	0.0007292	0.0019192	0.0000551	0.0000432	0.000022	0.0033246	0.0008711	0.0000347	0.0000272	1.92E-15	8.26E-15	19.66022	0.6802453	14.25778	4.264728	72.52098	21.63751	221.7222	62.41563
0.00915	0.000018	0.959706	0.0009593	662.0	0.9	1797.1	0.047727	0.0007292	0.0026604	0.0000565	0.0000607	0.000022	0.0020332	0.0008705	0.0000423	0.0000241	2.66E-15	1.15E-14	17.93975	0.4693827	13.18931	2.736607	73.52002	15.2128	206.0167	40.39256
0.00915	0.000018	0.959706	0.0009593	688.8	0.7	897.0	0.0221043	0.0007094	0.0020851	0.000056	0.0000222	0.0000225	-0.0002731	0.0009307	-0.0000226	0.0000247	2.09E-15	9.02E-15	10.09222	0.4350419	13.3275	3.571279	132.0571	35.48843	208.0557	52.66333
0.00915	0.000018	0.959706	0.0009593	699.8	1.3	1797.1	0.065386	0.0007616	0.0046178	0.0000609	0.0000638	0.0000211	0.003873	0.0008817	0.0001246	0.0000253	4.62E-15	1.99E-14	14.1595	0.2490938	6.100727	1.645731	43.08575	11.61975	98.21767	25.75844
0.00915	0.000018	0.959706	0.0009593	722.4	0.8	1197.2	0.0579686	0.0004658	0.0045473	0.0001077	0.0000688	0.0000283	0.0042882	0.0012226	0.0000514	0.0000449	4.55E-15	1.97E-14	12.74795	0.3187241	9.37093	2.958873	73.50933	23.15276	148.7487	45.08743
0.00915	0.000018	0.959706	0.0009593	732.7	1.1	1497.4	0.0728208	0.0005701	0.0059489	0.000026	0.0000729	0.0000164	0.0048531	0.0004576	0.0000578	7.59E-06	5.95E-15	1.19E-14	12.241	0.0702256	9.33902	0.3856838	76.29297	3.145769	148.2624	5.878648
0.00915	0.000018	0.959706	0.0009593	772.9	0.4	887.5	0.1257368	0.0004982	0.0118662	0.0001016	0.0001589	0.0000225	0.0185186	0.00111	0.0000165	0.0000391	1.19E-14	4.76E-14	10.59618	0.0999725	10.18229	0.9892246	96.09398	9.307331	161.0701	14.9718
0.00915	0.000018	0.959706	0.0009593	781.0	0.4	597.3	0.111619	0.0004	0.0093374	0.0000471	0.0002043	0.000013	0.0218064	0.000358	0.0002306	9.90E-06	9.34E-15	3.72E-14	11.95396	0.0739253	4.580104	0.3202854	38.31453	2.675878	74.23127	5.085862
0.00915	0.000018	0.959706	0.0009593	788.0	0.4	297.1	0.0593808	0.0005904	0.0052672	0.0000652	0.0000409	0.0000364	0.0131508	0.0010415	0.0000398	0.0000302	5.27E-15	2.10E-14	11.27375	0.1789202	9.018542	1.716546	79.99591	15.21465	143.371	26.23472
0.00915	0.000018	0.959706	0.0009593	795.0	0.3	297.6	0.0786344	0.0005054	0.0063808	0.0000599	0.000114	0.0000332	0.0136062	0.0010107	0.0000448	0.000029	6.38E-15	2.54E-14	12.32358	0.1486223	10.22958	1.363015	83.00823	11.05062	161.7858	20.62046
0.00915	0.000018	0.959706	0.0009593	801.9	0.3	297.1	0.0887799	0.0006058	0.0072186	0.0000612	0.000116	0.0000332	0.0126465	0.0009947	-0.0000131	0.0000287	7.22E-15	2.87E-14	12.29878	0.1337829	12.84266	1.193046	104.4222	9.686306	200.892	17.66291
0.00915	0.000018	0.959706	0.0009593	808.9	0.4	297.5	0.1146534	0.0006222	0.0088542	0.0000717	0.0001202	0.0000326	0.0149424	0.0010627	0.0001055	0.0000302	8.85E-15	3.52E-14	12.94904	0.126204	9.396573	1.022105	72.51947	7.88125	149.048	15.5723
0.00915	0.000018	0.959706	0.0009593	814.9	0.4	297.1	0.1130868	0.0006112	0.0082729	0.0000581	0.0001426	0.0000336	0.0137489	0.0010296	0.0000511	0.0000294	8.27E-15	3.28E-14	13.66963	0.1211147	11.82629	1.065093	86.51508	7.782019	185.7818	15.90091
0.00915	0.000018	0.959706	0.0009593	823.1	1.3	297.5	0.1493913	0.0006337	0.0115477	0.0000709	0.0001687	0.0000336	0.0169835	0.0010308	0.0001084	0.0000029	1.15E-14	4.56E-14	12.93692	0.0965693	10.13423	0.7541302	78.33576	5.818888	160.3427	11.41802
0.00915	0.000018	0.959706	0.0009593	833.9	2.6	297.1	0.1920088	0.0006641	0.015495	0.0000747	0.0001631	0.0000332	0.0173911	0.001002	0.0000921	0.0000285	1.55E-14	6.12E-14	12.39169	0.073557	10.61738	0.5531736	85.68147	4.45476	167.6431	8.341661
0.00915	0.000018	0.959706	0.0009593	845.4	1.7	297.0	0.1605013	0.0006642	0.0142977	0.0001691	0.0001611	0.0000329	0.0101706	0.0010175	0.0000315	0.0000302	1.43E-14	5.66E-14	11.22564	0.0788369	10.56709	0.6342218	94.13349	5.63792	166.8846	9.567852
0.00915	0.000018	0.959706	0.0009593	858.0	2.6	297.0	0.1312887	0.0006642	0.012346	0.0000763	0.0001929	0.0000332	0.0077951	0.0010343	0.0000555	0.000029	1.23E-14	4.90E-14	10.63409	0.0849421	9.292282	0.7054512	87.38199	6.626595	147.5499	10.75683
0.00915	0.000018	0.959706	0.0009593	870.9	1.4	297.0	0.1439582	0.0006969	0.0135666	0.0000869	0.0001703	0.0000326	0.0077255	0.0010299	0.0000478	0.0000294	1.57E-14	6.18E-14	9.189208	0.0676704	8.277587	0.5630224	90.07943	6.122116	132.0111	8.659146
0.00915	0.000018	0.959706	0.0009593	882.0	2.0	297.1	0.1356677	0.0006969	0.015712	0.0000886	0.000186	0.0000325	0.0104593	0.001021	0.0000745	0.0000284	1.57E-14	6.24E-14	8.634668	0.0658765	7.218302	0.5437249	83.59676	6.293981	115.6457	8.438385
0.00915	0.000018	0.959706	0.0009593	881.8	1.0	297.1	0.0881421	0.0006457	0.0094229	0.0000694	0.0000852	0.0000326	0.0028101	0.00110677	0.0000544	0.000029	9.42E-15	3.70E-14	9.354072	0.0972029	7.628723	0.9227927	81.5551	9.864922	122.0041	14.27109
0.00915	0.000018	0.959706	0.0009593	898.6	0.8	298.6	0.0580036	0.0006068	0.0053175	0.0000677	0.0000336	0.0000233	0.0010233	8.43E-06	0.0000302	5.32E-15	5.27E-15	1.90E-14	10.90813	0.1794917	10.43473	1.70205	95.66011	15.58702	164.8867	25.70546
0.00915	0.000018	0.959706	0.0009593	907.3	1.6	297.1	0.0830981	0.0006519	0.0052673	0.0000625	0.0000512	0.0000332	0.0056712	0.0010569	0.0000335	0.0000293	5.27E-15	1.90E-14	15.77621	0.2242831	13.87438	1.676375	87.94497	10.59716	216.1023	24.61065
0.00915	0.000018	0.959706	0.0009593	913.0	1.1	297.6	0.0646605	0.0006225	0.0028798	0.0000569	0.0000492	0.0000332	0.0042526	0.0009965	0.0000706	0.0000294	2.88E-15	1.04E-14	22.45297	0.4937186	15.12952	3.065333	67.38317	13.60255	234.4357	44.54777

Table A.10: 18-IAF-05-MOS step heating data

J	± 1σ	Discrim	± 1σ	Temp (°C)	± 1σ (°C)	Heating duration (s)	^{40}Ar	± 1σ	^{39}Ar	± 1σ	^{38}Ar	± 1σ	^{37}Ar	± 1σ	^{36}Ar	± 1σ	^{39}Ar (Moles)	$^{40}Ar_r/^{39}Ar$	± 1σ	$^{40}Ar^*/^{39}Ar_K$	± 1σ	% ^{40}Ar*	± 1σ	Age (Ma)	± 1σ
0.00915	0.000018	0.959706	0.0009593	405.9	10.2	296.6	5.651195	0.005322	0.0766977	0.0001602	0.0035277	0.0000323	0.0155994	0.0002952	0.014027	0.0000648	7.67E-14	73.08141	0.1688591	19.07871	0.2646496	25.89352	0.3559194	290.9363	3.727769
0.00915	0.000018	0.959706	0.0009593	403.6	7.9	596.9	1.849989	0.0019448	0.0313671	0.0001013	0.0013539	0.0000339	0.0050667	0.0002706	0.0050689	0.0000361	3.14E-14	58.97857	0.2003384	10.7313	0.3504329	18.19525	0.5915644	169.3601	5.279387
0.00915	0.000018	0.959706	0.0009593	441.2	5.5	296.6	1.165255	0.0009735	0.0322538	0.0000868	0.0008347	0.000033	0.0059173	0.0003001	0.0023998	0.0000321	3.23E-14	36.12773	0.101751	13.91386	0.3013877	38.51297	0.8283964	216.6818	4.423216
0.00915	0.000018	0.959706	0.0009593	440.0	5.6	596.9	1.329366	0.0016518	0.0376952	0.0001071	0.0009832	0.0000328	0.0075578	0.0002578	0.0027278	0.0000313	3.77E-14	35.26616	0.1093576	13.66097	0.2547337	38.73677	0.7155042	212.9666	3.746204
0.00915	0.000018	0.959706	0.0009593	474.4	4.3	296.7	1.17859	0.0009704	0.0408083	0.0000902	0.0008248	0.0000306	0.0093564	0.0003001	0.0015998	0.00003	4.08E-14	28.88109	0.0681409	17.1767	0.2228766	59.47387	0.7654986	263.9447	3.20088
0.00915	0.000018	0.959706	0.0009593	475.1	4.4	596.8	1.346396	0.0016407	0.0489666	0.0001203	0.0009357	0.0000339	0.0120982	0.0002703	0.0019508	0.0000309	4.90E-14	27.49619	0.0754103	15.60158	0.1954579	56.74089	0.7004695	241.283	2.829808
0.00915	0.000018	0.959706	0.0009593	509.8	2.4	296.6	1.313385	0.0011024	0.0576692	0.0001225	0.000918	0.0000308	0.0172607	0.0003055	0.0011557	0.0000298	5.77E-14	22.77447	0.052029	16.79144	0.1593455	73.72922	0.6847046	258.428	2.285207
0.00915	0.000018	0.959706	0.0009593	527.2	2.7	296.7	1.388935	0.0011933	0.067003	0.0001315	0.0009649	0.0000304	0.0249617	0.0002812	0.0010987	0.0000293	6.70E-14	20.72944	0.044421	15.8337	0.1354363	76.38268	0.6392883	244.6405	1.957188
0.00915	0.000018	0.959706	0.0009593	544.0	3.9	296.6	1.29336	0.0010293	0.0655655	0.0001315	0.0009638	0.0000303	0.0294685	0.0002955	0.0009374	0.0000292	6.56E-14	19.72622	0.0425604	15.45779	0.1372577	78.36162	0.6806965	239.2	1.989486
0.00915	0.000018	0.959706	0.0009593	560.5	3.5	296.7	1.390838	0.0010648	0.0715112	0.0001315	0.0009932	0.0000301	0.0374846	0.0003114	0.0008658	0.0000291	7.15E-14	19.44952	0.0387288	15.83483	0.1257309	81.415	0.6319654	244.6567	1.816918
0.00915	0.000018	0.959706	0.0009593	576.9	2.7	296.7	1.424999	0.0011924	0.0716497	0.0001314	0.0009404	0.0000296	0.0435519	0.0003007	0.0007721	0.000029	7.16E-14	19.88841	0.0400976	16.67108	0.1256649	83.82312	0.6173709	256.7011	1.805344
0.00915	0.000018	0.959706	0.0009593	489.9	2.5	1796.7	0.4243832	0.0042644	0.0142189	0.0000539	0.0002997	0.0000271	0.0084129	0.0002404	0.0006666	0.0000248	1.42E-14	29.84642	0.3205205	15.84893	0.6034133	53.1016	2.081256	244.8605	8.718854
0.00915	0.000018	0.959706	0.0009593	514.9	1.9	1796.8	0.6689054	0.0042425	0.0262738	0.0000637	0.0004897	0.000028	0.0163344	0.0002488	0.0007981	0.0000242	2.63E-14	25.45106	0.1728638	16.38214	0.3216319	64.36723	1.318867	252.5487	4.627612
0.00915	0.000018	0.959706	0.0009593	535.0	2.5	1796.7	0.9570098	0.0042211	0.0438383	0.0000828	0.0006601	0.0000282	0.0296697	0.0002537	0.0007227	0.0000236	4.38E-14	21.83046	0.1047362	16.90818	0.1900617	77.45223	0.923753	260.1014	2.723193
0.00915	0.000018	0.959706	0.0009593	570.7	2.6	596.9	0.7783108	0.0013302	0.0373152	0.0001059	0.0004875	0.0000326	0.0206964	0.0003152	0.0002882	0.0000306	3.73E-14	20.85772	0.0690965	18.55168	0.2530994	88.94397	1.19661	283.4974	3.579774
0.00915	0.000018	0.959706	0.0009593	594.0	3.8	297.7	0.6876012	0.0005516	0.0328593	0.0000762	0.0004189	0.0000311	0.0249567	0.000293	0.0002253	0.0000289	3.29E-14	20.92563	0.0513309	18.87859	0.2670615	90.21755	1.261066	288.1153	3.767615
0.00915	0.000018	0.959706	0.0009593	594.1	3.4	596.8	1.114433	0.0014411	0.0513353	0.0001232	0.0006642	0.0000313	0.0407868	0.000271	0.0003744	0.000029	5.13E-14	21.70891	0.0591717	19.53123	0.1773291	89.96871	0.7963506	297.299	2.489026
0.00915	0.000018	0.959706	0.0009593	610.5	3.5	296.6	0.6980818	0.0005531	0.0315012	0.0000799	0.0004022	0.00003	0.025566	0.0003203	0.0001729	0.0000294	3.15E-14	22.16049	0.05891	20.52177	0.2837119	92.60521	1.260644	311.1493	3.951849
0.00915	0.000018	0.959706	0.0009593	611.0	3.5	596.0	1.15239	0.0015156	0.0507394	0.0001261	0.0006065	0.0000319	0.0413401	0.0002769	0.000335	0.0000296	5.07E-14	22.71194	0.0638607	20.74082	0.1830049	91.32121	0.7864928	314.1979	2.557313
0.00915	0.000018	0.959706	0.0009593	643.1	2.6	296.6	1.311151	0.0010315	0.0550691	0.0001068	0.0006955	0.0000313	0.0442803	0.0002991	0.0002155	0.0000282	5.51E-14	23.8092	0.049824	22.64075	0.1600763	95.09241	0.6508599	340.4264	2.193906
0.00915	0.000018	0.959706	0.0009593	642.8	2.2	596.9	1.65787	0.0020389	0.0691216	0.0001639	0.0008839	0.000032	0.0573047	0.0003025	0.0003863	0.0000303	6.91E-14	23.98484	0.064074	22.31636	0.1443571	93.04358	0.5715298	335.9751	1.983344
0.00915	0.000018	0.959706	0.0009593	676.1	0.9	296.7	1.50255	0.0014762	0.0584784	0.0001318	0.0007007	0.0000305	0.0460813	0.000322	0.0002624	0.0000292	5.85E-14	25.69409	0.0631716	24.35447	0.1600497	94.78627	0.5961699	363.7624	2.17759
0.00915	0.000018	0.959706	0.0009593	676.1	0.9	597.4	1.556827	0.0019629	0.0640263	0.0001472	0.0008003	0.0000317	0.0537142	0.0002898	0.0003678	0.0000293	6.40E-14	24.31543	0.0637505	22.60011	0.1495615	92.94556	0.5885693	339.8695	2.050427
0.00915	0.000018	0.959706	0.0009593	691.2	0.9	296.7	0.7071534	0.0006573	0.0291619	0.000076	0.0003912	0.0000311	0.0252817	0.000306	0.0001538	0.0000296	2.92E-14	24.24923	0.0671089	22.6743	0.3098124	93.50525	1.257159	340.8863	4.245014
0.00915	0.000018	0.959706	0.0009593	691.1	0.8	597.4	0.9035909	0.0013631	0.0389786	0.000103	0.000474	0.0000332	0.0343563	0.0002674	0.0002737	0.0000304	3.90E-14	23.18169	0.0705317	21.08523	0.2421078	90.95638	1.025583	318.9808	3.357767
0.00915	0.000018	0.959706	0.0009593	714.9	0.5	296.6	0.6138365	0.0005692	0.0275952	0.0000683	0.0003678	0.0000315	0.029576	0.000302	0.0001697	0.0000293	2.76E-14	22.24429	0.0587875	20.40783	0.3221191	91.74412	1.432715	309.5615	4.490769
0.00915	0.000018	0.959706	0.0009593	714.0	0.7	596.8	0.6932539	0.0013225	0.0341383	0.0001047	0.0004759	0.0000318	0.0300003	0.0002616	0.000242	0.0000304	3.41E-14	20.3072	0.0733524	18.19062	0.2748401	89.5772	1.336198	278.3835	3.898279
0.00915	0.000018	0.959706	0.0009593	750.0	0.5	597.4	1.13789	0.001577	0.0633833	0.0001391	0.0008443	0.0000322	0.0707932	0.000298	0.0003432	0.0000302	6.34E-14	17.95092	0.0466023	16.33427	0.1490125	90.99408	0.8155298	251.8598	2.144796
0.00915	0.000018	0.959706	0.0009593	748.3	1.8	1796.7	0.8645788	0.0041973	0.0672907	0.0000914	0.0008957	0.0000283	0.0518694	0.0002507	0.0004423	0.0000244	6.73E-14	12.8484	0.0647696	10.88612	0.1239318	84.7274	1.0567	171.6911	1.89476
0.00915	0.000018	0.959706	0.0009593	780.0	0.4	596.8	0.3705016	0.0012737	0.0385474	0.0001065	0.000599	0.0000325	0.0617664	0.0002934	0.0002198	0.0000289	3.85E-14	9.611595	0.0423895	7.909012	0.2271548	82.28616	2.369328	126.3336	3.504571
0.00915	0.000018	0.959706	0.0009593	800.0	0.3	597.4	0.4464042	0.0012827	0.0508146	0.0001168	0.0007248	0.0000325	0.088757	0.0003071	0.0002942	0.0000291	5.08E-14	8.784953	0.0323282	7.056381	0.1728507	80.32349	1.983794	113.131	2.701846
0.00915	0.000018	0.959706	0.0009593	826.0	0.3	296.6	0.4591769	0.0005235	0.049741	0.0000923	0.0007003	0.0000307	0.1175474	0.0003617	0.0002319	0.0000293	4.97E-14	9.231363	0.0201047	7.839645	0.1765434	84.92403	1.908383	125.2631	2.725346
0.00915	0.000018	0.959706	0.0009593	825.0	1.4	806.6	0.813463	0.0010845	0.0893797	0.0001171	0.0011617	0.0000361	0.0838458	0.0004411	0.0003805	0.0000295	8.94E-14	9.101204	0.0212265	7.830157	0.0710855	86.0343	0.7720713	125.1166	1.097454
0.00915	0.000018	0.959706	0.0009593	842.5	1.5	596.9	0.7018846	0.001351	0.0760235	0.0001472	0.0009842	0.0000315	0.0754194	0.0003162	0.0003193	0.0000299	7.60E-14	9.232463	0.0252061	7.978661	0.1196823	86.41964	1.296195	127.4078	1.845377
0.00915	0.000018	0.959706	0.0009593	859.0	0.3	596.9	0.8686482	0.0014014	0.0921076	0.0001813	0.0011523	0.0000327	0.0861391	0.000331	0.0002092	0.0000299	9.21E-14	9.430799	0.0240041	8.752527	0.0996922	92.8079	1.051889	139.3008	1.527072
0.00915	0.000018	0.959706	0.0009593	859.0	0.2	296.7	0.3536444	0.0008676	0.030337	0.0000994	0.0003861	0.0000315	0.0269213	0.000341	0.0001281	0.0000301	3.03E-14	11.65718	0.0477243	10.39641	0.2990834	89.18455	2.558323	164.3078	4.518398
0.00915	0.000018	0.959706	0.0009593	873.0	0.2	866.5	0.83675	0.0010791	0.0809415	0.0001629	0.0009974	0.0000368	0.1086928	0.0004609	0.0002316	0.0000186	8.09E-14	10.33771	0.024715	9.483391	0.072295	91.73593	0.6848021	150.4616	1.100591
0.00915	0.000018	0.959706	0.0009593	888.0	0.3	596.8	0.2799394	0.0013282	0.0170485	0.0000932	0.0002191	0.0000322	0.0392423	0.0002932	0.0000972	0.0000295	1.70E-14	16.4202	0.1188518	14.71792	0.5293747	89.63302	3.214727	228.4441	7.718815
0.00915	0.000018	0.959706	0.0009593	902.0	0.2	596.8	0.2250819	0.0012906	0.0063288	0.0000874	0.000078	0.0000318	0.0297968	0.0003001	0.0000723	0.0000304	6.33E-15	35.56458	0.331781	32.15146	1.513079	90.40304	4.100058	466.2902	19.3429
0.00915	0.000018	0.959706	0.0009593	902.0	0.2	296.6	0.0270839	0.0005083	0.0002333	0.0000634	-0.0000104	0.0000327	0.0024362	0.0003255	-0.0000256	0.0000306	2.33E-16	116.1071	31.61845	148.9122	56.3766	128.2542	33.90249	1554.543	394.7983

Table A.11: 18-IAF-05-MOS (silt) step heating data

J	± 1σ	Discrim	± 1σ	Temp (^{o}C)	± 1σ (^{o}C)	Heating duration (s)	^{40}Ar	± 1σ	^{39}Ar	± 1σ	^{38}Ar	± 1σ	^{37}Ar	± 1σ	^{36}Ar	± 1σ	^{39}Ar (Moles)	^{40}Ar/^{39}Ar	± 1σ	^{40}Ar*/^{39}Ar$_K$	± 1σ	% ^{40}Ar*	± 1σ	Age (Ma)	± 1σ
0.00915	0.000018	0.959706	0.0009593	388.5	2.9	296.7	8.49511	0.007713	0.1206533	0.0002061	0.0058351	0.0000362	0.0366719	0.0005056	0.0233236	0.0000826	1.21E-13	70.40926	0.1362261	12.72038	0.2152692	18.06271	0.3045574	199.0807	3.190231
0.00915	0.000018	0.959706	0.0009593	397.0	3.1	296.7	1.06144	0.003	0.0250769	0.000107	0.0007013	0.0000342	0.0034771	0.0004446	0.0024556	0.0000407	2.51E-14	42.3274	0.2166453	13.10282	0.5023285	30.95344	1.182538	204.7395	7.42111
0.00915	0.000018	0.959706	0.0009593	396.5	2.5	597.3	1.08059	0.0042638	0.029715	0.0001366	0.0007451	0.0000345	0.0042204	0.0004612	0.00221	0.0000496	2.97E-14	36.36511	0.2203268	14.17166	0.5223272	38.96742	1.433276	220.4613	7.649755
0.00915	0.000018	0.959706	0.0009593	406.3	2.4	297.7	0.45507	0.0024083	0.0148895	0.0000864	0.0003546	0.0000335	0.0020592	0.0005078	0.0008226	0.0000388	1.49E-14	30.56314	0.2399709	14.07973	0.7997597	46.06436	2.614262	219.1145	11.72163
0.00915	0.000018	0.959706	0.0009593	418.4	2.0	296.7	0.52464	0.0025456	0.0194424	0.0001026	0.0004127	0.0000338	0.0036123	0.0004584	0.0007566	0.0000388	1.94E-14	26.98427	0.1934276	15.38237	0.6159457	56.99915	2.279305	238.1065	8.933243
0.00915	0.000018	0.959706	0.0009593	427.1	2.3	296.6	0.53494	0.0026173	0.0213101	0.0001206	0.0003497	0.0000333	0.0041674	0.0004862	0.0006815	0.0000385	2.13E-14	25.10269	0.187749	15.57092	0.5608506	62.02225	2.227017	240.839	8.121899
0.00915	0.000018	0.959706	0.0009593	417.9	2.3	596.8	0.55382	0.0038079	0.0220558	0.0001279	0.0004071	0.0000345	0.0053144	0.0004031	0.0007988	0.0000485	2.21E-14	25.10997	0.2258595	14.31788	0.6839732	57.01282	2.731652	222.6016	10.0053
0.00915	0.000018	0.959706	0.0009593	430.7	1.8	596.9	0.64454	0.0038588	0.028708	0.0001366	0.0004877	0.0000355	0.0061585	0.0004092	0.0007174	0.0000483	2.87E-14	22.45158	0.1717074	15.00966	0.5245533	66.84569	2.348678	232.6929	7.630564
0.00915	0.000018	0.959706	0.0009593	448.3	2.0	296.6	0.46649	0.0026173	0.0222621	0.0001298	0.0003721	0.0000333	0.0046283	0.0004778	0.0003484	0.0000388	2.23E-14	20.95442	0.1695259	16.3005	0.5415583	77.78176	2.581231	251.3736	7.79696
0.00915	0.000018	0.959706	0.0009593	460.0	1.7	301.2	0.5636	0.0026173	0.028593	0.0001391	0.000386	0.0000335	0.0067481	0.0005116	0.0003528	0.0000388	2.86E-14	19.71112	0.1325553	16.04744	0.4223947	81.40282	2.139392	247.7266	6.093609
0.00915	0.000018	0.959706	0.0009593	469.1	1.8	296.7	0.57158	0.0026173	0.0310637	0.0001485	0.0004384	0.0000342	0.0071103	0.0005122	0.0003809	0.0000385	3.11E-14	18.40026	0.1217989	14.7589	0.3860722	80.20071	2.095031	229.0414	5.627462
0.00915	0.000018	0.959706	0.0009593	480.0	1.6	296.6	0.6193	0.0026173	0.0357748	0.000158	0.0004631	0.0000335	0.0096221	0.0004899	0.0003433	0.0000385	3.58E-14	17.31106	0.1058086	14.46936	0.3356969	83.57241	1.93595	224.8161	4.904629
0.00915	0.000018	0.959706	0.0009593	493.1	1.3	296.7	0.71328	0.0026907	0.044236	0.0001771	0.0005686	0.0000342	0.0132098	0.0004905	0.0003395	0.0000388	4.42E-14	16.12442	0.0887005	13.85867	0.2743591	85.93441	1.697303	215.8717	4.028344
0.00915	0.000018	0.959706	0.0009593	502.1	1.4	296.6	0.69037	0.0026173	0.0453472	0.0001771	0.0005804	0.0000345	0.0155783	0.0004805	0.0003095	0.0000388	4.53E-14	15.22408	0.0828656	13.21564	0.2667708	86.79094	1.75004	206.4055	3.937487
0.00915	0.000018	0.959706	0.0009593	429.9	1.8	1796.7	0.2440372	0.0019529	0.013105	0.000101	0.0001868	0.0000454	0.0048937	0.0004974	0.0003949	0.0000463	1.31E-14	18.62164	0.2068472	9.655242	1.0677	51.83817	5.733474	153.0759	16.23077
0.00915	0.000018	0.959706	0.0009593	460.0	1.7	1796.7	0.5019241	0.0021901	0.0323075	0.0001552	0.0004603	0.0000451	0.0118538	0.0004748	0.000466	0.0000457	3.23E-14	15.53583	0.1008069	11.26007	0.4309964	72.46306	2.769802	177.3088	6.464622
0.00915	0.000018	0.959706	0.0009593	490.2	1.4	1796.7	1.080272	0.0023557	0.0771013	0.000204	0.0010139	0.0000449	0.0316768	0.0004549	0.0005912	0.0000459	7.71E-14	14.01107	0.048038	11.75681	0.1829877	83.89127	1.299638	184.7442	2.733415
0.00915	0.000018	0.959706	0.0009593	514.9	1.3	596.8	0.726335	0.0033392	0.0528353	0.0000786	0.0006776	0.0000351	0.0283303	0.0005262	0.0002787	0.0000478	5.28E-14	13.74716	0.0664247	12.21837	0.2782712	88.85085	2.060142	191.6257	4.140941
0.00915	0.000018	0.959706	0.0009593	525.9	1.3	296.6	0.440648	0.0019424	0.0320875	0.0000776	0.0005048	0.0000358	0.0184706	0.0005447	0.0001514	0.0000382	3.21E-14	13.7327	0.0690368	12.37353	0.3618755	90.07148	2.655057	193.9332	5.378185
0.00915	0.000018	0.959706	0.0009593	535.1	1.8	296.6	0.506725	0.0019739	0.0368996	0.0000956	0.0004681	0.0000335	0.0222788	0.0005566	0.0001741	0.0000381	3.69E-14	13.73253	0.0642509	12.37645	0.3150383	90.09202	2.308164	193.9766	4.68198
0.00915	0.000018	0.959706	0.0009593	542.6	1.7	297.7	0.52237	0.0024083	0.0374356	0.0001298	0.0004874	0.0000335	0.0240056	0.0005823	0.0001865	0.0000377	3.74E-14	13.95382	0.0804875	12.5223	0.3105382	89.70571	2.241219	196.1428	4.609575
0.00915	0.000018	0.959706	0.0009593	552.0	1.5	296.6	0.579532	0.00195	0.0418228	0.000068	0.0005499	0.0000353	0.0302919	0.0005701	0.0001403	0.0000396	4.18E-14	13.85683	0.0517796	12.91831	0.2875416	93.18499	2.092237	202.0116	4.254386
0.00915	0.000018	0.959706	0.0009593	559.3	1.7	297.7	0.573821	0.0019138	0.0405143	0.0000783	0.0004995	0.0000333	0.0307708	0.0005298	0.0001361	0.0000384	4.05E-14	14.16343	0.0546006	13.2271	0.2884343	93.34463	2.051235	206.5746	4.256838
0.00915	0.000018	0.959706	0.0009593	564.9	1.5	296.7	0.552397	0.0018911	0.0383152	0.0000831	0.0004795	0.0000328	0.030626	0.0005352	0.0000945	0.000038	3.83E-14	14.41719	0.0584286	13.75064	0.3019126	95.32855	2.10822	214.2847	4.436798
0.00915	0.000018	0.959706	0.0009593	570.1	1.6	296.6	0.527952	0.0019104	0.0357683	0.000088	0.000419	0.0000345	0.0298258	0.000585	0.0001442	0.0000384	3.58E-14	14.76034	0.0645912	13.62962	0.3271445	92.29056	2.228671	212.5055	4.81233
0.00915	0.000018	0.959706	0.0009593	585.0	1.5	296.6	0.70288	0.0019138	0.0467329	0.0000855	0.0005556	0.0000353	0.0406325	0.0005856	0.0001814	0.0000387	4.67E-14	15.04037	0.0493453	13.95803	0.2520657	92.75226	1.685384	217.33	3.698033
0.00915	0.000018	0.959706	0.0009593	600.2	2.8	296.6	0.832412	0.0018942	0.0533824	0.0000701	0.0006255	0.0000362	0.0496326	0.0006145	0.0001439	0.0000381	5.34E-14	15.59338	0.0409666	14.87088	0.2170434	95.30951	1.402284	230.6729	3.160813
0.00915	0.000018	0.959706	0.0009593	620.1	1.9	297.6	1.168947	0.0018506	0.0709044	0.0000673	0.0008655	0.0000342	0.0698095	0.0005739	0.0001727	0.0000382	7.09E-14	16.48623	0.0304303	15.84679	0.1637293	96.05986	0.9999211	244.8296	2.365801
0.00915	0.000018	0.959706	0.0009593	640.0	1.6	296.7	1.358473	0.0018439	0.0820359	0.0000633	0.0009641	0.0000331	0.080608	0.0005508	0.0002061	0.0000376	8.20E-14	16.5595	0.0258574	15.89733	0.1393691	95.93996	0.8478751	245.5597	2.012996
0.00915	0.000018	0.959706	0.0009593	559.9	1.6	1796.7	0.3874046	0.0014044	0.0220956	0.0000716	0.0002799	0.0000454	0.0215574	0.0005542	0.0001546	0.0000504	2.21E-14	17.53308	0.0852756	15.531	0.6857824	88.52476	3.911487	240.2609	9.934262
0.00915	0.000018	0.959706	0.0009593	575.0	1.4	1796.7	0.4384043	0.0014596	0.0274575	0.00007	0.0003111	0.0000454	0.0272405	0.0005985	0.0001641	0.0000472	2.75E-14	15.96666	0.0669429	14.26935	0.5173889	89.31217	3.243978	221.8916	7.571439
0.00915	0.000018	0.959706	0.0009593	595.1	2.3	1796.7	0.6075657	0.0013824	0.039906	0.0000767	0.0004961	0.0000448	0.0404105	0.0005082	0.0001757	0.0000495	3.99E-14	15.22494	0.0453585	13.99937	0.3735177	91.88998	2.454251	217.9364	5.478006
0.00915	0.000018	0.959706	0.0009593	623.0	1.8	1797.7	1.018352	0.0013384	0.0674571	0.0000525	0.0008129	0.0000454	0.0679445	0.0005336	0.0002418	0.0000462	6.75E-14	15.09628	0.023054	14.11484	0.2058842	93.43787	1.366505	219.6291	3.01667
0.00915	0.000018	0.959706	0.0009593	639.9	1.1	1796.7	1.045931	0.0014312	0.0676653	0.0000759	0.0008254	0.0000465	0.064385	0.000535	0.0002453	0.0000458	6.77E-14	15.45741	0.0273485	14.45901	0.2038993	93.48353	1.320322	224.6648	2.979278
0.00915	0.000018	0.959706	0.0009593	661.9	0.9	896.6	0.704255	0.0010548	0.0444215	0.0000578	0.0005513	0.0000304	0.0373308	0.0006959	0.0001618	0.0000247	4.44E-14	15.85391	0.031445	14.84069	0.1690835	93.55868	1.068184	230.2332	2.462969
0.00915	0.000018	0.959706	0.0009593	673.1	0.8	896.6	0.628907	0.0010218	0.0425788	0.0000632	0.000589	0.0000304	0.0364135	0.0007166	0.0001615	0.0000277	4.26E-14	14.77044	0.0325113	13.7133	0.1971005	92.79229	1.335082	213.736	2.897396
0.00915	0.000018	0.959706	0.0009593	686.1	0.7	896.6	0.559114	0.0010026	0.0419444	0.0000605	0.0005247	0.0000288	0.0374289	0.0007287	0.0002038	0.0000271	4.19E-14	13.3299	0.030674	11.95655	0.1955823	89.64652	1.46951	187.7254	2.916736
0.00915	0.000018	0.959706	0.0009593	693.0	0.7	597.4	0.284773	0.0033577	0.0234256	0.000084	0.0002483	0.0000345	0.0204242	0.0005298	0.0000572	0.0000479	2.34E-14	12.15648	0.1498128	11.50239	0.6292509	94.56772	5.281359	180.9397	9.419357
0.00915	0.000018	0.959706	0.0009593	697.9	1.0	597.4	0.245419	0.0033407	0.0211649	0.0001001	0.0002806	0.0000343	0.0169892	0.0004964	0.0000765	0.0000486	2.12E-14	11.59555	0.1671016	10.58504	0.7051817	91.24019	6.18902	167.1554	10.63676
0.00915	0.000018	0.959706	0.0009593	705.8	1.5	596.8	0.256095	0.0033596	0.0227768	0.0000872	0.000263	0.0000348	0.0180872	0.0004941	0.000086	0.0000481	2.28E-14	11.24368	0.1536559	10.18449	0.6494051	90.53555	5.883621	161.1035	9.828279
0.00915	0.000018	0.959706	0.0009593	715.3	1.2	297.7	0.1394	0.0018232	0.0128762	0.0000694	0.0001463	0.0000342	0.0095337	0.0005289	-3.10E-06	0.0000387	1.29E-14	10.82617	0.1531395	10.96139	0.9104061	101.2038	8.491622	172.8233	13.68932
0.00915	0.000018	0.959706	0.0009593	727.2	0.8	296.7	0.19859	0.0018578	0.0176049	0.0000768	0.0002228	0.0000353	0.0151059	0.0005403	0.0000584	0.0000387	1.76E-14	11.28041	0.1164354	10.36379	0.6664056	91.82536	5.953183	163.8149	10.07046
0.00915	0.000018	0.959706	0.0009593	739.4	1.0	296.6	0.241693	0.0018682	0.0242653	0.0000847	0.000244	0.0000342	0.0264723	0.0005475	0.0000718	0.0000384	2.43E-14	9.960425	0.0844795	9.169501	0.4803991	91.99629	4.861328	145.6767	7.332791
0.00915	0.000018	0.959706	0.0009593	763.4	1.1	296.6	0.456373	0.0018764	0.049909	0.0000847	0.0006895	0.0000349	0.0893589	0.0006038	0.0001207	0.0000393	4.99E-14	9.144108	0.0406752	8.573999	0.2386735	93.65609	2.630566	136.5641	3.661509
0.00915	0.000018	0.959706	0.0009593	787.8	1.0	296.6	0.790922	0.0018764	0.0846863	0.0000965	0.0010539	0.0000332	0.1534486	0.000649	0.0002177	0.0000379	8.47E-14	9.339427	0.0245802	8.725408	0.1360099	93.31517	1.467469	138.8854	2.083861
0.00915	0.000018	0.959706	0.0009593	795.0	1.3	596.9	1.207624	0.0033218	0.1264016	0.0000846	0.001659	0.0000362	0.1409661	0.0006458	0.0004477	0.0000482	1.26E-13	9.553863	0.0270466	8.590657	0.1169828	89.85533	1.246864	136.8196	1.794389
0.00915	0.000018	0.959706	0.0009593	810.9	0.4	597.4	1.287607	0.0033127	0.1296293	0.0000852	0.0016255	0.0000338	0.1627555	0.0005793	0.0004663	0.0000482	1.30E-13	9.932991	0.0263769	8.965346	0.1140856	90.18615	1.169351	142.5578	1.744403
0.00915	0.000018	0.959706	0.0009593	825.2	0.9	596.8	1.08696	0.0033347	0.0915241	0.0000846	0.0011732	0.0000348	0.1401501	0.0005802	0.0003869	0.0000476	9.15E-14	11.87622	0.0380534	10.7458	0.1599764	90.39088	1.371409	169.5786	2.409806
0.00915	0.000018	0.959706	0.0009593	837.9	3.5	596.9	0.479066	0.0033615	0.0292701	0.0000859	0.0003313	0.0000348	0.0533875	0.0005512	0.0002336	0.0000486	2.93E-14	16.36709	0.1244831	14.14557	0.5109055	86.32121	3.165868	220.0793	7.484058
0.00915	0.000018	0.959706	0.0009593	867.0	0.4	596.9	0.148285	0.0033266	0.0053566	0.0000744	0.0000562	0.0000348	0.0183684	0.0005383	0.0000994	0.0000483	5.36E-15	27.68276	0.7303968	22.4651	2.788871	80.9607	10.15105	338.0175	38.27347
0.00915	0.000018	0.959706	0.0009593	886.0	0.3	596.9	0.293744	0.0034179	0.0076874	0.0000815	0.00016	0.0000371	0.0305557	0.0005988	0.0003002	0.0000506	7.69E-15	38.21121	0.6014732	26.94125	2.041254	70.31273	5.337733	398.4262	27.09301

Table A.12: 18-IAF-06-MOS step heating data

J	± 1σ	Discrim	± 1σ	Temp (°C)	± 1σ (°C)	Heating duration (s)	^{40}Ar	± 1σ	^{39}Ar	± 1σ	^{38}Ar	± 1σ	^{37}Ar	± 1σ	^{36}Ar	± 1σ	^{39}Ar (Moles)	^{40}Ar/^{39}Ar	± 1σ	^{40}Ar*/^{39}Ar$_K$	± 1σ	% ^{40}Ar*	± 1σ	Age (Ma)	± 1σ
0.00915	0.000018	0.959706	0.0009593	430.4	3.0	296.7	6.29137	0.0084235	0.1881203	0.0003537	0.0028435	0.0000269	0.0184345	0.0005138	0.0033197	0.0000358	1.88E-13	33.44333	0.077198	28.18358	0.0896887	84.26875	0.24399	414.8405	1.179656
0.00915	0.000018	0.959706	0.0009593	444.4	2.5	296.7	1.680839	0.0033593	0.0737918	0.0002256	0.0009672	0.0000246	0.0059896	0.0005065	0.0007081	0.0000347	7.38E-14	22.77814	0.0831965	19.92009	0.159634	87.45056	0.670953	302.749	2.233911
0.00915	0.000018	0.959706	0.0009593	457.4	2.6	296.7	1.694057	0.0031629	0.0716559	0.0002158	0.0009473	0.0000255	0.0064089	0.0005036	0.0004752	0.0000347	7.17E-14	23.64158	0.0837812	21.66911	0.164525	91.65393	0.6612961	327.0605	2.271607
0.00915	0.000018	0.959706	0.0009593	468.6	2.6	297.7	1.631306	0.0029669	0.0693558	0.0002061	0.0008779	0.0000244	0.0062967	0.0005077	0.0003868	0.0000347	6.94E-14	23.52083	0.0819471	21.86355	0.1682448	92.95106	0.6810917	329.7432	2.319522
0.00915	0.000018	0.959706	0.0009593	483.1	2.3	296.6	1.800285	0.0030646	0.0802977	0.0002158	0.0009407	0.0000249	0.0083441	0.000512	0.0003589	0.0000342	8.03E-14	22.42014	0.0713324	21.0946	0.1445272	94.08405	0.6141609	319.1108	2.004288
0.00915	0.000018	0.959706	0.0009593	494.7	2.2	296.7	1.810184	0.0029666	0.0845485	0.0002256	0.0010249	0.0000259	0.0099409	0.0005053	0.0001857	0.0000343	8.45E-14	21.40999	0.0670414	20.76442	0.1378547	96.98011	0.610592	314.5261	1.916608
0.00915	0.000018	0.959706	0.0009593	450.0	2.3	896.6	0.6735441	0.0026187	0.0355924	0.0001276	0.0004997	0.000031	0.0043013	0.000415	0.0002042	0.0000378	3.56E-14	18.9238	0.1000748	17.22084	0.3314077	90.99681	1.756536	264.5756	4.736656
0.00915	0.000018	0.959706	0.0009593	470.0	2.4	897.1	1.083977	0.0028385	0.0575192	0.0001658	0.0006801	0.0000304	0.0073845	0.0004137	0.000188	0.0000368	5.75E-14	18.84548	0.0733973	17.88074	0.2040539	94.87599	1.076645	273.9828	2.901314
0.00915	0.000018	0.959706	0.0009593	500.0	2.2	597.4	1.83981	0.0023	0.0925064	0.0002102	0.0012243	0.000011	0.0152377	0.0001879	0.0004616	0.000014	9.25E-14	19.88847	0.0515781	18.41308	0.0664206	92.57446	0.2839855	281.5359	0.9404559
0.00915	0.000018	0.959706	0.0009593	514.3	1.6	296.7	1.170098	0.0019042	0.059335	0.0001579	0.0006715	0.0000264	0.0103938	0.0005198	0.0000636	0.0000349	5.93E-14	19.72021	0.0615262	19.41547	0.1860045	98.44634	0.920041	295.6735	2.613144
0.00915	0.000018	0.959706	0.0009593	513.9	1.7	896.6	2.56044	0.0031	0.131905	0.0002702	0.001726	0.000012	0.0280382	0.0001507	0.000455	9.70E-06	1.32E-13	19.41125	0.0461945	18.4002	0.0495636	94.78102	0.2015579	281.3537	0.701846
0.00915	0.000018	0.959706	0.0009593	535.7	2.4	596.9	2.618944	0.0037909	0.1317013	0.0002736	0.0015593	0.0000318	0.0329945	0.0004257	0.0000979	0.0000363	1.32E-13	19.88549	0.0503559	19.68599	0.0962732	98.98315	0.4610143	299.47	1.349688
0.00915	0.000018	0.959706	0.0009593	557.7	2.3	297.7	1.884754	0.0025756	0.0903181	0.0001964	0.0010773	0.000025	0.0257716	0.0005073	0.0001076	0.0000346	9.03E-14	20.86797	0.0535938	20.53826	0.1261732	98.404	0.5811417	311.3791	1.757255
0.00915	0.000018	0.959706	0.0009593	569.0	2.4	296.6	2.113814	0.0026727	0.0994694	0.0002158	0.0011914	0.0000246	0.0292537	0.0005227	0.0000869	0.0000344	9.95E-14	21.2509	0.0533692	21.01695	0.1159334	98.8823	0.5168056	318.0336	1.608711
0.00915	0.000018	0.959706	0.0009593	580.7	2.2	297.6	2.366363	0.0031612	0.1097157	0.0002354	0.0013257	0.0000269	0.0352095	0.0005233	0.0000653	0.0000339	1.10E-13	21.56814	0.0545078	21.4199	0.1071355	99.29392	0.467803	323.6164	1.482047
0.00915	0.000018	0.959706	0.0009593	599.9	3.6	296.6	3.172612	0.0037513	0.1413363	0.0002944	0.0015812	0.0000255	0.049877	0.0005197	0.0000653	0.0000349	1.41E-13	22.44725	0.053762	22.34181	0.0912038	99.50912	0.3686097	336.3248	1.252821
0.00915	0.000018	0.959706	0.0009593	599.4	3.8	596.8	4.336826	0.0053914	0.186347	0.0003629	0.00214	0.0000326	0.0681503	0.0004473	0.0001042	0.0000365	1.86E-13	23.27285	0.0537684	23.13989	0.0793622	99.40655	0.3066082	347.2545	1.083588
0.00915	0.000018	0.959706	0.0009593	625.1	2.4	296.6	3.358057	0.0041463	0.1346144	0.0002747	0.0015338	0.0000255	0.0548995	0.0005211	0.0000788	0.0000356	1.35E-13	24.94575	0.0594921	24.80938	0.0987405	99.42806	0.3612245	369.9067	1.33139
0.00915	0.000018	0.959706	0.0009593	625.4	2.5	296.7	2.391566	0.0032591	0.0931599	0.0002256	0.0010894	0.000025	0.038455	0.0005258	0.0000705	0.0000352	9.32E-14	25.67164	0.0713338	25.48496	0.1334385	99.2472	0.4801373	378.9932	1.79023
0.00915	0.000018	0.959706	0.0009593	637.6	2.2	296.7	2.574895	0.0035541	0.0980644	0.0002256	0.0011153	0.0000259	0.0421281	0.0005223	0.0000266	0.0000341	9.81E-14	26.2572	0.0704428	26.21728	0.1254582	99.82095	0.4408932	388.7915	1.674068
0.00915	0.000018	0.959706	0.0009593	650.2	1.9	301.2	2.876874	0.0036526	0.1060206	0.0002256	0.0011925	0.0000255	0.0462991	0.0005315	0.0000677	0.0000349	1.06E-13	27.13505	0.0672364	26.98628	0.1190294	99.42426	0.4042985	399.0238	1.579323
0.00915	0.000018	0.959706	0.0009593	668.3	1.0	296.7	3.510203	0.0042452	0.1279525	0.0002648	0.0014524	0.0000243	0.05692	0.0005417	0.0000578	0.0000342	1.28E-13	27.43363	0.065761	27.34166	0.1033348	99.63659	0.337293	403.7329	1.367515
0.00915	0.000018	0.959706	0.0009593	684.0	0.7	296.6	3.662152	0.0047404	0.1322064	0.0002256	0.001536	0.0000247	0.0617606	0.0005117	0.0000462	0.0000352	1.32E-13	27.70025	0.0593284	27.64101	0.0992661	99.75639	0.3406172	407.6902	1.310798
0.00915	0.000018	0.959706	0.0009593	696.9	0.7	296.7	3.010481	0.0036526	0.1142052	0.0002354	0.0013042	0.0000255	0.0587999	0.0005333	0.0000293	0.000036	1.14E-13	26.36029	0.0630432	26.33306	0.1132059	99.86376	0.395721	390.3358	1.509289
0.00915	0.000018	0.959706	0.0009593	697.0	0.8	896.6	3.86905	0.0045	0.1668305	0.0003303	0.0021008	0.000012	0.0952232	0.0002428	0.0004734	9.10E-06	1.67E-13	23.1915	0.0532525	22.39757	0.0544241	96.54138	0.1762723	337.0906	0.7472805
0.00915	0.000018	0.959706	0.0009593	717.1	0.5	596.8	2.137099	0.0033847	0.1003196	0.0002146	0.0012312	0.000031	0.0702369	0.0004579	0.0001272	0.0000362	1.00E-13	21.30291	0.0566931	20.98905	0.121438	98.48214	0.551892	317.6465	1.685455
0.00915	0.000018	0.959706	0.0009593	734.0	0.5	296.7	1.068176	0.0016224	0.0535962	0.0001297	0.0006628	0.0000249	0.0395505	0.0005194	0.0000766	0.0000342	5.36E-14	19.93006	0.0569537	19.57119	0.1987408	98.15263	0.9793609	297.8599	2.7887
0.00915	0.000018	0.959706	0.0009593	747.0	0.5	297.7	1.085245	0.0015305	0.0585988	0.0001391	0.0007349	0.0000255	0.0465225	0.0005409	0.0000802	0.0000342	5.86E-14	18.51993	0.0511231	18.1835	0.181753	98.13314	0.962806	278.2824	2.578094
0.00915	0.000018	0.959706	0.0009593	756.0	0.4	296.6	0.9107144	0.0013501	0.0549375	0.0001391	0.0007126	0.0000255	0.0449989	0.0005368	0.0000531	0.0000342	5.49E-14	16.57728	0.0486266	16.36193	0.1923708	98.64907	1.142006	252.2578	2.76826
0.00915	0.000018	0.959706	0.0009593	767.0	0.4	296.7	0.7677421	0.0011761	0.0536353	0.0001205	0.000699	0.0000255	0.0461441	0.0005287	0.0001217	0.0000349	5.36E-14	14.31411	0.0389298	13.71203	0.1982063	95.74137	1.374927	213.7172	2.913682
0.00915	0.000018	0.959706	0.0009593	779.0	0.4	296.7	0.7342739	0.0011341	0.0569213	0.0001391	0.0007141	0.0000247	0.0564169	0.0005428	0.0001203	0.0000349	5.69E-14	12.8998	0.0372833	12.35495	0.186883	95.71572	1.4364	193.657	2.777875
0.00915	0.000018	0.959706	0.0009593	796.1	0.4	296.7	0.8780208	0.0013506	0.0743482	0.0001771	0.0009812	0.0000255	0.0834545	0.0005836	0.0001704	0.0000341	7.43E-14	11.80957	0.0334842	11.22219	0.1407503	94.95798	1.178351	176.7405	2.111812
0.00915	0.000018	0.959706	0.0009593	807.0	0.3	296.6	0.9220096	0.0012628	0.0776163	0.0001771	0.000995	0.0000255	0.0757751	0.0005598	0.0002049	0.0000346	7.76E-14	11.87908	0.0316109	11.17516	0.1367205	94.01626	1.137326	176.0347	2.05215
0.00915	0.000018	0.959706	0.0009593	807.0	0.3	296.6	0.7521993	0.0010769	0.0606828	0.0001391	0.0007595	0.0000259	0.0378947	0.0005272	0.0001395	0.0000349	6.07E-14	12.39558	0.0334926	11.76291	0.1749463	94.86036	1.400563	184.8353	2.613163
0.00915	0.000018	0.959706	0.0009593	807.0	0.3	596.9	1.252133	0.0024198	0.0972681	0.0001852	0.00122	0.0000314	0.0528452	0.0004571	0.0002686	0.0000365	9.73E-14	12.873	0.0349267	12.09539	0.117229	93.92921	0.9108728	189.7947	1.746246
0.00915	0.000018	0.959706	0.0009593	807.0	0.3	1796.7	2.69996	0.0114018	0.2011092	0.0004107	0.0025159	0.0000213	0.0906733	0.000339	0.0005385	0.0000369	2.01E-13	13.42534	0.0629758	12.66475	0.0829597	94.31027	0.7093312	198.2561	1.230001
0.00915	0.000018	0.959706	0.0009593	825.0	0.3	596.9	1.212311	0.0024092	0.0962494	0.000195	0.0011767	0.000031	0.0573667	0.0004438	0.0001718	0.0000375	9.62E-14	12.59552	0.0357438	12.11404	0.1214206	96.14312	0.9628929	190.0725	1.808407
0.00915	0.000018	0.959706	0.0009593	825.0	0.3	1796.7	2.7521	0.0112178	0.2112658	0.0003723	0.0026653	0.0000206	0.0907615	0.0003047	0.0005803	0.0000362	2.11E-13	13.02672	0.057848	12.24351	0.0768451	93.96493	0.6834395	191.9998	1.143292
0.00915	0.000018	0.959706	0.0009593	851.0	0.3	597.3	1.55086	0.0023953	0.1367205	0.0001658	0.0016273	0.000031	0.076343	0.0004555	0.0001947	0.0000361	1.37E-13	11.34328	0.022276	10.96585	0.0818039	96.64131	0.7268216	172.8902	1.229999
0.00915	0.000018	0.959706	0.0009593	851.0	0.2	1796.7	1.57784	0.0112379	0.1241894	0.000317	0.0015906	0.0000194	0.100322	0.0003814	0.0005148	0.0000366	1.24E-13	12.70511	0.0961243	11.53717	0.1296382	90.76157	1.185024	181.4603	1.940017
0.00915	0.000018	0.959706	0.0009593	870.1	0.2	296.6	0.1972959	0.0007681	0.0114967	0.0000646	0.0001423	0.0000247	0.0205624	0.0005305	0.0000414	0.0000352	1.15E-14	17.16103	0.1173043	16.2476	0.9235023	94.56363	5.361177	250.6118	13.30151
0.00915	0.000018	0.959706	0.0009593	870.1	0.2	597.4	0.2327966	0.0020408	0.0101199	0.0000549	0.0001091	0.0000318	0.0283641	0.0004578	0.0000497	0.0000368	1.01E-14	23.00388	0.2371134	21.8015	1.113366	94.59151	4.874262	328.8875	15.35678
0.00915	0.000018	0.959706	0.0009593	870.0	0.2	897.1	0.267596	0.0005	0.0063909	0.000028	0.0002445	0.000011	0.0279492	0.0001838	0.0004511	0.000012	6.39E-15	41.87164	0.1995917	21.2083	0.5754096	50.49769	1.355224	320.6869	7.972768
0.00915	0.000018	0.959706	0.0009593	870.0	0.2	1796.8	0.35642	0.0110427	0.0045718	0.0001486	0.0001123	0.0000194	0.0347936	0.0003538	0.0002792	0.0000375	4.57E-15	77.96048	3.500728	60.64825	3.984743	77.38284	5.020314	798.1764	42.39803
0.00915	0.000018	0.959706	0.0009593	890.0	0.2	596.9	0.1356671	0.0020346	0.0012051	0.0000479	0.0000231	0.0000318	0.0134459	0.0004397	0.00004	0.0000371	1.21E-15	112.5767	4.782373	104.3648	10.31066	91.98724	8.42096	1212.112	87.25901
0.00915	0.000018	0.959706	0.0009593	900.0	0.2	596.9	0.1363643	0.0020454	0.0010515	0.0000498	0.0000254	0.0000307	0.0128481	0.0004404	0.0000519	0.0000371	1.05E-15	129.6895	6.441329	116.9203	12.16888	89.38888	8.374241	1315.364	97.26902
0.00915	0.000018	0.959706	0.0009593	910.0	0.2	596.9	0.1848771	0.0020765	0.0010842	0.0000488	0.0000462	0.0000305	0.0184662	0.0004519	0.0000586	0.0000365	1.08E-15	170.5197	7.911969	157.5887	12.60892	91.32314	6.093492	1614.305	85.42798
0.00915	0.000018	0.959706	0.0009593	917.0	0.2	596.8	0.1862696	0.0020937	0.0010447	0.0000483	0.000028	0.0000305	0.0166666	0.000444	0.0000574	0.0000363	1.04E-15	178.3061	8.491677	165.0037	13.1778	91.51386	6.010893	1663.858	86.86866
0.00915	0.000018	0.959706	0.0009593	927.0	0.2	296.6	0.1047147	0.000747	0.0003813	0.0000526	-5.49E-06	0.0000247	0.0061365	0.0005305	0.0000309	0.000034	3.81E-16	274.6607	37.94697	254.6185	44.61756	91.66618	9.737823	2175.029	221.6918
0.00915	0.000018	0.959706	0.0009593	927.0	0.2	596.9	0.1581271	0.0021366	0.0005048	0.0000514	0.0000109	0.0000305	0.0070266	0.0004586	0.0000553	0.0000371	5.05E-16	313.2687	32.15506	284.4132	36.93235	89.91075	7.241853	2317.322	169.6188
0.00915	0.000018	0.959706	0.0009593	927.0	0.2	897.1	0.268062	0.00075	0.0009088	0.000019	0.000184	8.00E-06	0.009856	0.0001463	0.0004407	9.10E-06	9.09E-16	294.9502	6.226791	152.201	4.4793	51.21348	1.061214	1577.429	30.97345
0.00915	0.000018	0.959706	0.0009593	945.0	0.2	296.7	0.1195876	0.000784	0.0003086	0.0000542	-0.0000302	0.0000251	0.0042226	0.000552	-6.09E-06	0.0000349	3.09E-16	387.5355	68.08858	398.2872	78.4553	101.7972	8.769336	2776.687	279.4835
0.00915	0.000018	0.959706	0.0009593	930.0	0.2	1796.7	0.32559	0.0110549	0.0006424	0.0001531	0.0000713	0.0000194	0.0069373	0.0002746	0.0003065	0.0000368	6.42E-16	506.8111	121.9993	367.9919	91.68362	72.06446	5.378655	2665.41	347.3384
0.00915	0.000018	0.959706	0.0009593	950.0	0.2	897.1	0.19512	0.00063	0.0005126	0.000022	0.0001779	9.50E-06	0.0039602	0.0001738	0.0004352	0.000012	5.13E-16	380.6672	16.39972	128.4871	9.039814	33.57196	1.867575	1405.534	68.74258
0.00915	0.000018	0.959706	0.0009593	950.0	0.2	1796.7	0.307632	0.0110454	0.0004737	0.0001581	0.0001799	0.0000213	0.0023451	0.0003316	0.0005872	0.0000399	4.74E-16	649.4046	217.9612	280.6642	100.0847	43.07005	5.502255	2300.021	464.0771

Table A.13: 18-IAF-06-MOS (silt) step heating data

J	± 1σ	Discrim	± 1σ	Temp (°C)	± 1σ (°C)	Heating duration (s)	^{40}Ar	± 1σ	^{39}Ar	± 1σ	^{38}Ar	± 1σ	^{37}Ar	± 1σ	^{36}Ar	± 1σ	^{39}Ar (Moles)	^{40}Ar/^{39}Ar	± 1σ	^{40}Ar*/^{39}Ar$_K$	± 1σ	% ^{40}Ar*	± 1σ	Age (Ma)	± 1σ
0.00915	0.000018	0.959706	0.0009593	396.2	2.9	296.6	7.75241	0.0160449	0.0440066	0.0001391	0.004354	0.0000364	0.014752	0.0009372	0.0203486	0.0001063	4.40E-14	176.1648	0.6655713	38.11065	0.8170916	21.63352	0.4609337	540.9102	10.02324
0.00915	0.000018	0.959706	0.0009593	407.1	3.0	296.7	0.96462	0.0024187	0.0126088	0.0000673	0.0006568	0.0000322	0.0028155	0.0008799	0.0027877	0.0000379	1.26E-14	76.50359	0.4510967	10.49435	0.9202753	13.71746	1.20118	165.7868	13.89168
0.00915	0.000018	0.959706	0.0009593	417.7	2.9	297.0	0.57609	0.0021633	0.0114269	0.0000708	0.0004619	0.0000305	0.0044687	0.0008809	0.0015493	0.0000344	1.14E-14	50.41526	0.3653	9.935127	0.9213462	19.70659	1.82493	157.3256	13.97308
0.00915	0.000018	0.959706	0.0009593	429.7	1.8	296.6	0.45163	0.0020809	0.0124434	0.0000872	0.0003514	0.0000322	0.0026102	0.0009422	0.0011057	0.0000351	1.24E-14	36.29465	0.3043855	9.764127	0.8610861	26.90239	2.36823	154.7304	13.07793
0.00915	0.000018	0.959706	0.0009593	439.1	2.2	296.6	0.36869	0.0019209	0.0126822	0.0000948	0.000325	0.0000307	0.0034594	0.0009167	0.0008221	0.0000349	1.27E-14	29.0714	0.2648549	9.718409	0.839337	33.42945	2.881593	154.0359	12.75251
0.00915	0.000018	0.959706	0.0009593	450.3	2.4	296.7	0.40346	0.0019209	0.0143624	0.0000922	0.000313	0.000031	0.0042868	0.0009056	0.0006592	0.0000342	1.44E-14	28.09148	0.2245601	14.38843	0.7286649	51.21989	2.584491	223.6333	10.65297
0.00915	0.000018	0.959706	0.0009593	457.9	2.2	296.6	0.33788	0.0017692	0.0139936	0.0000855	0.0002752	0.0000307	0.0046461	0.0008762	0.0005898	0.0000352	1.40E-14	24.14529	0.1943527	11.56136	0.7650909	47.88248	3.16509	181.8223	11.44718
0.00915	0.000018	0.959706	0.0009593	470.1	2.4	296.6	0.36293	0.0019209	0.0164487	0.0001	0.0002759	0.0000322	0.0056313	0.0009464	0.000508	0.0000348	1.64E-14	22.06436	0.1778246	12.84381	0.6471495	58.21064	2.927845	200.909	9.580887
0.00915	0.000018	0.959706	0.0009593	485.8	2.1	296.6	0.45272	0.0019209	0.0209812	0.0001035	0.0003911	0.0000307	0.0083106	0.0008694	0.000521	0.0000344	2.10E-14	21.57743	0.1403834	14.16378	0.5035775	65.64164	2.327971	220.3459	7.375626
0.00915	0.000018	0.959706	0.0009593	500.1	2.2	296.6	0.4892	0.0029547	0.0234299	0.000158	0.0003933	0.0000314	0.0102846	0.0008984	0.0004512	0.0000341	2.34E-14	20.87934	0.1890121	15.12946	0.4637461	72.4614	2.210415	234.4348	6.739518
0.00915	0.000018	0.959706	0.0009593	514.9	1.7	297.7	0.6035	0.0019209	0.0280193	0.0001115	0.0004397	0.0000322	0.0124188	0.0009496	0.0005077	0.0000344	2.80E-14	21.53871	0.1097535	16.12892	0.3788676	74.88343	1.749891	248.9017	5.462121
0.00915	0.000018	0.959706	0.0009593	534.3	2.2	296.7	0.76386	0.002	0.0349789	0.0001298	0.0004866	0.0000322	0.0185966	0.0008741	0.0005098	0.0000341	3.50E-14	21.83776	0.0991646	17.48626	0.3037411	80.07353	1.374877	268.3653	4.33214
0.00915	0.000018	0.959706	0.0009593	550.8	2.2	296.6	0.80714	0.0019209	0.0351831	0.0001206	0.0005167	0.000031	0.0220211	0.0008813	0.000523	0.0000338	3.52E-14	22.94111	0.0957146	18.50287	0.2988399	80.65376	1.287368	282.8069	4.22833
0.00915	0.000018	0.959706	0.0009593	568.1	2.5	296.6	0.83026	0.002	0.0356251	0.0001115	0.0005569	0.0000314	0.0250208	0.000926	0.0004881	0.000033	3.56E-14	23.30549	0.0920422	19.21483	0.2886509	82.44765	1.227546	292.8526	4.061536
0.00915	0.000018	0.959706	0.0009593	576.3	2.3	296.7	0.74064	0.0019209	0.0285901	0.0001044	0.0003864	0.0000306	0.0218898	0.0008889	0.0004175	0.0000341	2.86E-14	25.90551	0.1160018	21.54502	0.3706581	83.16772	1.414768	325.3464	5.122552
0.00915	0.000018	0.959706	0.0009593	439.9	2.2	2997.1	0.119452	0.0023049	0.0031204	0.0000597	0.0001089	0.0000412	0.0029539	0.0007517	0.0002478	0.0000325	3.12E-15	38.28118	1.040318	14.56849	3.205003	38.05652	8.372792	226.2638	46.78855
0.00915	0.000018	0.959706	0.0009593	470.0	2.2	2996.5	0.17631	0.0023707	0.0044069	0.0000609	0.0001786	0.0000421	0.0051812	0.000731	0.0003342	0.0000331	4.41E-15	40.00817	0.7712595	17.36595	2.319964	43.406	5.797091	266.6484	33.12017
0.00915	0.000018	0.959706	0.0009593	500.2	2.1	2996.6	0.30418	0.0024187	0.0094247	0.0000708	0.0002122	0.0000418	0.0087198	0.0007537	0.0004183	0.0000328	9.42E-15	32.27492	0.3530772	19.02528	1.080613	58.94755	3.351661	290.1834	15.22751
0.00915	0.000018	0.959706	0.0009593	530.0	1.9	2996.6	0.68915	0.0024698	0.0255344	0.0000872	0.0003973	0.0000412	0.0249133	0.0007624	0.0005508	0.0000339	2.55E-14	26.98912	0.1336051	20.54902	0.4138638	76.13816	1.535678	311.5288	5.763537
0.00915	0.000018	0.959706	0.0009593	560.0	2.7	1797.8	0.81377	0.0029069	0.0300556	0.0000879	0.0004244	0.0000233	0.0317386	0.0005196	0.0003636	0.0000392	3.01E-14	27.07548	0.1250117	23.46351	0.4070896	86.65964	1.513992	351.6677	5.544736
0.00915	0.000018	0.959706	0.0009593	592.9	3.2	596.9	0.439163	0.0013285	0.0146442	0.0000617	0.0002097	0.0000214	0.0180543	0.0011357	0.0001502	0.0000237	1.46E-14	29.98895	0.1555246	26.92726	0.5054543	89.79059	1.664786	398.2405	6.709445
0.00915	0.000018	0.959706	0.0009593	603.8	4.5	296.6	0.23887	0.0014591	0.0077474	0.0000659	0.0000984	0.0000306	0.0093756	0.0009349	0.0000628	0.0000343	7.75E-15	30.83247	0.3229982	28.413	1.358671	92.15287	4.372643	417.8556	17.84052
0.00915	0.000018	0.959706	0.0009593	613.9	2.8	296.6	0.32016	0.0018439	0.0100832	0.0000776	0.0000954	0.0000318	0.0127996	0.0009905	0.0000525	0.0000337	1.01E-14	31.75184	0.3051176	30.1958	1.040722	95.0994	3.241597	441.1151	13.49091
0.00915	0.000018	0.959706	0.0009593	621.2	2.8	296.6	0.36822	0.0018439	0.0111164	0.0000776	0.0000722	0.000031	0.0141407	0.0010296	0.0000987	0.0000334	1.11E-14	33.12406	0.2844812	30.47134	0.9371925	91.99158	2.793809	444.6834	12.12491
0.00915	0.000018	0.959706	0.0009593	634.1	3.2	297.7	0.47811	0.0019209	0.0136212	0.0000776	0.0001481	0.0000305	0.0190514	0.0010307	0.0000765	0.0000334	1.36E-14	35.10036	0.2446153	33.42348	0.7697954	95.22262	2.159201	482.4789	9.753199
0.00915	0.000018	0.959706	0.0009593	650.5	2.6	296.6	0.73146	0.0018439	0.01769	0.0000708	0.0002094	0.000031	0.024431	0.0010319	0.0001397	0.0000337	1.77E-14	41.34874	0.1956055	38.99039	0.5991168	94.29645	1.418954	551.6699	7.305745
0.00915	0.000018	0.959706	0.0009593	661.6	2.0	296.6	0.61286	0.0018439	0.0171926	0.0000745	0.000185	0.0000306	0.0256065	0.0010194	0.0001121	0.0000329	1.72E-14	35.64672	0.1880563	33.69987	0.5994013	94.5385	1.655449	485.9773	7.579651
0.00915	0.000018	0.959706	0.0009593	672.0	1.3	296.6	0.6506	0.0018439	0.0176886	0.0000715	0.0002275	0.0000314	0.0272569	0.0010342	0.0001147	0.0000334	1.77E-14	36.78068	0.1816428	34.84532	0.5907138	94.73809	1.58261	500.4041	7.410431
0.00915	0.000018	0.959706	0.0009593	680.1	0.9	296.7	0.523959	0.0013695	0.0153621	0.0000592	0.0002314	0.0000303	0.0254384	0.0009972	0.0001222	0.0000344	1.54E-14	34.10719	0.1587267	31.73215	0.6845973	93.03654	1.989881	460.9219	8.777778
0.00915	0.000018	0.959706	0.0009593	687.2	0.7	296.7	0.41159	0.0016971	0.0127694	0.0000799	0.0002169	0.0000307	0.0280539	0.0010229	0.0001403	0.0000331	1.28E-14	32.23255	0.2415605	28.95336	0.8061971	89.82646	2.465176	424.9371	10.54469
0.00915	0.000018	0.959706	0.0009593	701.1	0.6	296.6	0.39922	0.0016971	0.0141001	0.000076	0.0002684	0.0000314	0.0352155	0.0010377	0.0001121	0.000034	1.41E-14	28.31335	0.1943964	25.94087	0.7435807	91.62061	2.608612	385.0994	9.942352
0.00915	0.000018	0.959706	0.0009593	714.0	0.6	296.7	0.34162	0.0016971	0.0136407	0.0000831	0.000235	0.0000314	0.0339393	0.0010389	0.0001495	0.0000332	1.36E-14	25.04419	0.19688	21.77214	0.7483368	86.93492	2.972281	328.4826	10.32421
0.00915	0.000018	0.959706	0.0009593	722.9	0.5	296.6	0.251876	0.001562	0.0111558	0.0000799	0.000168	0.000031	0.0247193	0.0010401	0.0001117	0.0000334	1.12E-14	22.57807	0.213925	19.58763	0.9161394	86.75512	4.045709	298.0906	12.85349
0.00915	0.000018	0.959706	0.0009593	625.2	2.5	1796.7	0.098017	0.0026661	0.0040631	0.0000563	0.0000528	0.0000246	0.0090766	0.0005967	0.0001215	0.0000403	4.06E-15	24.12373	0.7363935	15.19396	3.040979	62.98343	12.69167	235.3718	44.17097
0.00915	0.000018	0.959706	0.0009593	649.8	1.9	1796.7	0.118826	0.0026752	0.0053397	0.0000595	0.0000731	0.0000246	0.0121924	0.000518	0.0000758	0.00004	5.34E-15	22.25331	0.5590874	18.01667	2.300632	80.96176	10.45894	275.9145	32.6763
0.00915	0.000018	0.959706	0.0009593	680.0	0.7	1796.7	0.156805	0.0026979	0.0087651	0.0000616	0.0001715	0.0000246	0.0208	0.0005774	0.0001359	0.0000403	8.77E-15	17.88969	0.3324822	13.2608	1.410154	74.1254	7.967989	207.0719	20.80595
0.00915	0.000018	0.959706	0.0009593	712.0	0.6	1796.7	0.24449	0.0027786	0.0157447	0.0000932	0.0002116	0.0000266	0.0335395	0.0006249	0.0001513	0.00004	1.57E-14	15.52842	0.1989693	12.65842	0.7823446	81.51778	5.099846	198.1623	11.60002
0.00915	0.000018	0.959706	0.0009593	723.9	0.6	896.6	0.097047	0.0006544	0.0075919	0.000068	0.0000938	0.0000125	0.0142675	0.0012724	0.0000858	0.0000217	7.59E-15	12.78289	0.1433474	9.410451	0.8630961	73.61756	6.737967	149.3508	13.14752
0.00915	0.000018	0.959706	0.0009593	737.0	0.5	596.8	0.070192	0.0007021	0.0060709	0.0000627	0.0000529	0.0000224	0.0112727	0.0012955	0.0000816	0.0000234	6.07E-15	11.56197	0.1661903	7.550413	1.160835	65.30386	10.03873	120.7926	17.96447
0.00915	0.000018	0.959706	0.0009593	745.2	0.5	296.6	0.047657	0.0012528	0.0031967	0.0000592	0.0000494	0.0000314	0.0070631	0.0009965	0.0000544	0.0000337	3.20E-15	14.90808	0.4792599	9.83121	3.176986	65.94552	21.34605	155.7489	48.224
0.00915	0.000018	0.959706	0.0009593	756.1	0.4	296.6	0.051788	0.0012419	0.0042298	0.0000687	0.0000599	0.0000307	0.0085399	0.0010427	0.0000558	0.000034	4.23E-15	12.24353	0.3545835	8.305273	2.422341	67.83396	19.82083	132.4368	37.24624
0.00915	0.000018	0.959706	0.0009593	756.0	0.4	296.7	0.035886	0.0012278	0.0035194	0.0000621	0.000089	0.0000314	0.0066399	0.0009942	7.66E-06	0.0000337	3.52E-15	10.19653	0.3925173	9.54816	2.884618	93.64125	28.42307	151.4473	43.89039
0.00915	0.000018	0.959706	0.0009593	774.0	0.4	297.7	0.053265	0.0012369	0.0057457	0.0000627	0.0000908	0.0000306	0.0162574	0.001059	0.0000854	0.000034	5.75E-15	9.27035	0.2378656	4.834618	1.781335	52.15141	19.24511	78.26823	28.22301
0.00915	0.000018	0.959706	0.0009593	780.0	0.4	296.6	0.052058	0.0012369	0.0058401	0.0000687	0.0000791	0.0000305	0.0124089	0.0010211	0.0000616	0.000034	5.84E-15	8.913951	0.2363236	5.763086	1.752966	64.65244	19.71067	92.91912	27.54941
0.00915	0.000018	0.959706	0.0009593	787.0	0.3	297.6	0.051678	0.0012369	0.0058323	0.0000646	0.0000832	0.0000307	0.0134884	0.0010343	0.000044	0.0000337	5.83E-15	8.860729	0.2337043	6.607195	1.739636	74.56718	19.69674	106.1366	27.14079
0.00915	0.000018	0.959706	0.0009593	799.0	0.4	296.6	0.091587	0.0012649	0.0080287	0.0000715	0.0000931	0.0000303	0.0268627	0.0010355	0.0000383	0.0000337	8.03E-15	11.40742	0.1874918	9.983751	1.266131	87.51982	11.13754	158.0629	19.19423
0.00915	0.000018	0.959706	0.0009593	805.0	0.3	297.6	0.07327	0.0012618	0.0094551	0.0000776	0.0000919	0.0000318	0.0266611	0.0010246	9.76E-06	0.000034	9.46E-15	7.749236	0.1478174	7.440757	1.083811	96.01924	14.0614	119.0948	16.78825
0.00915	0.000018	0.959706	0.0009593	816.9	0.3	296.7	0.097875	0.0012649	0.0113437	0.0000847	0.0001339	0.000031	0.0349963	0.001051	0.0000871	0.0000332	1.13E-14	8.628128	0.1287938	6.33432	0.8816707	73.41477	10.24785	101.8743	13.78778
0.00915	0.000018	0.959706	0.0009593	817.0	0.3	901.2	0.283001	0.0009708	0.0255364	0.0001194	0.0003401	0.0000125	0.0430418	0.0013341	0.0001897	0.0000217	2.55E-14	11.08225	0.064261	8.864483	0.2603383	79.98814	2.335363	141.0149	3.984051
0.00915	0.000018	0.959706	0.0009593	832.1	6.9	296.6	0.101261	0.0012781	0.0106711	0.0000745	0.0001155	0.0000314	0.025554	0.001099	0.0000919	0.0000347	1.07E-14	9.489297	0.1368778	6.918539	0.9796531	72.90887	10.35219	110.9875	15.24303
0.00915	0.000018	0.959706	0.0009593	842.0	8.3	296.7	0.121049	0.0012649	0.0143104	0.0000905	0.0001896	0.000031	0.0329917	0.0010551	0.0001089	0.000034	1.43E-14	8.458827	0.1033308	6.186603	0.7162799	73.13784	8.489652	99.56284	11.21568
0.00915	0.000018	0.959706	0.0009593	841.6	7.1	596.8	0.178696	0.0008276	0.0233292	0.0000932	0.0003555	0.0000228	0.0286632	0.0013053	0.0001748	0.0000253	2.33E-14	7.659764	0.0468441	5.422608	0.3263753	70.7934	4.264132	87.56026	5.144499
0.00915	0.000018	0.959706	0.0009593	867.6	4.6	297.7	0.229036	0.0014648	0.0230031	0.0001115	0.0003088	0.0000318	0.0401688	0.0011031	0.0000916	0.0000347	2.30E-14	9.956755	0.0799008	8.768076	0.4569513	88.06159	4.604037	139.539	6.998601
0.00915	0.000018	0.959706	0.0009593	879.2	4.2	296.6	0.213424	0.0014151	0.0210159	0.0001097	0.0002766	0.0000322	0.0258947	0.0010337	0.0001053	0.000034	2.10E-14	10.15537	0.0856988	8.659831	0.4900267	85.27341	4.837867	137.8804	7.512066
0.00915	0.000018	0.959706	0.0009593	885.2	1.9	296.6	0.189222	0.0013507	0.0225106	0.000107	0.0003046	0.000031	0.0166304	0.0010896	0.0001592	0.000034	2.25E-14	8.405917	0.072095	6.295061	0.4562389	74.88845	5.442215	101.2603	7.137197
0.00915	0.000018	0.959706	0.0009593	892.1	0.9	296.6	0.204198	0.00136	0.0250021	0.0001298	0.0003372	0.0000302	0.0135723	0.0010483	0.0001109	0.0000331	2.50E-14	8.167223	0.0689651	6.842969	0.4006833	83.78575	4.918429	109.8113	6.238537
0.00915	0.000018	0.959706	0.0009593	893.0	5.0	296.6	0.182059	0.0013242	0.0153449	0.000088	0.0001981	0.0000304	0.0096645	0.0010239	0.0000604	0.000034	1.53E-14	11.86445	0.1099098	10.6895	0.6701765	90.0969	5.662955	168.7303	10.09995
0.00915	0.000018	0.959706	0.0009593	907.0	1.5	296.6	0.167905	0.0013118	0.0185714	0.0000931	0.0002723	0.0000314	0.0143217	0.0010338	0.0001098	0.000033	1.86E-14	9.041046	0.0839223	7.27554	0.5359427	80.47233	5.947468	116.5338	8.313525
0.00915	0.000018	0.959706	0.0009593	915.4	1.7	296.6	0.151468	0.0012962	0.0134623	0.0000831	0.000136	0.0000304	0.0145833	0.0010518	0.0000541	0.0000343	1.35E-14	11.25123	0.1187227	10.05181	0.7702811	89.33962	6.86663	159.0943	11.67061
0.00915	0.000018	0.959706	0.0009593	925.0	1.0	296.7	0.134282	0.0012888	0.0086923	0.0000673	0.0000666	0.0000318	0.0140467	0.0010806	0.000038	0.0000334	8.69E-15	15.44836	0.1904886	14.14158	1.160487	91.54095	7.529959	220.0208	17.00008
0.00915	0.000018	0.959706	0.0009593	932.1	0.7	296.6	0.115317	0.0012781	0.0081371	0.000076	0.0001095	0.0000305	0.0160985	0.0010675	0.0000679	0.000034	8.14E-15	14.17174	0.2054338	11.6786	1.262547	82.40768	8.922446	183.5755	18.87174
0.00915	0.000018	0.959706	0.0009593	928.9	2.6	597.4	0.192273	0.0015116	0.0075459	0.0001508	0.0003614	0.0000456	0.0186776	0.00219	0.0004787	0.0000536	7.55E-15	25.48057	0.5473361	6.54171	2.135871	25.67332	8.369055	105.1147	33.34147
0.0009593	0.000018	0.959706	0.0009593	929.0	2.7	296.7	0.06341	0.0012618	0.0016313	0.0000565	0.0000242	0.0000318	0.0041711	0.0010251	0.0000181	0.000034	1.63E-15	38.87158	1.552873	35.56116	6.391953	91.4837	16.23786	509.3621	79.78998
0.00915	0.000018	0.959706	0.0009593	919.7	1.0	296.6	0.044698	0.0012369	0.0005723	0.0000534	-0.0000108	0.00003	0.0015782	0.0010389	0.0000427	0.0000337	5.72E-16	78.09884	7.597779	55.82874	18.4614	71.48472	22.76491	746.1552	202.1644

Table A.14: 18-IAF-05-MOS (64 - 125μm step heating data

J	± 1σ	Discrim	± 1σ	Temp (°C)	± 1σ (°C)	Heating duration (s)	^{40}Ar	± 1σ	^{39}Ar	± 1σ	^{38}Ar	± 1σ	^{37}Ar	± 1σ	^{36}Ar	± 1σ	^{39}Ar (Moles)	^{40}Ar/^{39}Ar	± 1σ	^{40}Ar*/^{39}Ar$_K$	± 1σ	% ^{40}Ar*	± 1σ	Age (Ma)	± 1σ
0.00915	0.000018	0.959706	0.0009593	377.3	5.3	297.1	26.07646	0.027171	0.2093999	0.0063252	0.017819	0.0004403	0.0544054	0.0006008	0.0814511	0.0001925	2.09E-13	124.5295	0.2328883	8.397355	0.3039189	6.743267	0.2439301	133.8521	4.669441
0.00915	0.000018	0.959706	0.0009593	394.5	4.3	297.1	11.28263	0.0103561	0.0969748	0.0001792	0.0078583	0.0000341	0.0222607	0.0005798	0.0356412	0.0001015	9.70E-14	116.346	0.2400234	6.6166033	0.3304042	5.686516	0.2838377	106.2745	5.154382
0.00915	0.000018	0.959706	0.0009593	409.8	3.5	297.1	8.3518	0.0091201	0.0924803	0.0001792	0.0058936	0.0000336	0.0213578	0.0005621	0.0254433	0.0000828	9.25E-14	90.30898	0.2008402	8.168663	0.2852213	9.045239	0.3154963	130.3351	4.390702
0.00915	0.000018	0.959706	0.0009593	426.9	3.0	297.1	7.328695	0.0085554	0.1045896	0.0002176	0.005213	0.0000331	0.0248842	0.0005583	0.0210092	0.0000757	1.05E-13	70.07096	0.167141	9.841382	0.2320279	14.04488	0.3302484	155.9033	3.521689
0.00915	0.000018	0.959706	0.0009593	443.1	2.7	297.2	6.669461	0.0081813	0.1160884	0.0002467	0.0047855	0.0000347	0.0291346	0.000576	0.0179251	0.0000708	1.16E-13	57.45159	0.1409702	11.35125	0.1966774	19.75795	0.3406142	178.6759	2.947784
0.00915	0.000018	0.959706	0.0009593	459.1	2.7	297.1	6.293586	0.0080873	0.1308144	0.0002858	0.0044911	0.0000331	0.0359635	0.0005494	0.0155578	0.0000647	1.31E-13	48.11081	0.1219559	12.60304	0.1625387	26.19586	0.3346549	197.3409	2.411099
0.00915	0.000018	0.959706	0.0009593	474.9	2.9	297.1	5.993921	0.0077166	0.1489669	0.0003055	0.0043381	0.0000318	0.0429285	0.0005683	0.0138089	0.0000633	1.49E-13	40.23659	0.0974272	12.56075	0.1394717	31.21724	0.3430276	196.7135	2.06964
0.00915	0.000018	0.959706	0.0009593	490.9	2.2	297.1	5.783776	0.0075319	0.1707622	0.0003647	0.0042799	0.0000326	0.052522	0.0006007	0.0123479	0.0000618	1.71E-13	33.87086	0.0847243	12.28121	0.1196636	36.25947	0.3479251	192.5606	1.779788
0.00915	0.000018	0.959706	0.0009593	506.0	1.9	297.1	5.726021	0.0072569	0.1954804	0.0003845	0.0044688	0.0000305	0.0668342	0.0005719	0.0115755	0.0000605	1.95E-13	29.29205	0.0685396	11.61253	0.1021829	39.64398	0.3437058	182.5877	1.528199
0.00915	0.000018	0.959706	0.0009593	522.2	2.0	297.1	5.775206	0.0072559	0.2375924	0.0004937	0.0047608	0.0000331	0.0926359	0.0005974	0.0104338	0.000059	2.38E-13	24.3072	0.0590227	11.19598	0.0835172	46.06036	0.3350247	176.3473	1.253361
0.00915	0.000018	0.959706	0.0009593	429.9	2.7	1797.1	2.725266	0.018352	0.0334422	0.0002843	0.0019225	0.0000348	0.0116329	0.0006525	0.0081007	0.0000631	3.34E-14	81.49186	0.8837354	9.171554	0.7900123	11.25457	0.9676767	145.7081	12.0585
0.00915	0.000018	0.959706	0.0009593	470.1	2.3	1797.2	4.404115	0.0183524	0.1021122	0.0003363	0.003283	0.0000358	0.0400414	0.0006644	0.0113841	0.0000655	1.02E-13	43.13016	0.2290968	9.8844832	0.2646299	22.82586	0.6163201	155.9557	4.016401
0.00915	0.000018	0.959706	0.0009593	500.1	2.2	1797.2	5.708351	0.0184597	0.2226364	0.0003616	0.0047446	0.0000348	0.1002259	0.0006916	0.0114044	0.0000629	2.23E-13	25.6398	0.0927852	10.34624	0.1194415	40.35228	0.4793146	163.5498	1.805218
0.00915	0.000018	0.959706	0.0009593	550.3	2.8	597.8	5.356294	0.0182705	0.324823	0.0006678	0.0048375	0.0000355	0.1786922	0.0007714	0.005735	0.0000601	3.25E-13	16.48989	0.0656734	11.21854	0.0821214	68.03284	0.5313374	176.6857	1.232223
0.00915	0.000018	0.959706	0.0009593	568.4	2.7	297.1	2.72869	0.0046857	0.1712965	0.0003746	0.00252	0.0000314	0.1040546	0.0006547	0.0026929	0.0000526	1.71E-13	15.92963	0.0442918	11.23596	0.0987182	70.53494	0.6123071	176.9471	1.480995
0.00915	0.000018	0.959706	0.0009593	568.2	2.6	897.5	5.256378	0.0052054	0.3114752	0.000572	0.0047684	0.0000381	0.2076594	0.0006971	0.005788	0.000034	3.11E-13	16.87575	0.0352093	11.32777	0.0421501	67.12451	0.2271685	178.3239	0.6318649
0.00915	0.000018	0.959706	0.0009593	584.0	2.8	597.3	3.32124	0.0041785	0.2004104	0.000413	0.0029747	0.0000313	0.1495506	0.0006126	0.0032996	0.0000357	2.00E-13	16.5722	0.0400127	11.65665	0.0619162	70.33856	0.3555359	183.2473	0.9256517
0.00915	0.000018	0.959706	0.0009593	584.0	2.6	596.9	1.233835	0.0022672	0.0775654	0.0001586	0.0010398	0.0000301	0.0507562	0.0004963	0.000521	0.0000331	7.76E-14	15.96525	0.0481628	13.95993	0.1349582	87.43951	0.8344105	217.3579	1.979928
0.00915	0.000018	0.959706	0.0009593	599.6	4.5	296.6	0.6735381	0.003309	0.0407124	0.0001417	0.000523	0.0000314	0.0291418	0.0006178	0.0001964	0.0000523	4.07E-14	16.5481	0.0996057	15.10333	0.3954457	91.29297	2.411161	234.055	5.748132
0.00915	0.000018	0.959706	0.0009593	614.3	3.1	296.7	0.8120277	0.0033127	0.0484704	0.0001417	0.0006651	0.000031	0.0361568	0.0006089	0.000226	0.0000523	4.85E-14	16.75407	0.0840829	15.3622	0.3322744	91.69235	2.000329	237.8139	4.819853
0.00915	0.000018	0.959706	0.0009593	628.6	3.7	296.6	1.023812	0.0084	0.0587511	0.0001509	0.0007512	0.0000322	0.0468414	0.0005878	0.0002538	0.0000525	5.88E-14	17.4603	0.0732207	16.17052	0.2761583	92.61305	1.593478	249.5013	3.980045
0.00915	0.000018	0.959706	0.0009593	644.3	2.7	296.7	1.101877	0.0034039	0.0607572	0.0001509	0.0007588	0.000031	0.0494807	0.0005951	0.0002588	0.0000521	6.08E-14	18.13575	0.0718934	16.86409	0.2653287	92.98813	1.472941	259.4696	3.802943
0.00915	0.000018	0.959706	0.0009593	659.7	2.8	296.6	1.131863	0.0034079	0.0595259	0.0001509	0.0007615	0.0000314	0.0503378	0.0005847	0.0002662	0.0000523	5.95E-14	19.01461	0.0748494	17.67926	0.2721405	92.97724	1.439154	271.1158	3.875534
0.00915	0.000018	0.959706	0.0009593	673.1	2.3	296.6	1.126758	0.0034121	0.0576594	0.0001417	0.0007127	0.000031	0.0503164	0.000588	0.0002693	0.0000521	5.71E-14	19.7471	0.077335	18.65174	0.2828209	94.45307	1.441537	284.9121	3.997018
0.00915	0.000018	0.959706	0.0009593	673.2	2.2	296.6	0.756693	0.0033335	0.0370557	0.0001236	0.000439	0.0000304	0.0345743	0.0005929	0.0001965	0.0000521	3.71E-14	20.42042	0.1128237	18.83695	0.433735	92.24565	2.140562	287.5276	6.120979
0.00915	0.000018	0.959706	0.0009593	600.0	4.2	896.6	0.2361355	0.0011193	0.0103869	0.0000816	0.0001428	0.0000377	0.0099557	0.0004223	0.000152	0.0000315	1.04E-14	22.73404	0.208547	18.3658	0.9225071	80.7855	4.02616	280.8665	13.0667
0.00915	0.000018	0.959706	0.0009593	640.1	2.8	897.1	0.5177514	0.0013165	0.0262722	0.0000986	0.0003859	0.0000377	0.0250699	0.000423	0.00029	0.0000295	2.63E-14	19.70723	0.089333	16.41123	0.3444743	83.27516	1.732781	252.9671	4.955121
0.00915	0.000018	0.959706	0.0009593	640.1	3.0	896.6	0.3883073	0.0012181	0.0200388	0.0000949	0.0002473	0.0000373	0.0197121	0.0003935	0.0002022	0.0000307	2.00E-14	19.37777	0.1101124	16.36539	0.467257	84.45446	2.392579	252.3077	6.723751
0.00915	0.000018	0.959706	0.0009593	688.2	1.3	597.4	0.90086	0.0019849	0.046028	0.0001286	0.0006034	0.0000309	0.0422737	0.0004951	0.0002906	0.0000331	4.60E-14	19.572	0.069658	17.68687	0.2243816	90.36822	1.135858	271.2241	3.195211
0.00915	0.000018	0.959706	0.0009593	702.0	0.7	596.9	0.96798	0.0019849	0.0493245	0.0001194	0.0006265	0.0000313	0.0454072	0.0005203	0.0002583	0.0000325	4.93E-14	19.62475	0.0622459	18.0613	0.2052854	92.0333	1.039348	276.5483	2.914685
0.00915	0.000018	0.959706	0.0009593	717.1	0.6	596.8	1.00617	0.0020518	0.0550134	0.0001286	0.0007129	0.0000305	0.0600679	0.0005696	0.0002435	0.0000331	5.50E-14	18.28954	0.0567479	16.98827	0.1875868	92.7758	1.020137	260.9622	2.686454
0.00915	0.000018	0.959706	0.0009593	731.0	0.6	597.4	0.87322	0.0019209	0.0531215	0.000138	0.0006939	0.0000296	0.0535388	0.0005306	0.0002248	0.0000334	5.31E-14	16.43818	0.0559672	15.1747	0.1917132	92.31376	1.159253	235.0921	2.785113
0.00915	0.000018	0.959706	0.0009593	745.0	0.6	597.4	0.69958	0.0018601	0.0479721	0.000138	0.0006181	0.0000296	0.0474668	0.0005407	0.00022	0.0000334	4.80E-14	14.58305	0.0571135	13.2137	0.2149592	90.60999	1.470656	206.3769	3.172808
0.00915	0.000018	0.959706	0.0009593	756.3	1.1	596.8	0.48419	0.0018601	0.0377976	0.0001286	0.0005326	0.0000313	0.0362205	0.0005513	0.0002106	0.0000328	3.78E-14	12.81009	0.0657486	11.14701	0.266081	87.01746	2.082895	175.6122	3.994761
0.00915	0.000018	0.959706	0.0009593	773.0	0.4	597.3	0.5713	0.0018601	0.0469511	0.0001475	0.0006056	0.0000309	0.0606229	0.0005521	0.000209	0.0000331	4.70E-14	12.16798	0.0550562	10.83881	0.2167071	89.07649	1.782583	170.979	3.261842
0.00915	0.000018	0.959706	0.0009593	781.3	3.6	597.4	0.342162	0.0018028	0.0338385	0.000138	0.0004277	0.0000309	0.0393799	0.0005529	0.0001826	0.0000325	3.38E-14	10.11163	0.0673786	8.500911	0.2933456	84.07066	2.91458	135.4425	4.50303
0.00915	0.000018	0.959706	0.0009593	707.3	3.4	596.9	0.426062	0.0018028	0.0447719	0.0001571	0.0005845	0.0000301	0.0757913	0.0006596	0.0001806	0.0000331	4.48E-14	9.516283	0.0523044	8.311896	0.2260725	87.34394	2.284606	132.5387	3.475926
0.00915	0.000018	0.959706	0.0009593	812.1	3.6	596.9	0.55905	0.0018601	0.0587375	0.0001763	0.0007881	0.0000313	0.1030528	0.0006222	0.0002675	0.0000328	5.87E-14	9.517772	0.0426492	8.158253	0.1712565	85.716	1.805535	130.1748	2.636539
0.00915	0.000018	0.959706	0.0009593	809.3	3.7	1796.7	0.9099569	0.0179187	0.0865674	0.0004346	0.0012568	0.0000376	0.0457368	0.000889	0.0008926	0.0000619	8.66E-14	10.51155	0.2136126	7.433262	0.2996075	70.71521	3.152307	118.9787	4.641221
0.00915	0.000018	0.959706	0.0009593	822.9	0.8	597.3	0.27275	0.0018028	0.026632	0.0001286	0.000373	0.0000309	0.0204248	0.0005052	0.0001983	0.0000322	2.66E-14	10.24143	0.0938435	8.018857	0.3691955	78.29822	3.622182	128.0275	5.69066
0.00915	0.000018	0.959706	0.0009593	822.2	0.7	1796.7	0.8457314	0.01791	0.0637657	0.0003822	0.0010738	0.0000414	0.0360257	0.0009699	0.001241	0.0000662	6.38E-14	13.26312	0.2910077	7.452668	0.420631	56.19092	3.370533	119.2793	6.514013
0.00915	0.000018	0.959706	0.0009593	863.0	0.3	596.8	0.95689	0.0021213	0.0919514	0.0002152	0.0011739	0.0000297	0.1494477	0.0005803	0.0003902	0.000032	9.20E-14	10.40647	0.0335472	9.1139578	0.1084527	87.82588	1.040076	145.2199	1.655835
0.00915	0.000018	0.959706	0.0009593	863.0	0.2	1976.7	1.5332	0.0180292	0.1239618	0.0005083	0.0019499	0.0000488	0.0775887	0.0010152	0.0020175	0.0000683	1.24E-13	12.36833	0.1540296	7.5069321	0.2216979	60.71412	1.913287	120.1566	3.432086
0.00915	0.000018	0.959706	0.0009593	882.0	0.3	596.8	0.368097	0.0017372	0.0351516	0.000138	0.0004052	0.0000296	0.0264933	0.0005277	0.0002075	0.0000331	3.52E-14	10.4717	0.0656147	8.70924	0.2875685	83.16932	2.756726	138.6376	4.406554
0.00915	0.000018	0.959706	0.0009593	882.0	0.2	1801.2	0.6683887	0.0173119	0.0650553	0.0003616	0.000935	0.0000367	0.0108268	0.0007137	0.0002858	0.0000593	6.51E-14	10.27417	0.2721698	6.81793	0.3825571	66.35993	4.084414	109.4214	5.957601
0.00915	0.000018	0.959706	0.0009593	900.0	0.3	596.8	0.377083	0.0018028	0.010408	0.0000963	0.0001606	0.0000296	0.0586244	0.0005799	0.0001017	0.0000327	1.04E-14	36.23014	0.2795526	33.31323	0.9762819	91.94894	2.67289	481.0814	12.37892
0.00915	0.000018	0.959706	0.0009593	900.0	0.2	1796.7	0.3368783	0.0173599	0.0170431	0.0002822	0.0002105	0.0000339	0.0593969	0.0008109	0.0002499	0.0000578	1.70E-14	19.76629	1.069879	15.38794	1.455402	77.84943	8.298825	238.1873	21.15069
0.00915	0.000018	0.959706	0.0009593	921.0	0.2	596.8	0.109464	0.0015977	0.0015836	0.0000539	0.0000658	0.0000301	0.0112677	0.0005377	0.0000838	0.0000331	1.58E-15	69.12396	2.560299	53.3263	6.570895	77.14589	9.205093	718.542	73.06294

Table A.15: 18-IAF-06-MOS (64 - 125μm step heating data

Bibliography

Aldrich, L. T. & Nier, A. O. (1948), 'Argon 40 in potassium minerals', *Physical Review* **74**(8), 876.

Altherr, R., Mertz-Kraus, R., Volker, F., Kreuzer, H., Henjes-Kunst, F. & Lange, U. (2019), 'Geodynamic setting of upper miocene to quaternary alkaline basalts from harrat al 'uwayrid (nw saudi arabia): Constraints from kar dating, chemical and sr-nd-pb isotope compositions, and petrological modeling', *Lithos* **330**, 120–138.

Amidon, W. H. & Clark, A. C. (2015), 'Interaction of outburst floods with basaltic aquifers on the snake river plain: Implications for martian canyons', *Bulletin* **127**(5-6), 688–701.

Amidon, W. H. & Farley, K. A. (2011), 'Cosmogenic 3he production rates in apatite, zircon and pyroxene inferred from bonneville flood erosional surfaces', *Quaternary Geochronology* **6**(1), 10–21.

Anderson, R. C., Jandura, L., Okon, A., Sunshine, D., Roumeliotis, C., Beegle, L., Hurowitz, J., Kennedy, B., Limonadi, D., McCloskey, S. et al. (2012), 'Collecting samples in gale crater, mars; an overview of the mars science laboratory sample acquisition, sample processing and handling system', *Space science reviews* **170**(1-4), 57–75.

Antoniak, C. E. (1974), 'Mixtures of dirichlet processes with applications to bayesian nonparametric problems', *The annals of statistics* pp. 1152–1174.

Arnaud, N. & Kelley, S. (1997), 'Argon behaviour in gem-quality orthoclase from madagascar: Experiments and some consequences for 40ar39ar geochronology', *Geochimica et Cosmochimica Acta* **61**(15), 3227–3255.

Atwater, B. F. (1984), 'Periodic floods from glacial lake missoula into the sanpoil arm of glacial lake columbia, northeastern washington', *Geology* **12**(8), 464–467.

Atwater, B. F. (1986), Pleistocene glacial-lake deposits of the sanpoil river valley, northeastern washington, Technical report, USGPO,.

Audi, G., Bersillon, O., Blachot, J. & Wapstra, A. H. (2003), 'The nubase evaluation of nuclear and decay properties', *Nuclear Physics A* **624**, 1–124.

Baerg, A. (1983), 'Electron capture to positron branching ratios in the decay of 22na and 44sc', *Canadian Journal of Physics* **61**(8), 1222–1226.

Bahcall, J. N. (1962), 'Electron capture and nuclear matrix elements of be 7', *Physical Review* **128**(3), 1297.

Baksi, A. K. (1989), 'Reevaluation of the timing and duration of extrusion of', *Volcanism and Tectonism in the Columbia River Flood-Basalt Province* **239**, 105.

Balbas, A. M., Barth, A. M., Clark, P. U., Clark, J., Caffee, M., O'Connor, J., Baker, V. R., Konrad, K. & Bjornstad, B. (2017), '10be dating of late pleistocene megafloods and cordilleran ice sheet retreat in the northwestern united states', *Geology* **45**(7), 583–586.

Bambynek, W., Behrens, H., Chen, M., Crasemann, B., Fitzpatrick, M., Ledingham, K., Genz, H., Mutterer, M. & Intemann, R. (1977), 'Orbital electron capture by the nucleus', *Reviews of Modern Physics* **49**(1), 77.

Bé, M.-M., Chisté, V., Dulieu, C., Mougeot, X., Browne, E., Chechev, V., Kuzmenko, N., Kondev, F., Luca, A., Galan, M. et al. (2010), 'Table of radionuclides (vol. 5-a= 22 to 244)'.

Beckinsale, R. & Gale, N. (1969), 'A reappraisal of the decay constants and branching ratio of 40k', *Earth and Planetary Science Letters* **6**(4), 289–294.

Benito, G. & O'Connor, J. E. (2003), 'Number and size of last-glacial missoula floods in the columbia river valley between the pasco basin, washington, and portland, oregon', *Geological Society of America Bulletin* **115**(5), 624–638.

Bethe, H. A. & Bacher, R. F. (1936), 'Nuclear physics a. stationary states of nuclei', *Reviews of Modern Physics* **8**(2), 82.

Boehnke, P. & Harrison, T. M. (2016), 'Illusory late heavy bombardments', *Proceedings of the National Academy of Sciences* **113**(39), 10802–10806.

Boehnke, P., Harrison, T. M., Heizler, M. & Warren, P. (2016), 'A model for meteoritic and lunar 40 ar/39 ar age spectra: Addressing the conundrum of multi-activation energies', *Earth and Planetary Science Letters* **453**, 267–275.

Bond, G., Broecker, W., Johnsen, S., McManus, J., Labeyrie, L., Jouzel, J. & Bonani, G. (1993), 'Correlations between climate records from north atlantic sediments and greenland ice', *Nature* **365**(6442), 143–147.

Bosch, H., Davidson, J., Davidson, M. & Szybisz, L. (1977), 'The electron capture to positron emission ratios in the decay of 22 na and 65 zn', *Zeitschrift für Physik A Atoms and Nuclei* **280**(4), 321–327.

Bretz, J. H. (1923), 'The channeled scablands of the columbia plateau', *The Journal of Geology* **31**(8), 617–649.

Bretz, J. H. (1925), 'The spokane flood beyond the channeled scablands', *The Journal of Geology* **33**(2), 97–115.

Bretz, J. H., SMITH, H. U. & Neff, G. E. (1956), 'Channeled scabland of washington: New data and interpretations', *Geological Society of America Bulletin* **67**(8), 957–1049.

Carling, P. A., MARTINI, I. P., HERGET, J., Borodavko, P. & Parnachov, S. (2009), '13 megaflood sedimentary valley fill: Altai mountains, siberia', *This page intentionally left blank* p. 243.

Carrapa, B., DeCelles, P. G., Reiners, P. W., Gehrels, G. E. & Sudo, M. (2009), 'Apatite triple dating and white mica 40ar/39ar thermochronology of syntectonic detritus in the central andes: A multiphase tectonothermal history', *Geology* **37**(5), 407–410.

Carter, J. N., Tremblay, M. M. & Mark, D. F. (2020), 'A bayesian approach to the deconvolution of 40ar/39ar data from mineral mixtures', *Chemical Geology* **554**, 119784.

Cassata, W. S. (2014), 'In situ dating on mars: A new approach to the k–ar method utilizing cosmogenic argon', *Acta Astronautica* **94**(1), 222–233.

Cassata, W. S. & Renne, P. R. (2013), 'Systematic variations of argon diffusion in feldspars and implications for thermochronometry', *Geochimica et Cosmochimica Acta* **112**, 251–287.

Cassata, W. S., Renne, P. R. & Shuster, D. L. (2009), 'Argon diffusion in plagioclase and implications for thermochronometry: a case study from the bushveld complex, south africa', *Geochimica et Cosmochimica Acta* **73**(21), 6600–6612.

Cassata, W. S., Shuster, D. L., Renne, P. R. & Weiss, B. P. (2010), 'Evidence for shock heating and constraints on martian surface temperatures revealed by 40ar/39ar thermochronometry of martian meteorites', *Geochimica et Cosmochimica Acta* **74**(23), 6900–6920.

Chen, J. (2017), 'Nuclear data sheets for a= 40', *Nuclear Data Sheets* **140**, 1–376.

Cho, Y., Horiuchi, M., Shibasaki, K., Kameda, S. & Sugita, S. (2017), 'Quantitative potassium measurements with laser-induced breakdown spectroscopy using low-energy lasers: Application to in situ k–ar geochronology for planetary exploration', *Applied spectroscopy* **71**(8), 1969–1981.

Clarke, G., Leverington, D., Teller, J. & Dyke, A. (2003), 'Superlakes, megafloods, and abrupt climate change', *Science* **301**(5635), 922–923.

Clauer, N. (2013), 'The k-ar and 40ar/39ar methods revisited for dating fine-grained k-bearing clay minerals', *Chemical Geology* **354**, 163–185.

Cohen, B. A., Swindle, T. & Roark, S. (2014), 'In situ geochronology on the mars 2020 rover with karle (potassium-argon laser experiment)'.

Copeland, P. & Harrison, T. M. (1990), 'Episodic rapid uplift in the himalaya revealed by 40ar/39ar analysis of detrital k-feldspar and muscovite, bengal fan', *Geology* **18**(4), 354–357.

Crank, J. (1979), *The mathematics of diffusion*, Oxford university press.

Cresswell, A., Carter, J. & Sanderson, D. (2018), 'Dose rate conversion parameters: Assessment of nuclear data', *Radiation Measurements* **120**, 195–201.

Cresswell, A. J., Sanderson, D. C. & Carter, J. (2019), 'Review of nuclear data for naturally occurring radionuclides applied to environmental applications', *The European Physical Journal Plus* **134**(2), 69.

Dalrymple, G. B. & Ryder, G. (1993), '40ar/39ar age spectra of apollo 15 impact melt rocks by laser step-heating and their bearing on the history of lunar basin formation', *Journal of Geophysical Research: Planets* **98**(E7), 13085–13095.

Denlinger, R. P. & O'Connell, D. (2010), 'Simulations of cataclysmic outburst floods from pleistocene glacial lake missoula', *Bulletin* **122**(5-6), 678–689.

Di Stefano, P., Brewer, N., Fijałkowska, A., Gai, Z., Goetz, K., Grzywacz, R., Hamm, D., Lechner, P., Liu, Y., Lukosi, E. et al. (2020), The kdk (potassium decay) experiment, *in* 'Journal of Physics: Conference Series', Vol. 1342, IOP Publishing, p. 012062.

Diebolt, J. & Robert, C. P. (1994), 'Estimation of finite mixture distributions through bayesian sampling', *Journal of the Royal Statistical Society: Series B (Methodological)* **56**(2), 363–375.

Dong, H., Hall, C. M., Peacor, D. R. & Halliday, A. N. (1995), 'Mechanisms of argon retention in clays revealed by laser 40ar-39ar dating', *Science* **267**(5196), 355–359.

Dong, H., Hall, C. M., Peacor, D. R., Halliday, A. N. & Pevear, D. R. (2000), 'Thermal 40ar/39ar separation of diagenetic from detrital illitic clays in gulf coast shales', *Earth and Planetary Science Letters* **175**(3-4), 309–325.

Duane, S., Kennedy, A. D., Pendleton, B. J. & Roweth, D. (1987), 'Hybrid monte carlo', *Physics letters B* **195**(2), 216–222.

Dyke, A. S. & Evans, D. J. (2003), 'Ice-marginal terrestrial landsystems: northern laurentide and innuitian ice sheet margins', *Glacial landsystems* **24**.

Ehlmann, B. L. & Edwards, C. S. (2014), 'Mineralogy of the martian surface', *Annual Review of Earth and Planetary Sciences* **42**, 291–315.

Eide, E. A., Haabesland, N. E., Osmundsen, P. T., Andersen, T. B., Roberts, D. & Kendrick, M. A. (2005), 'Modern techniques and old red problems-determining the age of continental sedimentary deposits with 40 ar/39 ar provenance analysis in west-central norway.', *Norwegian Journal of Geology/Norsk Geologisk Forening* **85**.

Emery, G. (1975), Ionization through nuclear electron capture and internal conversion, *in* 'Atomic inner-shell processes. Vol. I'.

Endt, P. (1990), 'Energy levels of a= 21–44 nuclei (vii)', *Nuclear Physics A* **521**, 1–400.

Endt, P. & Van der Leun, C. (1973), 'Energy levels of a= 21- 44 nuclei (v)', *Nuclear Physics A* **214**, 1–625.

Endt, P. & Van der Leun, C. (1978), 'Energy levels of a= 21–44 nuclei (vi)', *Nuclear Physics A* **310**(1-2), 1–751.

Engelkemeir, D., Flynn, K. & Glendenin, L. (1962), 'Positron emission in the decay of k 40', *Physical Review* **126**(5), 1818.

Farley, K., Malespin, C., Mahaffy, P., Grotzinger, J., Vasconcelos, P., Milliken, R., Malin, M., Edgett, K., Pavlov, A., Hurowitz, J. et al. (2014), 'In situ radiometric and exposure age dating of the martian surface', *science* **343**(6169), 1247166.

Fechtig, H. & Kalbitzer, S. (1966), The diffusion of argon in potassium-bearing solids, *in* 'Potassium argon dating', Springer, pp. 68–107.

Ferguson, T. S. (1973), 'A bayesian analysis of some nonparametric problems', *The annals of statistics* pp. 209–230.

Fermi, E. (1934), 'An attempt of a theory of beta radiation. 1.', *Z. Phys.* **88**(UCRL-TRANS-726), 161–177.

Feroz, F., Hobson, M. & Bridges, M. (2009), 'Multinest: an efficient and robust bayesian inference tool for cosmology and particle physics', *Monthly Notices of the Royal Astronomical Society* **398**(4), 1601–1614.

Fireman, E. (1949), 'On the decay of k 40', *Physical Review* **75**(9), 1447.

Fleck, R. J., Sutter, J. F. & Elliot, D. H. (1977), 'Interpretation of discordant 40ar/39ar age-spectra of mesozoic tholeiites from antarctica', *Geochimica et Cosmochimica Acta* **41**(1), 15–32.

Foland, K. (1974), 'Ar40 diffusion in homogenous orthoclase and an interpretation of ar diffusion in k-feldspars', *Geochimica et Cosmochimica Acta* **38**(1), 151–166.

Foland, K. (1994), Argon diffusion in feldspars, *in* 'Feldspars and their reactions', Springer, pp. 415–447.

Foland, K. & Xu, Y. (1990), 'Diffusion of 40ar and 39ar in irradiated orthoclase', *Geochimica et Cosmochimica Acta* **54**(11), 3147–3158.

Forster, M. & Lister, G. (2004), 'The interpretation of 40ar/39ar apparent age spectra produced by mixing: application of the method of asymptotes and limits', *Journal of Structural Geology* **26**(2), 287–305.

Fuhrmann, U., Lippolt, H. & Hess, J. (1987), 'Examination of some proposed k-ar standards: 40ar39ar analyses and conventional k ar data', *Chemical Geology: Isotope Geoscience section* **66**(1-2), 41–51.

Gallagher, K. (2012), 'Transdimensional inverse thermal history modeling for quantitative thermochronology', *Journal of Geophysical Research: Solid Earth* **117**(B2).

Gallagher, K., Charvin, K., Nielsen, S., Sambridge, M. & Stephenson, J. (2009), 'Markov chain monte carlo (mcmc) sampling methods to determine optimal models, model resolution and model choice for earth science problems', *Marine and Petroleum Geology* **26**(4), 525–535.

Garner, E., Machlan, L. & Barnes, I. (1975), The isotopic composition of lithium, potassium, and rubidium in some apollo 11, 12, 14, 15, and 16 samples, *in* 'Lunar and Planetary Science Conference Proceedings', Vol. 6, pp. 1845–1855.

Gautheron, C. & Tassan-Got, L. (2010), 'A monte carlo approach to diffusion applied to noble gas/helium thermochronology', *Chemical Geology* **273**(3-4), 212–224.

Gaylord, D. R., Pope, M. C., Cabbage, P., Glover III, J., Anfinson, O., Baar, E. & Vervoort, J. (2007), Provenance of glacial outburst flood deposits in the channeled scabland, wa; influence of glacial lake missoula, meltwater, snake river, and bonneville flood sources, *in* 'Geological Society of America Abstracts with Programs', Vol. 39, p. 82.

Gelman, A., Carlin, J. B., Stern, H. S., Dunson, D. B., Vehtari, A. & Rubin, D. B. (2013), *Bayesian data analysis*, Chapman and Hall/CRC.

Gemignani, L., Kuiper, K., Wijbrans, J., Sun, X. & Santato, A. (2019), 'Improving the precision of single grain mica 40ar/39ar-dating on smaller and younger muscovite grains: Application to provenance studies', *Chemical Geology* **511**, 100–111.

Gemignani, L., Sun, X., Braun, J., van Gerve, T. & Wijbrans, J. R. (2017), 'A new detrital mica 40ar/39ar dating approach for provenance and exhumation of the eastern alps', *Tectonics* **36**(8), 1521–1537.

Gillespie, A., Huneke, J. & Wasserburg, G. (1982), 'An assessment of 40ar-39ar dating of incompletely degassed xenoliths', *Journal of Geophysical Research: Solid Earth* **87**(B11), 9247–9257.

Gombosi, D. J., Baldwin, S. L., Watson, E. B., Swindle, T. D., Delano, J. W. & Roberge, W. G. (2015), 'Argon diffusion in apollo 16 impact glass spherules: Implications for 40ar/39ar dating of lunar impact events', *Geochimica et Cosmochimica Acta* **148**, 251–268.

Gopalan, K. & Kumar, A. (2008), 'Phlogopite k–ca dating of narayanpet kimberlites, south india: implications to the discordance between their rb–sr and ar/ar ages', *Precambrian Research* **167**(3-4), 377–382.

Grimmer, J. C., Ratschbacher, L., McWilliams, M., Franz, L., Gaitzsch, I., Tichomirowa, M., Hacker, B. R. & Zhang, Y. (2003), 'When did the ultrahigh-pressure rocks reach the surface? a 207pb/206pb zircon, 40ar/39ar white mica, si-in-white mica, single-grain provenance study of dabie shan synorogenic foreland sediments', *Chemical Geology* **197**(1-4), 87–110.

Hanson, M. A. & Clague, J. J. (2016), 'Record of glacial lake missoula floods in glacial lake columbia, washington', *Quaternary Science Reviews* **133**, 62–76.

Harrison, T. M. (1983), 'Some observations on the interpretation of 40ar/39ar age spectra', *Chemical geology* **41**, 319–338.

Harrison, T. M., Célérier, J., Aikman, A. B., Hermann, J. & Heizler, M. T. (2009), 'Diffusion of 40ar in muscovite', *Geochimica et Cosmochimica Acta* **73**(4), 1039–1051.

Harrison, T. M., Duncan, I. & McDougall, I. (1985), 'Diffusion of 40ar in biotite: temperature, pressure and compositional effects', *Geochimica et Cosmochimica Acta* **49**(11), 2461–2468.

Harrison, T. M., Lovera, O. M. & Matthew, T. H. (1991), '40ar39ar results for alkali feldspars containing diffusion domains with differing activation energy', *Geochimica et Cosmochimica Acta* **55**(5), 1435–1448.

Hastings, W. K. (1970), 'Monte carlo sampling methods using markov chains and their applications'.

Hemming, S., Broecker, W., Sharp, W., Bond, G., Gwiazda, R., McManus, J., Klas, M. & Hajdas, I. (1998), 'Provenance of heinrich layers in core v28-82, northeastern atlantic: 40ar/39ar ages of ice-rafted hornblende, pb isotopes in feldspar grains, and nd–sr–pb isotopes in the fine sediment fraction', *Earth and Planetary Science Letters* **164**(1-2), 317–333.

Hemming, S. R., Vorren, T. O. & Kleman, J. (2002), 'Provinciality of ice rafting in the north atlantic: Application of 40ar/39ar dating of individual ice rafted hornblende grains', *Quaternary International* **95**, 75–85.

Hjort, N. L., Holmes, C., Müller, P. & Walker, S. G. (2010), *Bayesian nonparametrics*, Vol. 28, Cambridge University Press.

Hoffman, M. D. & Gelman, A. (2014), 'The no-u-turn sampler: adaptively setting path lengths in hamiltonian monte carlo.', *Journal of Machine Learning Research* **15**(1), 1593–1623.

Horgan, B. H., Anderson, R. B., Dromart, G., Amador, E. S. & Rice, M. S. (2020), 'The mineral diversity of jezero crater: Evidence for possible lacustrine carbonates on mars', *Icarus* **339**, 113526.

Huneke, J. & Villa, I. (1981), '39ar loss during neutron irradiation and the aging of allende inclusions', *Meteoritics* **16**, 329.

Jessberger, E., Huneke, J., Podosek, F. & Wasserburg, G. (1974), High resolution argon analysis of neutron-irradiated apollo 16 rocks and separated minerals, *in* 'Lunar and Planetary Science Conference Proceedings', Vol. 5, pp. 1419–1449.

Jourdan, F. & Eroglu, E. (2017), '40ar/39ar and (u-th)/he model age signatures of elusive mercurian and venusian meteorites', *Meteoritics & Planetary Science* **52**(5), 884–905.

Jourdan, F., Matzel, J. P. & Renne, P. R. (2007), '39ar and 37ar recoil loss during neutron irradiation of sanidine and plagioclase', *Geochimica et Cosmochimica Acta* **71**(11), 2791–2808.

Kasbohm, J. & Schoene, B. (2018), 'Rapid eruption of the columbia river flood basalt and correlation with the mid-miocene climate optimum', *Science advances* **4**(9), eaat8223.

Keller, C. B., Schoene, B. & Samperton, K. M. (2018), 'A stochastic sampling approach to zircon eruption age interpretation', *Geochemical Perspectives Letters (Online)* **8**(LLNL-JRNL-738859).

Kelley, S. (2002), 'Excess argon in k–ar and ar–ar geochronology', *Chemical Geology* **188**(1-2), 1–22.

Komatsu, G., Miyamoto, H., Ito, K., Tosaka, H. & Tokunaga, T. (2000), 'The channeled scabland: Back to bretz?: Comment and reply: Comment', *Geology* **28**(6), 573–574.

Koop, G. M. (2003), *Bayesian econometrics*, John Wiley & Sons Inc.

Krane, K. S., Halliday, D. et al. (1987), *Introductory nuclear physics*.

Kreger, W. (1954), 'K capture to positron ratio for na 22', *Physical Review* **96**(6), 1554.

Kuiper, K., Deino, A., Hilgen, F., Krijgsman, W., Renne, P., Wijbrans & JR (2008), 'Synchronizing rock clocks of earth history', *science* **320**(5875), 500–504.

Kula, J. & Baldwin, S. L. (2011), 'Jarosite, argon diffusion, and dating aqueous mineralization on earth and mars', *Earth and Planetary Science Letters* **310**(3-4), 314–318.

Kula, J., Spell, T. L. & Zanetti, K. A. (2010), '40ar/39ar analyses of artificially mixed micas and the treatment of complex age spectra from samples with multiple mica populations', *Chemical Geology* **275**(1-2), 67–77.

Kunze, V., Schmidt-Ott, W.-D. & Behrens, H. (1990), 'Remeasurement of capture to positron decay ratios in 22 na and 65 zn and comparison with theory', *Zeitschrift für Physik A Atomic Nuclei* **337**(2), 169–173.

Lamb, M. P., Dietrich, W. E., Aciego, S. M., DePaolo, D. J. & Manga, M. (2008), 'Formation of box canyon, idaho, by megaflood: Implications for seepage erosion on earth and mars', *science* **320**(5879), 1067–1070.

Lang, K. A., Huntington, K. W. & Montgomery, D. R. (2013), 'Erosion of the tsangpo gorge by megafloods, eastern himalaya', *Geology* **41**(9), 1003–1006.

Lanphere, M. A. & Dalrymple, G. B. (1976), 'Identification of excess 40ar by the 40ar/39ar age spectrum technique', *Earth and Planetary Science Letters* **32**(2), 141–148.

Larsen, I. J. & Lamb, M. P. (2016), 'Progressive incision of the channeled scablands by outburst floods', *Nature* **538**(7624), 229–232.

Lee, J. K. (1995), 'Multipath diffusion in geochronology', *Contributions to Mineralogy and Petrology* **120**(1), 60–82.

Lesemann, J.-E. & Brennand, T. A. (2009), 'Regional reconstruction of subglacial hydrology and glaciodynamic behaviour along the southern margin of the cordilleran ice sheet in british columbia, canada and northern washington state, usa', *Quaternary Science Reviews* **28**(23-24), 2420–2444.

Leutz, H., Schulz, G. & Wenninger, H. (1965), 'The decay of potassium-40', *Zeitschrift fuer Physik* **187**(2), 151–164.

Li, Z.-X., Wartho, J.-A., Occhipinti, S., Zhang, C.-L., Li, X.-H., Wang, J. & Bao, C. (2007), 'Early history of the eastern sibao orogen (south china) during the assembly of rodinia: new mica 40ar/39ar dating and shrimp u–pb detrital zircon provenance constraints', *Precambrian Research* **159**(1-2), 79–94.

Liu, J. S. (1996), Metropolized gibbs sampler: an improvement, Technical report, Technical report, Dept. Statistics, Stanford Univ.

Lovera, O. M., Grove, M. & Harrison, T. M. (2002), 'Systematic analysis of k-feldspar 40ar/39ar step heating results ii: Relevance of laboratory argon diffusion properties to nature', *Geochimica et Cosmochimica Acta* **66**(7), 1237–1255.

Lovera, O. M., Richter, F. M. & Harrison, T. M. (1989), 'The 40ar/39ar thermochronometry for slowly cooled samples having a distribution of diffusion domain sizes', *Journal of Geophysical Research: Solid Earth* **94**(B12), 17917–17935.

Lovera, O. M., Richter, F. M. & Harrison, T. M. (1991), 'Diffusion domains determined by 39ar released during step heating', *Journal of Geophysical Research: Solid Earth* **96**(B2), 2057–2069.

MacMahon, T. & Baerg, A. (1976), 'The electron capture to positron branching ratio in the decay of 22na', *Canadian Journal of Physics* **54**(14), 1433–1437.

Mahaffy, P. R., Webster, C. R., Cabane, M., Conrad, P. G., Coll, P., Atreya, S. K., Arvey, R., Barciniak, M., Benna, M., Bleacher, L. et al. (2012), 'The sample analysis at mars investigation and instrument suite', *Space Science Reviews* **170**(1-4), 401–478.

Margold, M., Jansen, J. D., Codilean, A. T., Preusser, F., Gurinov, A. L., Fujioka, T. & Fink, D. (2018), 'Repeated megafloods from glacial lake vitim, siberia, to the arctic ocean over the past 60,000 years', *Quaternary Science Reviews* **187**, 41–61.

Mark, D., Barfod, D., Stuart, F. & Imlach, J. (2009), 'The argus multicollector noble gas mass spectrometer: Performance for 40ar/39ar geochronology', *Geochemistry, Geophysics, Geosystems* **10**(10).

Mark, D. F., Renne, P. R., Dymock, R. C., Smith, V. C., Simon, J. I., Morgan, L. E., Staff, R. A., Ellis, B. S. & Pearce, N. J. (2017), 'High-precision 40ar/39ar dating of pleistocene tuffs and temporal anchoring of the matuyama-brunhes boundary', *Quaternary Geochronology* **39**, 1–23.

Martin, P., Farley, K., Baker, M., Malespin, C., Schwenzer, S., Cohen, B., Mahaffy, P., McAdam, A., Ming, D., Vasconcelos, P. et al. (2017), 'A two-step k-ar experiment on mars: Dating the diagenetic formation of jarosite from amazonian groundwaters', *Journal of Geophysical Research: Planets* **122**(12), 2803–2818.

McCann, M. & Smith, K. (1969), 'Direct measurement of the k electron capture to positron emission ratio in the decay of 22na', *Journal of Physics A: General Physics* **2**(3), 392.

McDannell, K. T., Zeitler, P. K., Janes, D. G., Idleman, B. D. & Fayon, A. K. (2018), 'Screening apatites for (u-th)/he thermochronometry via continuous ramped heating: He age components and implications for age dispersion', *Geochimica et Cosmochimica Acta* **223**, 90–106.

McDougall, I. & Harrison, T. M. (1999), *Geochronology and Thermochronology by the 40Ar/39Ar Method*, Oxford University Press on Demand.

McDougall, I. & Wellman, P. (2011), 'Calibration of ga1550 biotite standard for k/ar and 40ar/39ar dating', *Chemical Geology* **280**(1-2), 19–25.

Merrihue, C. & Turner, G. (1966), 'Potassium-argon dating by activation with fast neutrons', *Journal of Geophysical Research* **71**(11), 2852–2857.

Metropolis, N., Rosenbluth, A. W., Rosenbluth, M. N., Teller, A. H. & Teller, E. (1953), 'Equation of state calculations by fast computing machines', *The journal of chemical physics* **21**(6), 1087–1092.

Min, K., Mundil, R., Renne, P. R. & Ludwig, K. R. (2000), 'A test for systematic errors in 40ar/39ar geochronology through comparison with u/pb analysis of a 1.1-ga rhyolite', *Geochimica et Cosmochimica Acta* **64**(1), 73–98.

Miyamoto, H., Itoh, K., Komatsu, G., Baker, V. R., Dohm, J. M., Tosaka, H. & Sasaki, S. (2006), 'Numerical simulations of large-scale cataclysmic floodwater: A simple depth-averaged model and an illustrative application', *Geomorphology* **76**(1-2), 179–192.

Miyamoto, H., Komatsu, G., Baker, V. R., Dohm, J. M., Ito, K. & Tosaka, H. (2007), 'Cataclysmic scabland flooding: Insights from a simple depth-averaged numerical model', *Environmental Modelling & Software* **22**(10), 1400–1408.

Morgan, L. E., Munk, M., Davidheiser-Kroll, B., Warner, N. H., Gupta, S., Slaybaugh, R., Harkness, P. & Mark, D. F. (2017), 'Instrumentation development for in situ 40ar/39ar planetary geochronology', *Geostandards and Geoanalytical Research* **41**(3), 381–396.

Morgan, L., Mark, D., Imlach, J., Barfod, D. & Dymock, R. (2014), 'Fcs-ek: A new sampling of the fish canyon tuff 40ar/39ar neutron flux monitor', *Geological Society, London, Special Publications* **378**(1), 63–67.

Mougeot, X. (2018), 'Improved calculations of electron capture transitions for decay data and radionuclide metrology', *Applied Radiation and Isotopes* **134**, 225–232.

Nähle, O., Kossert, K. & Klein, R. (2008), 'Activity standardization of 22na', *Applied Radiation and Isotopes* **66**(6-7), 865–871.

Najman, Y., Bickle, M., Garzanti, E., Pringle, M., Barfod, D., Brozovic, N., Burbank, D. & Ando, S. (2009), 'Reconstructing the exhumation history of the lesser himalaya, nw india, from a multitechnique provenance study of the foreland basin siwalik group', *Tectonics* **28**(5).

Najman, Y., Mark, C., Barfod, D. N., Carter, A., Parrish, R., Chew, D. & Gemignani, L. (2019), 'Spatial and temporal trends in exhumation of the eastern himalaya and syntaxis as determined from a multitechnique detrital thermochronological study of the bengal fan', *Bulletin* **131**(9-10), 1607–1622.

Niespolo, E. M., Rutte, D., Deino, A. L. & Renne, P. R. (2017), 'Intercalibration and age of the alder creek sanidine 40ar/39ar standard', *Quaternary Geochronology* **39**, 205–213.

Onstott, T. C., Miller, M., Ewing, R., Arnold, G. & Walsh, D. (1995), 'Recoil refinements: Implications for the 40ar/39ar dating technique', *Geochimica et Cosmochimica Acta* **59**(9), 1821–1834.

O'Connor, J. E., Baker, V. R., Waitt, R. B., Smith, L. N., Cannon, C. M., George, D. L. & Denlinger, R. P. (2020), 'The missoula and bonneville floods—a review of ice-age megafloods in the columbia river basin', *Earth-Science Reviews* p. 103181.

Paine, J. H., Nomade, S. & Renne, P. R. (2006), 'Quantification of ^{39}ar recoil ejection from ga1550 biotite during neutron irradiation as a function of grain dimensions', *Geochimica et Cosmochimica Acta* **70**(6), 1507–1517.

Parsons, I., Brown, W. & Smith, J. (1999), '40 ar/39 ar thermochronology using alkali feldspars: real thermal history or mathematical mirage of microtexture?', *Contributions to Mineralogy and Petrology* **136**(1-2), 92–110.

Parsons, I. & Lee, M. R. (2005), 'Minerals are not just chemical compounds', *The Canadian Mineralogist* **43**(6), 1959–1992.

Popov, D. V. & Spikings, R. A. (2020), 'Diffusion vs. fluid alteration in alkali feldspar 40ar/39ar thermochronology: Does cross-correlation of log (r/r0) and age spectra validate thermal histories?', *Chemical Geology* **539**, 119506.

Pradler, J., Singh, B. & Yavin, I. (2013), 'On an unverified nuclear decay and its role in the dama experiment', *Physics Letters B* **720**(4-5), 399–404.

Preece, K., Mark, D. F., Barclay, J., Cohen, B. E., Chamberlain, K. J., Jowitt, C., Vye-Brown, C., Brown, R. J. & Hamilton, S. (2018), 'Bridging the gap: 40ar/39ar dating of volcanic eruptions from the 'age of discovery"', *Geology* **46**(12), 1035–1038.

Rahman, M. J. J. & Faupl, P. (2003), '40ar/39ar multigrain dating of detrital white mica of sandstones of the surma group in the sylhet trough, bengal basin, bangladesh', *Sedimentary Geology* **155**(3-4), 383–392.

Rampe, E., Ming, D., Blake, D., Bristow, T., Chipera, S., Grotzinger, J., Morris, R., Morrison, S., Vaniman, D., Yen, A. et al. (2017), 'Mineralogy of an ancient lacustrine mudstone succession from the murray formation, gale crater, mars', *Earth and Planetary Science Letters* **471**, 172–185.

Rampe, E., Ming, D., Morris, R., Blake, D., Bristow, T., SJ, C., Vaniman, D., Yen, A., Grotzinger, J., Downs, R. et al. (2016), 'Diagenesis in the murray formation, gale crater, mars'.

Ramsey, C. B. (2009), 'Bayesian analysis of radiocarbon dates', *Radiocarbon* **51**(1), 337–360.

Reed, J. C., Tucholke, B. E. & Wheeler, J. O. (2005), *Decade of North American Geology: Geologic Map of North America: Perspectives and Explanation*, Geological Society of America Boulder, Colorado.

Renne, P. R. (2000), '40ar/39ar age of plagioclase from acapulco meteorite and the problem of systematic errors in cosmochronology', *Earth and Planetary Science Letters* **175**(1-2), 13–26.

Renne, P. R., Balco, G., Ludwig, K. R., Mundil, R. & Min, K. (2011), 'Response to the comment by wh schwarz et al. on "joint determination of 40k decay constants and 40ar/40k for the fish canyon sanidine standard, and improved accuracy for 40ar/39ar geochronology" by pr renne et al.(2010)', *Geochimica et Cosmochimica Acta* **75**(17), 5097–5100.

Renne, P. R., Deino, A. L., Hilgen, F. J., Kuiper, K. F., Mark, D. F., Mitchell, W. S., Morgan, L. E., Mundil, R. & Smit, J. (2013), 'Time scales of critical events around the cretaceous-paleogene boundary', *Science* **339**(6120), 684–687.

Renne, P. R., Mundil, R., Balco, G., Min, K. & Ludwig, K. R. (2010), 'Joint determination of 40k decay constants and 40ar/40k for the fish canyon sanidine standard, and improved accuracy for 40ar/39ar geochronology', *Geochimica et Cosmochimica Acta* **74**(18), 5349–5367.

Renne, P. R., Swisher, C. C., Deino, A. L., Karner, D. B., Owens, T. L. & DePaolo, D. J. (1998), 'Intercalibration of standards, absolute ages and uncertainties in 40ar/39ar dating', *Chemical Geology* **145**(1-2), 117–152.

Renne, P., Sharp, W., Deino, A., Orsi, G. & Civetta, L. (1997), '40ar/39ar dating into the historical realm: calibration against pliny the younger', *Science* **277**(5330), 1279–1280.

Rex, D., Guise, P. & Wartho, J.-A. (1993), 'Disturbed 40ar 39ar spectra from hornblendes: Thermal loss or contamination', *Chemical Geology* **103**(1-4), 271–281.

Rivera, T. A., Storey, M., Zeeden, C., Hilgen, F. J. & Kuiper, K. (2011), 'A refined astronomically calibrated 40ar/39ar age for fish canyon sanidine', *Earth and Planetary Science Letters* **311**(3-4), 420–426.

Salvatier, J., Wiecki, T. V. & Fonnesbeck, C. (2016), 'Probabilistic programming in python using pymc3', *PeerJ Computer Science* **2**, e55.

Sambridge, M. & Compston, W. (1995), 'Mixture modeling of multi-component data sets with application to ion-probe zircon ages', *Earth and Planetary Science Letters* **128**(3), 373–390.

Schon, S. C., Head, J. W. & Fassett, C. I. (2012), 'An overfilled lacustrine system and progradational delta in jezero crater, mars: Implications for noachian climate', *Planetary and Space Science* **67**(1), 28–45.

Sethuraman, J. (1994), 'A constructive definition of dirichlet priors', *Statistica sinica* pp. 639–650.

Sharman, G. R. & Johnstone, S. A. (2017), 'Sediment unmixing using detrital geochronology', *Earth and Planetary Science Letters* **477**, 183–194.

Shaw, J., Munro-Stasiuk, M., Sawyer, B., Beaney, C., Lesemann, J.-E., Musacchio, A., Rains, B. & Young, R. R. (1999), 'The channeled scabland: back to bretz?', *Geology* **27**(7), 605–608.

Shaw, J. & Sharpe, D. R. (1987), 'Drumlin formation by subglacial meltwater erosion', *Canadian Journal of Earth Sciences* **24**(11), 2316–2322.

Shuster, D. L. & Cassata, W. S. (2015), 'Paleotemperatures at the lunar surfaces from open system behavior of cosmogenic 38ar and radiogenic 40ar', *Geochimica et Cosmochimica Acta* **155**, 154–171.

Singer, B. S., Ackert Jr, R. P. & Guillou, H. (2004), '40ar/39ar and k-ar chronology of pleistocene glaciations in patagonia', *Geological Society of America Bulletin* **116**(3-4), 434–450.

Skilling, J. et al. (2006), 'Nested sampling for general bayesian computation', *Bayesian analysis* **1**(4), 833–859.

Smith, R. S. & Kay, B. D. (1999), 'The existence of supercooled liquid water at 150? k', *Nature* **398**(6730), 788–791.

Solé, J. (2014), 'In situ determination of k–ar ages from minerals and rocks using simultaneous laser-induced plasma spectroscopy and noble gas mass spectrometry', *Chemical Geology* **388**, 9–22.

Steiger, R. H. & Jäger, E. (1977), 'Subcommission on geochronology: convention on the use of decay constants in geo-and cosmochronology', *Earth and planetary science letters* **36**(3), 359–362.

Swindle, T. (2000), 'In situ noble-gas based chronology on mars'.

Sỳkora, I. & Povinec, P. (1986), 'Measurement of electron capture to positron emission ratios in light and medium nuclides', *Nuclear Instruments and Methods in Physics Research Section B: Beam Interactions with Materials and Atoms* **17**(5-6), 467–471.

Tolan, T. L. & Beeson, M. H. (1984), 'Intracanyon flows of the columbia river basalt group in the lower columbia river gorge and their relationship to the troutdale formation', *Geological Society of America Bulletin* **95**(4), 463–477.

Trotta, R. (2008), 'Bayes in the sky: Bayesian inference and model selection in cosmology', *Contemporary Physics* **49**(2), 71–104.

Turner, G. (1968), The distribution of potassium and argon in chondrites, *in* 'Origin and Distribution of the Elements', Elsevier, pp. 387–398.

Turner, G. et al. (1977), 'Potassium-argon chronology of the moon.'.

Turzewski, M. D., Huntington, K. W., Licht, A. & Lang, K. A. (2020), 'Provenance and erosional impact of quaternary megafloods through the yarlung-tsangpo gorge from zircon u-pb geochronology of flood deposits, eastern himalaya', *Earth and Planetary Science Letters* **535**, 116113.

Van Hoang, L., Clift, P. D., Mark, D., Zheng, H. & Tan, M. T. (2010), 'Ar–ar muscovite dating as a constraint on sediment provenance and erosion processes in the red and yangtze river systems, se asia', *Earth and Planetary Science Letters* **295**(3-4), 379–389.

Vaniman, D., Bish, D., Ming, D., Bristow, T., Morris, R., Blake, D., Chipera, S., Morrison, S., Treiman, A., Rampe, E. et al. (2013), 'Mineralogy of a mudstone at yellowknife bay, gale crater, mars', *Science* p. 1243480.

VanLaningham, S., Duncan, R. A. & Pisias, N. G. (2006), 'Erosion by rivers and transport pathways in the ocean: A provenance tool using 40ar-39ar incremental heating on fine-grained sediment', *Journal of Geophysical Research: Earth Surface* **111**(F4).

VanLaningham, S., Duncan, R. A., Pisias, N. G. & Graham, D. W. (2008), 'Tracking fluvial response to climate change in the pacific northwest: a combined provenance approach using ar and nd isotopic systems on fine-grained sediments', *Quaternary Science Reviews* **27**(5-6), 497–517.

VanLaningham, S. & Mark, D. F. (2011), 'Step heating of 40ar/39ar standard mineral mixtures: investigation of a fine-grained bulk sediment provenance tool', *Geochimica et Cosmochimica Acta* **75**(9), 2324–2335.

Vatai, E., Varga, D. & Uchrin, J. (1968), 'Measurement of the $/\beta+$ ratio in the decay of 22na and 74as', *Nuclear Physics A* **116**(3), 637–642.

Villa, I. M. & Hanchar, J. M. (2013), 'K-feldspar hygrochronology', *Geochimica et Cosmochimica Acta* **101**, 24–33.

Villaseñor, T., Jaeger, J. M. & Foster, D. A. (2016), 'Linking late pleistocene alpine glacial erosion and continental margin sedimentation: Insights from 40ar/39ar dating of silt-sized sediment, canterbury basin, new zealand', *Earth and Planetary Science Letters* **433**, 303–316.

Von Eynatten, H. & Wijbrans, J. (2003), 'Precise tracing of exhumation and provenance using 40ar/39ar geochronology of detrital white mica: the example of the central alps', *Geological Society, London, Special Publications* **208**(1), 289–305.

Waitt Jr, R. B. (1980), 'About forty last-glacial lake missoula jökulhlaups through southern washington', *The Journal of Geology* **88**(6), 653–679.

Waitt, R. B. (2016), 'Megafloods and clovis cache at wenatchee, washington', *Quaternary Research* **85**(3), 430–444.

Waitt, R. B., Denlinger, R. P. & O'Connor, J. (2009), 'Many monstrous missoula floods down channeled scabland and columbia valley, washington'.

Wang, M., Audi, G., Kondev, F., Huang, W., Naimi, S. & Xu, X. (2017), 'The ame2016 atomic mass evaluation (ii). tables, graphs and references', *Chinese Physics C* **41**(3), 030003.

Wartho, J.-A. (1991), Argon isotope systematics and mineralogy of metamorphic hornblendes from the Karakoram., PhD thesis, University of Leeds.

Wartho, J.-A., Kelley, S. P., Brooker, R. A., Carroll, M. R., Villa, I. M. & Lee, M. R. (1999), 'Direct measurement of ar diffusion profiles in a gem-quality madagascar k-feldspar using the ultra-violet laser ablation microprobe (uvlamp)', *Earth and Planetary Science Letters* **170**(1-2), 141–153.

Wasserburg, G. & Hayden, R. (1955), 'A40-k40 dating', *Geochimica et Cosmochimica Acta* **7**(1-2), 51–60.

Weckwerth, P., Wysota, W., Piotrowski, J. A., Adamczyk, A., Krawiec, A. & Dabrowski, M. (2019), 'Late weichselian glacier outburst floods in north-eastern poland: Landform evidence and palaeohydraulic significance', *Earth-Science Reviews* **194**, 216–233.

Williams, A. (1964), 'Measurement of the ratio of electron capture to positon emission in the decay of na-22', *Nuclear Physics* **52**, 324–332.

Williford, K. H., Farley, K. A., Stack, K. M., Allwood, A. C., Beaty, D., Beegle, L. W., Bhartia, R., Brown, A. J., de la Torre Juarez, M., Hamran, S.-E. et al. (2018), The nasa mars 2020 rover mission and the search for extraterrestrial life, *in* 'From Habitability to Life on Mars', Elsevier, pp. 275–308.

Winsemann, J., Alho, P., Laamanen, L., Goseberg, N., Lang, J. & Klostermann, J. (2016), 'Flow dynamics, sedimentation and erosion of glacial lake outburst floods along the middle pleistocene scandinavian ice sheet (northern central europe)', *Boreas* **45**(2), 260–283.

Yu, S.-Y., Colman, S. M. & Li, L. (2016), 'Bemma: a hierarchical bayesian end-member modeling analysis of sediment grain-size distributions', *Mathematical Geosciences* **48**(6), 723–741.

Yukawa, H. & Sakata, S. (1935), 'On the theory of the β-disintegration and the allied phenomenon', *Proceedings of the Physico-Mathematical Society of Japan. 3rd Series* **17**, 467–479.

Zeitler, P. K. (1987), 'Argon diffusion in partially outgassed alkali feldspars: Insights from 40ar39ar analysis', *Chemical Geology: Isotope Geoscience section* **65**(2), 167–181.